Photocatalytic Studies of Undoped and Doped ZnS Nanostructures

A
Thesis
Submitted for the award of degree of

Doctor of Philosophy

By

Jagdeep Kaur

Under the guidance of

Dr. O. P. Pandey

Senior Professor and Dean (Research and Sponsored Projects)

School of Physics & Materials Science
Thapar University, Patiala-147004
August 2015

Dedicated to

My beloved

Parents

CERTIFICATE

This is to certify that the thesis entitled **"Photocatalytic Studies of Undoped and Doped ZnS Nanostructures"** which is being submitted by Jagdeep Kaur in fulfillment of the requirements for the award of the degree of Doctor of Philosophy in the School of Physics and Materials Science, Thapar University, Patiala (Punjab), India is an exclusive record of candidate's own research work under my supervision. The thesis in part or in full has not been submitted in any other university or institute for the award of any degree. The thesis is fit to be considered for the award of degree of Doctor of Philosophy.

Dr. O.P. Pandey
Senior Professor and Dean (Research and Sponsored Projects)
School of Physics and Materials Science
Thapar University
Patiala-147004
INDIA

ACKNOWLEDGEMENT

This thesis is the end of my journey in obtaining my Ph.D. I have not travelled in a vacuum in this journey. The best and worst moments have been shared with many people during my doctoral journey. It has been a great privilege to spend several years in the School of Physics and Materials Science at Thapar University. No matter how much enterprising and entrepreneurial one's thinking is, yet nobody can do everything all by himself/herself without some help and guidance. It is inhumane if the concerned person's assistance goes without appreciation and thanks. At the end of my thesis, it gives me pleasure to express my thanks to all those who have contributed in many ways to make this thesis possible and has made it an unforgettable experience for me.

My first and foremost offering of thanks goes to the architect who shaped my dreams into reality, my guide and mentor **Dr. Om Prakash Pandey** for his excellent guidance, care and providing me with an excellent atmosphere for doing research. Perseverance, exuberance and positive approach are just some of the traits he imprinted on my personality. He steered me this journey through his invaluable advice, positive criticism, stimulating discussion and consistent encouragement. His meticulous attention towards my proceedings, his devoted time and his ideas have enabled me to make the project a success. His faith in me has always made me more confident. It had been my privilege to work under his guidance.

I would like to express my thanks to the members of doctoral committee: **Dr. D. P. Singh, Dr. S. D. Tiwari and Dr. H. Bhunia** for their encouragement, insightful comments and fruitful criticism.

I am thankful to **Dr. Manoj Sharma**, Head, School of Physics and Materials Science for providing any kind of help and support when required.

I am also very grateful to the faculty of School of Physics and Materials Science, **Dr. Kulvir Singh, Dr. N. K. Verma, Dr. B. N. Chudasama, Dr. Loveleen Brar** for their valuable suggestions during my PhD work. I am indebted to **Dr. Manoj Sharma** (Assistant Professor and Department In-charge, Department of Nanotechnology, Sri Guru Granth Sahib World University, Fatehgarh Sahib, Punjab) for any kind of help and valuable suggestions whenever I needed out of his busy schedule. I am grateful to him for sharing his time and expertise. His comments and views were very insightful and helpful. I also express my sincere thanks to **SAI Labs**, Thapar University Patiala, **AIRF**, JNU, New Delhi and **SAIF**, IIT Bombay for characterizing my samples. I am indeed grateful to **Dr. Rajesh Kumar, Dr.**

Vijay Laxmi, Mr. Rajesh, Mr. Sandeep and Ms. Richa of School of Chemistry and Biochemistry for providing me help in difficult hours.

I would also like to acknowledge **Mrs. Parveen, Mrs. Neelam, Mr. Indermani Mishra, Mr. Jant Singh and Mr. Vijay** for their kind help and support during various stages of administrative formalities.

Mrs. Sushila Pandey is highly acknowledged for her unconditional love and kind support. Words are inadequate in expressing my sincere thanks to my dear friends and labmates **Dr. Ranvir Panwar, Mrs. Shalu Panwar, Mr. Suresh Kumar, Dr. Gurbinder Chaudhary, Mrs. Sakshi Gupta, Mrs. Suninder Jeet Kaur, Mr. Deepak Kumar, Mr. Manish Mittal, Ms. Parveer Kaur, Ms. Gitanjali Dhir, Mr. Mintu Tyagi, Dr. Jaspal Singh, Mrs. Kamaldeep Kaur, Mr. Satwinder Singh, Mr. Gaurav Singla, Mr. Paramjyot Jha, Dr. Kapil Sood, Dr. Chandni Khurana, Mrs. Samiksha Verma, Ms. Navjot Kaur, Ms. Purnima Sharma, Mrs. Pooja Singla** for their support in every moment of difficulty.

My in-laws family especially my husband, **Mr. Satwant Singh** deserves special thanks for his patience and moral support during this phase of life. Words are not enough to express my gratitude towards him. I am also thankful to my sisters **Ms. Rajvir Kaur** and **Mrs. Sukhvir Kaur** and brother, **Mr. Amandeep Singh** for their moral support whenever I needed.

Last but not the least, I would like to pay high regards to my father **Mr. Rajinder Singh** and my mother, **Mrs. Karamjit Kaur** for their sincere encouragement and inspiration throughout my research work and lifting me uphill this phase of life. I owe everything to them.

Above all, I would like to thank the Almighty, **God**. He has given me the power to believe in myself and pursue my dreams. I could never have done this without the faith I have in Him.

Jagdeep Kaur

(Jagdeep Kaur)

LIST OF PUBLICATIONS

Research Publications

[1] **Jagdeep Kaur**, Manoj Sharma and O. P. Pandey, Effect of pH on Photocatalytic Activity of Capped ZnS Nanoparticles, **Journal of Nanoscience and Nanotechnology** 13 (2013) 4861-4871.

[2] **Jagdeep Kaur**, Manoj Sharma and O. P. Pandey, Synthesis, Characterization, Photocatalytic and Reusability Studies of Capped ZnS Nanoparticles, **Bulletin of Materials Science** 37 (2014) 1-10.

[3] **Jagdeep Kaur**, Manoj Sharma and O. P. Pandey, Photocatalytic Studies of Capped ZnS Nanoparticles, **AIP Conference Proceedings** 1536 (2013) 81-82; doi: 10.1063/1.4810110

[4] **Jagdeep Kaur**, Manoj Sharma and O. P. Pandey, Effect of pH on Size of ZnS Nanoparticles and its Application for Dye Degradation, **Particulate Science and Technology** 33 (2015) 184-188.

[5] **Jagdeep Kaur**, Manoj Sharma and O. P. Pandey, Structural and optical studies of undoped and copper doped zinc sulphide nanoparticles for photocatalytic application, **Superlattices and Microstructures** 77 (2015) 35-53.

[6] **Jagdeep Kaur**, Manoj Sharma and O. P. Pandey, Photoluminescence and photocatalytic studies of metal ions (Mn and Ni) doped ZnS nanoparticles, **Optical Materials** 47 (2015) 7-17.

[7] **Jagdeep Kaur**, Manoj Sharma and O. P. Pandey, Photocatalytic studies of 1-thioglycerol capped ZnS nanoparticles synthesized at different pH, **Advanced Powder Technology** (under review).

List of Papers presented in Conferences (International/ National)

[1] **Jagdeep Kaur**, Manoj Sharma, O. P. Pandey, Synthesis and Photocatalytic Studies of ZnS Nanoparticles, International Conference on Energy Efficient Materials Manufacturing Methods & Machineries for Ceramic Industries (IC2E4MCI-11), 19th-22nd December 2011, Agra **(Poster presentation)**.

[2] **Jagdeep Kaur**, Manoj Sharma, O. P. Pandey, Synthesis and optical studies of co-doped Zinc Sulphide nanoparticles, 4th National Symposium for Materials Research Scholars (MR-12) & Workshop on Advanced Characterization Techniques, 3rd – 5th May 2012, IIT Bombay **(Poster presentation)**.

[3] **Jagdeep Kaur**, Manoj Sharma, O. P. Pandey, Effect of doped and capped ZnS nanoparticles as photo-catalyst in UV Visible light, International Conference on Solar Energy Photovoltaic (ICSEP-2012), 19th - 21st December 2012, KIIT University **(Poster presentation)**.

[4] **Jagdeep Kaur**, Manoj Sharma, O. P. Pandey, Photocatalytic Studies of Capped ZnS Nanoparticles, Proceeding of International Conference on Recent Trends in Applied Physics and Material Science (RAM 2013), 1st-2nd February 2013, Bikaner **(Poster presentation and full paper)**.

[5] **Jagdeep Kaur**, Manoj Sharma, O. P. Pandey, Structural and Optical Studies of Mn Doped ZnS Nanostructures, National conference on innovative molecules for sustainable future (NCIMSF-2013), 24th -26th October 2013, Thapar University Patiala **(Poster presentation)**.

[6] **Jagdeep Kaur**, Manoj Sharma, O. P. Pandey, Effect of pH on Size of ZnS Nanoparticles and its Application for Dye Degradation, International conference on powder, granule and bulk solids:innovations and applications (PGBSIA 2013), 28th-30th November 2013, Thapar University, Patiala **(Poster presentation and full paper)**.

[7] **Jagdeep Kaur**, Manoj Sharma, O. P. Pandey, Effect of Mn^{2+} on optical properties of ZnS Nanostructures, International Conference on Nano Science and Technology (ICONSAT 2014), 3rd-5th March 2014 **(Poster presentation)**.

INDEX

Contents		Page No.
Certificate		i
Acknowledgement		ii
List of publications		iv
List of papers presented in conferences (International/National)		v
List of figures		x
List of tables		xviii
Preface		xx
Chapter 1	**Introduction**	**1-19**
	Overview	1
1.1	Background	2
1.2	Photocatalysis	3
	1.2.1 Molecular electronic excitation	4
	1.2.2 Semiconductor electronic excitation	5
	1.2.2.1 Band edge positions	7
	1.2.2.2 Adsorption	8
	1.2.2.3 Role of traps	8
	1.2.2.4 Photocatalyst size	9
1.3	Synthesis	10
	1.3.1 Top-down approach	10
	1.3.2 Bottom-up approach	10
	1.3.2.1 Electrostatic stabilization	12
	1.3.2.2 Polymeric stabilization	13
	1.3.2.2(a) Steric stabilization	13
	1.3.2.2(b) Depletion stabilization	14
1.4	Photocatalysis on ZnS	15
	References	16
Chapter 2	**Literature Review**	**20-40**
	Overview	20
2.1	Introduction	21
2.2	Plan of work	35
	References	35
Chapter 3	**Experimental Details**	**41-46**
	Overview	41

3.1	Raw Materials	42
3.2	Sample preparation	42
	3.2.1 ZnS nanoparticles with varying dopants and dopant concentrations	42
	3.2.2 Undoped ZnS nanoparticles with varying solution pH	43
	3.2.3 ZnS/ZnO and ZnS/Ag_2S nanocomposites	43
	3.2.4 ZnS/ZnO core-shell particles	43
3.3	Characterization Techniques	44
3.4	Apparatus for photocatalytic study	44
	References	46
Chapter 4	**Results and Discussion (Undoped ZnS nanoparticles)**	**47-76**
	Overview	47
4.1	Studies of undoped ZnS	48
	4.1.1 Introduction	48
	4.1.2 XRD Studies	48
	4.1.3 TEM Analysis	49
	4.1.4 FTIR Analysis	50
	4.1.5 UV-Vis studies	51
	4.1.6 Photoluminescence studies	53
	4.1.7 Photocatalytic studies	54
	4.1.8 UV irradiation study of TG capped ZnS NPs	57
	4.1.9 Photocatalytic studies of UV irradiated sample	59
4.2	Effect of pH on structural, optical and photocatalytic properties of undoped ZnS NPs	60
	4.2.1 Introduction	60
	4.2.2 DLS Studies	60
	4.2.3 XRD Analysis	62
	4.2.4 TEM Analysis	63
	4.2.5 FTIR Analysis	64
	4.2.6 UV-Vis Analysis	65
	4.2.7 Photoluminescence studies	67
	4.2.8 Photocatalytic studies	68
	References	74
Chapter 5	**Results and Discussion (Doped ZnS nanoparticles)**	**77-146**

	Overview	77
5.1	Introduction	78
5.2	Cu doped ZnS	79
	5.2.1 XRD and EDX studies	79
	5.2.2 TEM analysis	82
	5.2.3 FTIR Analysis	83
	5.2.4 UV-Vis studies	85
	5.2.5 Photoluminescence studies	88
	5.2.6 Photocatalytic studies	89
5.3	Ni doped ZnS	95
	5.3.1 XRD and EDX studies	95
	5.3.2 TEM analysis	98
	5.3.3 FTIR Analysis	99
	5.3.4 UV-Vis studies	101
	5.3.5 Photoluminescence studies	104
	5.3.6 Photocatalytic studies	105
5.4	Mn doped ZnS	109
	5.4.1 XRD and EDX studies	109
	5.4.2 TEM analysis	113
	5.4.3 FTIR Analysis	114
	5.4.4 UV-Vis studies	116
	5.4.5 Photoluminescence studies	118
	5.4.6 Photocatalytic studies	120
5.5	Ag_2S modified ZnS	124
	5.5.1 Synthesis	124
	5.5.2 XRD and EDX studies	125
	5.5.3 TEM analysis	129
	5.5.4 FTIR Analysis	132
	5.5.5 UV-Vis studies	133
	5.5.6 Photoluminescence studies	136
	5.5.7 Photocatalytic studies	138
	References	143
Chapter 6	**Results and Discussion (ZnS/ZnO and ZnS/Ag_2S Nanocomposites)**	**147-186**
	Overview	147

6.1	Nanocomposites	148
	6.1.1 Introduction	148
	6.1.2 ZnS/ZnO nanocomposites	149
	6.1.2.1 XRD analysis	149
	6.1.2.2 TEM analysis	150
	6.1.2.3 UV-Vis studies	151
	6.1.2.4 Photoluminescence studies	154
	6.1.2.5 Photocatalytic studies	157
	6.1.3 ZnS/Ag_2S nanocomposites	162
	6.1.3.1 XRD analysis	162
	6.1.3.2 TEM analysis	163
	6.1.3.3 UV-Vis studies	164
	6.1.3.4 Photoluminescence studies	165
	6.1.3.5 Photocatalytic studies	167
6.2	ZnS-ZnO core shell nanoparticles	171
	6.2.1 Introduction	171
	6.2.2 XRD studies	173
	6.2.3 TEM studies	174
	6.2.4 UV-Vis studies	175
	6.2.5 Photoluminescence studies	177
	6.2.6 Photocatalytic studies	180
	References	184
Chapter 7	**Conclusions and Future Scope**	**187-192**
	Overview	187
7.1	Conclusions	188
7.2	Future Scope	192

LIST OF FIGURES

		Page No.
Chapter 1		
Figure 1.1	Catalyzed photoreaction, (a) initial excitation of adsorbate, and (b) Sensitized photoreaction, initial excitation of photocatalyst.	4
Figure 1.2	Excitation and de-excitation processes in a molecule.	5
Figure 1.3	Fate of charge carriers upon photoexcitation of semiconductor.	6
Figure 1.4	Band edge positions of various semiconductors in aqueous electrolytes.	8
Figure 1.5	Illustration of nucleation and growth during the synthesis of NPs.	11
Figure 1.6	Colloidal particles (a) in the absence of double layer are free to collide and agglomerate, (b) presence of electrical double layer prevents agglomeration.	13
Figure 1.7	Steric stabilization of NPs (a) entropic effect, (b) osmotic repulsion.	14
Figure 1.8	A sketch of non-adsorbing polymer chains around two spherical colloids.	15
Chapter 3		
Figure 3.1	Sketch of photoreactor set-up to carry out photocatalytic experiments.	45
Chapter 4		
Figure 4.1	X-Ray Diffraction pattern of undoped ZnS NPs in the range 20°-70°.	48
Figure 4.2	(a-b) HRTEM images of undoped ZnS. Lattice fringing have been encircled for better understanding.	49
Figure 4.3	FTIR spectra of TG capped undoped ZnS NPs.	50
Figure 4.4	Diffuse reflectance spectra (DRS) of undoped ZnS NPs.	51
Figure 4.5	Absorption spectra of undoped ZnS NPs.	52
Figure 4.6	Tauc plot for undoped ZnS NPs to determine band gap.	53
Figure 4.7	Photoluminescence emission spectra of undoped ZnS NPs.	53

Figure 4.8	Absorbance spectra of crystal violet. Inset shows molecular structure of the same.	55
Figure 4.9	Absorbance spectra of crystal violet degraded in the presence of undoped ZnS.	55
Figure 4.10	Variation of C_t/C_0 with irradiation time.	56
Figure 4.11	Plot between $\ln(C_t/C_0)$ and irradiation time to determine the value of rate constant k.	56
Figure 4.12	Absorbance spectra of TG capped ZnS irradiated with UV light in different intervals of time. Inset shows the change in absorption wavelength in different intervals of irradiation time.	58
Figure 4.13	Mechanism of photochemical reactions occurring in ZnS-H_2O system in presence of UV light.	58
Figure 4.14	Variation of C_t/C_0 with irradiation time for as prepared undoped ZnS and UV irradiated ZnS.	59
Figure 4.15	Cumulative particle size distribution of ZnS synthesized at different pH.	61
Figure 4.16	Variation of particle size with pH of solution.	61
Figure 4.17	XRD patterns of samples in the range 20°-70°.	63
Figure 4.18	HRTEM image of ZnS synthesized at pH 10.	63
Figure 4.19	FTIR spectra of ZnS synthesized at different pH.	64
Figure 4.20	UV-Vis absorption spectra of samples synthesized at pH 5.6, 8, 10 and 12.	66
Figure 4.21	Tauc plots for as prepared samples to determine band gap.	66
Figure 4.22	Variation of optical band gap with the change in pH of the solution.	67
Figure 4.23	Photoluminescence spectra of as prepared samples.	68
Figure 4.24	Absorbance spectra of crystal violet degraded in the presence of ZnS synthesized at different pH values.	70
Figure 4.25	Variation of C_t/C_0 with irradiation time for photochemical reactions catalysed with as prepared samples.	71
Figure 4.26	Plot between $\ln(C_t/C_0)$ and irradiation time to determine the value of rate constant k.	72
Figure 4.27	Degradation percentage of crystal violet in the presence of sample	72

synthesized at (a) pH 5.6, (b) pH 8, (c) pH 10 and (d) pH 12 at different irradiation times.

Chapter 5

Figure 5.1 XRD patterns of $Zn_{1-x}Cu_xS$; x = 0, 0.01, 0.02, 0.03 and 0.04 in the range 20°-70°. 79

Figure 5.2 EDX patterns of $Zn_{1-x}Cu_xS$; (a) x = 0, (b) x=0.01, (c) x=0.02, (d) x=0.03 and (e) x=0.04. 81

Figure 5.3 XRD patterns of $Zn_{1-x}Cu_xS$; x = 0, 0.01, 0.02, 0.03 and 0.04 in the range 22°-38°. 82

Figure 5.4 (a) TEM image of thioglycerol capped $Zn_{1-x}Cu_xS$; x = 0.02, (b) HRTEM image of the same sample. 83

Figure 5.5 FTIR spectra of $Zn_{1-x}Cu_xS$; x = 0, 0.03. 84

Figure 5.6 Absorption spectra of undoped ZnS. Inset shows corresponding Tauc plot. 85

Figure 5.7 Absorption spectra of $Zn_{1-x}Cu_xS$; x = 0.01, 0.02, 0.03 and 0.04 plotted by Kubelka Munk method. 86

Figure 5.8 Tauc plots for $Zn_{1-x}Cu_xS$; x = 0.01, 0.02, 0.03 and 0.04 to determine band gap. 87

Figure 5.9 Variation in band gap of ZnS with Cu doping. 87

Figure 5.10 Photoluminescence emission spectra of $Zn_{1-x}Cu_xS$; x = 0, 0.01, 0.02, 0.03 and 0.04 at λ_{exc}=320 nm. 88

Figure 5.11 Absorbance spectra of crystal violet degraded in the presence of $Zn_{1-x}Cu_xS$ (a) x = 0, (b) x= 0.03. 90

Figure 5.12 Variation of C_t/C_0 with irradiation time for $Zn_{1-x}Cu_xS$; x = 0, 0.01, 0.02, 0.03 and 0.04. 91

Figure 5.13 Plot between $\ln(C_t/C_0)$ and irradiation time to determine the value of rate constant k. 91

Figure 5.14 Degradation percentage of crystal violet in the presence of $Zn_{1-x}Cu_xS$ (a) x = 0, (b) 0.01, (c) 0.02, (d) 0.03 and (e) 0.04 at different irradiation times. 92

Figure 5.15 Schematic energy level diagram showing the emission and photocatalytic mechanism in undoped and Cu doped ZnS NPs. 94

Figure 5.16 XRD patterns of $Zn_{1-x}Ni_xS$; x = 0, 0.01, 0.02, 0.03 and 0.04 in the range 20°-70°. 95

Figure 5.17	EDX patterns of $Zn_{1-x}Ni_xS$; (a) x = 0, (b) x=0.01, (c) x=0.02, (d) x=0.03 and (e) x=0.04.	97
Figure 5.18	XRD patterns of $Zn_{1-x}Ni_xS$; x = 0, 0.01, 0.02, 0.03 and 0.04 in the range 22°-38°.	98
Figure 5.19	(a) TEM image of thioglycerol capped $Zn_{1-x}Ni_xS$; x = 0.02, (b) HRTEM image of the same sample.	99
Figure 5.20	FTIR spectra of $Zn_{1-x}Ni_xS$; x = 0, 0.01.	100
Figure 5.21	Absorption spectra of $Zn_{1-x}Ni_xS$; x = 0.01, 0.02, 0.03 and 0.04 plotted by Kubelka Munk method.	101
Figure 5.22	Tauc plots for $Zn_{1-x}Ni_xS$; x = 0.01, 0.02, 0.03 and 0.04 to determine band gap.	102
Figure 5.23	Variation in band gap of ZnS with Ni doping.	102
Figure 5.24	Photoluminescence emission spectra of $Zn_{1-x}Ni_xS$; x = 0.01, 0.02, 0.03 and 0.04 at λ_{exc}=320 nm.	104
Figure 5.25	Absorbance spectra of crystal violet degraded in the presence of $Zn_{1-x}Ni_xS$ (a) x = 0.01, (b) x= 0.04.	106
Figure 5.26	Variation of C_t/C_0 with irradiation time for $Zn_{1-x}Ni_xS$; x = 0, 0.01, 0.02, 0.03 and 0.04.	107
Figure 5.27	Plot between $\ln(C_t/C_0)$ and irradiation time to determine the value of rate constant k.	107
Figure 5.28	Degradation percentage of crystal violet in the presence of $Zn_{1-x}Ni_xS$ (a) x = 0, (b) 0.01, (c) 0.02, (d) 0.03 and (e) 0.04 at different irradiation times.	108
Figure 5.29	XRD patterns of $Zn_{1-x}Mn_xS$; x = 0, 0.01, 0.02, 0.03 and 0.04 in the range 20°-70°.	110
Figure 5.30	EDX patterns of $Zn_{1-x}Mn_xS$; (a) x = 0, (b) x=0.01, (c) x=0.02, (d) x=0.03 and (e) x=0.04.	112
Figure 5.31	XRD patterns of $Zn_{1-x}Mn_xS$; x = 0, 0.01, 0.02, 0.03 and 0.04 in the range 22°-38°.	112
Figure 5.32	(a) TEM image of thioglycerol capped $Zn_{1-x}Mn_xS$; x = 0.01, (b) HRTEM image of the same sample.	114
Figure 5.33	FTIR spectra of $Zn_{1-x}Mn_xS$; x = 0, 0.03.	115
Figure 5.34	Absorption spectra of $Zn_{1-x}Mn_xS$; x = 0.01, 0.02, 0.03 and 0.04	116

plotted by Kubelka Munk method.

Figure 5.35 Tauc plots for $Zn_{1-x}Mn_xS$; x = 0.01, 0.02, 0.03 and 0.04 to determine band gap. 116

Figure 5.36 Variation in band gap of ZnS with Mn doping. 117

Figure 5.37 Photoluminescence emission spectra of $Zn_{1-x}Mn_xS$; x = 0.01, 0.02, 0.03 and 0.04 in the range (a) 350-800 nm and (b) 350-500 nm. 119

Figure 5.38 Absorbance spectra of crystal violet degraded in the presence of $Zn_{1-x}Mn_xS$ (a) x = 0.01, (b) x= 0.03. 121

Figure 5.39 Variation of C_t/C_0 with irradiation time for $Zn_{1-x}Mn_xS$; x = 0, 0.01, 0.02, 0.03 and 0.04. 122

Figure 5.40 Plot between $\ln(C_t/C_0)$ and irradiation time to determine the value of rate constant k. 122

Figure 5.41 Degradation percentage of crystal violet in the presence of $Zn_{1-x}Mn_xS$ (a) x = 0, (b) 0.01, (c) 0.02, (d) 0.03 and (e) 0.04 at different irradiation times. 123

Figure 5.42 XRD patterns of $Zn_{1-x}Ag_xS$; x = 0, 0.01, 0.02, 0.03 and 0.04 in the range 20°-70°. 126

Figure 5.43 EDX patterns of $Zn_{1-x}Ag_xS$; (a) x = 0, (b) x=0.01, (c) x=0.02, (d) x=0.03 and (e) x=0.04. 128

Figure 5.44 XRD patterns of $Zn_{1-x}Ag_xS$; x = 0, 0.01, 0.02, 0.03 and 0.04 in the range 22°-38°. 128

Figure 5.45 HRTEM image of thioglycerol capped $Zn_{1-x}Ag_xS$; x = 0.01. Inset shows the portion of same image at 1 nm scale. 129

Figure 5.46 (a-b) TEM images of thioglycerol capped $Zn_{1-x}Ag_xS$; x = 0.02 (c) HRTEM image of the same sample. 131

Figure 5.47 (a-b) HRTEM images of thioglycerol capped $Zn_{1-x}Ag_xS$; x = 0.03. 132

Figure 5.48 FTIR spectra of $Zn_{1-x}Ag_xS$; x = 0, 0.04. 132

Figure 5.49 Absorption spectra of $Zn_{1-x}Ag_xS$; x = 0.01, 0.02, 0.03 and 0.04 plotted by Kubelka Munk method. 134

Figure 5.50 Tauc plots for $Zn_{1-x}Ag_xS$; x = 0.01, 0.02, 0.03 and 0.04 to determine band gap. 135

Figure 5.51 Variation in band gap of ZnS with the addition of $AgNO_3$. 135

Figure 5.52 Photoluminescence emission spectra of $Zn_{1-x}Ag_xS$; x = 0.01, 0.02, 137

0.03 and 0.04.

Figure 5.53 Absorbance spectra of crystal violet degraded in the presence of $Zn_{1-x}Ag_xS$ (a) x = 0.03, (b) x= 0.04. 139

Figure 5.54 Variation of C_t/C_0 with irradiation time for $Zn_{1-x}Ag_xS$; x = 0, 0.01, 0.02, 0.03 and 0.04. 139

Figure 5.55 Plot between $\ln(C_t/C_0)$ and irradiation time to determine the value of rate constant k. 140

Figure 5.56 Degradation percentage of crystal violet in the presence of $Zn_{1-x}Ag_xS$ (a) x = 0, (b) 0.01, (c) 0.02, (d) 0.03 and (e) 0.04 at different irradiation times. 141

Figure 5.57 Possible mechanism of photocatalysis in presence of $Zn_{1-x}Ag_xS$; x = 0.03 and 0.04 photocatalysts. 142

Chapter 6

Figure 6.1 XRD patterns of ZnS/ZnO NCs. 149

Figure 6.2 (a-b) TEM images of z2. 151

Figure 6.3 Diffuse reflectance spectra of ZnS/ZnO NCs. 151

Figure 6.4 Absorption spectra of ZnS/ZnO NCs plotted by Kubelka Munk method. 152

Figure 6.5 Tauc plots for ZnS/ZnO NCs to determine band gap. 153

Figure 6.6 Band gap variation in as prepared ZnS/ZnO NCs. 154

Figure 6.7 Photoluminescence excitation spectra of ZnS/ZnO NCs at λ_{em}=508 nm. 156

Figure 6.8 Photoluminescence emission spectra of ZnS/ZnO NCs at λ_{exc}=350 nm. 156

Figure 6.9 Absorbance spectra of crystal violet degraded in the presence of (a) z3, (b) z4. 158

Figure 6.10 Variation of C_t/C_0 with irradiation time for z1, z2, z3 and z4. 158

Figure 6.11 Plot between $\ln(C_t/C_0)$ and irradiation time to determine the value of rate constant k. 159

Figure 6.12 Degradation percentage of crystal violet in the presence of z1, z2, z3 and z4 at different irradiation times. 159

Figure 6.13 Variation in pH of solution in which the composites have been 160

synthesized.

Figure 6.14 XRD patterns of ZnS/Ag_2S NCs. 162

Figure 6.15 HRTEM images of $Zn_{1-x}Ag_xS$; x = 0.04. 164

Figure 6.16 Absorption spectra of $Zn_{1-x}Ag_xS$; x = 0, 0.01, 0.02, 0.03 and 0.04 NCs. 164

Figure 6.17 Photoluminescence emission spectra of (a) ZnS and (b) ZnS/Ag_2S NCs at λ_{exc}=390 nm. 166

Figure 6.18 Absorbance spectra of crystal violet degraded in the presence of $Zn_{1-x}Ag_xS$ (a) x = 0.03, (b) x= 0.04 NCs. 168

Figure 6.19 Variation of C_t/C_0 with irradiation time for $Zn_{1-x}Ag_xS$; x = 0, 0.01, 0.02, 0.03 and 0.04 NCs. 168

Figure 6.20 Plot between $\ln(C_t/C_0)$ and irradiation time to determine the value of rate constant k. 169

Figure 6.21 Degradation percentage of crystal violet in the presence of $Zn_{1-x}Ag_xS$ (a) x = 0, (b) 0.01, (c) 0.02, (d) 0.03 and (e) 0.04 NCs at different irradiation times. 170

Figure 6.22 XRD patterns of ZnS, ZnS-ZnO CS and ZnS prepared at pH 10. 173

Figure 6.23 (a) TEM image of ZnS-ZnO CSNPs, (b-c) HRTEM image of the same sample. 175

Figure 6.24 Absorption spectra of ZnS-ZnO CS, ZnS and ZnS synthesized at pH 10. 176

Figure 6.25 Tauc plots for ZnS-ZnO CS, ZnS and ZnS synthesized at pH 10 to determine band gap. 177

Figure 6.26 Photoluminescence emission spectra of ZnS-ZnO CSNPs (a) at λ_{exc}=350 nm. Inset of the figure shows excitation spectra at λ_{em}=508 nm and (b) at λ_{exc}=450 nm. 178

Figure 6.27 Photoluminescence emission spectra of ZnS/ZnO NCs at λ_{exc}=350 nm. Inset of the figure shows excitation spectra at λ_{em}=508 nm. 179

Figure 6.28 Absorbance spectra of crystal violet degraded in the presence of ZnS-ZnO CS. 180

Figure 6.29 Variation of C_t/C_0 with irradiation time for ZnS-ZnO CS, ZnS and ZnS synthesized at pH 10. 181

Figure 6.30 Plot between $\ln(C_t/C_0)$ and irradiation time to determine the value of rate constant k. 181

Figure 6.31 Degradation percentage of crystal violet in the presence of (a) ZnS-ZnO CS, (b) ZnS and (c) ZnS synthesized at pH 10 at different irradiation times. 182

Figure 6.32 Proposed mechanism for photocatalytic application of ZnS-ZnO CSNPs. 183

LIST OF TABLES

Page No.

Chapter 2

Table 2.1 Summary of photocatalytic studies of ZnS by various research groups and their main findings. 24

Chapter 4

Table 4.1 Peak assignment of various bonds in thioglycerol capped ZnS NPs. 51

Table 4.2 Hydrodynamic size obtained for all samples. 62

Table 4.3 Peak assignment of various bonds in ZnS synthesized at different pH. 65

Table 4.4 Calculated band gap values and corresponding absorption wavelengths of ZnS synthesized at different pH. 67

Table 4.5 First order rate constants for the photocatalytic degradation of crystal violet and corresponding percent degradation for different photochemical reactions. 73

Chapter 5

Table 5.1 Peak assignment of various bonds in thioglycerol capped $Zn_{1-x}Cu_xS$; x = 0, 0.03. 84

Table 5.2 Calculated band gap values and corresponding absorption wavelengths of $Zn_{1-x}Cu_xS$; x = 0, 0.01, 0.02, 0.03 and 0.04. 88

Table 5.3 First order rate constants for the photocatalytic degradation of crystal violet and corresponding percent degradation using $Zn_{1-x}Cu_xS$; x = 0, 0.01, 0.02, 0.03 and 0.04 as photocatalysts. 93

Table 5.4 Peak assignment of various bonds in thioglycerol capped $Zn_{1-x}Ni_xS$; x = 0, 0.01. 100

Table 5.5 Calculated band gap values and corresponding absorption wavelengths of $Zn_{1-x}Ni_xS$; x = 0, 0.01, 0.02, 0.03 and 0.04. 103

Table 5.6 First order rate constants for the photocatalytic degradation of crystal violet and corresponding percent degradation using $Zn_{1-x}Ni_xS$; x = 0, 0.01, 0.02, 0.03 and 0.04 as photocatalysts. 109

Table 5.7 Peak assignment of various bonds in thioglycerol capped $Zn_{1-x}Mn_xS$; x = 0, 0.03. 115

Table 5.8 Calculated band gap values and corresponding absorption wavelengths of $Zn_{1-x}Mn_xS$; x = 0, 0.01, 0.02, 0.03 and 0.04. 118

Table 5.9 First order rate constants for the photocatalytic degradation of crystal violet and corresponding percent degradation using $Zn_{1-x}Mn_xS$; x = 0, 0.01, 0.02, 0.03 and 0.04 as photocatalysts. 123

Table 5.10 Peak assignment of various bonds in thioglycerol capped $Zn_{1-x}Ag_xS$; x = 0, 0.04. 133

Table 5.11 Calculated band gap values and corresponding absorption wavelengths of $Zn_{1-x}Ag_xS$; x = 0, 0.01, 0.02, 0.03 and 0.04. 136

Table 5.12 First order rate constants for the photocatalytic degradation of crystal violet and corresponding percent degradation using $Zn_{1-x}Ag_xS$; x = 0, 0.01, 0.02, 0.03 and 0.04 as photocatalysts. 141

Chapter 6

Table 6.1 Calculated band gap values and corresponding absorption wavelengths of ZnS/ZnO NCs. 154

Table 6.2 First order rate constants for the photocatalytic degradation of crystal violet and corresponding percent degradation using z1, z2, z3 and z4 as photocatalysts. 160

Table 6.3 pH of the solution in which the different photocatalysts have been synthesized. 161

Table 6.4 First order rate constants for the photocatalytic degradation of crystal violet and corresponding percent degradation using $Zn_{1-x}Ag_xS$; x = 0, 0.01, 0.02, 0.03 NCs as photocatalysts. 170

Table 6.5 Calculated band gap values and corresponding absorption wavelengths of ZnS@pH 10, ZnS and ZnS-ZnO CS. 177

Table 6.6 First order rate constants for the photocatalytic degradation of crystal violet and corresponding percent degradation using ZnS-ZnO CS, ZnS and ZnS synthesized at pH 10 as photocatalysts. 182

PREFACE

The present work deals with the synthesis and characterization of undoped and doped ZnS nanoparticles (NPs). Studies related to nanocomposites (NCs) and core shell nanoparticles (CSNPs) have also been discussed. The entire work has been divided into **seven chapters**.

Chapter 1 deals with the introduction about the conventional methods used for degradation of organic pollutants. Role of photocatalysis in degrading organic pollutants is described. Also, various chemical reactions occurring in the process are discussed. The main factors which affect the catalytic activity of a photocatalyst are described in detail. Further, approaches developed to synthesize NPs have also been discussed. Methods to prevent agglomeration of NPs and to stabilize them are explained. A brief introduction about ZnS and its application in photocatalysis is also provided.

In **Chapter 2**, reported work which describes synthesis, structural, optical and photocatalytic studies of ZnS is reviewed. Effect of various parameters like synthesis method, reaction temperature and doping with metal or non metal ions on optical and photocatalytic properties of ZnS has been described in detail. Besides this, other techniques developed to enhance the photocatalytic activity of ZnS at nanoscale has also been discussed. At the end of the chapter, the reasons for selecting main objectives behind this work are presented.

Chapter 3 describes the details of the synthesis procedure to prepare ZnS using different chemicals. Details of different techniques which have been employed to characterize as prepared samples like X-Ray diffraction (XRD) technique, transmission electron microscopy (TEM), high resolution transmission electron microscopy (HRTEM), Fourier transfer infrared (FTIR) spectroscopy, UV-Vis spectroscopy and photoluminescence (PL) spectroscopy including their model number have been provided. The set up used to perform photocatalytic experiments has been given in the end of the chapter. A brief introduction about the model pollutant selected for the entire photocatalytic study is also provided.

In **Chapter 4**, the studies of undoped ZnS NPs prepared via chemical precipitation route have been discussed. In the next section of this chapter, photocatalytic degradation of crystal violet has been carried out with the aim to study photocatalytic properties of as prepared ZnS NPs. Effect of UV irradiation on photocatalytic properties of ZnS has also been investigated. At the end of the chapter, effect of pH of the solution (in which the NPs are being synthesized) on optical and photocatalytic properties of undoped ZnS has also been discussed.

Chapter 5 describes the studies of doped ZnS NPs prepared via chemical precipitation route. Effect of doping ZnS with metal ions like Cu, Mn, Ni on photocatalytic properties of as

prepared ZnS NPs has been studied. Structural, optical and photocatalytic properties of thioglycerol capped and Ag_2S modified ZnS have also been discussed.

In **Chapter 6,** studies related to NCs of ZnS/ZnO and ZnS/Ag_2S prepared via chemical precipitation route have been presented. At the end of the chapter, a brief introduction has been given about core shell particles. Structural and optical studies of as synthesized ZnS-ZnO CSNPs have also been done to demonstrate their photocatalytic activity in degrading the organic pollutants.

Chapter 7 summarizes the results of the study made on ZnS which has been synthesized under different conditions. UV irradiation of undoped ZnS has shown better photocatalytic activity towards crystal violet. ZnS synthesized at pH 12 has shown superior photocatalytic properties as compared to that of samples synthesized at pH 5.6, 8 and 10. Doping of ZnS with Cu impurities has led to the enhancement in photocatalytic activity of ZnS. However, at higher concentration of Cu, photocatalytic activity has decreased. Doping with Ni and Mn ions has reduced the photocatalytic activity of ZnS. It has been concluded that dopant ions may reduce or enhance the photocatalytic activity of a semiconductor depending upon the type of transition involved in the emission pathway. Ag_2S modified ZnS has shown better catalytic activity at higher $AgNO_3$ content. All the prepared NCs have shown better photocatalytic activity towards crystal violet as compared to ZnS alone. ZnS-ZnO CSNPs have served as a better photocatalyst as compared to bare or organically passivated semiconductor ZnS NPs.

CHAPTER 1
INTRODUCTION

Overview

The present chapter gives the introduction about the conventional methods used for degradation of organic pollutants. Role of photocatalysis in degrading organic pollutants is described. Also, various chemical reactions occurring in the process are discussed. The main factors which affect the catalytic activity of a photocatalyst are described in detail. Further, approaches developed to synthesize nanoparticles have also been discussed. In this section, methods to prevent agglomeration of nanoparticles and to stabilize them are explained. In the last section of this chapter, a brief introduction about ZnS and its application in photocatalysis is provided.

1.1 Background

Among the various pollutions, air and water pollutions are of major concern. However, water pollution directly affects health of all living organisms. The textile industries contribute the most among the existing water pollution sources. It has direct connection with the environmental aspects which need to be considered. Major pollution in textile wastewater comes from dyeing and finishing processes. Dyeing is a combined process of bleaching and coloring, which generates voluminous quantities of wastewater and in turn causes water pollution. Out of various activities carried out in textile industry, discharge of large variety of dyes is the main issue of concern. The dyes used in these processes often have a complex aromatic molecular structure. Due to their good solubility, these dyes easily dissolve in water. However, these colored compounds do not degrade easily under natural conditions as these are photo stable and are resistant to aerobic digestion. These colored compounds are not only aesthetically displeasing but also have toxic and carcinogenic effects [1-2]. Till now, many methods have been developed to remove these dye effluents from wastewater. Broadly classifying, these methods fall in three different categories viz. physical, chemical and biological treatments. Physical methods include adsorption using activated carbon, silica gel, membrane filteration, ion exchange, irradiation, electrokinetic coagulation, and many more. Chemical methods include oxidation, H_2O_2-Fe (II) salts (Fentons reagents), ozonation, photochemical, sodium hypochloride (NaOCl), and electrochemical destruction [3-4]. Biological methods include decolourisation by white rot fungi, adsorption by living/dead microbial biomass, anaerobic textile dye bioremediation systems and other microbial cultures [3]. All the above methods have their own advantages and disadvantages. These methods do not remove dye effluents completely from water but only convert these effluents from one phase to another [3]. Although effective decolourization of both soluble and insoluble dyes is possible with Fentons reagents but the reaction ceases after complete consumption of Fe^{2+}. Also, it generates large amount of sludge [3]. Disposal of this toxic sludge is the severe drawback of these methods. Same is the problem with membrane filtration and electrokinetic coagulation. The second problem associated with membrane filtration is that only low molar mass dyes can pass through the filter system. With the aid of NaOCl, cleavage of azo-bond of dye is accelerated but in return, it releases aromatic amines [3]. Methods like ozonation, adsorption with activated carbon and electrochemical destruction are unfavourable due to their high cost although they remove dye to a greater extent. Activated carbon adsorption involves phase transfer of pollutants without decomposition and thus induces another pollution problem [3-4]. Biological treatment methods have also proved to be incapable of

obtaining satisfactory color elimination with current technologies. Although many organic molecules are degraded with these methods, but many others are recalcitrant due to their complex chemical structure and synthetic organic origin [3-4]. Moreover, slow reaction rates, disposal of sludge and need for strict control of proper pH and temperature are the other major obstacles faced during biological treatment of wastewater containing organic pollutants [5].

1.2. Photocatalysis

To overcome the problems as mentioned in above section, one of the methods adopted to remove dye effluents is semiconductors assisted photocatalytic degradation of dye (photocatalysis). Photocatalysis is generally defined as the acceleration of a photoreaction in the presence of a catalyst. In 1972, Fujishima and Honda discovered the photocatalytic splitting of water on TiO_2 electrodes [6]. Since then, research efforts are being made in understanding the fundamental mechanisms involved in the process to make it more efficient for degradation of organic pollutants. This method of dye degradation is more appealing as it offers many advantages over the above mentioned conventional methods.

- Decomposition of the pollutants can be conducted until total mineralization (CO_2, water, ions) [7].
- Most of the semiconductors used in this process are non-toxic, inexpensive and are capable of extended use without any substantial loss in their photocatalytic activity.
- Photocatalytic process can be operated at mild conditions and can be activated by sunlight (near UV region) thus, reducing the electric power required and therefore the operating costs.
- Expensive oxidizing chemicals like hydrogen peroxide and ozone are not required as ambient oxygen plays the role of an oxidant [8].
- Photocatalysts used in the process are self-produced and can be reused or recycled.
- By making photocatalyst visible responsive, sunlight can be used as a source of irradiation thereby reducing the use of UV light; the direct exposure of which impose harmful effects on human health.

In a heterogeneous photocatalytic system, photoinduced molecular transformations occur at the surface of catalyst. The process of photocatalysis is generally divided into two categories depending upon the fact that how the initial excitation takes place.

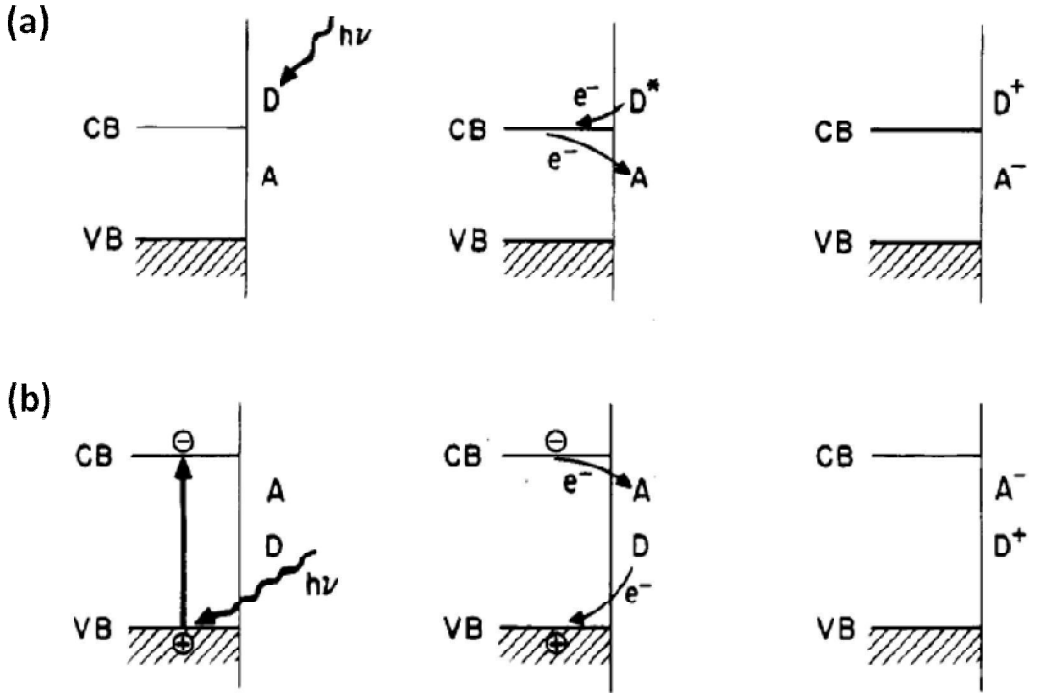

Figure 1.1: Catalyzed photoreaction, (a) initial excitation of adsorbate, and (b) Sensitized photoreaction, initial excitation of photocatalyst [9].

When initial photoexcitation takes place in an adsorbate (dye molecule), which interacts with the ground state substrate (catalyst), the process is known as catalyzed photoreaction [9]. Figure 1.1(a) shows the mechanism of catalyzed photoreaction. In sensitized photoreaction, initial excitation takes place in the catalyst substrate and the excited catalyst transfers energy into a ground state molecule (Figure 1.1(b)) [9]. After the initial photoexcitation, subsequent electron or energy transfer occurs. The de- excitation processes via electron or energy transfer leads to a number of chemical reactions in heterogeneous photocatalysis which help in mineralization of organic pollutants.

1.2.1 Molecular electronic excitation

Various excitation and de excitation processes occurring on absorption of radiation by a molecule are illustrated in energy level diagram in Figure 2. Initial absorption of radiation by a molecule results in its excitation from the ground state (S_0) to one of the excited singlet states (S_2 or S_1) [9]. According to the selection rules for an electronic excitation process, direct photoexcitation from the singlet ground state to the triplet excited state is spin forbidden. The absorption of a photon of radiation is a very fast process (~10^{-15} s) [10]. The deexcitation of the excited molecule favors the route which minimizes the lifetime of the excited state. Depending upon different decay pathways, it can occur via radiative emission

such as fluorescence or phosphorescence (indicated in Figure 1.2 as straight lines), or a non radiative decay, indicated in Figure 1.2 as curvy lines.

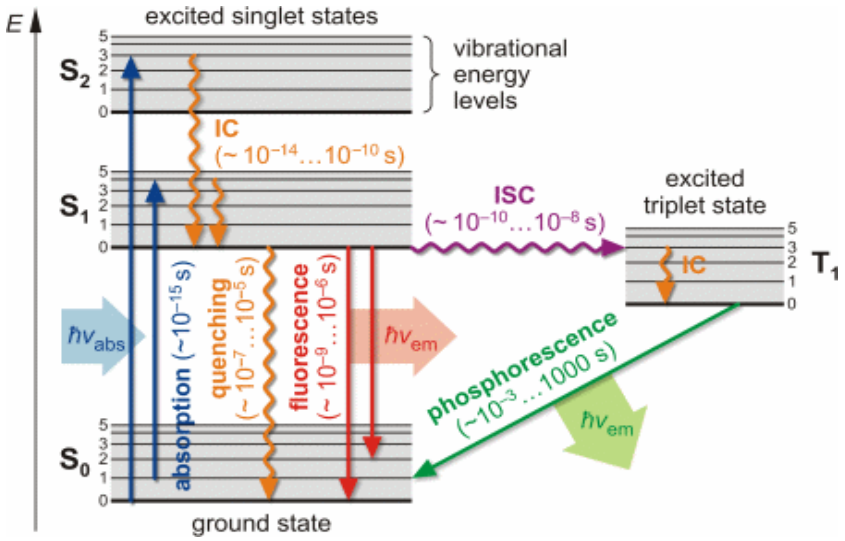

Figure 1.2: Excitation and de-excitation processes in a molecule [9].

The lifetime of the excited state for fluorescence emission is 10^{-10} to 10^{-7} s. After the excitation of a molecule from the ground state to a higher nondissociative excited state, radiationless internal conversion transitions to the lower excited states generally take place before any radiative emission processes. Once the transition occurs, the molecule undergoes vibrational relaxations to the ground vibrational state of the S_1 electronic excited state at a significant rate. The time scale for internal conversion is 10^{-11} to 10^{-9} s [10]. Intersystem crossing is a process in which the spin of the excited electron is reversed and the electrons become unpaired. The time required for such a process is in the range of 10^{-10} to 10^{-8} s. Once intersystem crossing occurs from a singlet to a triplet excited state, the molecule undergoes deactivation by phosphorescence. The time scale for the radiative phosphorescence process is of the order of 10^{-6} to 10 s. Relaxation of the excited singlet and triplet states can also occur by decomposition of the excited species to form new chemical species. These photochemical reactions occur within 10^{-12} to 10^{-9} s [10].

1.2.2 Semiconductor electronic excitation

Semiconductors possess a void energy region where no energy levels are available which can enhance electron hole recombination. This void region extends from top of the filled valence to the bottom of the empty conduction band and is known as band gap. When semiconductor

is photoexcited, there is sufficient time for electrons and holes to migrate to the surface and react with the adsorbed species [11]. If the semiconductor remains intact and also, if the charge transfer occurs continuously and exothermally, the process is called heterogeneous photocatalysis. In ideal case, a photocatalyst should be stable, inexpensive, non toxic and it should be photoactive. The process of photocatalysis starts with the photoexcitation of the semiconductor which results in the generation of electron hole pairs. Generally, the electrons can be promoted to the conduction band either by providing thermal energy or making light of certain wavelength (having energy equal to or greater than the band gap of semiconductor) incident on semiconductor surface. The promotion of electron to the conduction band leaves a positively charged vacancy in the valence band, which is referred to as a hole.

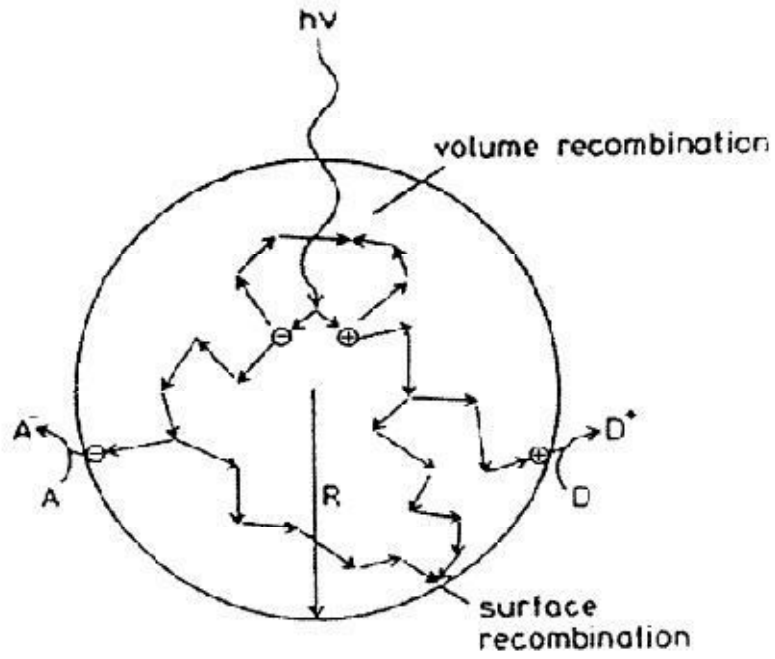

Figure 1.3: Fate of charge carriers upon photoexcitation of semiconductor [5].

This hole can be moved through space by the transfer of an electron to the vacancy; therefore, holes are considered to be mobile. The fate of these charge carriers may take different paths. Figure 1.3 illustrates various de excitation pathways which an electron and a hole may follow. Either they can get trapped or they can recombine, non-radiatively by dissipating the input energy as heat or radiatively by emitting the photon of lesser energy as compared to that of the incident photon. The other probability consists of charge separation and migration of photogenerated charge carriers to the surface of photocatalyst where they can react with electron donors or acceptors adsorbed on the surface of the photocatalyst [12]. Here, they can

participate in various oxidation and reduction (redox) reactions with adsorbed species such as water, oxygen, and other organic or inorganic species. These redox reactions are the basic mechanisms of photocatalytic treatment of organic pollutants. Various redox reactions occurring upon excitation of photocatalyst are as follows

$$Photocatalyst + h\upsilon = e_{CB}^{-} + h_{VB}^{+} \quad (1.1)$$

$$OH^{-} + h^{+} = OH\cdot \quad (1.2)$$

$$H_2O + h^{+} = OH\cdot + H^{+} \quad (1.3)$$

$$O_2 + e^{-} = O_2^{\cdot -} \quad (1.4)$$

$$O_2^{\cdot -} + e^{-} + 2H^{+} = H_2O_2 \quad (1.5)$$

$$2O_2^{\cdot -} + 2H^{+} = O_2 + H_2O_2 \quad (1.6)$$

$$H_2O_2 + e^{-} = OH^{-} + OH\cdot \quad (1.7)$$

The resulting species ($\cdot OH$, $\cdot O_2^-$) are known to be very powerful oxidizing agents which help in complete mineralization of the organic pollutants [13]. The important points for these reactions to occur include active sites present on the surface of photocatalyst and surface area [14]. If the active sites do not exist on photocatalyst surface then they will recombine. High surface area of photocatalysts facilitates the adsorption of organic compounds which result in their efficient degradation. Various important factors which help the photocatalytic process to occur efficiently are listed below.

1.2.2.1 Band edge positions

An important factor that affects the overall photocatalytic activity of semiconductors is the relative position of their band energy and the redox potential of the electron acceptor and donor species. Due to thermal requirements, the relevant potential level of the electron acceptor species should be below (more positive) the semiconductor conduction band potential to accept the electron donated by the semiconductor, while the potential level of the electron donor species must be above (more negative) the valence band potential of the semiconductor to donate the electron to combine with the surface hole [9]. The band edge positions of various semiconductors are shown in Figure 1.4. It is observed that WO_3 serves as a good photocatalyst for O_2 evolution under visible light irradiation in the presence of an electron acceptor such as Ag^+ and Fe^{3+} [14] but is not active for H_2 evolution due to its low conduction band level as shown in the figure 1.4. Therefore, the band structure of

semiconductor is just a thermodynamic requirement for photocatalysis but not a sufficient condition. It should be noted that the pH of the electrolyte solution affects the band edge positions of the semiconductors compared to the redox potential of the adsorbates [9]. Thus by varying the pH of the solution, potential of certain semiconductors can be modulated for their better performance in photocatalysis.

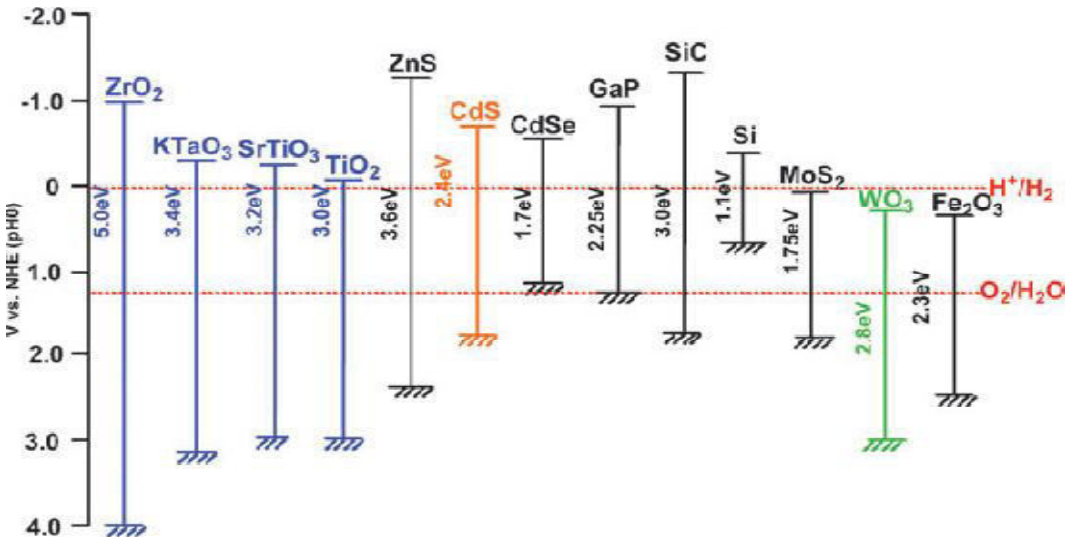

Figure 1.4: Band edge positions of various semiconductors in aqueous electrolytes [14].

1.2.2.2 Adsorption

Adsorption of an organic compound on photocatalyst surface is one of the key reaction steps in photocatalysis. Adsorption not only affects the photodegradation rate, but also influences the mechanisms involved in the process. Surface charge of organic compound and catalyst loading are the main factors which affect the extent of adsorption. Adsorption can be modulated by changing the pH of the solution as it will facilitate more or less number of dye molecules to get adsorbed on the surface of photocatalyst depending upon the surface charge of both the dye and the photocatalyst. Upto optimum level of catalyst loading, adsorption will be enhanced due to availability of more number of active sites in the system [15].

1.2.2.3 Role of traps

Trapping of charge carriers can suppress their recombination and hence lifetime of the separated electron and hole can be increased to more than fraction of a nanosecond. Synthesis of ideal crystal lattices of semiconductors has always remained a challenge for concerned researchers. Surface and bulk irregularities naturally emanate during the preparation process.

These irregularities are linked with surface electron states having energy different from the bands present in the bulk semiconductor. These electron states may serve as charge carrier traps and hence can decrease the probability of recombination of charge carriers. Traps can also be introduced extrinsically by doping semiconductors with certain transition metal ions which help in extending the lifetime of one or both of the charge carriers [16]. The competition between charge-carrier recombination and charge-carrier trapping followed by the competition between recombination of trapped carriers and interfacial charge transfer determine the overall quantum efficiency for interfacial charge transfer [12].

1.2.2.4 Photocatalyst size

Photoexcited charge carriers have to travel longer distance to reach at the surface active sites. As a result, they recombine before they reach the surface active sites to participate in redox reactions. However, this probability is minimized by making the size of photocatalyst much smaller so that transportation of charge carriers to the surface of photocatalyst could be made rapidly. Semiconductors exhibit size dependant structural and optical properties when their size becomes smaller than that of Bohr exciton radius. This phenomenon leads to quantum confinement effect. The energy levels can then be modelled using the particle in a box model in which the energy of different states is dependent on the length of the box. For a size-quantized particle, the increase in band gap energy, ΔE_g is given by the relation as given below.

$$\Delta E_g = \frac{h^2}{8\mu R^2} - \frac{1.8e^2}{\varepsilon R} \qquad (1.8)$$

where h is Planck's constant, h=6.626*10^{-34}J,

$\mu = \frac{1}{m_e} + \frac{1}{m_h}$; m_e is rest mass of electron, m_h is rest mass of hole

R is radius of particle,

Ɛ is dielectric constant of the semiconductor

The quantum size effects are observed most frequently as a broadening in band gap and are indicated by blue shift in absorption wavelength [17]. Hence optical properties of NPs like radiative and non-radiative electronic transitions are strongly affected by quantum confinement effect. The band edges shift to yield larger redox potentials [18]. The levels of the valence band are moderately shifted to lower energies, while those of the conduction band are strongly shifted to higher energies [18]. Another factor which may be advantageous in the process of photocatalysis is the fact that the fraction of atoms that are located at the surface of

a nanoparticle is very large as compared to its bulk counterpart [19]. The increased surface-to-volume ratio results in enhanced reactivity and selectivity [20]. Since photocatalytic reactions occur at the surface of catalysts, high surface-to-volume ratio is beneficial to increase the adsorption and hence the photodegradation rate. When the size of the photocatalyst attains nano dimensions, the photogenerated electron and hole pairs will be rapidly transferred to the reaction sites available at the surface thereby reducing chances of volume recombination which is dominant in bulk semiconductor particles [21]. However, when the nanoparticle size is lowered below a certain limit, surface recombination processes may dominate the interfacial charge carrier transfer processes since, most of the electrons and holes are generated very near to the surface, and also the former process occurs rapidly than the latter one [22]. So particle size plays very crucial role in studying the dynamics of photocatalytic processes.

1.3. Synthesis

During the last few decades, there has been tremendous development in the synthesis of NPs to obtain the desired size dependant structural and optical properties so that these can be used for different applications. There are more than 20 synthesis techniques which can be utilized for the preparation of inorganic nanoparticulate materials [23]. In general the synthesis procedures follow two different approaches.

1.3.1 Top-down approach

As the name clarifies, top down approach means from top (larger) to bottom (smaller). This approach can be best understood by taking example of making a statue from a stone. In making of a statue, a bulk or big piece of stone is taken. Then carving and cutting is done until desired shape is achieved. Similarly, NPs are prepared from bulk materials through size reduction. Examples include electron beam, photo ion beam or X-ray lithograph cutting, etching, grinding, ball milling etc. [24].

1.3.2 Bottom-up approach

Bottom-up, or self-assembly, approaches to nanofabrication makes use of chemical or physical forces acting at the nanoscale to assemble basic units (atoms or molecules) into larger structures. The assembling of NPs using this approach can be done in matrices including solid, liquid and gaseous phases. Inspiration for bottom-up approaches comes from

biological systems, where nature has exploited chemical forces to create all the essential structures needed for life. For example: chemical synthesis, laser induced assembly, self assembly, colloidal aggregation etc. are bottom up approaches [24]. Besides this, all cells use enzymes to create DNA by taking constituent molecules and binding them together to make the final component.

Top-down approaches are good for producing structures with long-range order and for making macroscopic connections, while bottom-up approaches are best suited for assembly and establishing short-range order at nanoscale dimensions.

Among various processes developed to synthesize nanoparticles, chemical synthesis is the most energy efficient "bottom up" technique as the NPs thus formed are size controlled and un-agglomerated [25]. During the synthesis of NPs by chemical precipitation method, initially formed products are termed as seeds. As the time passes, more product molecules are formed and the seeds grow in size to form nanocrystallites in a thermodynamically controlled manner. Most of the physical and chemical properties of NPs are due to these crystallites. These crystallites agglomerate to form primary particles resulting growth in size. If this growth is not controlled, then due to Ostwald ripening and van Der Waals interactions between the particles, they will result in agglomeration and will finally settle down [26]. Figure 1.5 illustrates the nucleation and growth during the synthesis of NPs.

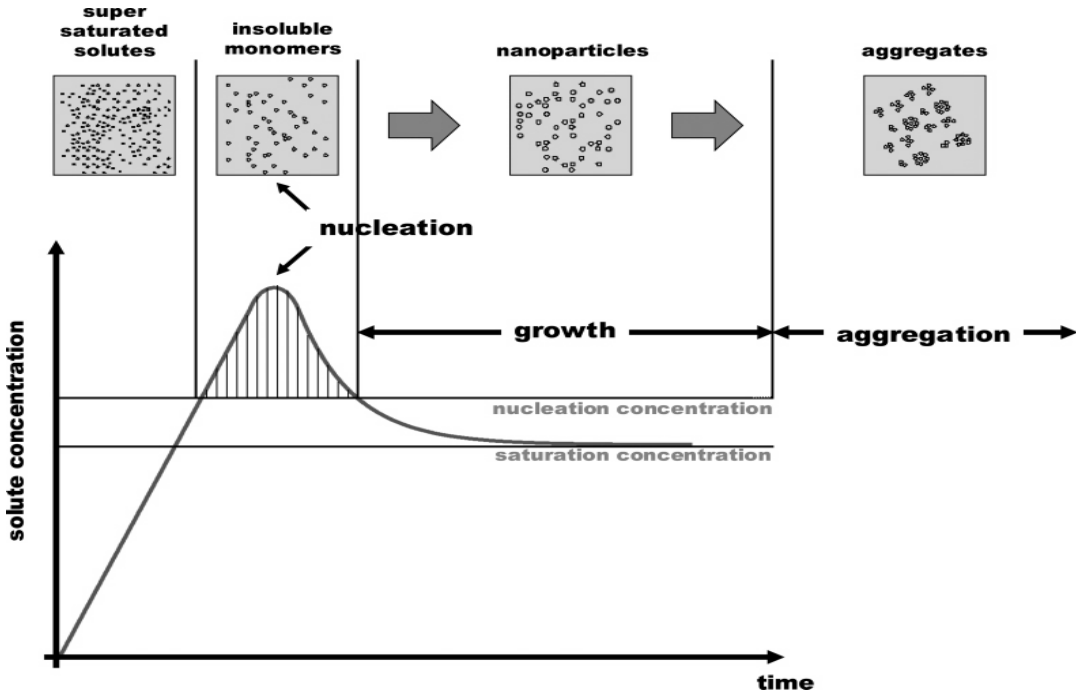

Figure 1.5: Illustration of nucleation and growth during the synthesis of NPs [27].

This agglomeration of particles is highly undesirable for their potential use in related areas. Stability of these colloidal dispersions is determined by the factor that how long the dispersed phase remains discrete over a prolonged period of time. Attractive interactions between the particles must be counterbalanced and the balance between the attractive and repulsive attractions determines the stability. The basis of colloid stability is Derjaguin, Verwey, Landau, and Overbeek (DVLO) theory. It states that the stability of colloidal particles with no adsorbed polymer layer results from the balance of the van der Walls attractive forces (V_A) and the repulsion between the particles induced by the electrical double layer (V_R)

$$V_T = V_A + V_R \qquad (1.9)$$

Where V_T is the net total energy of interaction.

Hence, charged colloids having no surface adsorbed polymers will undergo rapid coagulation. This is due to the fact that the particles are constantly undergoing Brownian motion, which leads to sticky collisions due to the long range and fairly strong van der Waals forces. Stability can be conferred on the dispersions either by electrostatic stabilization or polymeric stabilization.

1.3.2.1 Electrostatic stabilization

An effective way to overcome the van Der Waals attraction between colloidal particles in polar liquids is to provide the particles with Coulombic repulsion [28]. This is the basic principle of electrostatic stabilization. In liquid dispersion media, ionic groups can get adsorbed on the surface of the particle thus forming a charged layer around it. An equal number of counterions having opposite charge will surround the colloidal particles so that electroneutrality is maintained. This phenomenon will give rise to overall charge-neutral double layers. These electric double layers form spontaneously whenever surfaces carrying ionizable groups are suspended in a polar solvent like water. In electrostatic stabilization, mutual repulsion of these double layers surrounding particles provides stability. If the electric potential associated with this double layer is sufficiently high, the Coulombic repulsion between the particles can prevent their agglomeration. Schematic illustration of colloidal particles in the absence and presence of electrical double layer is shown in Figure 1.6(a) and 1.6(b) respectively.

1.3.2.2 Polymeric stabilization

Polymer is defined as a molecule of relatively high molecular weight having regular repeating units or chemically similar units. These molecules are usually interlinked to each other through covalent bonding. Polymers impart colloidal stability via two mechanisms. These are described below.

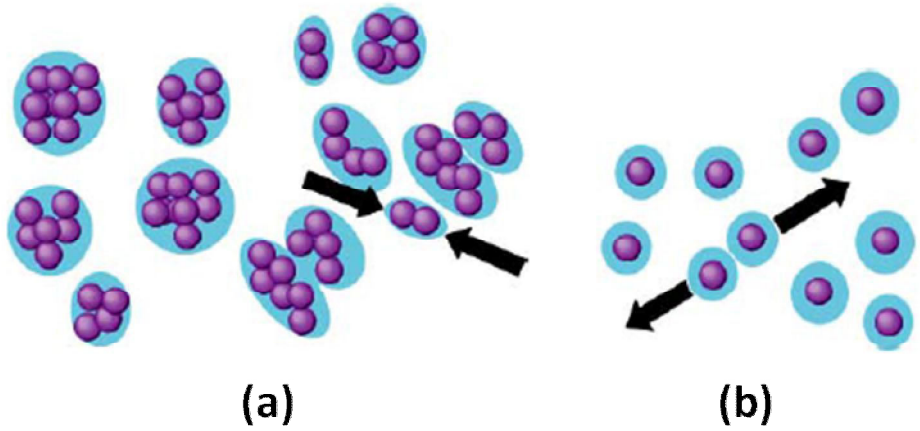

Figure 1.6: Colloidal particles (a) in the absence of double layer are free to collide and agglomerate, (b) presence of electrical double layer prevents agglomeration [28].

1.3.2.2(a) Steric stabilization

Steric stabilization of colloidal particles can be achieved by attaching (grafting or chemisorption) macromolecules to the surfaces of the particles. The stabilization due to the adsorbed layers of polymers on the dispersed particle is generally called steric stabilization. This stabilization is described by two distinct effects [28]. First effect describes the fact that the adsorbed molecules restricted in motion decrease the configurational entropic contribution to the free energy (Figure 1.7(a)). Second, when two particles or droplets containing an adsorbed polymer layer approach each other, the polymer layers may overlap with each other, or they may undergo some compression. This results in an increase of the local segment density of the polymer chains in the overlap region. This local increase in segment density in the interaction zone will result in strong repulsion as a result of the increase in the osmotic pressure in the overlap region. This phenomenon is known as osmotic repulsion (Figure 1.7(b)). The polymer must adsorb uniformly around the particle and it must have sufficient tail length to hinder the attraction between the particles and hence to have effective steric stabilization.

Various organic polymers like chitosan, polyvinylpyrrolidone, poly vinyl alchohol, poly ethylene oxide, sodium hexa meta phosphate, sodium poly phosphate, 2-mercaptoethanol, 1-thioglycerol have been used till now to control the growth of NPs. Besides providing stabilization, these polymers are also used to enhance optical properties of NPs as these eliminate the surface traps and therefore, some of the non - radiative relaxation pathways.

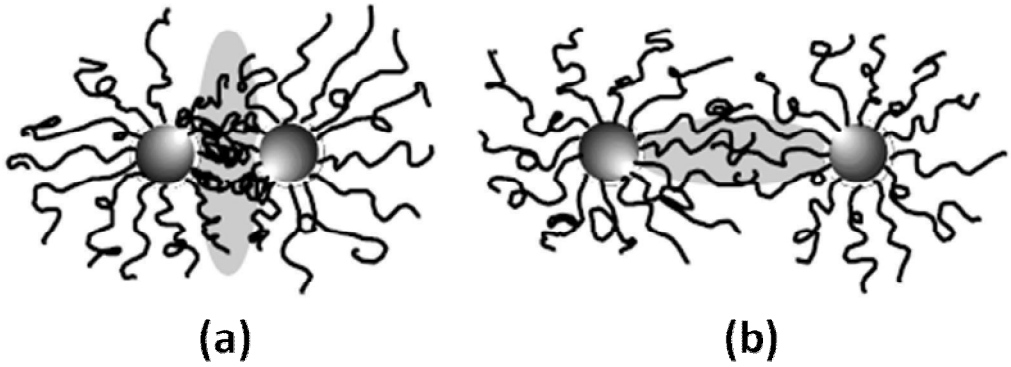

Figure 1.7: Steric stabilization of NPs (a) entropic effect, (b) osmotic repulsion [28].

In addition, capping molecules are capable of passivating the surface states of NP by forming different bonds with dangling bonds present on the surface. Steric stabilization could be achieved effectively if the following criteria are fulfilled.

- Particle surface should be completely covered by adsorbed layer as exposed particle surface can result in flocculation due to van der Waals forces.
- Polymer should have high affinity to particle surface and low affinity to dispersion medium.
- Extension of adsorbed polymer for a sufficient distance from the particle surface to counteract the van der Waals forces.
- Polymer chains which are protruded in the bulk phase should remain in good solvent conditions when there occur the addition of other molecules or there is any change in temperature [29].

In addition, the stabilizing polymer should possess high affinity with the solvent to solvate the particles and form an extended layer for screening the van Der Waals attraction between the particles [28].

1.3.2.2(b) Depletion stabilization

The addition of a free (non-adsorbing) polymer to an emulsion can cause depletion flocculation or depletion stabilization depending upon the concentration of the polymer [30].

In the case when polymer concentration is low; when the colloidal particles approach one another, so that the distance between them becomes too small to accommodate any polymer molecules, an area of pure solvent known as depletion zone is created. In that case, an attraction between the surfaces occurs because of the osmotic pressure of bulk polymer solution causing depletion flocculation. In the case when polymer concentration is high; the particles undergo closer approach, rendering the solvent between them inaccessible to the polymer molecules. The polymer molecules would have to distort their conformations drastically to fit into the interparticle region. Both the processes result in overall increase in the free energy of the system. Depending upon the magnitude of the free energy maximum, the dispersion may undergo depletion flocculation or depletion stabilization. If the polymer concentration is relatively small, the magnitude of free energy maximum is not too large. If this maximum free energy is less than thermal energy of the droplets, the droplets would undergo flocculation. At high polymer concentrations, the magnitude of maximum free energy would be much larger than the thermal energy of droplets. In this case, droplets would not flocculate and will be stabilized [30].

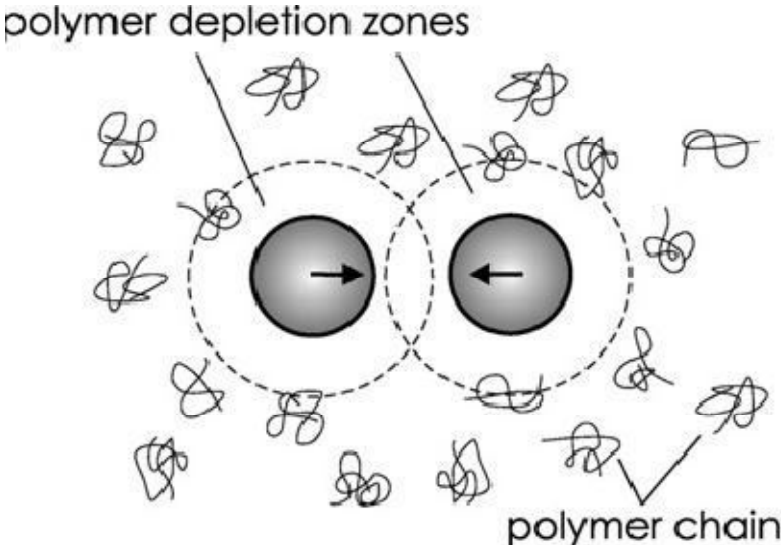

Figure 1.8: A sketch of non-adsorbing polymer chains around two spherical colloids [31].

1.4. Photocatalysis on ZnS

As an important direct band gap II-VI material, zinc sulfide (ZnS) mainly exists in cubic zinc blende (sphalerite) or hexagonal wurtzite phase. The rarely observed form of ZnS is cubic rock salt. The cubic zinc blende structure of ZnS is the most stable form in the bulk which transforms into a hexagonal wurtzite structure at 1020 °C and melts at 1650 °C. The lattice

parameters of zinc blende are a = b = c = 5.41 Å and that of wurtzite are a = b = 3.82 Å, c = 6.26 Å. In both cubic and hexagonal structures of ZnS, Zn and S atoms are tetrahedrally bonded. The only difference lies in their stacking sequence. Such little differences in atomic arrangements lead to large difference in properties of these materials, e.g. electronic structures and bandgaps [32]. The zinc blende phase has a bandgap of 3.54 eV at room temperature [33] while that of wurtzite phase is 3.7 eV [34]. With decreasing particle size, the structural and optical properties of two phases drastically change and hence low-temperature synthesis of small wurtzite ZnS nanoparticles is possible [35]. Owing to their unique structural and optical properties, both ZnS polymorphs have industrial applications in flat-panel displays, electroluminescence devices, photonic crystal devices, lasers sensors and DNA detectors [36-37]. Some new applications, include nonlinear optical devices, light-emitting diodes (LEDs; when doped), infrared windows, field emitters etc. [36-37]. Due to its non toxic nature and capability to emit in the whole visible region (by suitable doping), it is being utilized as fluorescence label in the detection of various biological molecules [38].

Also, they find application in the area of photocatalysis due to the rapid generation of the electron-hole pairs by photo-excitation and the highly negative reduction potentials of excited electrons, as conduction band position of ZnS in aqueous solution is higher than that of other widely studied semiconductors such as TiO_2 and ZnO. The trapped holes arising from surface defects on the sulphides also help in better photocatalytic activity of ZnS [39]. Recently, various strategies have been developed to utilize this material in photocatalysis in an efficient manner. To name a few,

- Effect of doping with metal and non metal ions.
- Effect of synthesis conditions (pH, temperature, capping).
- Coupling of ZnS with another suitable semiconductor.

However, the nanostructures of ZnS have not been investigated in much detail relative to the other most studied photocatalysts like TiO_2 and ZnO. So, the main motive of reviewing literature in the next chapter is to study the non existing work in which the structural, morphological and optical studies of ZnS have been done in order to understand the photocatalytic properties of this material.

References

[1] K.T. Chung, The significance of azo-reduction in the mutagenesis and carcinogenesis of azo dyes. Mutation Research/Reviews in Genetic Toxicology. **114** (1983) 269-281.

[2] K.T. Chung, S.E.J. Stevens and C.E. Cerniglia, The Reduction of Azo Dyes by the Intestinal Microflora. Critical Reviews in Microbiology, **18** (1992) 175-190.

[3] T. Robinson, G. McMullan, R. Marchant and P. Nigam, Remediation of dyes in textile effluent: a critical review on current treatment technologies with a proposed alternative. Bioresource Technology, **77** (2001) 247-255.

[4] C. Allègre, P. Moulin, M. Maisseu and F. Charbit, Treatment and reuse of reactive dyeing effluents. Journal of Membrane Science, **269** (2006) 15-34.

[5] S. Devipriya and S. Yesodharan, Photocatalytic degradation of pesticide contaminants in water. Solar Energy Materials & Solar Cells, **86** (2005) 309-348.

[6] A. Fujishima and K. Honda, Electrochemical Photolysis of Water at a Semiconductor Electrode. Nature, **238** (1972) 37-38.

[7] J.M. Herrmann, Heterogeneous photocatalysis: fundamentals and applications to the removal of various types of aqueous pollutants. Catalysis Today, **53** (1999) 115-129.

[8] R. Matthews, Photocatalysis in water purification: Possibilities, problems and prospects. In: Ollis D.F. and Al-Ekabi H. eds. Photocatalytic Purification and Treatment of Water and Air. New York, Elsevier Science Publishers. (1993) 121-139.

[9] A.L. Linsebigler, G. Lu and Jr. J.T. Yates, Photocatalysis on TiO_2 Surfaces: Principles, Mechanisms, and Selected Results, Chemical Reviews, **95** (1995) 735-758.

[10] B. Valeur and M.N. Berberan-Santos, Molecular Fluorescence: Principles and Applications, John Wiley & Sons, (2012) 53-54.

[11] Y. Nosaka and M.A. Fox, Kinetics for electron transfer from laser-pulse irradiated colloidal semiconductors to adsorbed methylviologen: dependence of the quantum yield on incident pulse width. Journal of Physical Chemistry, **92** (1988) 1893-1897.

[12] M.R. Hoffmann, S.T. Martin, W. Choi and D. Bahnemann, Environmental applications of semiconductor photocatalysis. Chemical Reviews, **95** (1995) 69-96.

[13] C.A.K. Gouvea, F. Wypych, S.G. Moraes, N. Duran, N. Nagata, P.P. Zamor, Semiconductor-assisted photocatalytic degradation of reactive dyes in aqueous solution, Chemosphere, **40** (2000) 433-440.

[14] A. Kudo and Y. Miseki, Heterogeneous photocatalyst materials for water splitting, Chemical Society Reviews, **38** (2009) 253-278.

[15] U.G. Akpan and B.H. Hameed, Parameters affecting the photocatalytic degradation of dyes using TiO_2-based photocatalysts: A review. Journal of Hazardous Materials, **170** (2009) 520-529.

[16] S.H. Mohamed, Photocatalytic, optical and electrical properties of copper-doped zinc sulphide thin films, Journal of Physics D: Applied Physics, **43** (2010) 035406-035413.

[17] A. Henglein, Q-particles: Size quantization effects in colloidal semiconductors. Progress in Colloid Polymer Science, **73** (1987) 1-4.

[18] R.F. Howe, Recent developments in photocatalysis. Developments in Chemical Engineering and Mineral Processing, **6** (1998) 55-84.

[19] A. Henglein, Nanoclusters of semiconductors and metals-colloidal nano-particles of semiconductors and metals: Electronic structure and process. Berichte der Bunsen-Gesellschaft-Physical Chemistry, **101** (1997) 1562-1572.

[20] A.J. Hoffmann, G. Mills, H. Yee and M.R. Hoffmann, Q-sized CdS: Synthesis, characterisation, and efficiency of photoinitation of polymerisation of several vinylic monomers. Journal of Physical Chemistry, **96** (1992) 5546-5552.

[21] Z. Zhang, C.C. Wang, R. Zakaria and J.Y. Ying, Role of particle size in nanocrystalline TiO_2-based photocatalysts. Journal of Physical Chemistry B, **102** (1998) 10871-10878.

[22] D. Beydoun, R. Amal, G. Low and S. McEvoy, Role of nanoparticles in Photocatalysis, Journal of Nanoparticle Research, **1** (1999) 439-458.

[23] D.A. Atwood, The Rare Earth Elements: Fundamentals and Applications. John Wiley & Sons, (2012) 406-407.

[24] V.M. Rotello, Nanoparticles: Building Blocks for Nanotechnology. Springer science and business media, (2004) 32-33.

[25] H.C. Warad, S.C. Ghosh, B. Hemtanon, C. Thanachayanont and J. Dutta, Luminescent nanoparticles of Mn doped ZnS passivated with sodium hexametaphosphate. Science and Technology of Advanced Materials, **6** (2005) 296-301.

[26] J.H. Yao, K.R. Elder, H. Guo and M. Grant, Theory and simulation of Ostwald ripening. Physical Review B, **47** (1993) 14110-14125.

[27] J. deMello and A. deMello, Microscale reactors: nanoscale products. Lab Chip, **4** (2004) 11N-15N.

[28] J. Dutta and H. Hofmann, Self-organization of colloidal nanoparticles, in: H.S. Nalwa (Ed.), Encyclopedia of Nanoscience and Nanotechnology, American Scientific Publisher, California, CA, (2004) 617-640.

[29] P. Somasundaran, Encyclopedia of Surface and Colloid Science. Taylor and Francis Group, CRC Press, **7** (2006) 5778-5781.

[30] Daniel Schuster, Encyclopedia of Emulsion Technology. CRC Press, **4** (1996) 146-147.

[31] T.H. Fan and R. Tuinier, Hydrodynamic interaction of two colloids in nonadsorbing polymer solutions. Soft Matter, **6** (2010) 647-654.

[32] C.Y. Yeh, Z.W. Lu, S. Froyen and A. Zunger, Zinc blende wurtzite polytypism in semiconductors. Physical Review B, **46** (1992) 10086-10097.

[33] R.A. Rosenberga, G.K. Shenoy, F. Heigl, S.T. Lee, P.S.G. Kim, X.T. Zhou and T.K. Sham, Effects of in situ vacuum annealing on the surface and luminescent properties of ZnS nanowires. Applied Physics Letters, **86** (2005) 263115-1-263115-3.

[34] Q. Li and C. Wang, Fabrication of wurtzite ZnS nanobelts via simple thermal evaporation, Applied Physics Letters, **83** (2003) 359-361.

[35] H. Tong, Y.J. Zhu, L.X. Yang, L. Li, L. Zhang, J. Chang, L.Q. An and S.W. Wang, Journal of Physical Chemistry C, **111** (2007) 3893-3900.

[36] X. Fang, Y. Bando, U.K. Gautam, T. Zhai, H. Zeng, X. Xu , M. Liao and D. Golberg, ZnO and ZnS Nanostructures: Ultraviolet-Light Emitters, Lasers, and Sensors. Critical Reviews in Solid State and Materials Sciences, **34** (2009) 190-223.

[37] X. Fang, T. Zhai, U.K. Gautam, L. Li, L. Wua, Y. Bando and D. Golberg, ZnS nanostructures: From synthesis to applications. Progress in Materials Science **56** (2011) 175-287.

[38] K. Manzoor, S. Johny, D. Thomas, S. Setua, D. Menon, S.K. Nair, Bio-conjugated luminescent quantum dots of doped ZnS: a cyto-friendly system for targeted cancer imaging. Nanotechnology, **20** (2009) 065102-065114.

[39] S. Yanagida, K. Mizumoto and C.J. Pac, Semiconductor photocatalysis. Part 6. Cis-trans photoisomerization of simple alkenes induced by trapped holes at surface states. Journal of the American Chemical Society, **108** (1986) 647-654.

CHAPTER 2
LITERATURE REVIEW

Overview

In this chapter, reported work which describes synthesis, structural, optical and photocatalytic studies of Zinc Sulphide (ZnS) is reviewed. Effect of various parameters like synthesis method, reaction temperature and doping with metal or non metal ions on optical and photocatalytic properties of ZnS has been described in detail. Besides this, other techniques developed to enhance the photocatalytic activity of ZnS at nanoscale has also been discussed. At the end, the reasons for selecting main objectives behind this work are presented.

2.1 Introduction

Zinc sulfide (ZnS), one of the first semiconductors discovered has shown remarkable properties for different diverse applications [1]. To name a few, ZnS was used by Ernest Rutherford and others in the initial years of nuclear physics as a scintillation detector due to its unique property of emitting light upon excitation by X-rays or electron beams [2]. The first observation of the luminescence in ZnS was in 1866, when a French chemist, Thèodore Sidot observed that ZnS crystals grown by a sublimation method and doped with small impurities of copper exhibited phosphorescence [3]. These crystals were later called Sidot's blende. After the research of Sidot, it became clear that when ZnS is doped with small amount of metallic salt, it emits light which is the characteristic of the incorporated impurity. In the 1920s, it was established that a small amount of copper incorporated in ZnS produces a green luminescence. The research on the luminescence of bulk ZnS expanded during the period from the 1950 to the 1970. This material has been used as phosphor in cathode ray tube (CRT) and also in oscilloscopes. Besides this, it is observed that metal ion doping of ZnS has greatly enhanced its optical properties for their application in electroluminescent (EL) panels [4]. It is suitable for visible-blind ultraviolet (UV)-light based devices such as sensors/photodetectors due to its wide band gap.

In 1985, Brus and co-workers successfully synthesized ZnS nanocrystals in aqueous and methanolic media using Na_2S and $Zn(ClO_4)_2$ as precursors [5]. However, the size tunability and monodispersity of these nanocrystals was limited. Since then, a number of research groups have studied the effect of synthesis conditions (reaction time, reaction temperature, nature and concentration of precursors, nature and concentration of capping agent) on structural and optical properties of ZnS. The luminescence properties of ZnS at nanoscale were first reported by Bhargava et al. [6] in 1994 where they have shown visible luminescence from Mn doped ZnS NPs. Since then, a vast data is available in literature which describes the effect of various operational parameters on the potential application of this material. In the past few decades, ZnS has emerged as a promising candidate for the photocatalytic degradation of the organic pollutants. In 1982, Yanagida et al. [7] reported photocatalytic cleavage of water in the presence of some electron donors like methanol, ethanol, or 2-propanol. They anticipated that the colloidal zinc sulfide facilitates the transfer of photoinduced conduction band electrons and valence band holes to the bulk water and the appropriate donor, respectively.

Reber et al. [8] showed that sulfide and sulfite ions act as hole scavengers which stabilize the ZnS surface very efficiently against anodic photocorrosion. Photocatalytic hydrogen

production in the presence of ZnS resulted in very high quantum yield (0.9). The high photoactivity obtained was ascribed to reduced metallic zinc nuclei, which acted as an electron transfer catalyst.

Reber et al. [9] reported photochemical hydrogen production with platinized suspensions of cadmium sulfide and cadmium zinc sulfide modified by silver sulfide. Coprecipitation of CdS with about 0.5-3 wt % silver sulfide enhanced the photochemical production of hydrogen from solutions containing S^{2-} ions as hole scavenger. Further improvement of the photoactivity was achieved by doping the Ag_2S activated CdS powders with zinc sulfide. However, the rate of hydrogen formation in solutions containing S^{2-} ions decreased with irradiation time due to the formation of disulfide ions which compete with the proton reduction. Addition of sulfite ions resulted in higher hydrogen production rate by efficiently suppressing the disulfide formation.

In their work, Anpo et al. [10] reported that the extrinsic surface energy states due to sulphur cluster species and/or radical-like sulphur species produced on the surfaces by mechanical grinding play an important role in trapping photo-formed holes. This results in a suppression of photoluminescence arising from recombination of photo-formed holes and electrons supplied from sulphur vacancies and an enhancement of photocatalytic activity of ZnS for cis-trans isomerisation reactions.

In their work, Yanagida et al. [11] reported that ZnS catalyze photoredox reactions of acetaldehyde, giving ethanol without much H_2 evolution as a two-electron reduction product; and acetic acid, biacetyl, and acetoin as oxidation products. When the ZnS was refluxed or dried to powder, the resulting ZnS showed an increased activity for H_2 evolution but a decreased activity for the two-electron reduction. The two-electron photoreduction was ascribed to the sequential transfer of electrons in the conduction band of defect-free ZnS microcrystallites. Reflux and drying resulted in the formation of surface states which play very important role in catalytic activities of ZnS.

Yanagida et al. [12] demonstrated a simple and efficient ZnS assisted photocatalysis in water for the reduction of aliphatic ketones in the presence of S^{2-} and SO_2^{2-} ions as electron donors. Highly efficient photoredox reactions of ZnS were attributed to suppression of the formation of the localized surface states. The effect of other inorganic electron donors like hydrogen sulfide (HS^-), hypophosphite (PO_2^{2-}), oxalate, thiosulfate ($S_2O_3^{2-}$) and dithionate ($S_2O_6^{2-}$) was also studied.

Kanemoto et al. [13] reported the efficient photofixation of CO_2 by using quantized ZnS at pH 7 in the presence of SH^- (to remove surface defects) and NaH_2PO_2 as an electron donor. A

large quantity of HCO_2^- accompanied by a small quantity of CO was formed. Simultaneously, large quantity of H_2 was also evolved as a result of water photoreduction. The remarkable efficiency could be obtained by controlling the concentration.

Kanemoto et al. [14] prepared colloidal solutions of ZnS nanocrystallites in N,N-dimethylformamide (DMF), acetonitrile (AN) or methanol (MeOH). In a ZnS-DMF solution, carbon dioxide underwent effective photoreduction in the presence of triethylamine as a sacrificial electron donor, giving formate and CO. The addition of a zinc ion to the system changed the product distribution without losing efficiency or changing emission behaviour; i.e. the competitive formation of CO with formate and the appearance of a red emission at ca. 460 nm was observed which was ascribed to the formation of surface sulfur vacancies. From the detailed comparison of photocatalytic properties and emission characteristics, they concluded that CO_2 strongly interact with the ZnS-DMF surface, and the reduction of CO, proceed effectively via adsorption. Also, the remarkable product switching between formate and CO can be achieved by controlling the surface characteristics of the photocatalyst.

Wada et al. [15] investigated the photocatalytic activity of ZnS nanocrystallites by photoreductive dechlorination of chlorinated benzene derivatives. Photo-reduction of chlorinated benzene derivatives (in the presence of triethylamine as a sacrificial electron donor) was effectively enhanced by using ZnS nanocrystallites as photocatalyst.

Torres-Martìnez et al. [16] synthesized glutathione capped ZnS nanocrystals with varying amounts of glutathione. Ethanol precipitation procedures improved the isolation of NCs that were uniform in size. Among the various capping concentrations used, the least capped nanocrystals showed maximum photoactivity. It was demonstrated that cap dependent decrease in the photoactivity of glutathione capped ZnS NCs is related to the ability of capping molecule to scavenge radicals.

In addition to these, various other research groups have explored the photocatalytic properties of ZnS with the aim to utilize this material effectively in the pertaining area. Work done by various research groups in the field, their main objectives and related outcomes have been summarized in Table 2.1.

Table 2.1: Summary of photocatalytic studies of ZnS by various research groups and their main findings.

Investigator (Year)	**System**	**Method**	• **Parameters studied** • **Organic compound**	**Outcomes**
Martinez et al. (2001) [17]	Cysteine capped ZnS nanocrystals (NCs)	Colloidal synthesis	• Effect of S^{2-}/Zn(II), ZnS/pNP and reaction pH on photocatalytic activity. • p-nitrophenol (pNP) acid orange-7(AO7).	• S^{2-}/Zn(II) of 5.0 was optimum in pNP degradation in cysteine capped ZnS. Cys-ZnS NCs having the least surface capping showed the fastest rates of degradation. • Optimum ratio of ZnS:pNP came out to be 10:1. • All tested reaction pH's produced significant degradation of AO7.
Tsuji et al. (2003) [18]	Pb and halogen co-doped ZnS	Chemical precipitation	• Effect of doping of Pb and halogen ions on optical properties and hence on photocatalytic activity. • H_2 production	• Visible-light absorption occured by the transition from the Pb6s levels to the conduction band level of ZnS. • H_2 evolution proceeds by the reduction of water by the photogenerated electrons in the conduction band accompanied with the oxidation of sulfite ions by holes formed in the Pb sites.
Li et al. (2004) [19]	EDTA capped ZnS nanoparticles	Homogeneous precipitation	• Effect of ethylene diamine tetraacetic acid (EDTA) on structural and optical properties of ZnS. • Basic Violet 5BN	• The introduction of EDTA stabilized the small particles and inhibited their agglomeration. • Also, due to the presence of −COOH group in EDTA molecules, ZnS nanocrystals surface was made hydrophilic. Such hydrophilic surface is beneficial for the photodegradation of dye-soluble pollutants.
Miao et al. (2006) [20]	ZnS/montmorillonite nanocomposites	Hydrothermal route	• Effect of introducing montmorillonite on adsorption and photocatalytic activity of ZnS. • Eosin B	• The prepared ZnS-MMT composites combined the adsorptive ability of MMT and the catalytic ability of ZnS was highly improved.
Xiaodan et al.	ZnS/TiO_2	Microemulsion	• Effect of ZnS content on	• The efficient photocatalytic activity of ZnS/TiO_2

(2006) [21]	nanocomposites	-mediated solvothermal method	optical and photocatalytic properties of ZnS/TiO_2 nanocomposites. • Parathion-methyl	nanocomposites was attributed to (i) the formation of the preassociated complex between the ZnS/TiO_2 composite and parathion-methyl molecules during the parathion-methyl adsorption process in the dark; (ii) the synergetic effect resulted from the combination of the cubic ZnS and anatase TiO_2; and (iii) the strong adsorption interaction between the parathionmethyl molecules and the ZnS/TiO_2 particles.
Ni et al. (2007) [22]	ZnS(en)0.5, ZnS, ZnO	Solvothermal method	• Effect of synthesis of ZnS and ZnO from ethylenediamine (en) complex on their structural and hence on photocatalytic activity. • Safranine T	• ZnS and ZnO were obtained by heating $ZnS(en)_{0.5}$ in vacuum at 450 °C and in air at 650 °C respectively. • Superior photocatalytic activity of ZnS was related to the structure of this compound. • After $ZnS\text{-}(en)_{0.5}$ has converted into ZnS in vacuum at high temperature, the sites occupied by en molecules were liberated, which led to the increase of the special surface. • Order of the special surfaces of the particles was ZnS > ZnO > $ZnS(en)_{0.5}$.
Zhang et al. 2007 [23]	Sensitized ZnS	Solid state method	• Effect of ZnO: thiourea mole ratio on structural, optical and photocatalytic properties of ZnS. • Methyl orange	• ZnS prepared with molar ratio 1 : 2 of ZnO: thiourea showed the highest photocatalytic ability which was ascribed to the sensitization of the thiocyanuric acid (calcined product of thiourea).
Jang et al. (2008) [24]	ZnS nanoplates	Solvothermal method	• Effect of synthesis of ZnS and ZnO from ethylenediamine (en) complex on their structural properties and hence on photocatalytic activity. • Hydrogen production, Acid red 14	• At calcinations temperatures of 400-500 °C, the grains in the porous plates were composed of wurtzite ZnS nanocrystallites embedded in the amorphous $ZnS(en)_{0.5}$. • Further oxidation at 550-600 °C transformed them to ZnO nanocrystallites. • ZnS calcined at 500 °C exhibited the highest hydrogen production from aqueous solutions of

				sacrificial reagents and ZnO calcined at 550-600 °C showed the superior photocatalytic activity towards Acid red 14.
Xie et al. (2008) [25]	ZnS/polymer composites	One pot route in CO_2 based supercritical media	• To investigate the photocatalytic activity of ZnS/polymer composites. • EosinB, methyl orange, methylene blue	• The ZnS/polymer composites were prepared via one-pot route performed in CO_2-based supercritical media, in which CO_2 acted as an antisolvent to facilitate the adsorption of the precursors on the polymer substrate. Using a polymer with a high -CN content as substrate, ZnS nanoparticles were uniformly and firmly deposited on the surface of polymer. • These composites exhibited high activity to degrade organic dyes.
Li et al. (2008) [26]	ZnS hollow spheres/dravite composites	Hydrothermal route	• To investigate the photocatalytic activity of ZnS hollow spheres/dravite composites. • Methylene blue	• ZnS/ dravite exhibited much higher catalytic activity. • Dravite afford a high strength of electric field, which reduce the combination of e^- and h^+ as the photoexcited electrons and holes are transferred in the field. • The composite of ZnS/dravite had a larger surface area than those of ZnS nanoparticle prepared without dravite, and the large surface area provided more sites to catalyze the degradation of methylene blue.
Feng et al. (2008) [27]	ZnS nanocrystals (NCs)	Controlled feeding rate and reaction temperature	• Effect of synthesis conditions on photocatalytic activity. • Methylene blue	• The restraining process resulted in stabilization of ZnS NC surfaces. • Slowing down the feeding rate of reactants allowed initially formed ZnS NCs to get more time to stabilize. • The stabilization of ZnS NC surfaces was further improved by suitably increasing reaction temperature. • Aggregation restraint effectively improved the photoactivity of ZnS NCs.

Yang et al. (2008) [28]	Mesoporous ZnS nanoparticles	Chemical precipitation	• To investigate the influence of structure on photocatalytic performance of ZnS NPs. • Eosin B	• The formation of the mesoporous nanostructures was attributed to the 'cluster by cluster' growth mode in which the space between crystallites formed voids or pores during the quick agglomeration of crystallites. • Mesoporous ZnS nanoparticles exhibit superior catalytic activity even compared to smaller solid nanoparticles.
Štengl et al. (2008) [29]	TiO_2/ZnS nanocomposites	Homogeneous hydrolysis	• To investigate the effect of synthesis conditions and wavelength dependence on photocatalytic degradation of dye. • Orange II	• The composite which was obtained by hydrolysis of mixture solutions 0.63 M $TiOSO_4$ and 0.08 M $ZnSO_4.7H_2O$ exhibit highest catalytic activity due to high surface area. • Photocatalytic activity at wavelength 254 nm was highest. .
Wang et al. (2009) [30]	1D CdS@ZnS Core-Shell nanocomposites	Solvothermal method, chemical precipitation	• To compare the photocatalytic activities of neat CdS nanowires and 1D CdS@ZnS core-shell nanocomposites. • Methylene blue, 4-chlorophenol	• CdS nanowires were coated with a uniform layer of ZnS shell. • Compared to the neat CdS nanowires, the as-obtained 1D CdS@ZnS core-shell nanocomposites showed significantly enhanced photocatalytic activities owing to the effective passivation of the surface electronic states by the ZnS shells.
El-Kemary et al. (2009) [31]	Ammonia capped ZnS nanoparticles	Chemical precipitation	• To study the interaction between ZnS nanoparticles and safranin O (SO) dye and their photocatalytic activity. • Safranin O	• Fluorescence enhancement was observed from dye molecules with nanoparticles upon excitation at 325 nm. The fluorescence of the dye monitored at 520 nm was quenched by ZnS nanoparticles. • Second-order photodegradation kinetics was due to the aggregation or dimer formation with increasing dye concentration.
Jang et al. (2009) [32]	N-doped ZnS based nanohybrid		• To invesitigate the photocatalytic activity of hybrids with different synthesis conditions and	• The increased activity of ZnS prepared in 24 hr. and calcined at 400 °C as compared to ZnS prepared in 24 hr. is attributed to removal of organic residuals and increased doping with treatment at high

			wavelength dependence on photocatalytic degradation of dye. • Orange II	temperature. • The maximum decomposition of the dye was recorded with the filter of λ>299 nm.
Muruganandham et al. (2009) [33]	N, C co-doped ZnS microspheres	Thermal decomposition method	• To study the optical properties and photocatalytic activity of samples prepared with different synthesis conditions. • Acid Orange 7	• Nitrogen and carbon co-doping shifted the absorption wavelength to the visible region. • ZnS prepared at 500 °C recorded the highest adsorption and photocatalytic activity as compared to sample prepared at 300 and 400 °C and also commercial ZnS which was due to its higher surface area, pore volume, and higher degree of crystallinity.
Franco et al. (2009) [34]	TiO_2/ZnS nanocomposites	Chemical deposition	• To investigate the effect of catalyst composition, catalyst amount and solution pH on photocatalytic activity of nanocomposites. • Methylene blue	• TiO_2/ZnS (0.2%) exhibit superior photocatalytic activity. • 50 mg of TiO_2/ZnS (0.2%) was optimum for superior degradation. • At pH 10, dye degraded much faster as compared to that of 3 and 7.
Porambo et al. (2010) [35]	PVP capped ZnS:Mn^{2+} nanoparticles	Colloidal synthesis	• To study the effect of Mn^{2+} doping on photocatalytic activity of ZnS NPs and to investigate the effect of nitrogen purging on apparent rate constant. • 2-chlorophenol	• 0.4% Mn doped ZnS showed the maximum photocatalytic activity which was attributed to the increase in the formation of electron-hole pairs. • Nitrogen purging reduced the apparent rate constants. • The reactive oxygen species involved in photocatalytic degradation was superoxide.
Mohamed (2010) [36]	Thin films of ZnS:Cu^{2+} nanoparticles	Electron beam evaporation	• To investigate the effect of annealing and dopant (Cu^{2+}) concentration on photocatalytic activity of thin films. • Methylene blue	• The films with a low Cu content (upto 3%) exhibit better decomposition efficiency than those with a high Cu content. Doping of ZnS with transition metal ions such as Cu ions offers a way to trap charge carriers and extends the lifetime of one or both of the charge carriers. Besides that the Cu^{2+} ion can be reduced to a Cu^{+} ion by a hole produced with

				semiconductor. This ion is strongly oxidative. • Annealing the ZnS:Cu films at 200 and 300 °C decreased the decomposition efficiency of methylene blue which was ascribed to the increase in grain size.
Wang et al. (2010) [37]	ZnS nanoribbon film	Solvothermal process	• To study the effect of synthesis conditions on structural and photocatalytic properties of ZnS nanoribbon films. • Reactive brilliant dye X-3B	• Due to higher crystallinity, the sample heated for 24 hrs. at 140 °C showed better photocatalytic activity as compared to the sample heated for 6 hrs.
Zhang et al. (2010) [38]	Sr doped CdS-ZnS solid solution	Chemical precipitation method	• To investigate the effect of Zn/Cd ratio and Sr doping on optical and photocatalytic properties of CdS-ZnS solid solution. • H_2 evolution	• Photocatalytic H_2 evolution results showed that Sr-doping efficiently improved the photocatalytic activities while the molar ratio of Zn was greater than 20% in the absence of noble metal as cocatalyst. • Recombination of photoelectrons and holes was efficiently suppressed by doping metal ions on the shallow surface of CdS-ZnS.
Muruganandham et al. (2010) [39]	ZnS microspheres	Hydrothermal method	• To study the effect of synthesis conditions, zinc precursors and adding 2-propanol to the solution. • Methyl orange	• The sample in which the hydrothermal reaction time was 10 hr exhibited superior photocatalytic activity despite of the smaller surface area as compared to the catalyst prepared in 3h. This was due to the difference in crystallization of the two samples. • Photocatalyst prepared using zinc sulphate recorded highest photocatalytic activity due to higher surface area. • The decrease in degradation rate in the presence of 2-propanol was due to hydroxyl scavenging effect which decreases the availability of hydroxyl radical for dye degradation.

Lin et al. (2010) [40]	ZnO-ZnS Nanocables	Template-assisted method	• To investigate the effect of sulfuration on structural and photocatalytic properties of electrospun ZnO nanofibres. • Rhodamine B	• Photocatalytic degradation of dye was maximum in case of sample sulfurized for 12 hrs. • Excess sulfuration time deteriorated the coupling of ZnO and ZnS by introducing more defects and split at the interface.
Yu et al. (2010) [41]	CuS/ZnS Nanocomposite Hollow Spheres	Ion-exchange method	• Effect of synthesis conditions on structural, optical and photocatalytic properties of samples. • Rhodamine B	• The prepared CuS/ZnS composite hollow spheres exhibit enhanced photocatalytic activity due to the combined effects of several factors, including heterojunction structures, intense UV-visible absorption, a hierarchically nanoporous structure.
Li et al. (2010) [42]	ZnS coated $ZnIn_2S_4$	Solvothermal process	• Effect of composition of ZnS-$ZnIn_2S_4$, initial concentration of glucose and concentration of NaOH on photocatalytic activity. • H_2 production	• Pt/ZnS–$ZnIn_2S_4$ exhibit better activity for hydrogen generation than pure $ZnIn_2S_4$ (using glucose as an electron donor) which may be attributed to enhancement of the adsorption of glucose by ZnS on the $ZnIn_2S_4$ surface.
Li et al. (2011) [43]	ZnS-In_2S_3-CuS Nanospheres	Solvothermal method	• Effect of synthesis conditions on structural and photocatalytic properties of samples. • H_2 evolution	• $ZnIn_{0.25}Cu_{0.02}S_{1.395}$ prepared at 180 °C for 18 hrs. showed the best photocatalytic activity for hydrogen production from water, using Na_2SO_3 and Na_2S as sacrificial reagents. • The high activities of the nanospheres with a nanoporous structure were attributed to the combined effect high surface area, the existence of mesopores, and the presence of special nanorods in the shell.
Maji et al. (2011) [44]	ZnS nanocrystals NCs (rod and sphere)	Solvothermal method	• To study the effect of structure directing solvents on morphology and photocatalytic activity and to detect the hydroxyl radicals using terephthalic acid	• The greater catalytic activity of spherical ZnS was attributed to its smaller size and higher surface to volume ratio. • With ZnS NCs, no significant luminescence due to 2-hydroxylterephthalic acid was observed even on long exposure to light, indicating the lack of

			photoluminescence probing technique. • Rose bengal dye	hydroxyl radical formation. • For ZnS, direct participation of the photogenerated holes seemed to be operative.
Li et al. (2011) [45]	ZnS nanoparticles	Composite molten salt method	• To study the effect of synthesis procedure on photocatalytic activity. • Methyl orange	• The effective catalytic degradation of methyl orange by the ZnS nanoparticles was due to its unique assembled structure and its narrowed band gap which provided high tremendous specific surface area for contact of methyl orange and more effective absorption of sunlight than that of common nanoparticles.
Zhang et al. 2011 [46]	CuS/ZnS Porous Nanosheets	Hydrothermal and cation exchange reaction	• To study the influence of synthesis procedure on optical and photocatalytic activity of the samples. • H_2 production	• With increasing the content of CuS an enhanced absorption in the visible light region was observed. • There was no shift in the absorption edge of the CuS/ZnS samples in comparison to that of pure ZnS which imply that CuS was only deposited on the ZnS surface. • The optimal CuS loading content was found to be about 2 mol %. The high photocatalytic H_2-production activity of CuS/ZnS samples was due to the interfacial charge transfer from the valence band of ZnS to CuS, which causes the reduction of partial CuS to Cu_2S.
Zhang et al. (2011) [47]	Bi-doped ZnS hollow spheres	Cation exchange-hydrothermal reaction	• To study the effect of bismuth doping on optical and hence on photocatalytic properties of ZnS. • H_2 production	• Visible light absorption band shifts to a longer wavelength as the doping amount increased. The visible-light absorption band was assigned to the electron transition from Bi 6s level to the conduction band of ZnS. • 0.3% doped ZnS showed highest H_2 production.
Liu et al. (2011) [48]	ZnS spheres	Green wet chemical route.	• To study the effect of synthesis procedure and to detect the hydroxyl radical.	• The prepared sample exhibit superior photocatalytic activity than Degussa P25 and commercial ZnS. • Increase in PL intensity of coumarin in the presence

			• Azo dye X-3B (X-3B), trichloroacetate (TCA) and phenol	of ZnS indicated the production of •OH radicals on the ZnS surface which act as a photo-oxidant.
Sharma and Pandey (2012) [49]	Thioglycerol (TG) capped ZnS nanoparticles	Chemical precipitation	• Effect of capping on optical and photocatalytic activity of ZnS NPs. • Bromophenol blue, crystal violet, reactive red dye	• TG capping resulted in surface charge modification and passivation of surface electronic states of ZnS. • Absence of Zn^{2+} defects on the photocatalyst surface created fewer hole trap states in comparison to uncapped ZnS NPs. This in turn increased electron to hole ratio. These electrons present on the surface of NPs enhanced the photocatalytic activity of capped NPs as compared to that of uncapped.
Altın et al. (2012) [50]	ZnO and ZnS microrods coated on glass	spray pyrolysis method	• To compare the photocatalytic activity of ZnS and ZnO coated on glass. • Methylene blue	• ZnO degraded the dye more effectively as compared to ZnS.
Chen et al. (2012) [51]	ZnS films	chemical bath deposition	• To investigate the effect of annealing temperature and heating rate on structural, optical and photocatalytic properties of films. • Methyl orange	• The increasing of annealing temperature and heating rate increased the crystallinity and the mean grain size of ZnS films. • Absorption in the visible region enhanced with increase in annealing temperature and heating rate. • Increase in both parameters led to increase in photocatalytic activity due to the presence of sulfur vacancies, larger grain size and higher crystallinity.
Zhang et al. 2013 [52]	ZnS–Ag_2S composite microspheres	Hydrothermal method	• Optimum ZnS/$AgNO_3$ weight ratio. • Methylene orange	• ZnS/$AgNO_3$ weight ratio of 13:1 was optimum for photocatalytic degradation. • When the two semiconductors ZnS and Ag_2S are coupled, the excited electrons on the conduction band of ZnS get injected into the more positive conduction band of Ag_2S. The electrons react with O_2 adsorbed on the surface of the composite to produce $•O_2^-$ and H_2O_2 that decomposed methyl

				orange. The effective separation of the photoexcited electron-hole pairs greatly reduced the recombination of the photogenerated charge carriers. The holes left on the valence band of ZnS reacted with H_2O and produce reactive oxygen species •OH.
Chauhan et al. (2013) [53]	Fe doped ZnS nanoparticles	Chemical precipitation	• Optimum Fe/Zn ratio. • Methylene blue	• Optimum Fe concentration for efficient degradation of dye was 3 mol%. • Fe ions lengthened the charge carrier recombination and hence increased the photocatalytic efficiency. • At higher concentration of Fe, photocatalytic activity of ZnS nanocrystals decreased as the recombination of trapped carrier dominated the interfacial charge transfer.
Li et al. (2013) [54]	ZnO/ZnS core/shell particles	Hydrothermal method	• Effect of ZnS layer on PL properties of core shell particles and hence on photocatalytic activity. • Methyl orange	• The photoluminescence analysis of ZnO/ZnS show that ZnS layer play an important role to enhance optical properties of ZnO particles. • ZnO/ZnS exhibit good photocatalytic activity.
Zhang et al. (2013) [55]	Au-Loaded ZnS Flowers	Hydrothermal approach combined with a deposition-precipitation method	• Effect of Au loading on optical and photocatalytic properties of ZnS flowers. • H_2 evolution	• The band gap of ZnS is narrowed by the incorporation of a small portion of Au(I). Optimal Au loading concentration for photocatalytic hydrogen production was found to be 4 wt%. • Although all Au loaded samples exhibit strong SPR absorption at 553 nm, all the samples exhibit no activities in the visible light region ($\lambda > 420$ nm). This was ascribed to the highly negative reduction potential of the ZnS conduction band which prevented the excited energetic electrons in the SPR state from injecting into the conduction band.
Chauhan et al. (2014) [56]	Cu doped ZnS nanoparticles	Chemical precipitation	• Effect of Cu doping on photocatalytic activity. • Methylene blue	• Optimal Cu concentration was 3 mol%. • At 3 mol%, concentration of Cu ions serve as shallow trapping sites for the charge carriers and

				increases the photocatalytic efficiency by separating the arrival time of electron and hole at the surface. • At higher concentrations of Cu cubic and small traces of hexagonal phase are formed which decrease the photocatalytic activity of $Zn_{1-x}Cu_xS$ nanocrystals as the recombination of trapped carrier dominates the interfacial charge transfer.
Labiadh et al. (2014) [57]	Cu-doped ZnS QDs/TiO_2 nanocomposites	Hydrothermal method	• Effect of UV irradiation on PL intensity of Cu:ZnS QDs and effect of integrating p-type Cu:ZnS QDs with n-type TiO_2 on photocatalytic properties. • Salicylic acid	• Cu:ZnS QDs exhibit the ability to generate hydroxyl radicals upon UV light irradiation. • Superior photocatalytic activity of TiO_2/Cu:ZnS nanocomposite as compared to TiO_2/ZnS and TiO_2 is due to the synergetic effects of (i) an effective electron-hole pair separation by the p–n heterojunction constructed by n-type TiO_2 and p-type Cu:ZnS and (ii) the ability of Cu:ZnS dots to generate hydroxyl radicals and to behave as a co-catalyst once associated to TiO_2 and thus increase its oxidizing capacity.

2.2 Plan of work

Although tremendous efforts have been made to enhance the absorption characteristics of ZnS to employ this material in the process of photocatalysis, yet some points are there which need to be explored in a systematic manner. These are (a) Effect of solution pH in which ZnS is being synthesized, (b) Effect of UV-Vis irradiation and (c) Effect of different metal dopant ions needs to be investigated in more detail. So, considering these points, the main objectives behind the present work were as below:

1. Synthesis of undoped and doped ZnS nanostructures by chemical precipitation method to make it an effective catalyst in near visible region.
2. Characterization of synthesized nanostructures by different tools/techniques.

References

[1] W.L. Davidson, X-ray diffraction evidence for ZnS formation in zinc activated rubber vulcanizates. Physical Review, **74** (1948) 116-117.

[2] X. Fang, Y. Bando, U.K. Gautam, T. Zhai, H. Zeng, X. Xu , M. Liao and D. Golberg, ZnO and ZnS Nanostructures: Ultraviolet-Light Emitters, Lasers, and Sensors. Critical Reviews in Solid State and Materials Sciences, **34** (2009) 190-223.

[3] M. Sidot, Recherches sur la cristallisation de quelques sulfures métalliques'. Comptes rendus de l'Académie des sciences Paris, **62** (1866) 999-1001.

[4] A.A. Bol, J. Ferwerda, J.A. Bergwerff and A. Meijerink, Luminescence of nanocrystalline ZnS:Cu^{2+}. Journal of Luminescence, **99** (2002) 325-334.

[5] R. Rossetti, R. Hull, J.M. Gibson and L.E. Brus, Excited electronic states and optical spectra of ZnS and CdS crystallites in the 15 to 50 Å size range: Evolution from molecular to bulk semiconducting properties. Journal of Chemical Physics, **82** (1985) 552-559.

[6] R.N. Bhargava, D. Gallagher, X. Hong and A. Nurmikko, Physical Review Letters, **72** (1994) 416-419.

[7] S. Yanagida, T. Azuma and H. Sakurai, Photocatalytic hydrogen evolution from water using zinc sulfide and sacrificial electron donors. Chemistry Letters, **7** (1982) 1069-1070.

[8] J.F. Reber and K. Meier, Photochemical Production of Hydrogen with Zinc Sulfide Suspensions. Journal of Physical Chemistry, **88** (1984) 5903-5913.

[9] J.F. Reber and M. Rusek, Photochemical Hydrogen Production with Platinized Suspensions of Cadmium Sulfide and Cadmium Zinc Sulfide Modified by Silver Sulfide. Journal of Physical Chemistry, **90** (1986) 824-834.

[10] M. Anpo, A. Matsumoto and S. Kodama, Direct Evidence for the Participation of Extrinsic Surface Sites in the Enhancement of Photocatalytic Activity of Luminescent Zinc Sulphide Catalysts. Journal of Chemical Society-Chemical Communications, (1987) 1038-1039.

[11] S. Yanagida, Y. Ishimaru, Y. Miyake, T. Shiragami, C. Pac, K. Hashimoto and T. Sakata, Semiconductor Photocatalysis-ZnS-Catalyzed Photoreduction of Aldehydes and Related Derivatives: Two-Electron-Transfer Reduction and Relationship with Spectroscopic Properties. Journal of Physical Chemistry, **93** (1989) 2516-2582.

[12] S. Yanagida, M. Yoshiya, T. Shiragami, C. Pac, H. Mori and H. Fujita, Semiconductor Photocatalysis-Quantitative Photoreduction of Aliphatic Ketones to Alcohols Using Defect-Free ZnS Quantum Crystallites. Journal of Physical Chemistry, **94** (1990) 3104-3111.

[13] M. Kanemoto, T. Shiragami, C. Pac and S. Yanagida, Semiconductor Photocatalysis-Effective Photoreduction of Carbon Dioxide Catalyzed by ZnS Quantum Crystallites with Low Density of Surface Defects. Journal of Physical Chemistry, **96** (1992) 3521-3526.

[14] M. Kanemoto, H. Hosokawa, Y. Wada, K. Murakoshi, S. Yanagida, T. Sakata, H. Mori, M. Ishikawa and H. Kobayashi, Semiconductor Photocatalysis Part 20-Role of surface in the photoreduction of carbon dioxide catalysed by colloidal ZnS nanocrystallites in organic solvent. Journal of Chemical Society, Faraday Transactions, **92** (1996) 2401-2411.

[15] Y. Wada, H. Yin, T. Kitamura and S. Yanagida, Photoreductive dechlorination of chlorinated benzene derivatives catalyzed by ZnS nanocrystallites. Chemical Communications, (1998) 2683-2684.

[16] C.L.T. Martínez, L. Nguyen, R. Kho, W. Bae, K. Bozhilov, V. Klimov and R.K. Mehra, Biomolecularly capped uniformly sized nanocrystalline materials: glutathione-capped ZnS nanocrystals. Nanotechnology, **10** (1999) 340-354.

[17] C.L.T. Martínez, R. Kho, O.I. Mian and R.K. Mehra, Efficient Photocatalytic Degradation of Environmental Pollutants with Mass-Produced ZnS Nanocrystals. Journal of Colloid and Interface Science, **240** (2001) 525-532.

[18] I. Tsuji and A. Kudo, H_2 evolution from aqueous sulfite solutions under visible light irradiation over Pb and halogen-codoped ZnS photocatalysts. Journal of Photochemistry and Photobiology A: Chemistry, **156** (2003) 249-252.

[19] J. Li, Y. Xu, Y. Liu, D. Wu and Y. Sun, Synthesis of hydrophilic ZnS nanocrystals and their application in photocatalytic degradation of dye pollutants. China Particuology, **2** (2004) 266-269.

[20] S. Miao, Z. Liu, B. Han, H. Yang, Z. Miao and Z. Sun, Synthesis and characterization of ZnS-montmorillonite nanocomposites and their application for degrading eosin B. Journal of Colloid and Interface Science, **301** (2006) 116-122.

[21] Y. Xiaodan, W. Qingyin, J. Shicheng and G. Yihang, Nanoscale ZnS/TiO_2 composites: Preparation, characterization, and visible-light photocatalytic activity. Materials Characterization, **57** (2006) 333-341.

[22] Y. Ni, X. Cao, G. Hu, Z. Yang, X. Wei, Y. Chen and J. Xu, Preparation, Conversion, and Comparison of the Photocatalytic and Electrochemical Properties of $ZnS(en)_{0.5}$, ZnS, and ZnO. Crystal Growth and Design, **7** (2007) 280-285.

[23] H. Zhang, X. Chen, Z. Li, J. Kou, T. Yu and Z. Zou, Preparation of sensitized ZnS and its photocatalytic activity under visible light irradiation. Journal of Physics D: Applied Physics, **40** (2007) 6846-6849.

[24] J.S. Jang, C.J. Yu, S.H. Choi, S.M. Ji, E.S. Kim and J.S. Lee, Topotactic synthesis of mesoporous ZnS and ZnO nanoplates and their photocatalytic activity. Journal of Catalysis, **254** (2008) 144-155.

[25] Y. Xie, C. Zhang, S. Miao, Z. Liu, K. Ding, Z. Miao, G. An and Z. Yang, One-pot synthesis of ZnS/polymer composites in supercritical CO_2–ethanol solution and their applications in degradation of dyes. Journal of Colloid and Interface Science, **318** (2008) 110-115.

[26] J.H. Li, A.H. Lu, F. Liu and L.Z. Fan, Synthesis of ZnS/dravite composite and its photocatalytic activity on degradation of methylene blue. Solid State Ionics, **179** (2008) 1387-1390.

[27] S. Feng, J. Zhaoa and Z. Zhu, Kinetically restraining aggregation of ZnS nanocrystals and the effect on Photocatalysis. Materials Science and Engineering B, **150** (2008) 116-120.

[28] J. Yang, J.J. Peng, R. Zou, F. Peng, H. Wang, H. Yu and J.Y. Lee, Mesoporous zinc-blende ZnS nanoparticles: synthesis, characterization and superior photocatalytic properties. Nanotechnology, **19** (2008) 255603-255609.

[29] V. Štengl, S. Bakardjieva, N. Murafa, V. Houšková and K. Lang, Visible-light photocatalytic activity of TiO_2/ZnS nanocomposites prepared by homogeneous hydrolysis. Microporous and Mesoporous Materials, **110** (2008) 370-378.

[30] L. Wang, H. Wei, Y. Fan, X. Liu and J. Zhan, Synthesis, Optical Properties, and Photocatalytic Activity of One-Dimensional CdS@ZnS Core-Shell Nanocomposites. Nanoscale Research Letters, **4** (2009) 558-564.

[31] M. El-Kemary and H. El-Shamy, Fluorescence modulation and photodegradation characteristics of safranin O dye in the presence of ZnS nanoparticles. Journal of Photochemistry and Photobiology A: Chemistry, **205** (2009) 151-155.

[32] J.W. Jang, S.H. Choi, J.S. Jang, J.S. Lee, S. Cho and K.H. Lee, N-Doped ZnS Nanoparticles Prepared through an Inorganic-Organic Hybrid Complex ZnS·$(piperazine)_{0.5}$. Journal of Physical Chemistry C, **113** (2009) 20445-20451.

[33] M. Muruganandham and Y. Kusumoto, Synthesis of N, C codoped hierarchical porous microsphere ZnS as a visible light-responsive photocatalyst. Journal of Physical Chemistry C, **113** (2009) 16144-16150.

[34] A. Franco, M.C. Neves, M.M.L. Ribeiro Carrott, M.H. Mendonça, M.I. Pereira and O.C. Monteiro, Photocatalytic decolorization of methylene blue in the presence of TiO_2/ZnS nanocomposites. Journal of Hazardous Materials, **161** (2009) 545-550.

[35] M.W. Porambo, H.R. Howard and A.L. Marsh, Dopant Effects on the Photocatalytic Activity of Colloidal Zinc Sulfide Semiconductor Nanocrystals for the Oxidation of 2-Chlorophenol. Journal of Physical Chemistry C, **114** (2010) 1580-1585.

[36] S.H. Mohamed, Photocatalytic, optical and electrical properties of copper-doped zinc sulphide thin films. Journal of Physics D: Applied Physics, **43** (2010) 035406-035413.

[37] C. Wang, Y. Ao, P. Wang, S. Zhang, J. Qian and J. Hou, A simple method for large-scale preparation of ZnS nanoribbon film and its photocatalytic activity for dye degradation. Applied Surface Science, **256** (2010) 4125-4128.

[38] K. Zhang, D. Jing, Q. Chen and L. Guo, Influence of Sr-doping on the photocatalytic activities of CdS-ZnS solid solution photocatalysts. International Journal of Hydrogen Energy, **35** (2010) 2048-2057.

[39] M. Muruganandham, R. Amuthaa, E. Repoa, M. Sillanpää, Y. Kusumoto and Md. Abdulla-Al-Mamun, Controlled mesoporous self-assembly of ZnS microsphere for photocatalytic degradation of Methyl Orange dye. Journal of Photochemistry and Photobiology A: Chemistry, **216** (2010) 133–141.

[40] D. Lin, H. Wu, R. Zhang, W. Zhang and W. Pan, Facile Synthesis of Heterostructured ZnO-ZnS Nanocables and Enhanced Photocatalytic Activity. Journal of the American Ceramic Society, **93** (2010) 3384-3389.

[41] J. Yu, J. Zhang and S. Liu, Ion-Exchange Synthesis and Enhanced Visible-Light Photoactivity of CuS/ZnS Nanocomposite Hollow Spheres. Journal of Physical Chemistry C, **114** (2010) 13642-13649.

[42] Y. Li, J. Wang, S. Peng, G. Lu and S. Li, Photocatalytic hydrogen generation in the presence of glucose over ZnS-coated $ZnIn_2S_4$ under visible light irradiation. International Journal of Hydrogen Energy, **35** (2010) 7116-7126.

[43] B.Y. Li, G. Chen, Q. Wang , X. Wang , A. Zhou and Z. Shen, Hierarchical ZnS-In_2S_3-CuS Nanospheres with Nanoporous Structure: Facile Synthesis, Growth Mechanism and Excellent Photocatalytic Activity. Advanced Functional Materials, **20** (2010) 3390-3398.

[44] S.K. Maji, A.K. Dutta, D.N. Srivastava, P. Paul, A. Mondal and B. Adhikary, Effective photocatalytic degradation of organic pollutant by ZnS nanocrystals synthesized via thermal decomposition of single-source precursor. Polyhedron, **30** (2011) 2493-2498.

[45] X. Li, C. Huan, H. Liu, J. Xu, B. Wan and X. Wang, ZnS nanoparticles self-assembled from ultrafine particles and their highly photocatalytic activity. Physica E, **43** (2011) 1071-1075.

[46] J. Zhang, J. Yu, Y. Zhang, Q. Li and J.R. Gong, Visible Light Photocatalytic H_2-Production Activity of CuS/ZnS Porous Nanosheets Based on Photoinduced Interfacial Charge Transfer. Nano Letters, **11** (2011) 4774-4779.

[47] J. Zhang, S. Liu, J. Yu and M. Jaroniec, A simple cation exchange approach to Bi-doped ZnS hollow spheres with enhanced UV and visible-light photocatalytic H_2-production activity, Journal of Materials Chemistry, **21** (2011) 14655-14662.

[48] Y. Liu, J. Hu, C. Ngo, S. Prikhodko, S. Kodambaka, J. Li and R. Richards, Gram-scale wet chemical synthesis of wurtzite-8H nanoporous ZnS spheres with high photocatalytic activity. Applied Catalysis B: Environmental, **106** (2011) 212-219.

[49] M. Sharma, T. Jain, S. Singh and O.P. Pandey, Photocatalytic degradation of organic dyes under UV–Visible light using capped ZnS nanoparticles. Solar Energy, **86** (2012) 626-633.

[50] İ. Altın, İ. Polat, E. Bacaksız and M. Sökmen, ZnO and ZnS microrods coated on glass and photocatalytic activity. Applied Surface Science, **258** (2012) 4861-4865.

[51] Y. Chen, G.F. Huang, W.Q. Huang, L.L. Wang, Y. Tian, Z.L. Ma and Z.M. Yang, Annealing effects on photocatalytic activity of ZnS films prepared by chemical bath deposition. Materials Letters, **75** (2012) 221-224.

[52] H. Zhang, B. Wei, L. Zhu, J. Yu, W. Sun and L. Xu, Cation exchange synthesis of ZnS-Ag_2S microspheric composites with enhanced photocatalytic activity. Applied Surface Science, **270** (2013) 133-138.

[53] R. Chauhan, A. Kumar and R.P. Chaudhary, Photocatalytic degradation of methylene blue with Fe doped ZnS nanoparticles. Spectrochimica Acta Part A: Molecular and Biomolecular Spectroscopy, **113** (2013) 250-256.

[54] W. Li, G. Song, F. Xie, M. Chen and Y. Zhao, Preparation of spherical ZnO/ZnS core/shell particles and the photocatalytic activity for methyl orange. Materials Letters, **96** (2013) 221-223.

[55] J. Zhang, Y. Wang, J. Zhang, Z. Lin, F. Huang and J. Yu, Enhanced Photocatalytic Hydrogen Production Activities of Au-Loaded ZnS Flowers. ACS Applied Materials & Interfaces, **5** (2013) 1031-1037.

[56] R. Chauhan, A. Kumar and R.P. Chaudhary, Photocatalytic degradation of methylene blue with Cu doped ZnS nanoparticles. Journal of Luminescence, **145** (2014) 6-12.

[57] H. Labiadh, T.B. Chaabane, L. Balan, N. Becheik, S. Corbel, G. Medjahdi and R. Schneider, Preparation of Cu-doped ZnS QDs/TiO_2 nanocomposites with high photocatalytic activity. Applied Catalysis B: Environmental, **144** (2014) 29-35.

CHAPTER 3
EXPERIMENTAL DETAILS

Overview

This chapter describes the details of the synthesis procedure to prepare ZnS using different chemicals. Different techniques used to generate and analyze the data have been discussed. The details of the instruments including their model number have been provided. The set up used to perform photocatalytic experiments has been given in the end of the chapter. A brief introduction about the model pollutant selected for the entire photocatalytic study is also provided.

3.1 Raw materials

In the present work, raw materials used were zinc acetate $Zn(CH_3COO)_2$ (99.99%, Sigma Aldrich), copper acetate $Cu(CH_3COO)_2$ (99.99%, Sigma Aldrich), manganese acetate $Mn(CH_3COO)_2.2H_2O$ (99.99%, Sigma Aldrich), silver nitrate $AgNO_3$ (>99.00%, Sigma Aldrich), sodium sulphide nonahydrate $Na_2S.9H_2O$ (≥99.99%, Sigma Aldrich), 1-thioglycerol $C_3H_8O_2S$ (≥99.0%, Sigma Aldrich), sodium hydroxide NaOH (≥98.0%, Sigma Aldrich), crystal violet $C_{25}N_3H_{30}Cl$ (≥90.0%) and acetone (Merk). All chemicals used in this work were of analytical grade and were used as such without further purification. Ultrapure water was used in the entire synthesis.

3.2 Sample preparation

3.2.1 ZnS nanoparticles with varying dopants and dopant concentrations

Doped ZnS NPs ($Zn_{1-x}M_xS$; x = 0, 0.01, 0.02, 0.03 and 0.04; M=Cu, Mn, Ni and Ag) were synthesized by simple chemical precipitation method [1]. These NPs were synthesized under similar conditions to compare their structural, optical and photocatalytic properties. Only dopant and dopant concentration with respect to the host was varied. In the first step, 20 ml homogeneous solution of .25M $Zn(ac)_2$ was prepared in ultrapure water and was stirred for 30 min. Also (1, 2, 3, 4 at. wt.%) solutions of $M(ac)_2/AgNO_3$; M= Cu, Mn and Ni were prepared in 20 ml ultrapure water and were allowed to stir for 30 min. After 30 min., solution of $M(ac)_2/AgNO_3$ was added dropwise into the homogeneously stirred solution of $Zn(ac)_2$. Thioglycerol (TG) was used as an organic capping agent during the synthesis to avoid agglomeration and to passivate the surface defects. A solution of known amount of TG (1%) was prepared in 20 ml and was stirred for 30 min. Solution of .25M Na_2S was also prepared separately and was stirred for 30 min. To the stirred solution of $M(ac)_2/AgNO_3$ and $Zn(ac)_2$, solution of TG was added dropwise. This solution was allowed to stir for 30 min. Then to this reaction mixture, homogeneous solution of .25M Na_2S was added dropwise. Soon after the addition of Na_2S, precipitation phenomenon occurred and concentration of precipitates increased with the increase in addition of Na_2S solution. The reaction was allowed to proceed for 3 h at 80 °C followed by overnight ageing. The resulting solution was centrifuged at 12000 rpm to remove the unreacted species and excess capping agent. The washed precipitates were then dried at 80 °C for 24 h and were crushed to obtain fine powder. All the doped samples were synthesized without varying pH i. e. without the addition of NaOH.

3.2.2 Undoped ZnS nanoparticles with varying solution pH

ZnS NPs with varying pH were prepared by adopting similar process as described in section 3.2.1. Solution pH without the addition of NaOH came out to be 5.6. After stirring the final reaction mixture containing solutions of $Zn(ac)_2$, TG and Na_2S for 30 min. (details given in section 3.2.1), the solution pH was adjusted to 8, 10 and 12 by adding appropriate amount of NaOH. This reaction mixture was further allowed to stir for 2.5 h at room temperature. The solution was then centrifuged and washed several times to get rid of unreacted species and excess TG. White precipitates thus obtained were dried at 80 °C for 24 h and were crushed to obtain fine powder.

3.2.3 ZnS/ZnO and ZnS/Ag_2S nanocomposites

ZnO_xS_{1-x}; x=0.25, 0.5 and 0.75 nanocomposites (NCs) were synthesized by simple chemical precipitation method. Solution of .25M $Zn(ac)_2$ was prepared in ultrapure water and was stirred for 30 min. Also, solutions of Na_2S and NaOH with varying ratios (Na_2S:NaOH=0.75:0.25, 0.5:0.5 and 0.25:0.75) were prepared separately and were stirred for 30 min. After that, solution of Na_2S was poured into the solution of NaOH dropwise and this solution was also stirred for 30 min. After that, the homogeneously stirred solution of Na_2S and NaOH was injected drop by drop into the solution of $Zn(ac)_2$. White coloured precipitates appeared during the addition of Na_2S and NaOH solution. The resulting solution was further stirred for 3 h. The whole synthesis process was carried out at 80 °C. After that, solution was aged overnight. Then, the solution was centrifuged and washed several times to get rid of unreacted species in the solution. The separated precipitates were dried at 80 °C in an oven for 24 h. The as synthesized powders were then calcined at 250 °C for 3 h to get pure ZnO phase. The dried precipitates were then crushed to obtain fine powder. For comparative study, pure ZnS (ZnO_xS_{1-x}; x=0) was also synthesized using the above mentioned process. $Zn_{1-x}Ag_xS$; x = 0, 0.01, 0.02, 0.03 and 0.04 NCs have also been prepared by the similar procedure which was used for ZnS/ZnO nanocomposites.

3.2.4 ZnS/ZnO core-shell particles

ZnS NPs were synthesized at solution pH 10 as discussed in section 3.2.2. The crushed powder was redispersed in 80 ml of ultrapure water and was UV irradiated for 3 h. The UV irradiated solution was then centrifuged at 12000 rpm and washed properly and was then dried at 80 °C for 24 h. The dried powder was again crushed properly to obtain fine powder.

This powder was redispersed in 40 ml of ultrapure water and was ultrasonicated for 30 min. The temperature was maintained at 10 °C. To this solution, homogeneously stirred solution of 0.1M $Zn(ac)_2$ and 0.1M of NaOH was added dropwise. The solution was then ultrasonicated for 1 h and was aged overnight. This solution was again centrifuged and washed properly to get rid of unreacted species. After that the precipitates were dried in oven at 80 °C for 24 h. To get pure ZnO phase, calcination of the dried powder was done at 250 °C for 3 h and were then crushed to obtain fine powder.

3.3 Characterization Techniques

The as prepared samples were characterized by X-ray diffraction (XRD) technique using Panalytical's X'Pert Pro diffractometer with Cu Kα radiation. Elemental analysis of as prepared samples was done using scanning electron microscope (SEM; JEOL, JSM-6510LV) equipped with energy dispersive X-ray spectrometer (EDS; Oxford INCA). Transmission electron microscope (TEM) images were recorded using TEM (PHILIPS, Model-CM 200) having accelerating voltage of 300 kV. Morphological study of the samples was done by high resolution transmission electron microscope (HRTEM) JEOL 2100F having operating voltage of 200 kV. FTIR spectrum was recorded using Bruker Alpha-T. Optical absorption spectra of the samples were recorded with a double beam UV-Visible spectrophotometer (Hitachi, Model-U-3900H). Diffuse reflectance spectra of powdered samples was taken using the same UV-Visible spectrophotometer (Hitachi, Model-U-3900H) equipped with integrating sphere. Photoluminescence (PL) emission spectra of samples has been recorded with Edinburgh Instruments FS920 spectrometer equipped with 450W Xenon Arc Lamp and a cooled single photon counting photomultiplier (Hamamatsu R2658P). Photoluminescence (PL) emission spectra at room temperature were measured by using a spectrofluorimeter (Perkin Elmer, Model- LS55). Photocatalytic experiments were carried out in dark using self designed photoreactor at room temperature the details of which are described in the next section.

3.4 Apparatus for photocatalytic study

The apparatus for photocatalytic experiments consisted of a cylindrical glass cell of 1 L capacity. A mercury lamp (having broad emission spectrum in UV and visible region) of 125 W was placed axially in a glass tube. The lamp and the tube were then immersed in a water jacket to cool the system. The glass cylinder was filled with 1 mg/L of dye solution and 0.5

g/L of catalyst. This solution was stirred using magnetic stirrer for 30 min. to ensure adsorption/desorption equilibrium of the dye molecules on the photocatalyst surface. After that, lamp was switched on to start the photocatalytic process. To determine the degradation of dye, the samples were collected at regular intervals of time (60 min.) and centrifuged to separate supernatant (dye solution) from catalyst. As crystal violet dye absorbs in visible region (λ_{max}=590 nm), therefore, photometric analysis of samples before and after light irradiation was used to study their percentage degradation. The sketch of photoreactor set up is given in Figure 3.1.

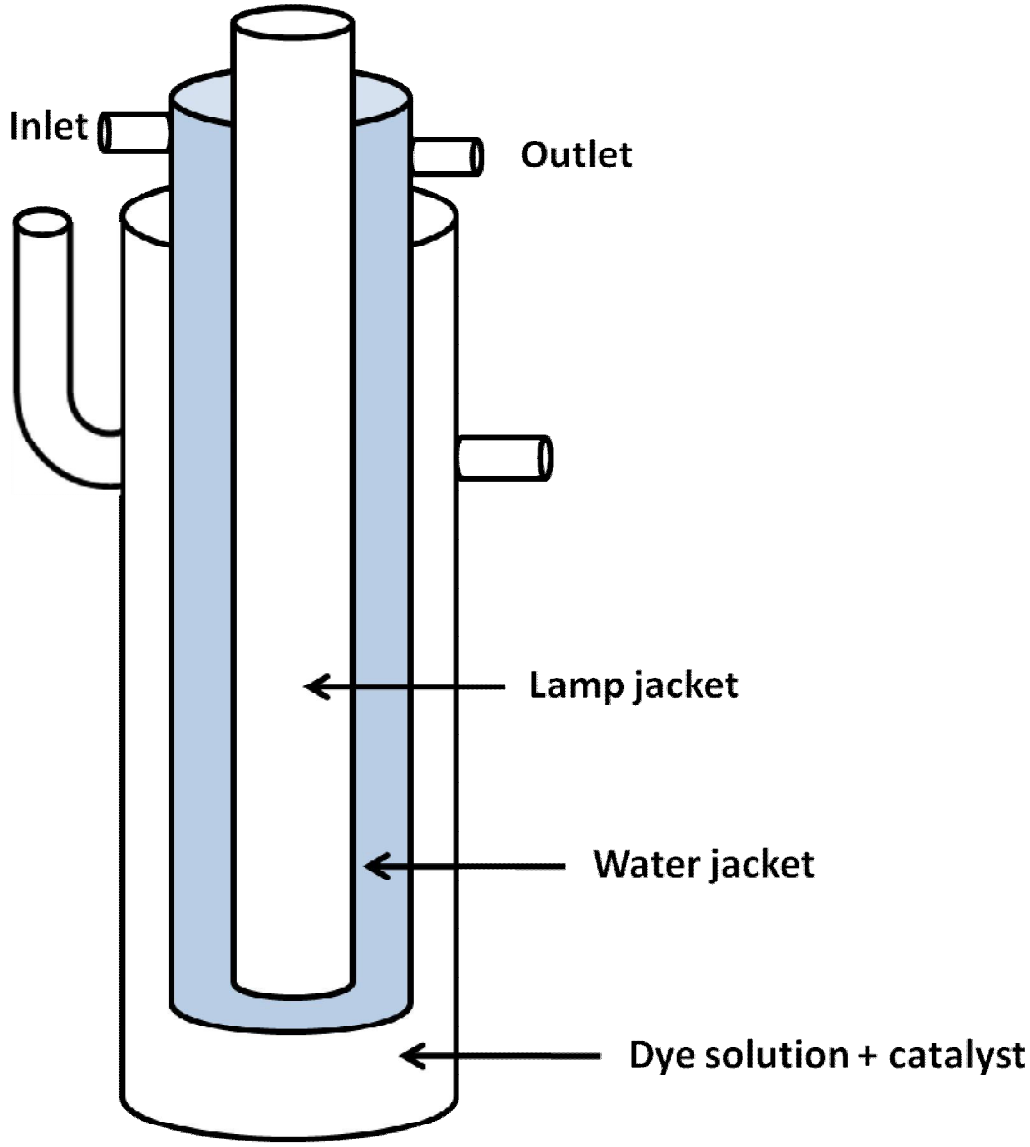

Figure 3.1: Sketch of photoreactor set-up to carry out photocatalytic experiments.

The model pollutant selected for entire photocatalytic study of the as prepared samples is crystal violet. It is a triarylmethane dye with molecular formula $C_{25}N_3H_{30}Cl$. It is widely used in paper industry to dye paper. Although this dye has many applications in medical and non-medical area, but it is very toxic to aquatic organisms as it may cause long-term adverse effects in the aquatic environment. The exposure to this dye can have possible risk of irreversible effects on mankind and may even cause cancer [2]. This compound is considered as a mitotic poison as well as a clastogen in vitro. Therefore this compound is regarded as biohazardous substance [3]. A simple procedure has also been developed for the detection of low concentrations of this dye in water. Concentrations of this dye in the range 0.5-1.0 μgl^{-1} of water could be reproducibly detected by employing this method. The dye can be detected not only in potable water, but also in river ones [4].

References

[1] K. Manzoor, S.R. Vadera, N. Kumar and T.R.N. Kutty, Synthesis and photoluminescent properties of ZnS nanocrystals doped with copper and halogen. Materials Chemistry and Physics, **82** (2003) 718-725.

[2] P. Drinkwater, Gentian violet-is it safe?. Australian and New Zealand Journal of Obstetrics and Gynaecology, **30** (1990) 65-66.

[3] W. Au, S. Pathak, C.J. Collie and T.C. Hsu, Cytogenetic toxicity of gentian violet and crystal violet on mammalian cells in vitro. Mutation Research/Genetic Toxicology, **58** (1978) 269-276.

[4] I. Šafařík and M. Šafaříková, Detection of low concentrations of malachite green and crystal violet in water. Water Research, **36** (2002) 196-200.

CHAPTER 4

RESULTS AND DISCUSSION

Undoped ZnS nanoparticles

Overview

The present chapter describes the studies of undoped ZnS nanoparticles (NPs) prepared via chemical precipitation route. Structural studies have been done using X-Ray diffraction (XRD) technique, transmission electron microscopy (TEM) and high resolution transmission electron microscopy (HRTEM). Fourier transfer infrared (FTIR) spectroscopy has been employed to determine the nature of chemical bonds present on the surface of ZnS NPs. UV-Vis spectroscopy and photoluminescence (PL) spectroscopy has been utilized to investigate the absorption and emission characteristics of undoped ZnS NPs. Photocatalytic degradation of crystal violet has been carried out with the aim to study photocatalytic properties of as prepared ZnS NPs. Effect of UV irradiation on photocatalytic properties of ZnS has also been investigated. At the end of the chapter, effect of pH of the solution (in which the NPs are being synthesized) on optical and photocatalytic properties of undoped ZnS has also been discussed in detail.

4.1 Studies of undoped ZnS

4.1.1 Introduction

Undoped ZnS nanoparticles (NPs) have been synthesized by simple chemical precipitation route. These NPs have been synthesized with the aim to compare their structural and optical properties with that of doped ZnS NPs (discussed in next chapter). Photocatalytic degradation of crystal violet has also been carried out for comparative purpose. Further, ZnS NPs with varying solution pH (during synthesis) have also been prepared to investigate the effect of pH (in which the NPs are being synthesized) on their optical and photocatalytic studies. The results of undoped ZnS NPs are presented below.

4.1.2 XRD Studies

Figure 4.1 shows the XRD pattern of undoped ZnS NPs. Diffraction peaks from (111), (220) and (311) planes match well with those of the β-ZnS (cubic) reported in the ICDD powder diffraction file no. 80-0020. Broadening of diffraction peaks indicate nanosize formation of ZnS [1].

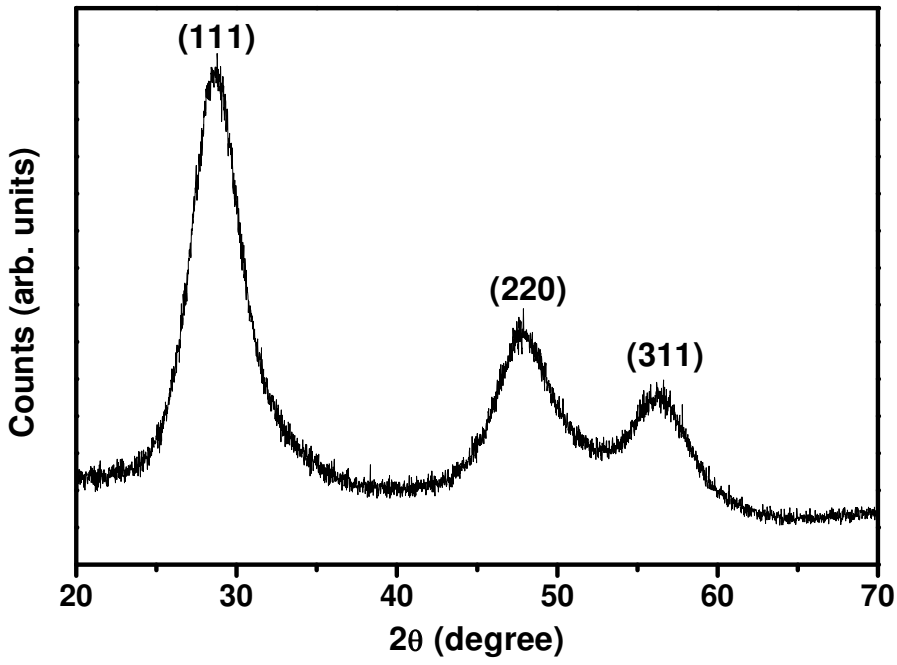

Figure 4.1: X-Ray Diffraction pattern of undoped ZnS NPs in the range 20°-70°.

Crystallite size of NPs was calculated by following Scherrer's equation

$$t = \frac{k\lambda}{\beta\cos\theta} \qquad (4.1)$$

where k = 0.9, t is the crystallite size (Å), λ (Å), the wavelength of Cu Kα radiation and β is the corrected half width of the diffraction peak [2]. FWHM of the most intense peak (111) is 3.93°. The average crystallite size calculated from the above equation came out to be ~2.08 nm.

4.1.3 TEM Analysis

Figure 4.2(a-b) shows micrographs of undoped ZnS.

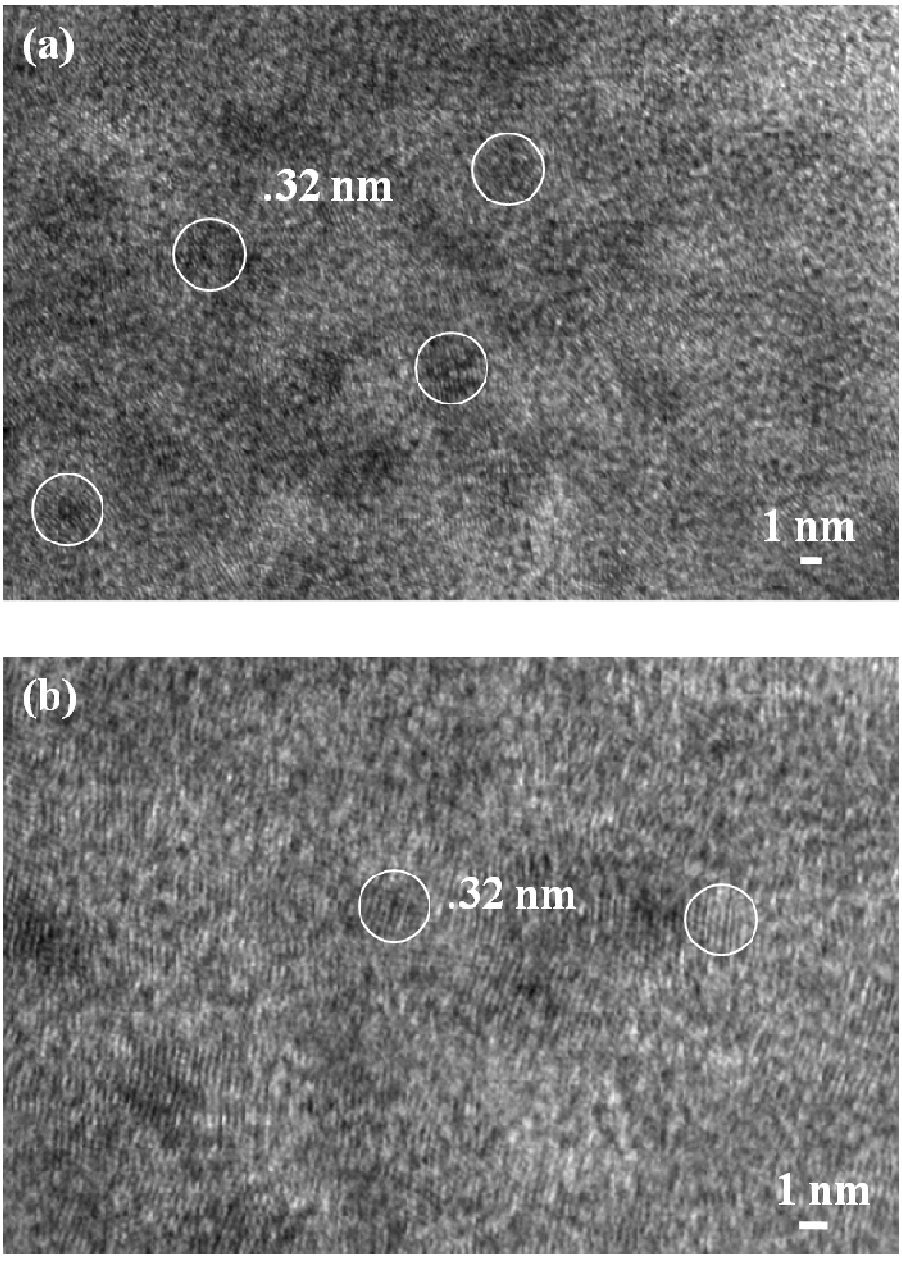

Figure 4.2: (a-b) HRTEM images of undoped ZnS. Lattice fringing have been encircled for better understanding.

As observed in Figure 4(a), the particles of undoped ZnS are irregularly spherical. In all the micrographs, lattice fringes can be clearly observed with the d spacing of ca. 0.31 nm which corresponds to the (111) plane of the cubic ZnS. This result is also in good agreement with the XRD pattern of the same. Observation of lattice fringing clearly indicates that the particles are formed at nanoscale.

4.1.4 FTIR Analysis

To investigate various functional groups present in thioglycerol (TG) capped undoped ZnS, FTIR studies were done. Figure 4.3 shows FTIR spectra of undoped ZnS NPs. The peak positions alongwith peak assignments are marked in Figure 4.3 and are given in Table 4.1.

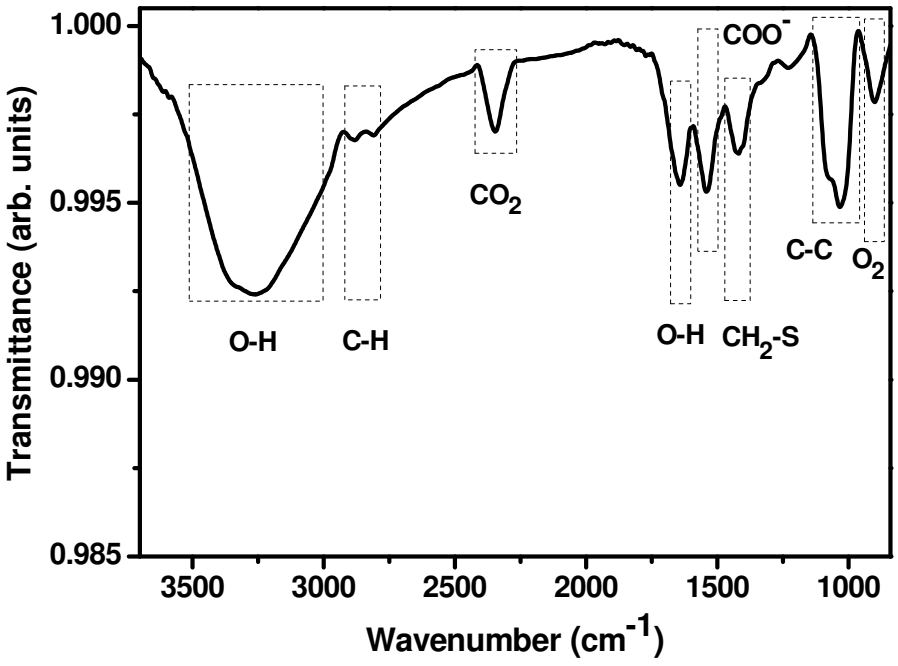

Figure 4.3: FTIR spectra of TG capped undoped ZnS NPs.

Pure TG exhibit S-H vibration band at 2557 cm^{-1}. This peak was not observed in the undoped sample. It is attributed to the fact that the thiolate functional group of the TG ligands are connected to the Zn^{2+} sites on the ZnS nanocrystals surfaces which confirm the capping of TG on ZnS surface [3]. The peak observed at ~ 900 cm^{-1} is due to the oxygen stretching and bending frequency [4].

Table 4.1: Peak assignment of various bonds in thioglycerol capped ZnS NPs.

Peak position (cm^{-1})	Peak assignment
3265	O-H stretching [3]
2885	C-H symmetrical stretching [3]
2810	C-H asymmetrical stretching [3]
2346	Interference from CO_2 [5]
1642	O-H bending [3]
1540	COO^- [6]
1416	$–CH_2–S$ [7]
1033	C–C stretch [7]
900	O_2 stretching and bending [4]

4.1.5 UV-Vis studies

Figure 4.4 shows the diffuse reflectance spectra of undoped ZnS NPs. The relation between reflectance R and absorption coefficient α as given by Kubelka–Munk method [8] is

$$F(R) = \frac{(1-R)^2}{2R} = \frac{\alpha}{S} \qquad (4.2)$$

where F(R) is the Kubelka–Munk function, S is the scattering coefficient. From the above equation, the Kubelka–Munk function F(R) can be assumed to be proportional to α [7]. Absorption spectra have been plotted by employing the above equation which is shown in the Figure 4.5.

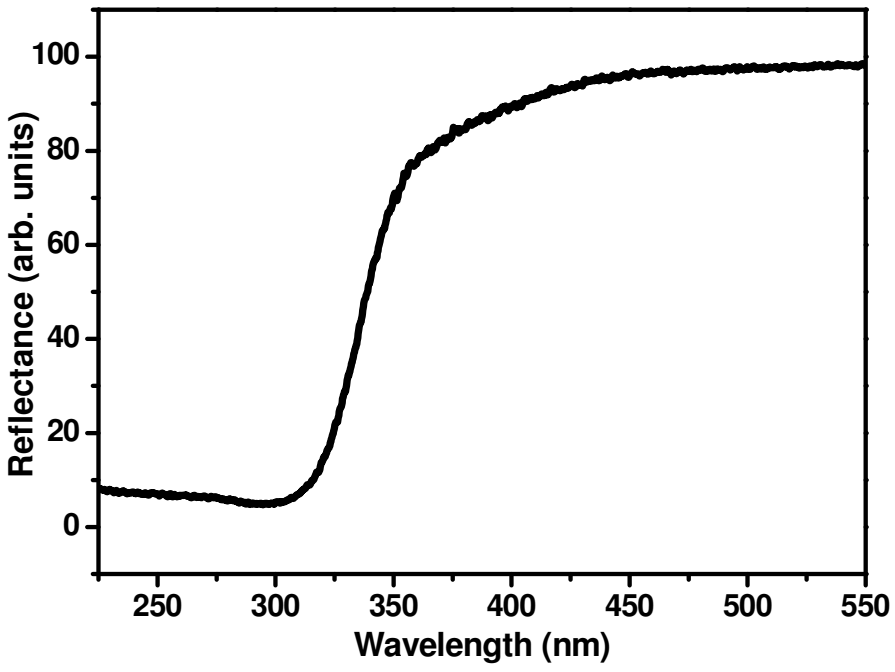

Figure 4.4: Diffuse reflectance spectra (DRS) of undoped ZnS NPs.

The relation between the incident photon energy (hυ) and the absorption coefficient (α) or F(R) is given by [8]

$$[F(R)h\upsilon]^{1/n} = A(h\upsilon - E_g) \qquad (4.3)$$

where A is a constant and E_g is the band gap of the material and the exponent n depends on the type of the transition i.e. 2, 3, 1/2, 1/3 values corresponding to indirect allowed, indirect forbidden, direct allowed and direct forbidden transitions. As shown in the Figure 4.6, square of the absorbed energy [F(R)hυ] was plotted against photon energy (hυ). Band gap energy for direct gap transition was determined by extrapolating the straight portion of the graph on hυ axis at F(R)=0 and it came out to be 3.85 eV which is quite higher as compared to its bulk counterpart (3.54 eV). This variation in band gap indicates formation of nano size crystals showing strong quantum confinement effect. The band gap of the semiconductor becomes larger with decreasing particle size, and is indicated by an absorption shift to shorter wavelengths. This is due to the fact that the levels of the valence band are moderately shifted to lower energies, while those of the conduction band are strongly shifted to higher energies. The shifting of band edges yields larger redox potentials which result in enhancement of photocatalytic activity of NPs [9]. The value of absorption wavelength came out to be 322.60 nm.

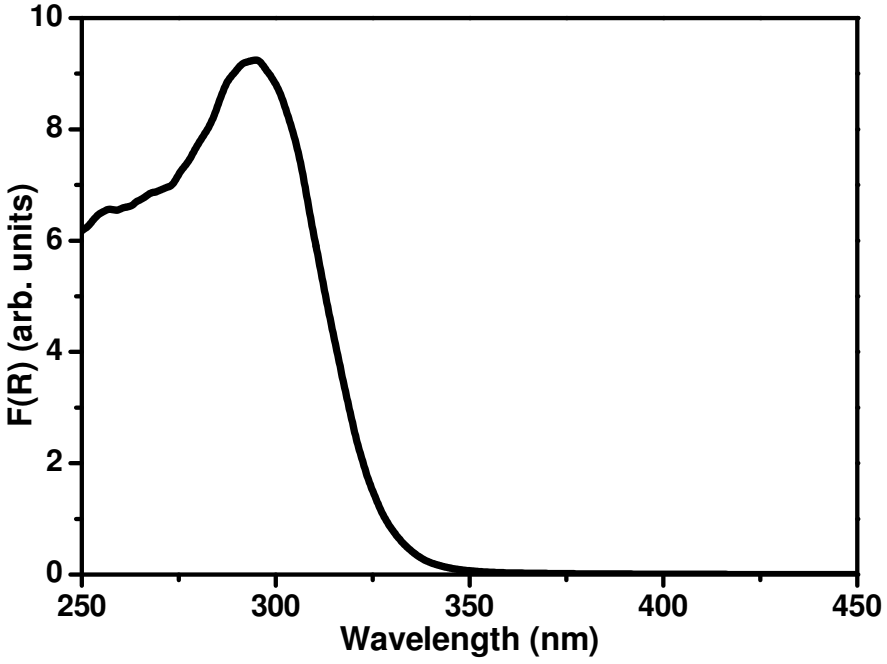

Figure 4.5: Absorption spectra of undoped ZnS NPs.

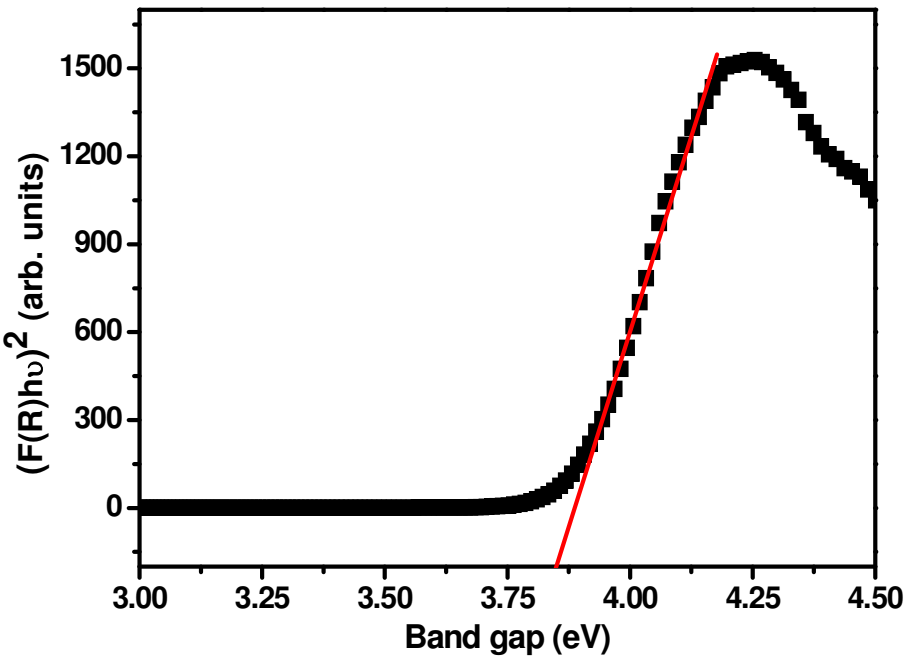

Figure 4.6: Tauc plot for undoped ZnS NPs to determine band gap.

4.1.6 Photoluminescence studies

Figure 4.7 shows photoluminescence (PL) emission spectra of undoped ZnS NPs. PL emission spectra have been recorded at room temperature with an excitation wavelength of 320 nm.

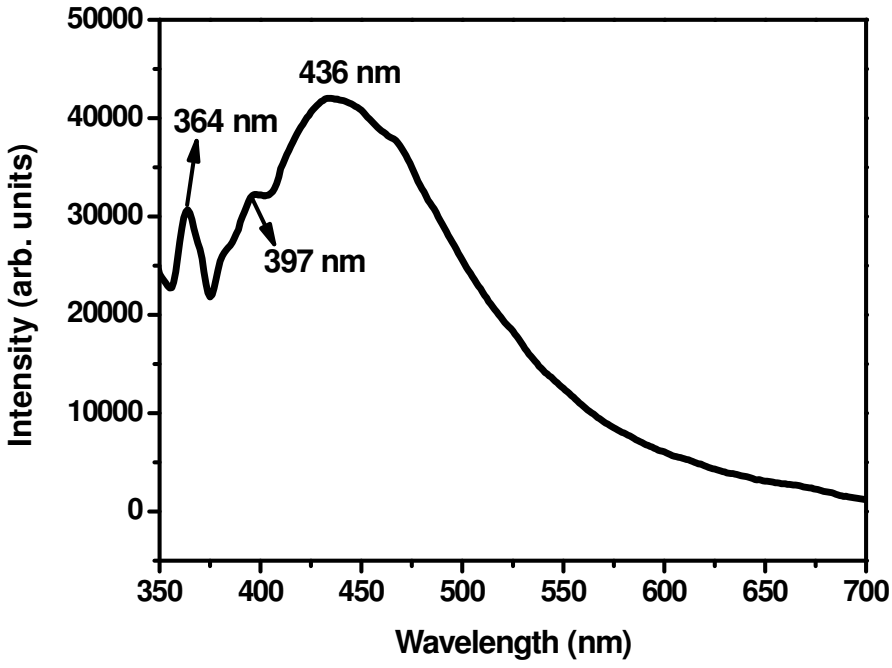

Figure 4.7: Photoluminescence emission spectra of undoped ZnS NPs.

As can be clearly seen in the figure, undoped ZnS exhibits blue emission peak at ~ 364 nm, 397 nm and 436 nm. It is well reported that emission peak at 363-392 nm is due to sulphur interstitial sites or band edge luminescence [10]. Emission peak observed at 436 nm is due to the presence of sulphur vacancies acting as donors, releasing electrons into the valence band during the transition [11]. As the particle size decreases to nanometer range, larger specific surface area increases which results in numerous surface defects such as lattice distortions, adsorbed impurities and dangling bonds. Generally, these surface defects deteriorate luminescence properties of a material which is not required for practical application of these optically active materials. These defects can be minimized by inorganic or organic capping. In our study, we have used thioglycerol (TG) as an organic capping agent to minimize these defect states. Uncapped ZnS give broad emission spectra in the UV and visible region depending upon the nature and density of defects. In our case, emission peak due to sulphur interstitials (392 nm) is lower than that of emission related to sulphur vacancies. As emission intensity originating from a particular defect is proportional to the population of that defect site present in the sample, so relative emission peak intensity of sulphur interstitial and sulphur vacancy levels can be explained in terms of the change in population of these sites with capping. It can be said that sulphur interstitial sites were more likely to become passivated by thioglycerol as compared to sulphur vacancies.

4.1.7 Photocatalytic studies

Photocatalytic degradation of crystal violet has been carried out to investigate the photocatalytic activity of as prepared ZnS. Figure 4.8 shows absorbance spectra of crystal violet with molecular structure in the inset. Figure 4.9 shows the spectral changes in absorbance of dye occurring during photocatalysis in time interval of 60 min. The characteristic absorption peak of this dye at 590 nm has been selected to monitor the photocatalytic degradation of the dye. Using Beer Lambert law, the decrease in concentration of dye is recorded at different intervals of time to measure the degradation rate. Figure 4.10 shows the photo degradation of dye catalysed with as prepared ZnS in terms of change in concentration with respect to the initial concentration. Since, in this study, concentration of solute is very low (1mg/L), so Langmuir-Hinshelwood kinetics model [12] can be simplified to pseudo first order kinetic model equation.

$$ln\left(\frac{C_t}{C_0}\right) = kT \qquad (4.4)$$

where C_t is the concentration of dye after irradiation in selected time interval t, C_0 is the initial concentration of dye, k is the first order rate constant, and T is irradiation time.

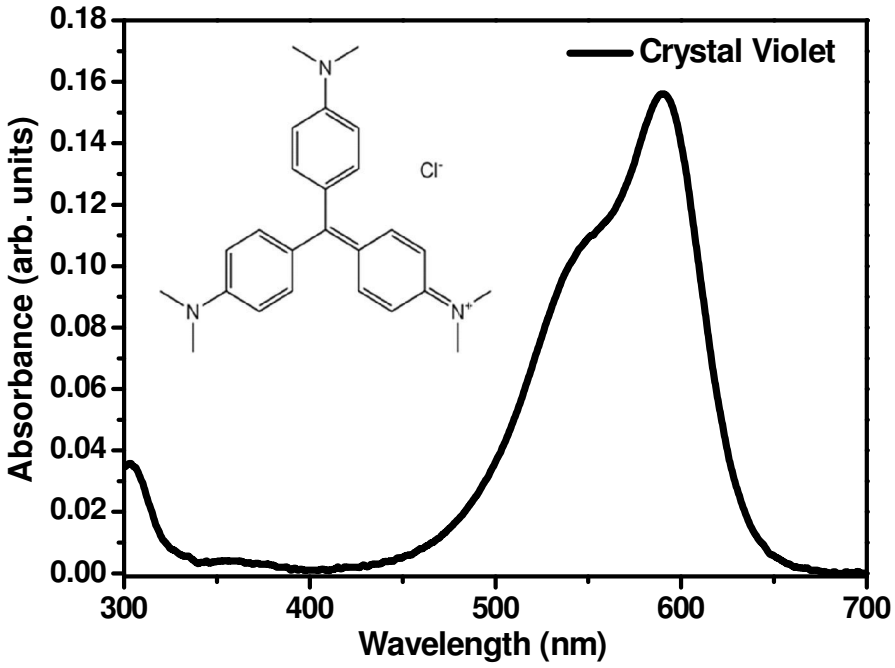

Figure 4.8: Absorbance spectra of crystal violet. Inset shows molecular structure of the same.

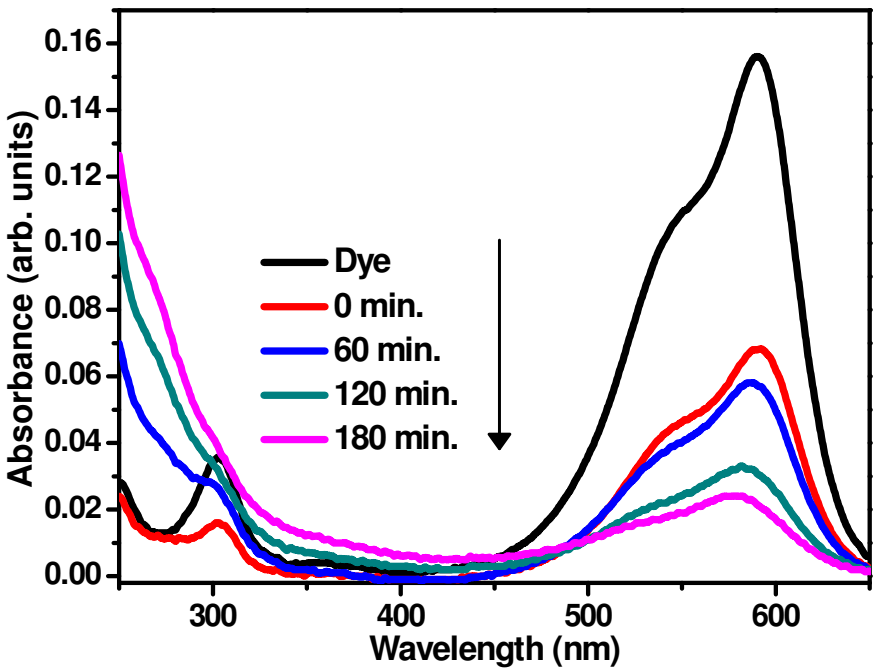

Figure 4.9: Absorbance spectra of crystal violet degraded in the presence of undoped ZnS.

Figure 4.11 shows corresponding plot between $\ln(C_t/C_0)$ and irradiation time to determine the value of rate constant k.

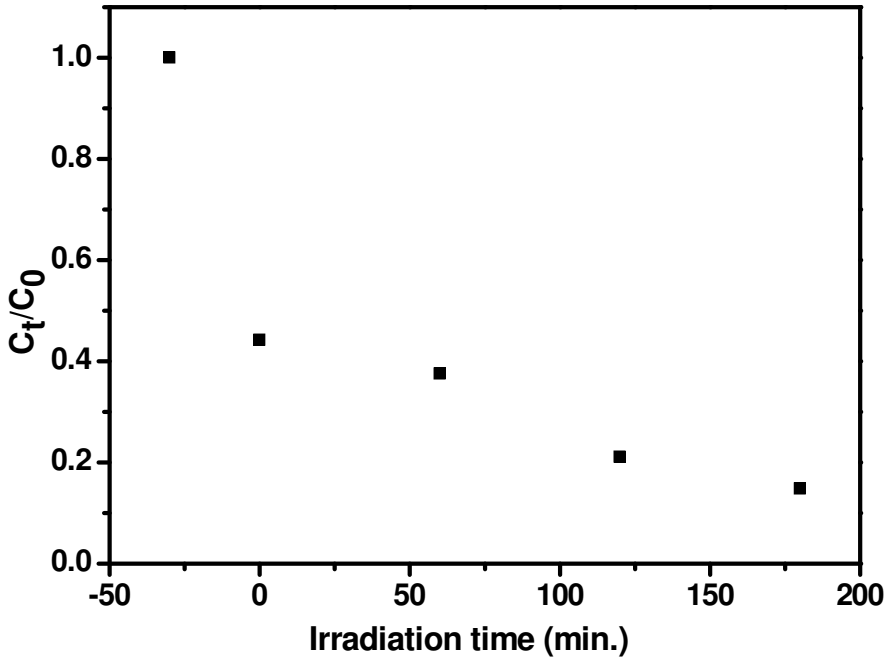

Figure 4.10: Variation of C_t/C_0 with irradiation time.

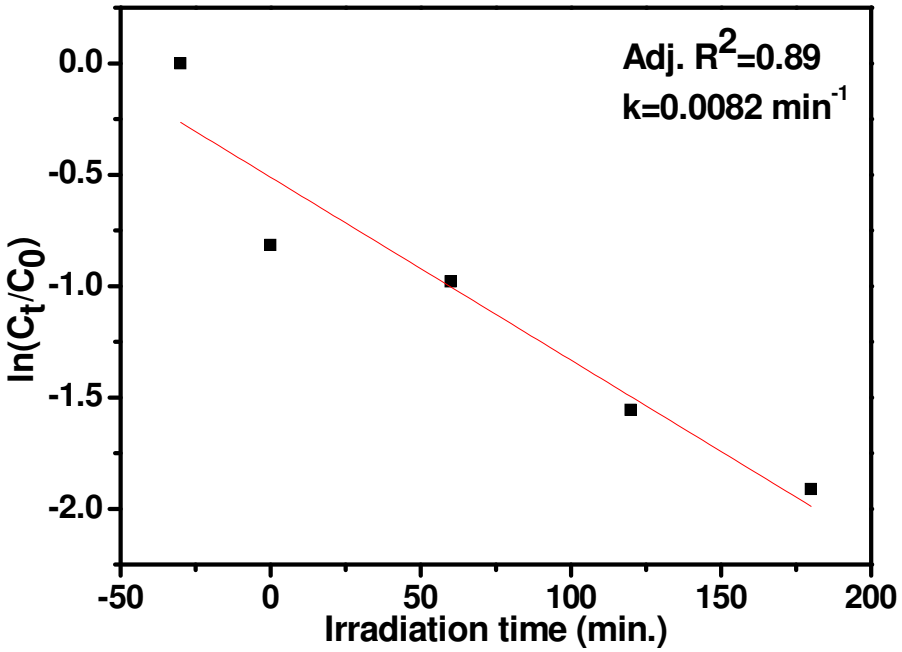

Figure 4.11: Plot between $\ln(C_t/C_0)$ and irradiation time to determine the value of rate constant k.

According to the first-order rate kinetics, the value of rate constant came out to be 0.0082 min^{-1}. The degradation efficiency has been calculated as

$$\%D = \left(1 - \frac{C_t}{C_0}\right) \times 100 \qquad (4.5)$$

where C_t is the concentration of dye after irradiation in selected time interval, C_0 is the initial concentration of dye. The degradation percentage in this photochemical reaction came out to be 85.35%.

As ZnS is a semiconductor material, therefore photodegradation of a dye is initiated by photoexcitation of semiconductor. The electrons are thus promoted to conduction band leaving hole in the valence band. If these charge carriers without undergoing recombination processes (radiative or non radiative) migrate to the surface of the semiconductor photocatalyst, then these react with the chemical species adsorbed on the surface of the photocatalyst. The resulting species (•OH radicals) are known to be very strong oxidizing agents which are beneficial in degrading the dye [13]. This phenomenon defines the indirect oxidation of dyes. Degradation efficiency depends largely on the total number of available free charge carriers on the catalyst surface. At nanoscale, the transportation length of electron-hole from crystal interface to the surface is short, which helps to accelerate the migration rate of charge carriers to the surface and hence to participate in photocatalytic process [9].

4.1.8 UV irradiation study of TG capped ZnS NPs

It is very important to investigate the effect of UV irradiation on the catalyst from the view point of their photostability; hence an experiment was conducted with the aim to study the effect of UV irradiation on TG capped ZnS NPs. Solution of the known amount of the prepared sample was kept under UV irradiation for 3 h. Aliquots were collected after every 60 min. of irradiation. UV-Vis absorption studies of the irradiated samples were done to investigate the optical changes taking place due to UV irradiation. Figure 4.12 shows the spectral changes occurring in the sample in different irradiation times. It can be clearly seen in the figure that absorption wavelength is blue shifted with the increase in irradiation time from 0 min. to 180 min. It is because of the various reactions occurring in TG capped ZnS-H_2O system on exposure of UV light. When light is made to fall on aqueous solution of TG capped ZnS NPs, then photo oxidation of thiol groups take place resulting in the formation of disulphide molecules which are easily dissolvable in water. As more NP surface is exposed to surroundings, therefore, water molecules get adsorb on the NPs surface which passivate the defect states. Prolonged exposure to UV light may result in formation of $Zn(OH)_2$ layer on NPs surface thereby reducing defect states to a large extent. As reported by various research groups [14-15], UV irradiation of thiol capped NPs cause red shift in absorption wavelength due to aggregation of NPs at longer irradiation times.

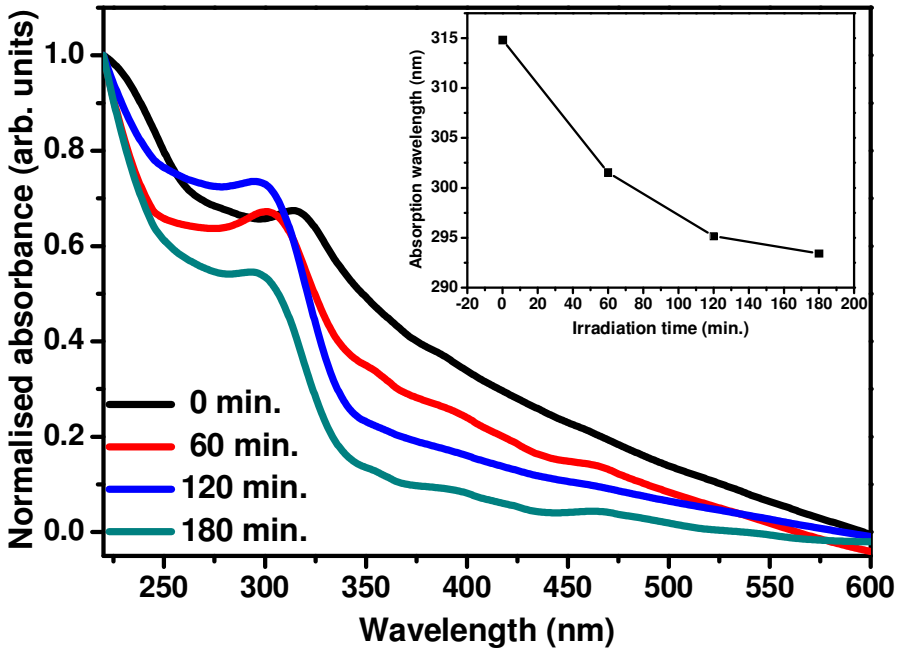

Figure 4.12: Absorbance spectra of TG capped ZnS irradiated with UV light in different intervals of time. Inset shows the change in absorption wavelength in different intervals of irradiation time.

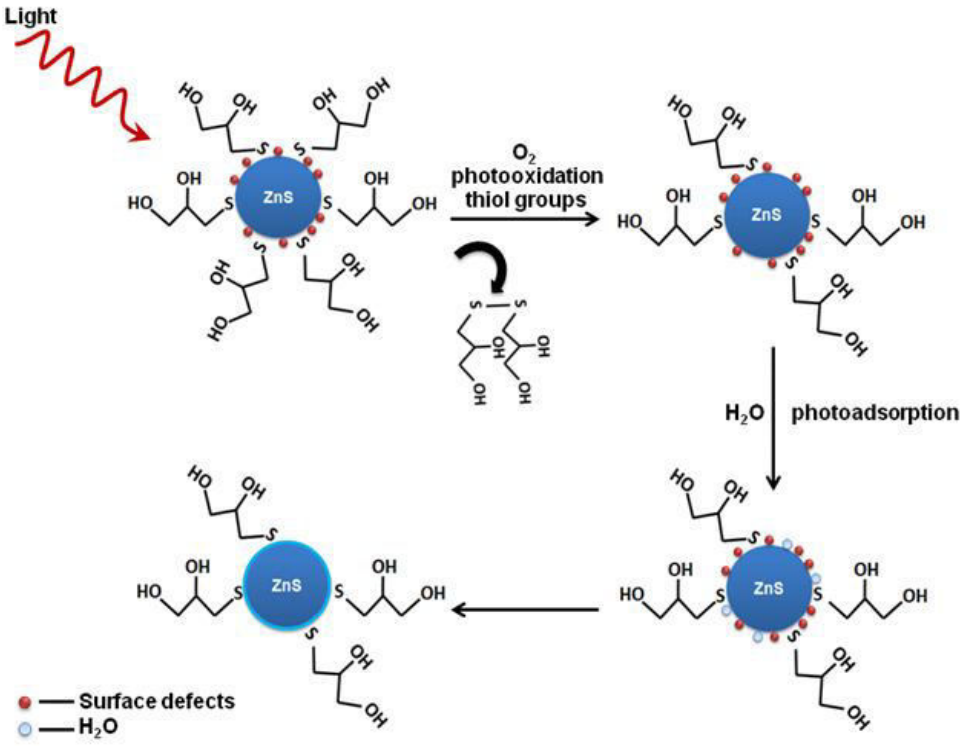

Figure 4.13: Mechanism of photochemical reactions occurring in ZnS-H_2O system in presence of UV light.

In the present work, as can be seen in the figure, blue shift is observed as irradiation time increases which indicate reduction in particle size. Another mechanism that can explain the observed blue shift is photoinduced oxidation of ZnS. As reported by Bol et al. [16], surface of ZnS NPs can be photooxidized to $ZnSO_4$ in presence of oxygen which result in decrease of ZnS particle size. Schematic representation of various reactions occurring in TG capped ZnS-H_2O system is given in Figure 4.13.

4.1.9 Photocatalytic studies of UV irradiated sample

In order to study the effect of UV irradiation on photocatalytic degradation of dye, similar experiment was performed using UV irradiated sample as discussed in section 2.4. Results showed the better degradation of the same dye (crystal violet) using UV irradiated sample as compared to the sample which was not UV irradiated (Figure 4.14).

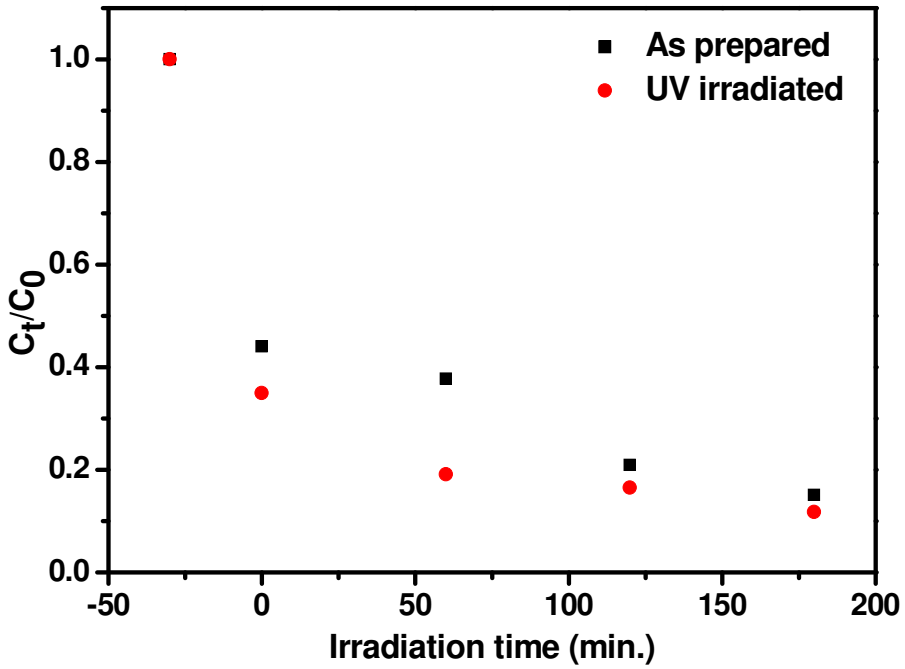

Figure 4.14: Variation of C_t/C_0 with irradiation time for as prepared undoped ZnS and UV irradiated ZnS.

This is attributed to the mechanism which is explained in the previous section. On UV irradiation, as explained above, NP surface is more exposed to surroundings. Hence, electrons will be promoted to the reaction sites more rapidly as there is less population of TG molecules on the surface which will enhance the photocatalytic activity of ZnS. Also, as observed in UV-Vis spectra of UV irradiated sample, absorption wavelength of ZnS is blue

shifted which indicates reduction in particle size. Hence, more dye molecules will get adsorbed on the surface of NP as more reaction sites will be available with reduction in particle size resulting in enhanced photocatalytic activity. Although UV irradiation studies of thiol capped NPs have been carried out on large scale [16-17], but, its effect on photocatalytic degradation of organic pollutants has not been explored. Our results show that UV irradiation of TG capped ZnS NPs can enhance their photocatalytic activity.

4.2 Effect of pH on structural, optical and photocatalytic properties of undoped ZnS NPs

4.2.1 Introduction

In this section, effect of solution pH (in which the NPs are being synthesized) on structural, optical and photocatalytic properties of ZnS is discussed. Solution pH plays very important role in determining the optical properties of NPs. In their work, Mehta et al. [18] reported that the absorbance corresponding to shoulder at 294 nm increases with increase in pH reflecting the maximum NPs formation in basic medium. Further, the particles get agglomerated at low and very high pH due to lack of effective capping by surfactant molecules. Synthesis pH conditions also affect emission intensity. In their work, Borse et al. [19] reported the maximum emission intensity at 5.0 pH. In studying the photocatalytic properties of semiconductors, much of the existing work is devoted to investigate the effect of pH of dye solution on its final degradation. But in the present case, NPs with varying solution pH were synthesized with the aim to study its effect on optical and photocatalytic properties.

4.2.2 DLS Studies

Hydrodynamic size and size distribution of as prepared ZnS NPs has been determined by DLS technique. Cumulative particle size distribution of ZnS NPs synthesized at different solution pH is shown in Figure 4.15. Variation of particle size with pH of solution is shown in Figure 4.16 and the corresponding values are also given in Table 4.2. It is evident from Figure 4.16 that with the increase in pH value of solution, hydrodynamic radius decreases upto pH 10 and then increases at pH 12. It is due to the reason that with the increase in amount of NaOH, OH^- ions occupy defect states and thus help in passivating the NP surface which further avoids agglomeration of NPs. In one of their works, Sastry et al. [20] reported that increase in pH leads to increase in concentration of OH^- thus increasing electrostatic repulsion and thereby providing stabilization. Also, as discussed by Vacassy et al. [21], the

aggregation of the NPs is more likely to occur at a pH value closer to the isoelectric point of the material. In the present case, isoelectric point of ZnS lies in the pH range 3-5.5 depending upon synthesis conditions. Hence, as we go beyond pH 5.62 to higher values i. e. 8, particle size becomes smaller. As discussed by Jiang [22], when pH value is far from isoelectric point, the electrostatic repulsive force is dominant over the vander Waals force which suppresses the agglomeration.

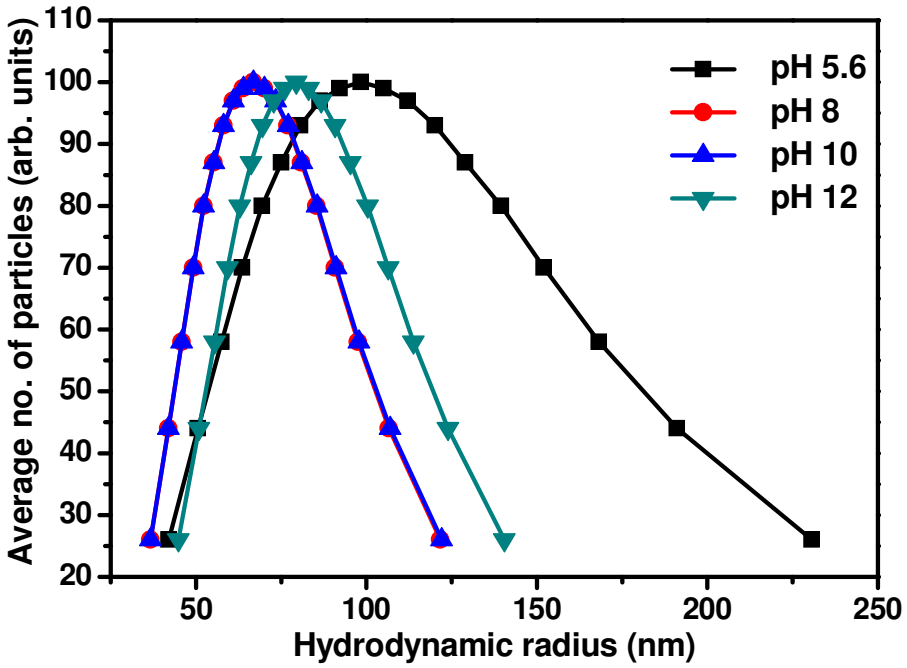

Figure 4.15: Cumulative particle size distribution of ZnS synthesized at different pH.

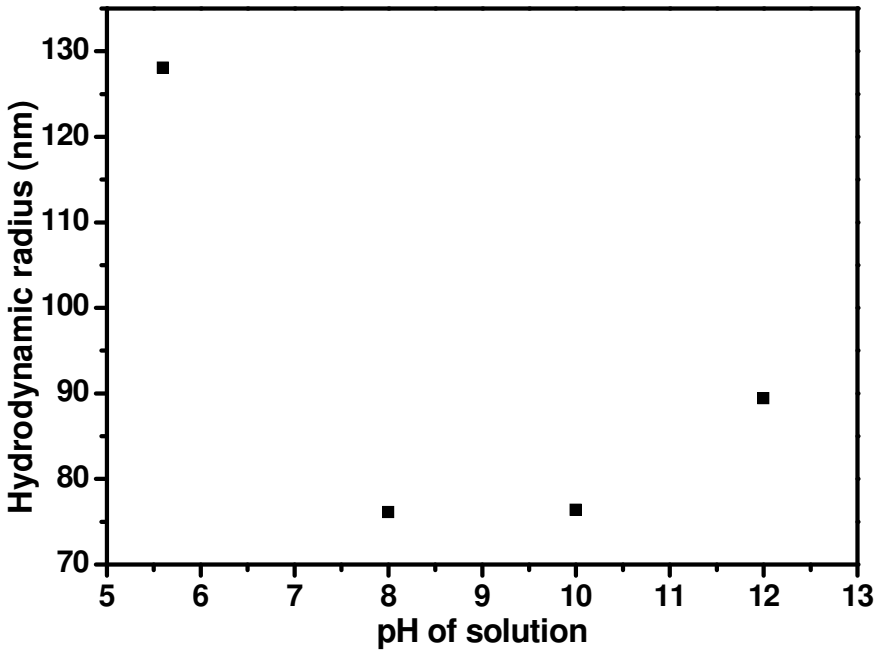

Figure 4.16: Variation of particle size with pH of solution.

At higher pH i. e. 10 and 12, there may be possibility of dissolution of particles having smaller hydrodynamic radius resulting in particles having larger hydrodynamic radius. It is to be noted that as pH of solution is increased from 5.6 to 12, the particle size distribution becomes narrower. Another reason for the increase in hydrodynamic radius of the sample synthesized at pH 12 may be as follows-

In aqueous system, Na_2S dissociates into ions as per the following reactions

$$Na_2S + H_2O \rightarrow S^{2-} + HS^- + Na^+ + OH^- \quad (4.6)$$

In basic medium,

$$HS^- + OH^- \rightarrow S^{2-} + H_2O \quad (4.7)$$

Thus, in more basic medium (i. e. pH 12), more S^{2-} ions are available to combine with Zn^{2+} ions to form more ZnS. As more ZnS will be formed at higher pH, hence capping will not be as effective as in case of samples synthesized at pH 8 and pH 10. Therefore, sample synthesized at pH 12 exhibits larger hydrodynamic radius as compared to other samples. This observation can also be explained by looking at the dissociation constant (pK_a) of thioglycerol which is 9.5. As the pH of the NP solution increased beyond the pK_a value of the thioglycerol, ionisation of the thiol groups and subsequent complexation with Zn^{2+} ions on the surface of the NPs gets progressively enhanced resulting in less effective capping which is in accordance with the observed results.

Table 4.2: Hydrodynamic size obtained for all samples.

pH of solution	Average hydrodynamic radius (nm)
5.6	128.04
8	76.09
10	76.36
12	89.40

4.2.3 XRD Analysis

To confirm whether there is any effect of solution pH on phase of ZnS NPs, XRD analysis has been carried out. As can be seen in Figure 4.17, there exists no additional phase i.e. ZnS remains in single phase even at pH 12. Also, from Figure 4.17, it is observed that XRD peaks are very broad corresponding to the (111), (220) and (311) planes. The peaks observed at 28.80º, 48.32º and 56.66º in the XRD patterns match well with those of the β-ZnS (cubic)

reported in the ICDD powder diffraction file no. 80-0020. Broadening of the XRD peaks indicate the formation of ZnS nanocrystals [1].

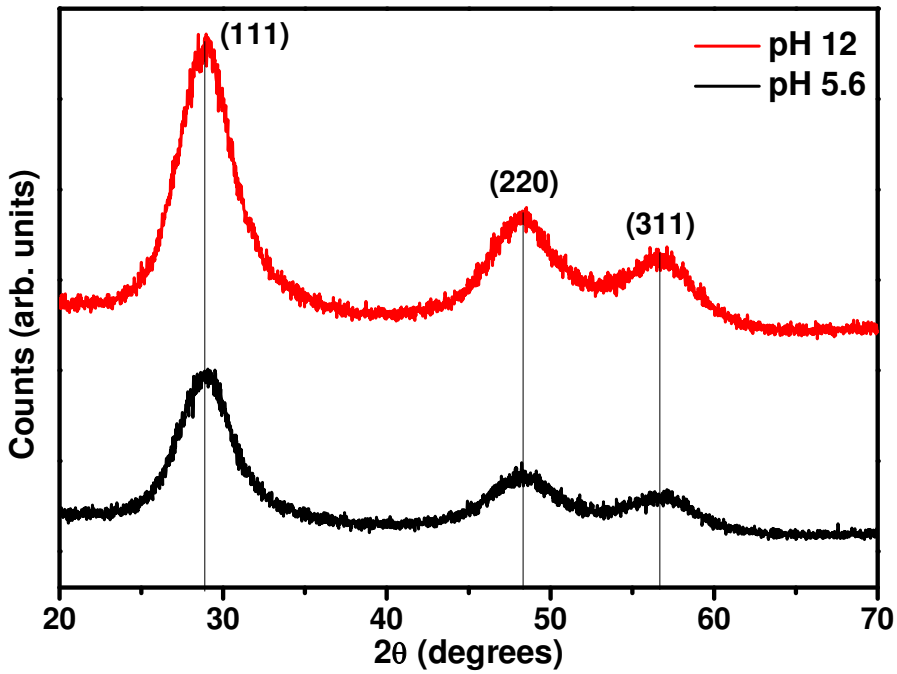

Figure 4.17: XRD patterns of samples in the range 20°-70°.

4.2.4 TEM Analysis

Figure 4.18 shows the HRTEM micrograph of ZnS synthesized at pH 10. As can be seen in figure, ZnS NPs are nearly spherical in shape.

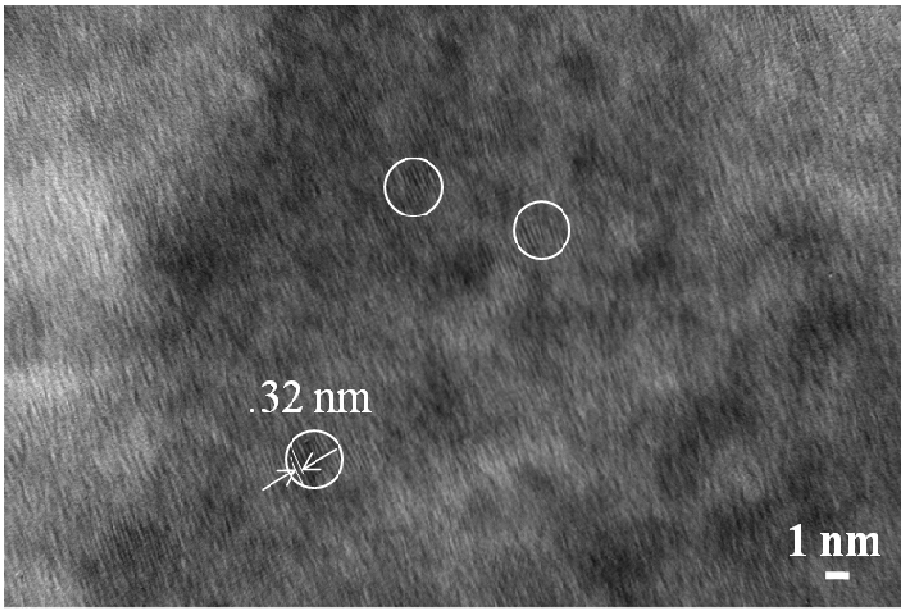

Figure 4.18: HRTEM image of ZnS synthesized at pH 10.

In this micrograph, lattice fringing is clearly observed with d spacing of 0.32 nm which corresponds to the (111) lattice plane spacing of ZnS in cubic phase. It indicates that the NPs exhibit crystalline nature.

4.2.5 FTIR Analysis

FTIR studies have been done to investigate various functional groups present in TG capped ZnS. Figure 4.19 represents FTIR spectra of ZnS synthesized in different solution pH. All samples exhibit almost similar IR spectra except the peak observed at 2888cm^{-1} which is absent in sample synthesized at solution pH 12. The O-H stretching is observed at ~3239 cm^{-1} which is confirmed by its bending vibration occurring at 1632 cm^{-1} [3]. Peak observed at 2888 cm^{-1} corresponds to C-H symmetrical stretching vibration [3].

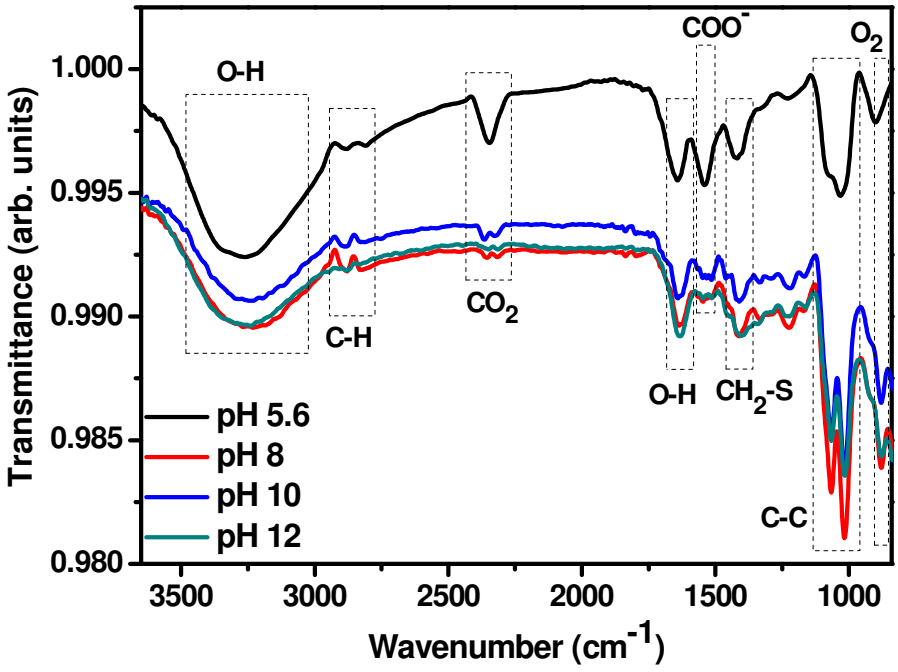

Figure 4.19: FTIR spectra of ZnS synthesized at different pH.

It may be noted here that this peak is of very less intensity in sample synthesized at pH 12. It is due to the reason that TG capping is not so effective in case of this sample as discussed in section 3.1. Pure TG exhibits S-H vibration band at 2557 cm^{-1}. This peak is not observed in all of the samples. It is attributed to the fact that the thiolate functions of the TG ligands are connected to the Zn^{2+} sites on the ZnS NP surfaces [3]. Additional peaks originated at 2322 cm^{-1} and 2360 cm^{-1} may be attributed to the interference from CO_2 [5]. The peak observed at 1410 cm^{-1} can be assigned to -CH_2-S [7]. Peak observed at ~1230 cm^{-1} is attributed to the

presence of acetate group present on surface of particles [6]. The doublet observed at 1063 cm^{-1} and 1015 cm^{-1} is due to C-C stretching [7]. The peak observed at ~ 900 cm^{-1} is due to the oxygen stretching and bending frequency [4]. Peak positions along with peak assignments for all the four samples are given in Table 4.3.

Table 4.3: Peak assignment of various bonds in ZnS synthesized at different pH.

Peak Position (cm^{-1})				Peak assignment
pH 5.6	**pH 8**	**pH 10**	**pH 12**	
3265	3233	3237	3246	O-H stretching [3]
2885	2883	2888	-	C-H symmetrical stretching [3]
2810	2810	2817	-	C-H asymmetrical stretching [3]
2346	2353	2365	2351	Interference from CO_2 [5]
-	2317	2324	2314	Interference from CO_2 [5]
1642	1634	1632	1631	O-H bending [3]
1416	1412	1410	1403	$-CH_2$-S [7]
1227	1229	1223	1230	Acetate [6]
1033	1067	1067	1067	C-C stretch [7]
-	1019	1019	1019	C-C stretch [7]
900	877	877	877	O_2 stretching and bending [4]

4.2.6 UV-Vis Analysis

UV-Vis analysis has been performed for all samples to investigate the effect of solution pH on optical properties of the samples. Figure 4.20 shows the UV-Vis absorption spectra of all the samples. From Figure 4.20, it is clearly visible that ZnS synthesized at pH 8, 10 and 12 shows strong quantum confinement effect as compared to the sample synthesized at pH 5.6. Absorption edge is strongly blue shifted in case of ZnS synthesized at pH 8, 10 and 12 as compared to that of sample synthesized at pH 5.6. Also, the absorption edge for all samples is blue shifted as compared to its bulk counterpart (340 nm). The relation between the incident photon energy (hυ) and the absorption coefficient (α) is given by

$$(\alpha h\upsilon)^{1/n} = A(h\upsilon - E_g) \qquad (4.3)$$

where A is a constant and E_g is the band gap of the material and the exponent n depends on the type of the transition. i.e. 2, 3, 1/2, 1/3 values corresponding to indirect allowed, indirect forbidden, direct allowed and direct forbidden [8].

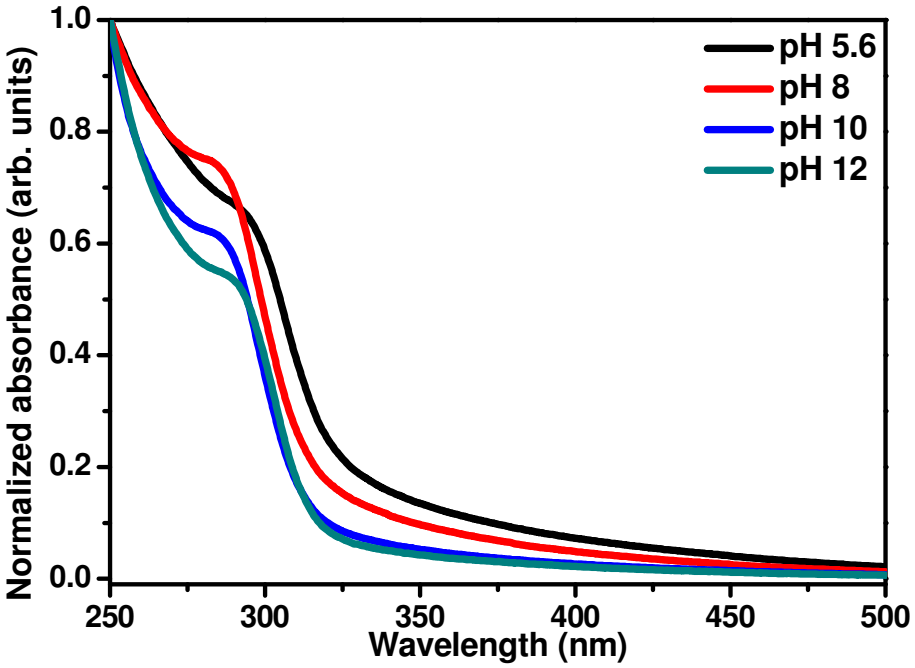

Figure 4.20: UV-Vis absorption spectra of samples synthesized at pH 5.6, 8, 10 and 12.

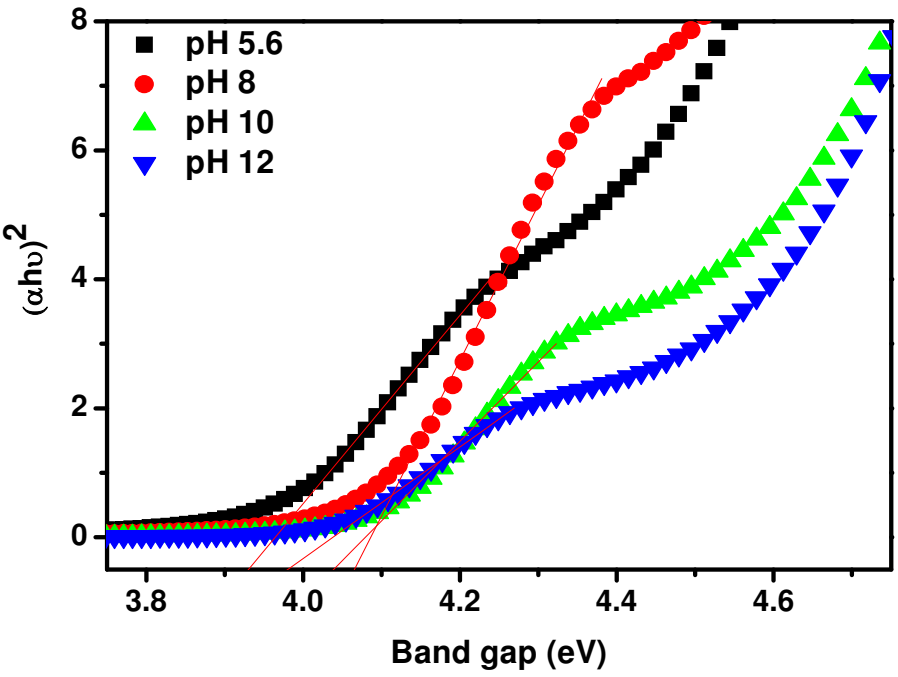

Figure 4.21: Tauc plots for as prepared samples to determine band gap.

To calculate the direct band gap value, $(\alpha h\upsilon)^2$ versus $h\upsilon$ is plotted and it is shown in Figure 4.21. By extrapolating the straight portion of the graph on $h\upsilon$ axis at $\alpha=0$, the optical band gaps are calculated. Absorption wavelengths and band gap values for all the samples calculated from Tauc's plot are given in Table 4.4. Variation of optical band gap with the

change in pH of solution is shown in Figure 4.22. The obtained band gap values are higher as compared to its bulk value (3.54 eV) due to reduced particle size showing strong quantum confinement effect. The valence band levels are moderately shifted to lower energies, while those of the conduction band are strongly shifted to higher energies. The shifting of band edges yields larger redox potentials which help in enhancement in photocatalytic activity of NPs [9].

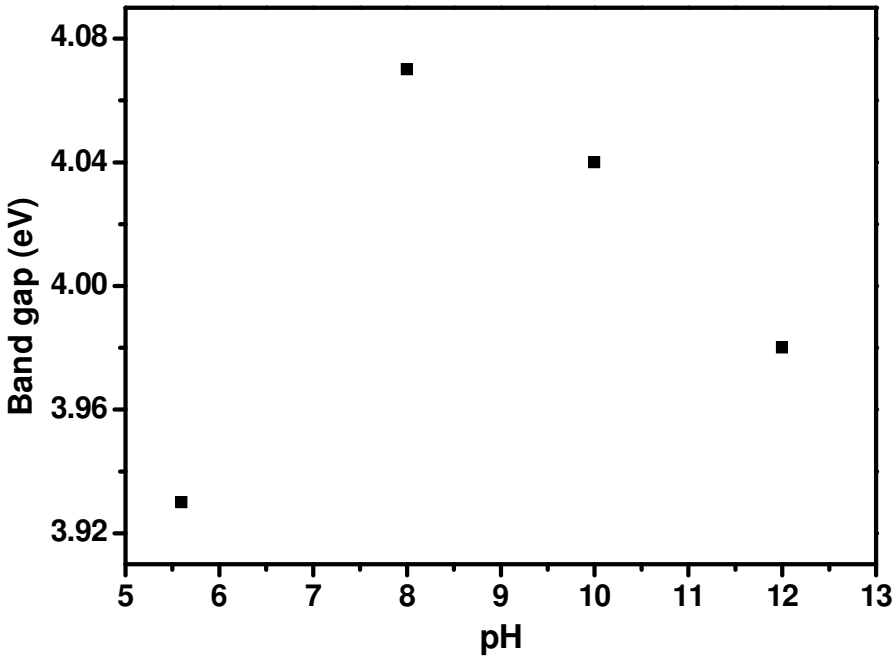

Figure 4.22: Variation of optical band gap with the change in pH of the solution.

Table 4.4: Calculated band gap values and corresponding absorption wavelengths of ZnS synthesized at different pH.

Sample	Optical band gap (from Tauc's plot)	Absorption Wavelength (nm)
pH 5.6	3.93	316.12
pH 8	4.07	305.25
pH 10	4.04	307.52
pH 12	3.98	312.15

4.2.7 Photoluminescence studies

Photoluminescence (PL) emission spectra of all samples have been recorded and is shown in Figure 4.23. The PL study of all the prepared samples has been performed at room temperature with an excitation wavelength of 325 nm where excitation and emission slit

width is 10 nm. As shown in Figure 4.23, all the four samples exhibit almost similar PL emission spectra with emission peaks centred at around 423 nm, 442 nm, 485 nm and 528 nm. It is well reported that emission peak observed around 423 nm is due to sulphur vacancies [23]. The peak at 442 nm is attributed to the interstitial zinc lattice defects [24]. Another emission band at 485 nm originates from the sulphur vacancy related emissions [24]. It is clearly observed in the figure that sample synthesized without the addition of NaOH (pH 5.6) exhibits highest PL intensity indicating large number of defect states present on the surface of ZnS. As pH is increased from 5.6 to 12, PL intensity keeps on decreasing. This phenomenon is attributed to the role of OH^- ions in passivating the defect states. In sample which is synthesized at pH 12, defect states are minimized which are attributed to the formation of $Zn(OH)_2$ layer on the surface of ZnS. If emission intensity related to a particular defect decreases, then, those defects are decreasing in the system. As discussed in section 4.2.2 that for the NPs synthesized in more basic medium, more S^{2-} ions will be available in the system thereby reducing defect states.

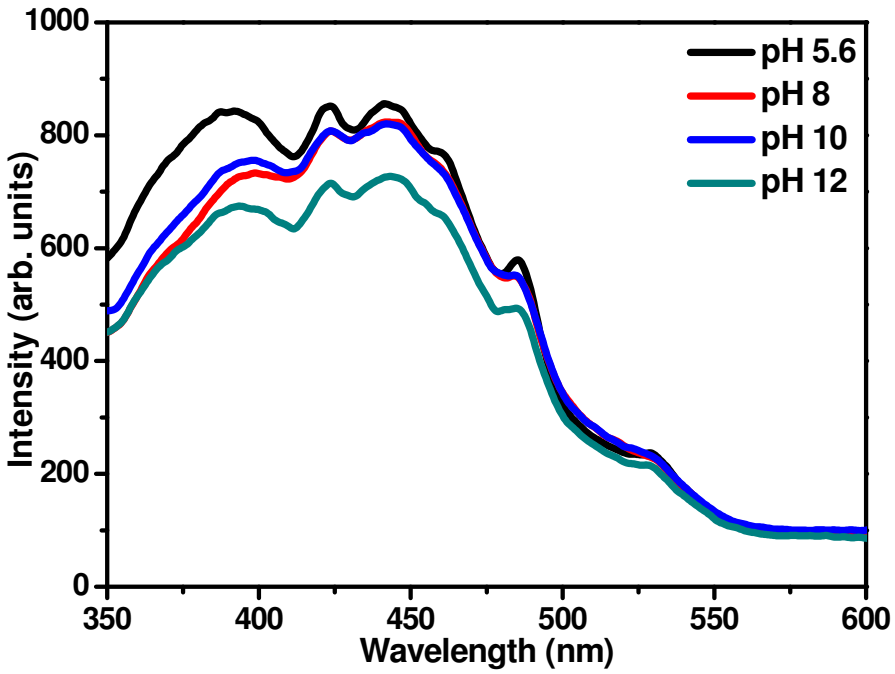

Figure 4.23: Photoluminescence spectra of as prepared samples.

4.2.8. Photocatalytic studies

The spectral changes taking place during the catalyst assisted photodegradation of crystal violet under UV-Vis irradiation are shown in Figure 4.24(a-d). The absorbance peak in case of samples synthesized at pH 8, 10 and 12 assisted photocatalytic degradation of dye at 590

nm shows hypsochromic shift with increasing irradiation time. This hypsochromic shift of the peak at 590 nm of the chromophore is of particular significance as it indicates N-demethylation process that ultimately leads to the destruction of the conjugated structure [25].

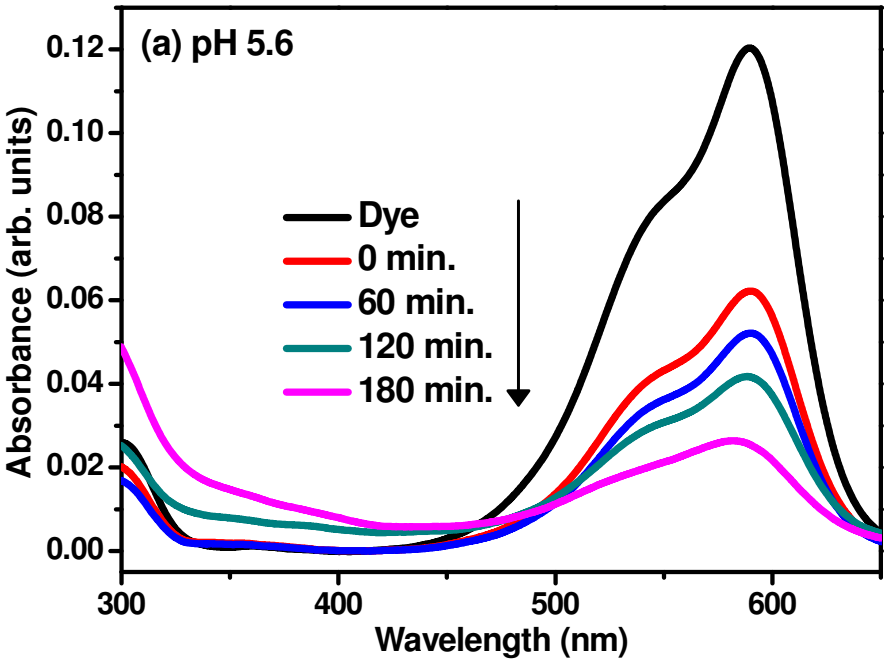

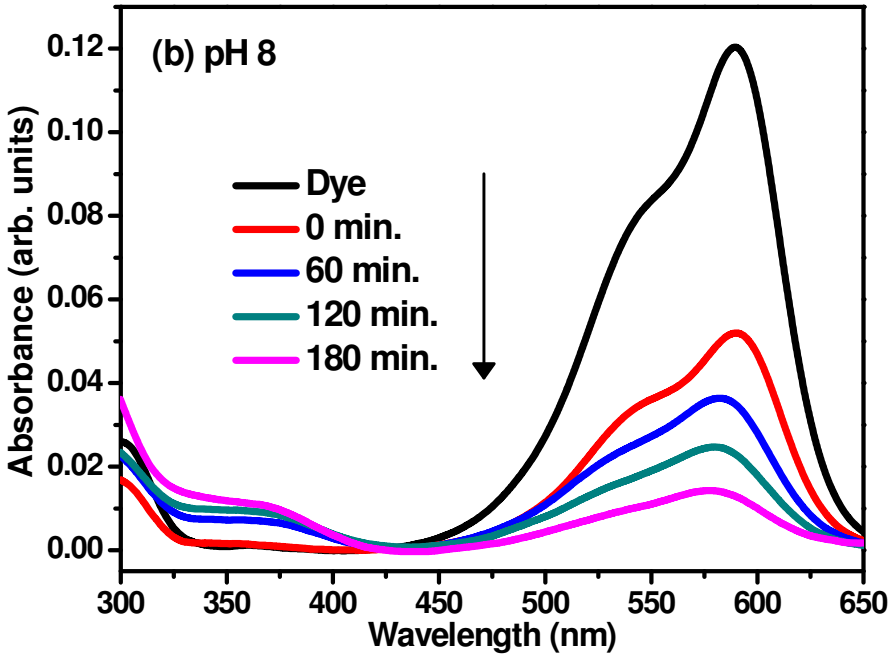

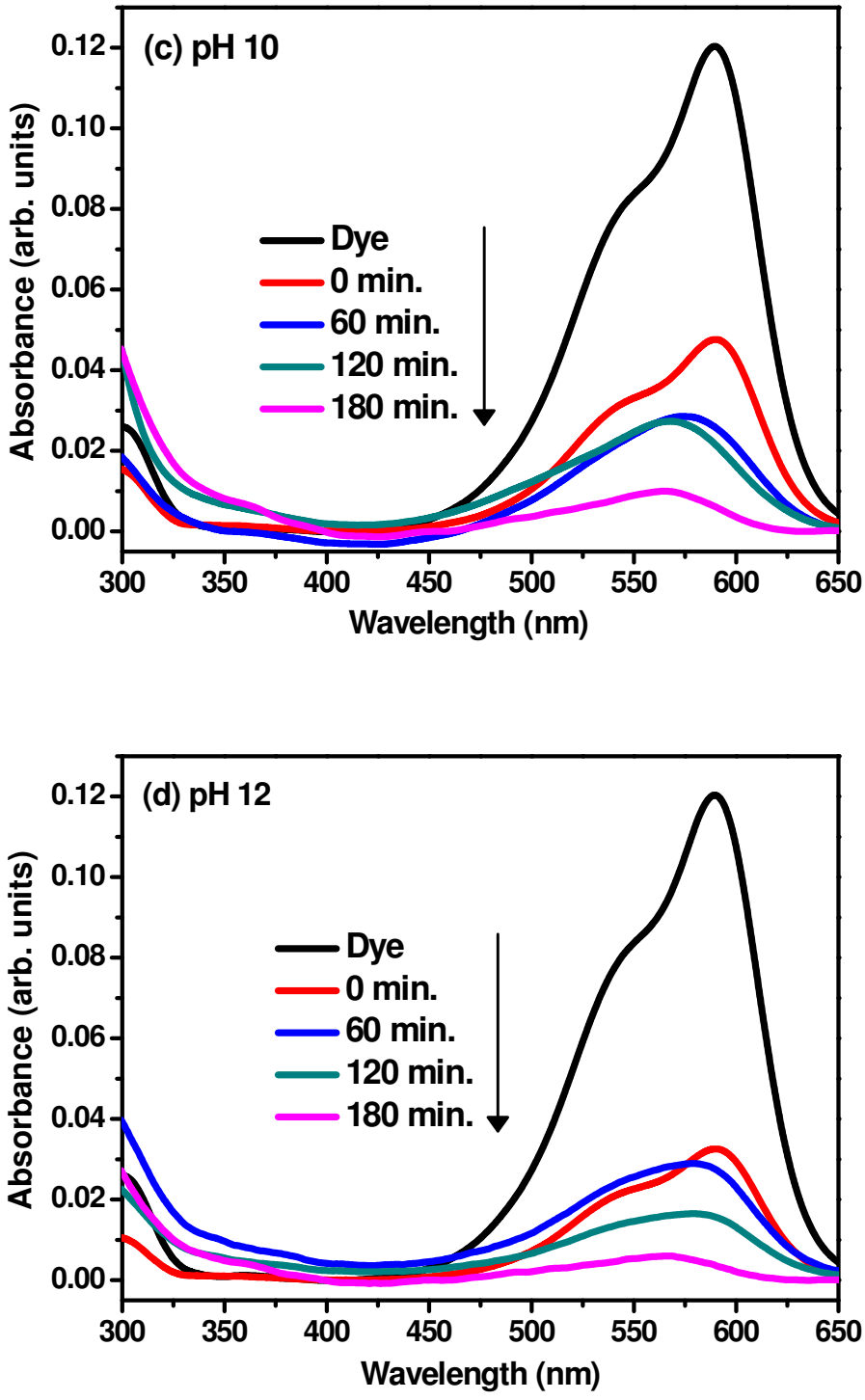

Figure 4.24: Absorbance spectra of crystal violet degraded in the presence of ZnS synthesized at different pH values.

Degradation of dye is indicated by decrease in absorbance of samples at λ_{max} (590 nm) in different time intervals. Dye degraded to higher extent with the assistance of catalyst synthesized at pH 12. Figure 4.25 shows the comparison of photo degradation of dye

catalysed with as prepared ZnS in terms of change in concentration with respect to the initial concentration under UV-Vis irradiation. The order of photo degradation rate is obtained as

pH 5.6 < pH 8 < pH 10 < pH 12

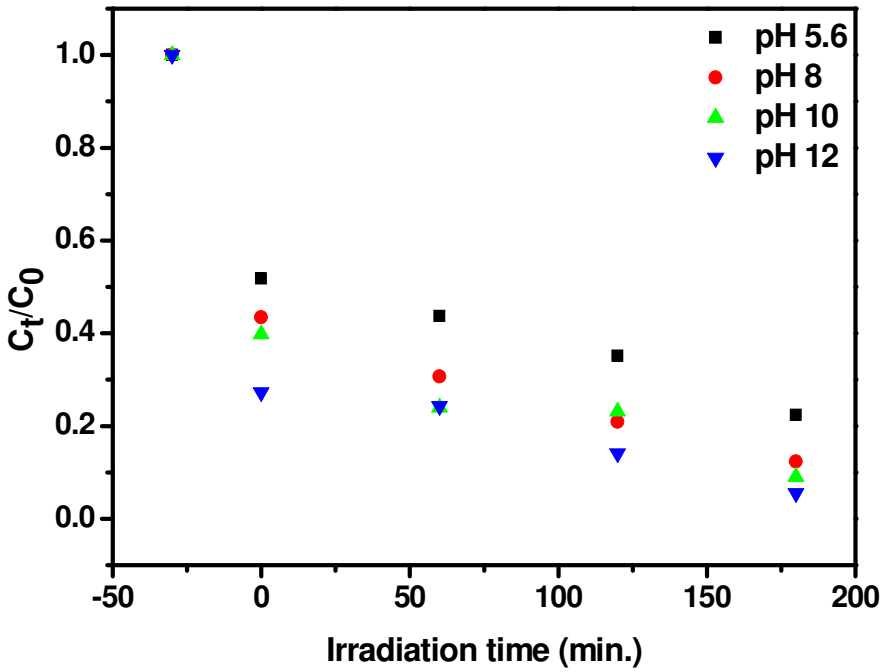

Figure 4.25: Variation of C_t/C_0 with irradiation time for photochemical reactions catalysed with as prepared samples.

Pseudo first order kinetic model equation [12] for low concentration of solute is given by-

$$ln\left(\frac{C_t}{C_0}\right) = kT \qquad (4.4)$$

where C_t is the concentration of dye after irradiation in selected time interval, C_0 is the initial concentration of dye, k is the first order rate constant, and T is irradiation time. The value of rate constant (k) for different photochemical reactions is obtained from the slope of plots of Figure 4.26. As can be seen from Table 4.5, the value of k is largest (0.0116) for the photochemical reaction catalysed with sample synthesized at pH 12 as compared to that of other photochemical reactions under UV-Vis illumination. Second order rate constants show lower values of R^2 as compared to that of first order. The degradation efficiency has been calculated as

$$\%D = \left(1 - \frac{C_t}{C_0}\right) \times 100 \qquad (4.5)$$

where C_t is the concentration of dye after irradiation in selected time interval, C_0 is the initial concentration of dye. As shown in Figure 4.27, %D in presence of ZnS NPs synthesized at

natural pH of 5.62 is 77.66% which is less as compared to other photochemical reactions. The value of degradation percentage for all samples is also listed in Table 4.5.

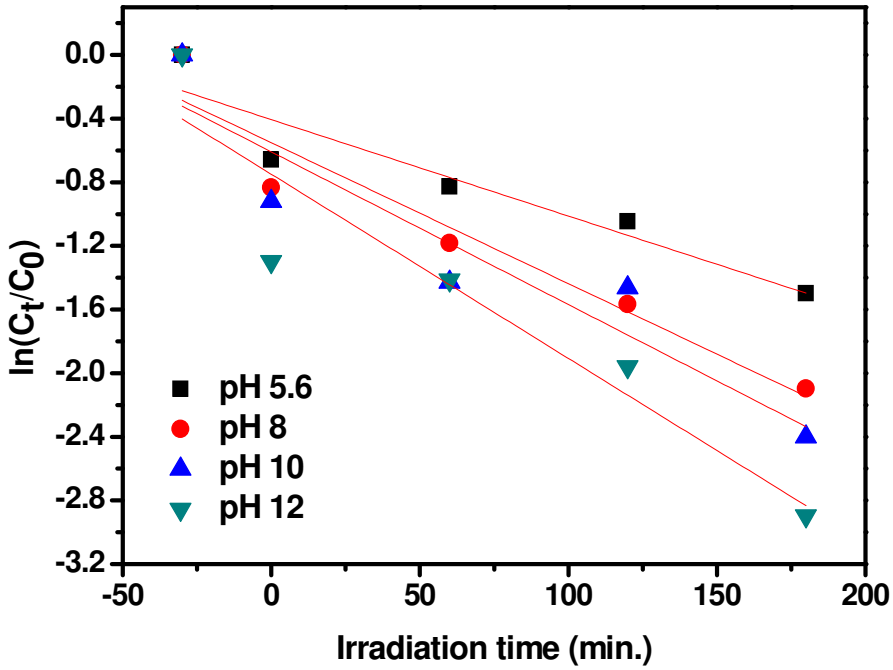

Figure 4.26: Plot between $\ln(C_t/C_0)$ and irradiation time to determine the value of rate constant k.

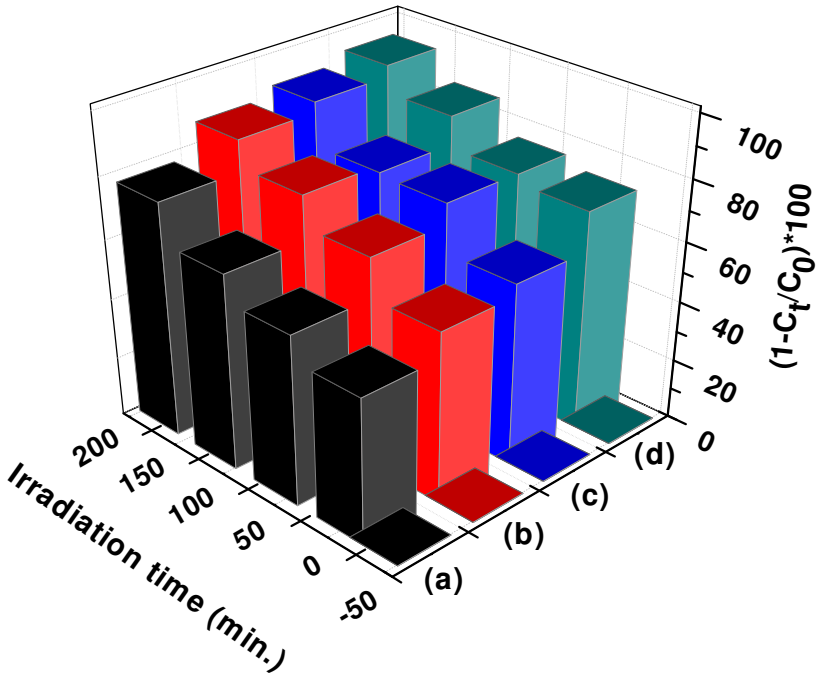

Figure 4.27: Degradation percentage of crystal violet in the presence of sample synthesized at (a) pH 5.6, (b) pH 8, (c) pH 10 and (d) pH 12 at different irradiation times.

Table 4.5: First order rate constants for the photocatalytic degradation of crystal violet and corresponding percent degradation for different photochemical reactions.

Photocatalyst	Adj. R^2	k (min^{-1})	$(1-C_t/C_0)*100$
ZnS@pH 5.6	0.86	0.0061	77.66
pH 8	0.91	0.0089	87.72
pH 10	0.85	0.0096	90.93
pH 12	0.85	0.0116	94.48

Since ZnS is a semiconductor material, so the photodegradation of the dye is initiated by photoexcitation of semiconductor. Photoexcitation of ZnS leads to generation of electron-hole pair. Aarthi et al. [26] have explained various chemical reactions occurring at semiconductor surface during photoexcitation. The as produced free radicals (•OH) are very strong oxidizing agents which help in mineralization of the dye [13]. Surface charge of NPs and adsorbant in aqueous solution plays an important role in degrading the dye. Interaction of dye molecules with catalyst surface largely depends on the surface charge of both. If the dye is cationic in nature, then the catalyst surface should be negatively charged in order to have sufficient adsorption. The dye (crystal violet) used in this work is cationic in nature. So, ZnS synthesized at pH 12 has facilitated more adsorption of dye molecules and hence more degradation has been observed. It is generally accepted that the photoluminescence signals incase of semiconductor materials result from the recombination of charge carriers. In most of the cases, the lower the PL intensity of semiconductor, the lower the recombination rate of photo-induced electron–hole pairs which leads to higher photocatalytic activity of semiconductor photocatalysts [27]. In the present case, sample synthesized at pH 12 exhibits maximum degradation activity because PL signal of the same sample is of lower intensity as compared to that of other samples (discussed in section 4.2.7). Hence, we can say that in case of ZnS synthesized at pH 12, recombination rate is lower as compared to that of other samples which leads to better photocatalytic activity as compared to other samples.

Other possible reason of the superior photocatalytic activity of ZnS synthesized at pH 12 as discussed by Gouvea et al. [13] is due to the main reaction represented by the hydroxyl radical attack, which is highly favoured by the high concentration of adsorbed hydroxyl groups at high pH values. It may be noted from DLS and UV-Vis studies that particle size of ZnS synthesized at pH 12 is larger as compared to that of ZnS synthesized at pH 8 and pH 10. But ZnS synthesized at pH 12 shows higher photocatalytic degradation of organic pollutant. Hence it can be concluded from the above discussion that it is not the particle size of the

photocatalyst which matters the most but pH of the solution (in which the NPs are being prepared) governs the photocatalytic activity of NPs.

It may be kept in mind that defect states also play a very important role in determining the photocatalytic activity of a photocatalyst. Inclusion of more defect states (by doping or surface treatment) in the semiconductor host lattice can enhance or reduce its overall photocatalytic activity depending upon the nature of dopant and surface treatment. So the main aim of the next chapter is to study the effect of doping metal ions on the structural, optical and photocatalytic properties of ZnS.

References

[1] S. Yang, Y. Liu, Y. Guo, J. Zhao, H. Xu and Z. Wang, Preparation of rutile titania nanocrystals by liquid method at room temperature. Materials Chemistry and Physics, **77** (2002) 501-506.

[2] S.T. Tan, B.J. Chen, X.W. Sun, W.J. Fan, H.S. Kwok, X.H. Zhang and S.J. Chua, Blue shift of optical band gap in ZnO thin films grown by metal-organic chemical-vapor deposition. Journal of Applied Physics, **98** (2005) 013505(1)-013505(5).

[3] A. Aboulaich, L. Balan, J. Ghanbaja, G. Medjahdi, C. Merlin and R. Schneider, Aqueous route to biocompatible ZnSe:Mn/ZnO core/shell quantum dots using 1-Thioglycerol as stabilizer. Chemistry of Materials, **23** (2011) 3706-3713.

[4] J. Zhu, D. Li, H. Chen, X. Yang, L. Lu and X. Wang, Highly dispersed CuO nanoparticles prepared by a novel quick-precipitation method. Materials Letters, **58** (2004) 3324-3327.

[5] C.B. Mendive, D. Hansmann, T. Bredow and D. Bahnemann, New insights into the mechanism of TiO_2 Photocatalysis: Thermal processes beyond the electron hole creation. Journal of Physical Chemistry C, **115** (2011) 19676-19685.

[6] R. Gui, X. An, H. Su, W. Shen, L. Zhu, X. Ma, Z. Chen and X. Wang, Rhodamine 6G conjugated-quantum dots used for highly sensitive and selective ratiometric fluorescence sensor of glutathione. Talanta, **94** (2012) 295-300.

[7] S.R. Husain, F. Ahmad and M. Ahmad, Synthesis of sulfur-containing derivatives from olefinic fatty esters. Journal of the American Oil Chemists' Society, **60** (1983) 1340-1344.

[8] C.C. Hu, J.N. Nian and H. Teng, Electrodeposited p-type Cu_2O as photocatalyst for H_2 evolution from water reduction in the presence of WO_3. Solar Energy Materials and Solar Cells, **92** (2008) 1071-1076.

[9] D. Beydoun, R. Amal, G. Low and S. McEvoy, Role of nanoparticles in Photocatalysis, Journal of Nanoparticle Research, **1** (1999) 439-458.

[10] W. Chen, Z. Wang, Z. Lin and L. Lin, Absorption and luminescence of the surface states in ZnS nanoparticles. Journal of Applied Physics, **82** (1997) 3111-3115.

[11] S. Liu, H. Zhang and M.T. Swihart, Spray pyrolysis synthesis of ZnS nanoparticles from a single-source precursor. Nanotechnology, **20** (2009) 235603-235610.

[12] C. Lizama, J. Freer, J. Baeza and H. Mansila, Optimized photodegradation of Reactive Blue 19 on TiO_2 and ZnO suspensions. Catalysis Today, **76** (2002) 235-246.

[13] C.A.K. Gouvea, F. Wypych, S.G. Moraes, N. Duran, N. Nagata and P.P. Zamor, Semiconductor-assisted photocatalytic degradation of reactive dyes in aqueous solution. Chemosphere, **40** (2000) 433-440.

[14] Y. Wang, Z. Tang, M.A. Correa-Duarte, I. Pastoriza-Santos, M. Giersig, N.A. Kotov and L.M. Liz-Marzán, Mechanism of strong luminescence photoactivation of citrate-stabilized water-soluble nanoparticles with CdSe cores. Journal of Physical Chemistry B, **108** (2004) 15461-15469.

[15] Y. Wang, Z. Tang, M.A. Correa-Duarte, L.M. Liz-Marzán and N.A. Kotov, Multicolor luminescence patterning by photoactivation of semiconductor nanoparticle films. Journal of American Chemical Society, **125** (2003) 2830-2831.

[16] A.A. Bol and A. Meijerink, Luminescence quantum efficiency of nanocrystalline ZnS:Mn^{2+}. 2. Enhancement by UV irradiation. Journal of Physical Chemistry B, **105** (2001) 10203-10209.

[17] C. Carrillo-Carrión, S. Cárdenas, B.M. Simonet and M. Valcárcel, Quantum dots luminescence enhancement due to illumination with UV/Vis light. Chemical Communications, (2009) 5214-5226.

[18] S.K. Mehta, S. Kumar, S. Chaudhary, K.K. Bhasin and M. Gradzielski, Evolution of ZnS Nanoparticles via Facile CTAB Aqueous Micellar Solution Route: A Study on Controlling Parameters. Nanoscale Research Letters, **4** (2009) 17-28.

[19] P.H. Borse, W. Vogel and S.K. Kulkarni, Effect of pH on photoluminescence enhancement in Pb-doped ZnS nanoparticles. Journal of Colloid and Interface Science, **293** (2006) 437-442.

[20] M. Sastry, K.S. Mayya and K. Bandyopadhyay, pH dependent changes in the optical properties of carboxylic acid derivatized silver colloidal particles, Colloids and Surfaces A, **127** (1997) 221-228.

[21] R. Vacassy, S.M. Scholz, J. Dutta, C.J.G. Plummer, R. Houriet and H. Hofmann, Synthesis of Controlled Spherical Zinc Sulfide Particles by Precipitation from Homogeneous Solutions. Journal of American Ceramic Society, **81** (1998) 2699-2705.

[22] J. Jiang, G. Oberdörster and P. Biswas, Characterization of size, surface charge, and agglomeration state of nanoparticle dispersions for toxicological studies. Journal of Nanoparticle Research, **11** (2009) 77-89.

[23] M. Sharma, S. Kumar and O.P. Pandey, Study of energy transfer from capping agents to intrinsic vacancies/defects in passivated ZnS nanoparticles, Journal of Nanoparticle Research, **12** (2010) 2655-2666.

[24] A.K. Kole, C.S. Tiwary and P. Kumbhakar, Ethylenediamine assisted synthesis of wurtzite zinc sulphide nanosheets and porous zinc oxide nanostructures: near white light photoluminescence emission and photocatalytic activity under visible light irradiation, Crystal Engineering Communications, **15** (2013) 5515-5525.

[25] X. Li, G. Liu and J. Zhao, Two competitive primary processes in the photodegradation of cationic triarylmethane dyes under visible irradiation in TiO_2 dispersions, New Journal of Chemistry, **23** (1999), 1193-1196.

[26] T. Aarthi, P. Narahari and G. Madras, Photocatalytic degradation of Azure and Suda dyes using nano TiO_2, Journal of Hazardous Materials, **149** (2007) 725–734.

[27] J. Liqiang, Q. Yichun, W. Baiqi, L. Shudan, J. Baojiang, Y. Libina, F. Wei, F. Honggang and S. Jiazhong, Review of photoluminescence performance of nano-sized semiconductor materials and its relationships with photocatalytic activity. Solar Energy Materials and Solar Cells, **90** (2006) 1773-1787.

CHAPTER 5

RESULTS AND DISCUSSION

Doped ZnS nanoparticles

Overview

The present chapter describes the studies of doped ZnS nanoparticles (NPs) prepared via chemical precipitation route. Structural studies have been done using X-Ray diffraction (XRD) technique and transmission electron microscopy (TEM). Fourier transfer infrared (FTIR) spectroscopy has been employed to determine the nature of chemical bonds present on the surface of ZnS NPs. UV-Vis spectroscopy has been utilized to investigate the effect of doping on absorption characteristics of doped ZnS NPs. Emission characteristics of the prepared samples have been investigated by photoluminescence (PL) spectroscopy. Effect of doping on photocatalytic properties of as prepared ZnS NPs has also been studied in the last section of each series.

5.1 Introduction

Owing to its large band gap, ZnS can easily host different transition metal ions acting as luminescent centres [1]. The band gap of ZnS can be modified by intercalating dopant energy levels in the host. Further, doping in host ZnS with transition metal ions such as Cu ions offers a way to trap charge carriers and extends the lifetime of one or both of the charge carriers. Consequently, dopants are expected to enhance the efficiency of the photocatalyst [2]. Till now, various attempts have been made to make ZnS as an efficient photocatalyst in near visible or visible region [2-6]. In his work, Mohamed [2] has investigated the photocatalytic activity of thin films of ZnS:Cu^{2+} nanoparticles (NPs) towards methylene blue dye. He has investigated the effect of annealing temperature on grain size and photocatalytic activity of ZnS:Cu thin films. Enhanced photocatalytic activity of Cu doped ZnS films has been attributed to the reason that Cu^{2+} ion can be reduced to a Cu^{+} ion by a hole produced with semiconductor which is strongly oxidative. Porambo et al. [4] have reported that doping of ZnS nanocrystals with Mn^{2+} leads to an initial increase in the apparent rate constants in case of degradation of 2-chlorophenol and then decreases at higher dopant concentrations. Pourtedal et al. [6] have studied the effect of Mn, Ni, Cu:ZnS NPs in photocatalytic degradation of methylene blue and safranin. In their work, emphasis has been made on the photocatalytic application of materials. The photocatalytic activity has been obtained in the order ZnS < ZnS macrocrystalline < ZnS nanocrystalline < ZnMnS < ZnNiS < ZnCuS.

The synthesis conditions, characteristics and concentrations of dopants are responsible for particular properties and efficiencies of semiconductor NPs. So, it becomes necessary to understand the role of dopant on structural, optical and photocatalytic properties of doped SC NPs from the view point of physics as well as its applications in related areas. Metal ions are expected to introduce trap states in the energy gap of a semiconductor. Hence, doping is done to enhance photocatalytic activity of a semiconductor material. It is not always the case that metal ions enhance photocatalytic activity of photocatalyst. It depends upon the type of transition involved in the emission pathway. In this chapter, the main aim is to synthesize metal doped ZnS NPs and to study their optical and photocatalytic properties. ZnS NPs doped with Cu, Mn and Ni ions have been successfully synthesized by simple chemical precipitation method. To have efficient doping, synthesis temperature has been kept at 80 °C the details of this are given in chapter 3. Apart from doping, ZnS has been modified with Ag_2S using the same synthesis technique and the obtained results are discussed in the last section of this chapter.

5.2 Cu doped ZnS

5.2.1 XRD and EDX studies

Figure 5.1 shows the XRD patterns of $Zn_{1-x}Cu_xS$; x = 0, 0.01, 0.02, 0.03 and 0.04. As can be seen in the figure, all samples exhibit cubic zinc blende phase with no impurity phase indicating that Cu is successfully doped in the host lattice. However, the presence of Cu in prepared samples has been confirmed through Energy Dispersive X-ray (EDX) spectroscopy analysis. EDX patterns for $Zn_{1-x}Cu_xS$; x = 0, 0.01, 0.02, 0.03 and 0.04 are shown in Figure 5.2. Diffraction peaks from (111), (220) and (311) planes match well with those of the β-ZnS (cubic) reported in the ICDD powder diffraction file no.80-0020. In all the samples, broadening of diffraction peaks indicates formation of nanosize ZnS [7]. The XRD peaks of doped ZnS NPs have become weaker and broader as compared to that of undoped ZnS. This suggests that the crystallinity of $Zn_{1-x}Cu_xS$; x = 0.01, 0.02, 0.03 and 0.04 NPs has been decreased with the increase in Cu content in the source materials.

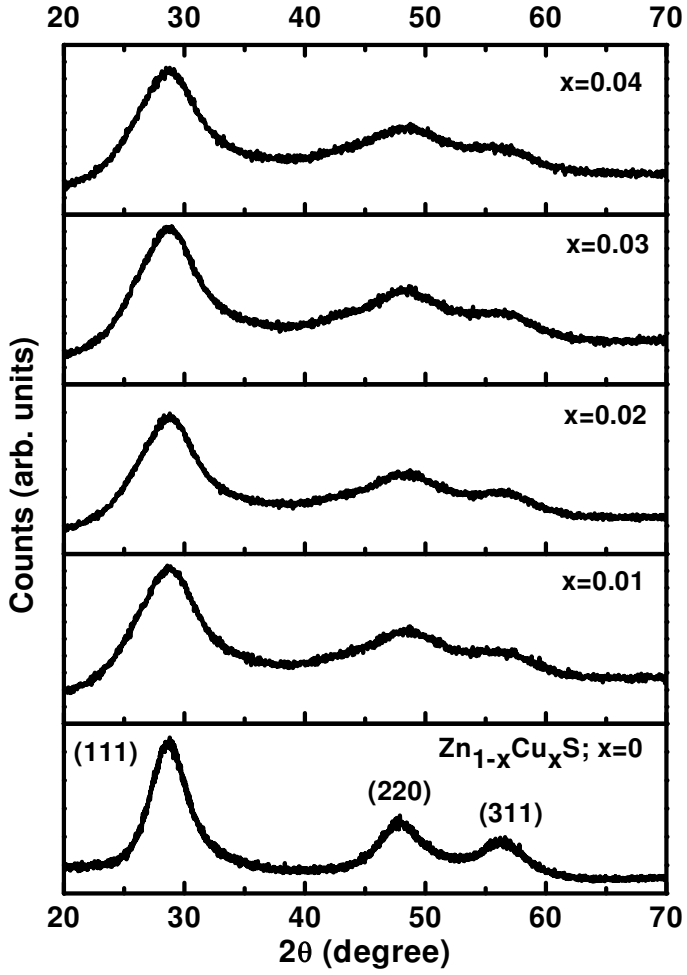

Figure 5.1: XRD patterns of $Zn_{1-x}Cu_xS$; x = 0, 0.01, 0.02, 0.03 and 0.04 in the range 20°-70°.

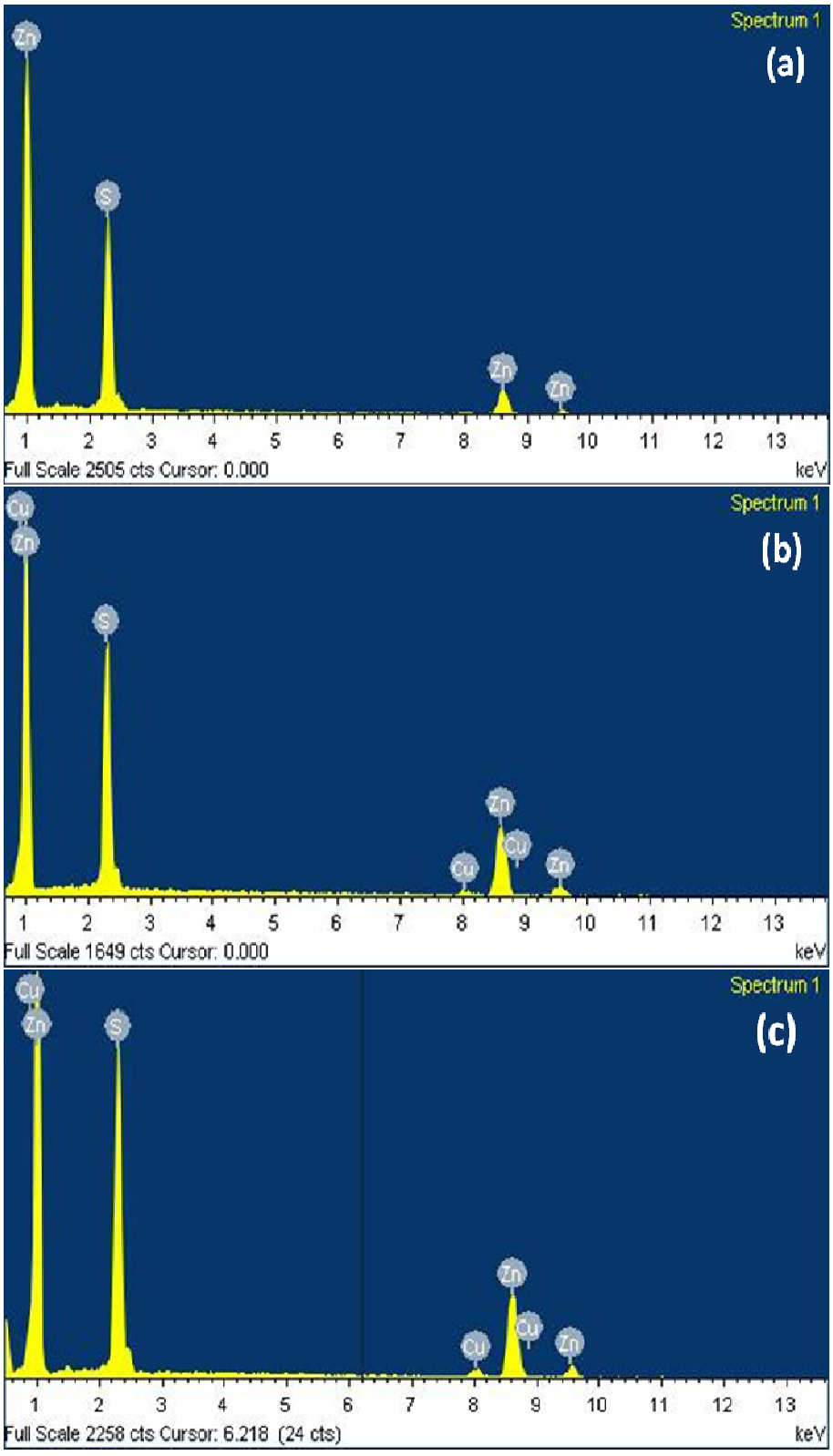
Spectrum 1
(a)
Zn
S
Zn
Zn
1 2 3 4 5 6 7 8 9 10 11 12 13
Full Scale 2505 cts Cursor: 0.000
keV
Spectrum 1
(b)
Cu
Zn
S
Zn
Cu
Cu
Zn
1 2 3 4 5 6 7 8 9 10 11 12 13
Full Scale 1649 cts Cursor: 0.000
keV
Spectrum 1
(c)
Cu
Zn
S
Zn
Cu
Cu
Zn
1 2 3 4 5 6 7 8 9 10 11 12 13
Full Scale 2258 cts Cursor: 6.218 (24 cts)
keV

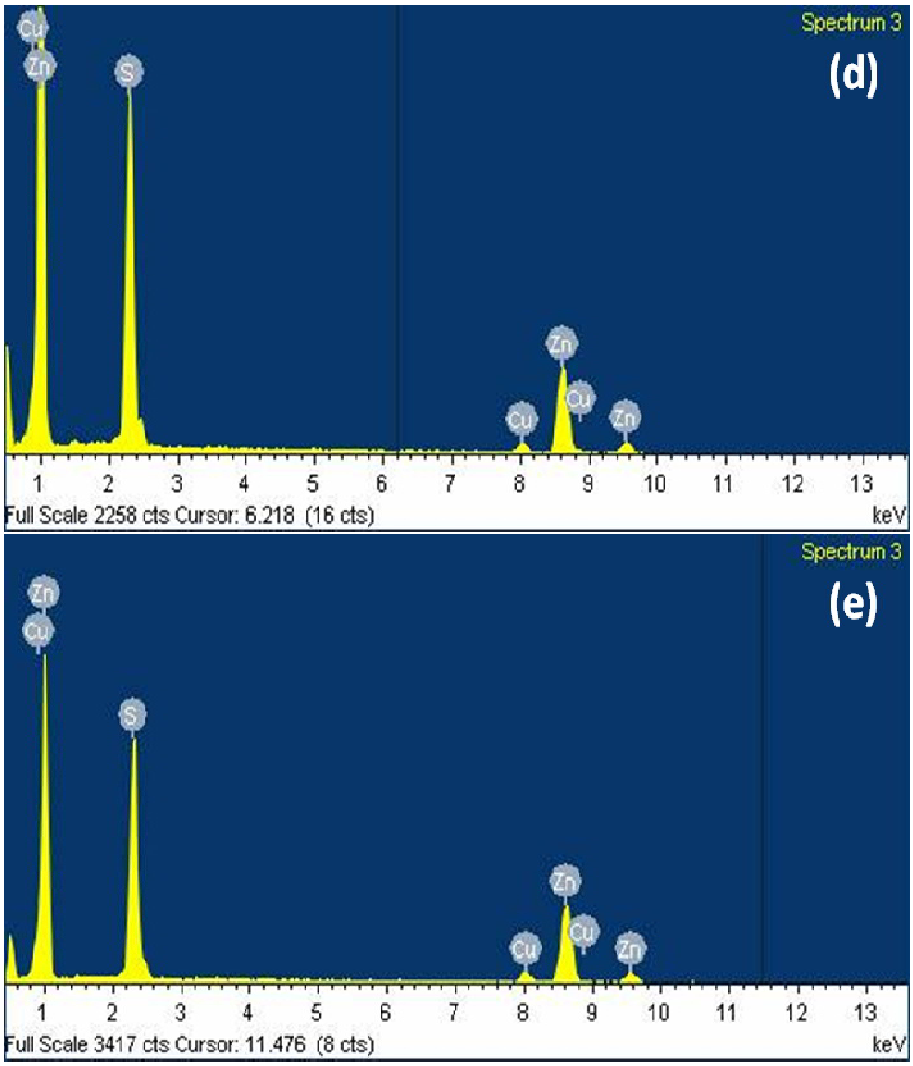

Figure 5.2: EDX patterns of $Zn_{1-x}Cu_xS$; (a) x = 0, (b) x=0.01, (c) x=0.02, (d) x=0.03 and (e) x=0.04.

To investigate the effect of Cu doping on ZnS host lattice, the most intense diffraction peak corresponding to (111) plane has been selected (Figure 5.3). A careful comparison of diffraction peak in the range 2θ = 22°-38° for all samples has been done. Larger line broadening in case of Cu doped samples indicates their smaller particle size as compared to the undoped ZnS sample. No appreciable peak shift has been observed in any sample which may be attributed to the very small difference in ionic radius of Cu^{2+} (0.57) and Zn^{2+} (0.6). Crystallite size of NPs ($Zn_{1-x}Cu_xS$; x = 0, 0.01, 0.02, 0.03 and 0.04) has been calculated by following Scherrer's equation

$$t = \frac{k\lambda}{\beta\cos\theta} \qquad (5.1)$$

where k = 0.9, t is the crystallite size (Å), λ(Å), the wavelength of Cu Kα radiation and β is the corrected half width of the diffraction peak [8]. Crystallite size has come out in the range

of 1.89-1.99 nm. Decreased crystallinity of Cu doped samples as compared to that of undoped ZnS indicates the increase in disorder due to incorporation of impurity ions.

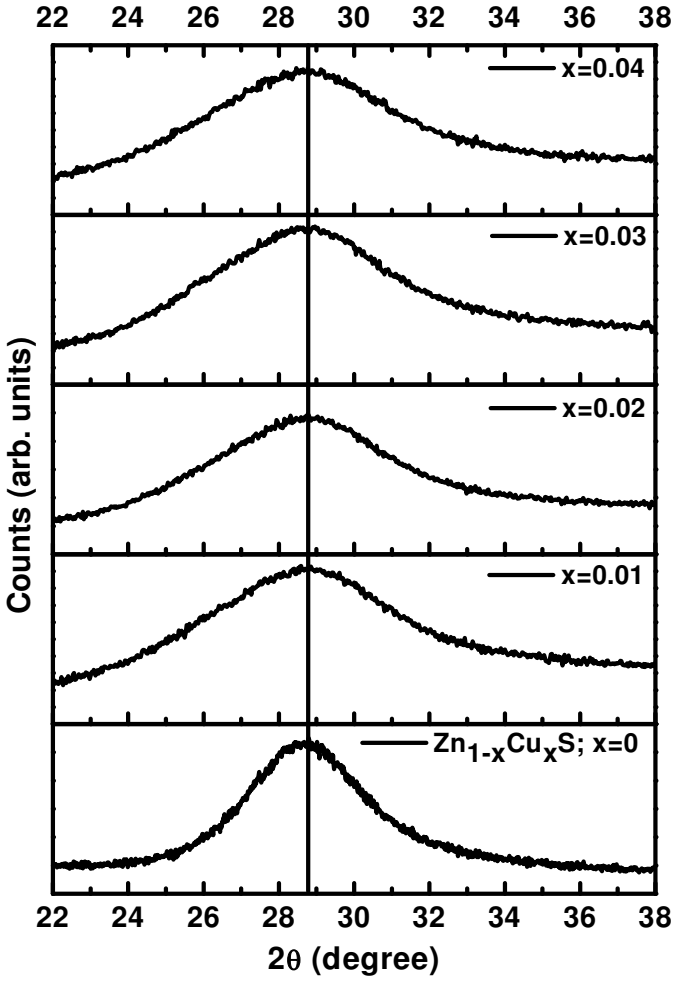

Figure 5.3: XRD patterns of $Zn_{1-x}Cu_xS$; x = 0, 0.01, 0.02, 0.03 and 0.04 in the range 22°-38°.

5.2.2 TEM analysis

Figure 5.4(a) shows TEM micrograph of one of the doped sample $Zn_{1-x}Cu_xS$; x=0.02. As observed in Figure 5.4(a), the particles of doped ZnS are irregularly spherical with the diameter ranging from 60-65 nm. The NPs have grown due to overnight ageing and also the sample was prepared at 80 °C to make the doping efficient. Amorphous layer corresponding to thioglycerol is clearly seen around the NPs surface which confirms that effective capping is obtained on NPs surface. From the high-resolution TEM (HRTEM) image in Figure 5.4(b), the lattice fringes can be clearly observed, suggesting the well-defined crystal structure. The

fringe with lattice spacing of ca. 0.31 nm corresponds to the (111) plane of the cubic ZnS which is in good agreement with the XRD pattern.

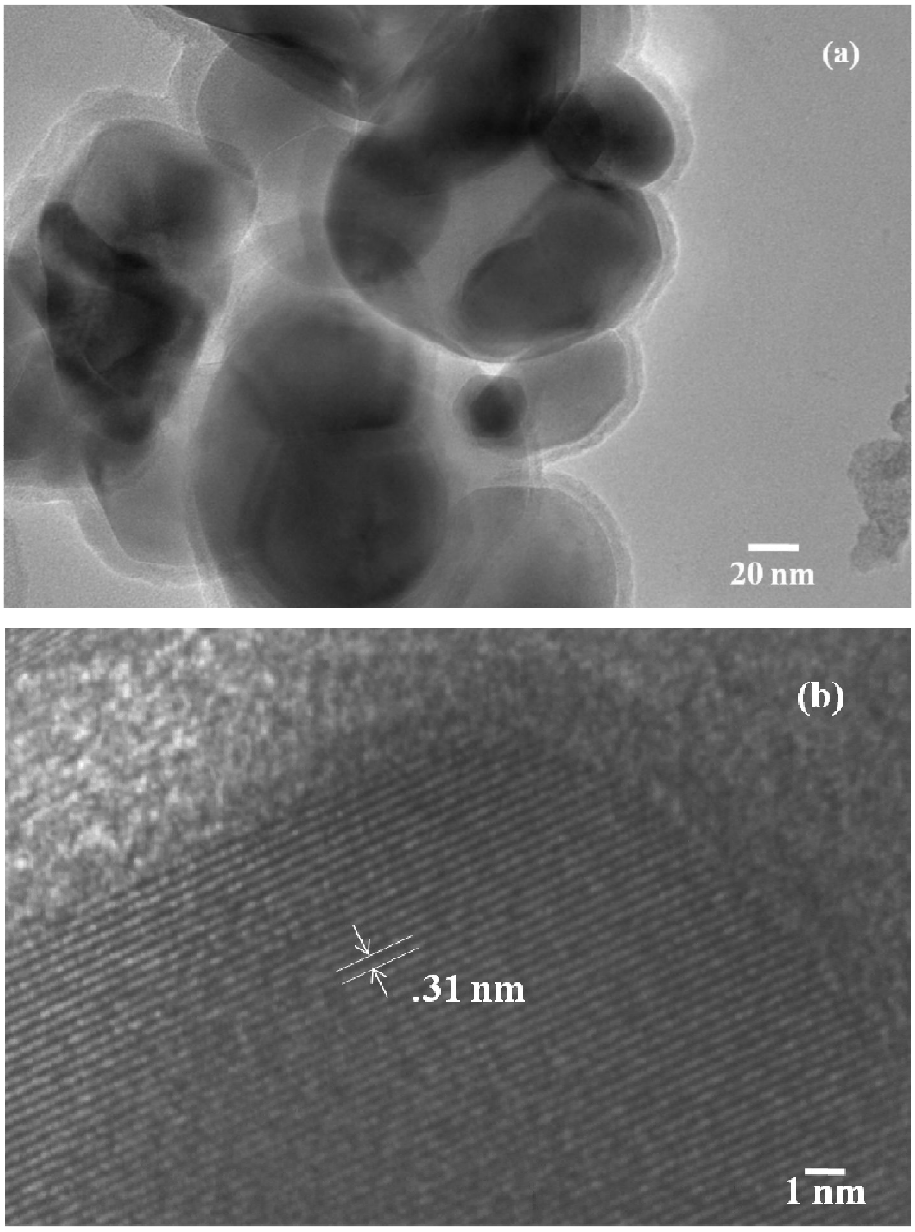

Figure 5.4: (a) TEM image of thioglycerol capped $Zn_{1-x}Cu_xS$; x = 0.02, (b) HRTEM image of the same sample.

5.2.3 FTIR Analysis

To investigate various functional groups present in TG capped and Cu doped ZnS, FTIR studies have been done. Figure 5.5 represents FTIR spectra of $Zn_{1-x}Cu_xS$; x = 0, 0.03. As can be seen in figure, both samples exhibit almost similar IR spectra. Therefore, we can say that doping has no profound effect on IR response of as prepared samples. The peak positions for both samples alongwith peak assignments are given in Table 5.1. Pure TG exhibit S-H

vibration band at 2557 cm^{-1}. This peak was not observed in both samples. It is attributed to the fact that the thiolate functions of the TG ligands are connected to the Zn^{2+} sites on the ZnS nanocrystals surfaces which confirm the capping of thioglycerol on ZnS surface [9].

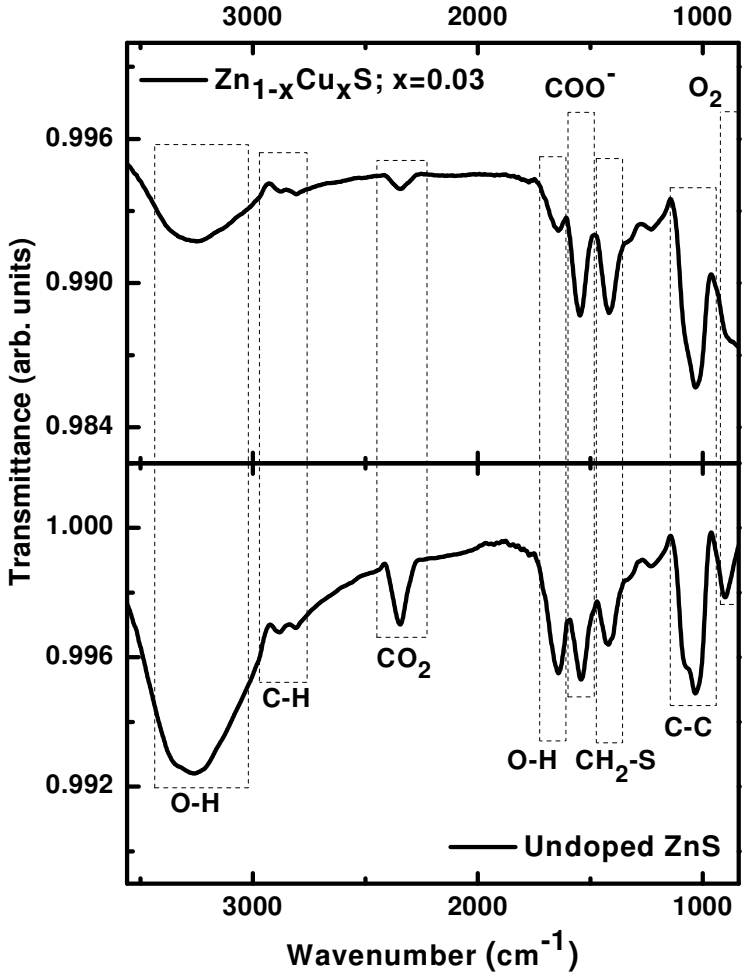

Figure 5.5: FTIR spectra of $Zn_{1-x}Cu_xS$; x = 0, 0.03.

Table 5.1: Peak assignment of various bonds in thioglycerol capped $Zn_{1-x}Cu_xS$; x = 0, 0.03.

Peak Position (cm^{-1}) $Zn_{1-x}Cu_xS$		**Peak assignment**
x=0	**x=0.03**	
3265	3246	O-H stretching [9]
2885	2878	C-H symmetrical stretching [9]
2810	2804	C-H asymmetrical stretching [9]
2346	2344	Interference from CO_2 [10]
1642	1645	O-H bending [9]
1540	1546	COO^- [11]
1416	1413	$–CH_2–S$ [12]
1033	1030	C–C stretch [12]
902	860	O_2 stretching and bending [13]

5.2.4 UV-Vis studies

To investigate the effect of Cu doping on optical response of ZnS, UV-Vis studies have been performed for all the samples in the range of 250-500 nm.

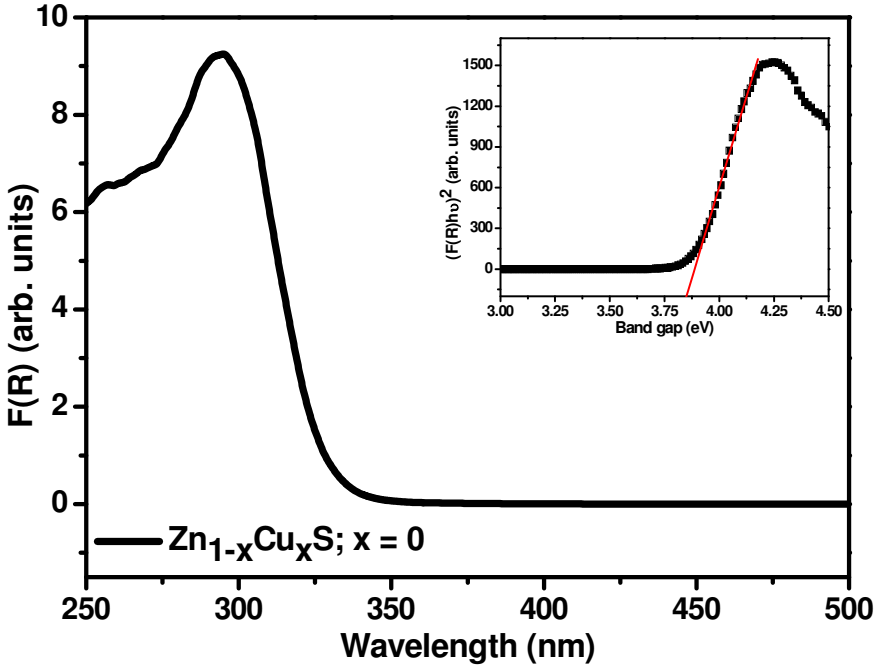

Figure 5.6: Absorption spectra of undoped ZnS. Inset shows corresponding Tauc plot.

The relation between reflectance R and absorption coefficient α as given by Kubelka–Munk method [14] is

$$F(R) = \frac{(1-R)^2}{2R} = \frac{\alpha}{S} \qquad (5.2)$$

where F(R) is the Kubelka–Munk function, S is the scattering coefficient. From the above equation, the Kubelka–Munk function F(R) can be assumed to be proportional to α [14]. Absorption spectra for all samples have been plotted by employing the above equation. As can be seen clearly in the Figure 5.6, absorption edge for undoped ZnS is blue shifted as compared to its bulk counterpart which is at 340 nm. Band gap for undoped ZnS has come out to be 3.85 eV which is quite higher as compared to its bulk counterpart (3.54 eV). This variation in band gap indicates nano size formation showing strong quantum confinement effect. The band gap of the semiconductor becomes larger with decreasing particle size, and is indicated by an absorption shift to shorter wavelengths. This is due to the reason that the levels of the valence band are moderately shifted to lower energies, while those of the conduction band are strongly shifted to higher energies. This shifting of band edges yields larger redox potentials which result in enhancement of photocatalytic activity of NPs [15].

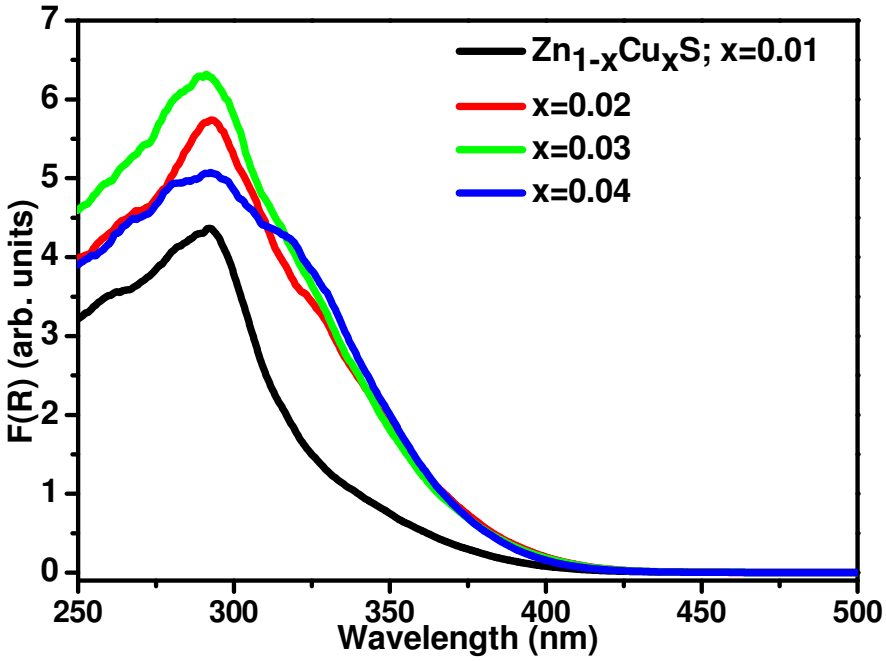

Figure 5.7: Absorption spectra of $Zn_{1-x}Cu_xS$; x = 0.01, 0.02, 0.03 and 0.04 plotted by Kubelka Munk method.

Figure 5.7 shows optical response of all the samples synthesized with different dopant concentrations. It is clearly seen in the figure that absorbance of Cu doped ZnS has significantly increased in near visible region as compared to that of undoped ZnS. Further, with increase in Cu content, absorption edge has red shifted indicating narrowing of band gap. Decrease in absorbance at x=0.04 might be due to the formation of CuS which hindered the penetration of light. The relation between the incident photon energy (hυ) and the absorption coefficient (α) or F(R) is given by [14]

$$[F(R)h\upsilon]^{1/n} = A(h\upsilon - E_g) \qquad (5.3)$$

where A is a constant and E_g is the band gap of the material and the exponent n depends on the type of the transition i.e. 2, 3, 1/2, 1/3 values corresponding to indirect allowed, indirect forbidden, direct allowed and direct forbidden transitions. As shown in the Figure 5.8, square of the absorbed energy (F(R)hυ) have been plotted against photon energy (hυ) to determine the energy for direct gap transition. Band gap energies for all samples have been determined by extrapolating the straight portion of the graph on hυ axis at F(R)=0. Variation of band gap with doping content is shown in Figure 5.9. The band-gap shrinkage with increasing Cu content is the result of the sp-d exchange interaction between host and dopant [16]. As discussed by Mohamed [2], Cu introduces some additional energy levels in ZnS band gap close to the valence band edge, with a consequent reduction in the energy associated with

direct transition. This further confirms the successful incorporation of Cu ions in the host lattice. Band gap values along with corresponding absorption wavelengths are given in Table 5.2.

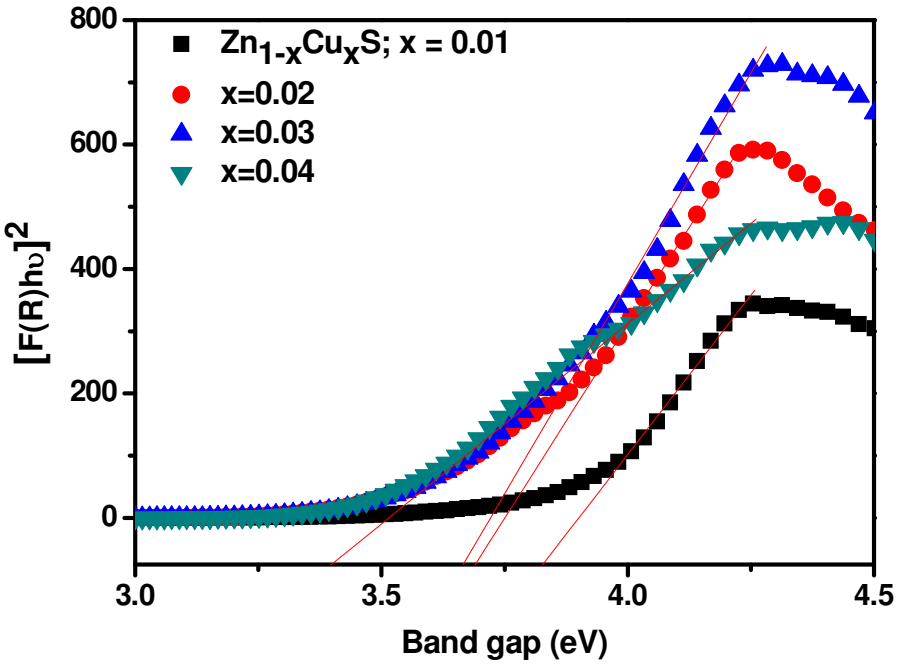

Figure 5.8: Tauc plots for $Zn_{1-x}Cu_xS$; x = 0.01, 0.02, 0.03 and 0.04 to determine band gap.

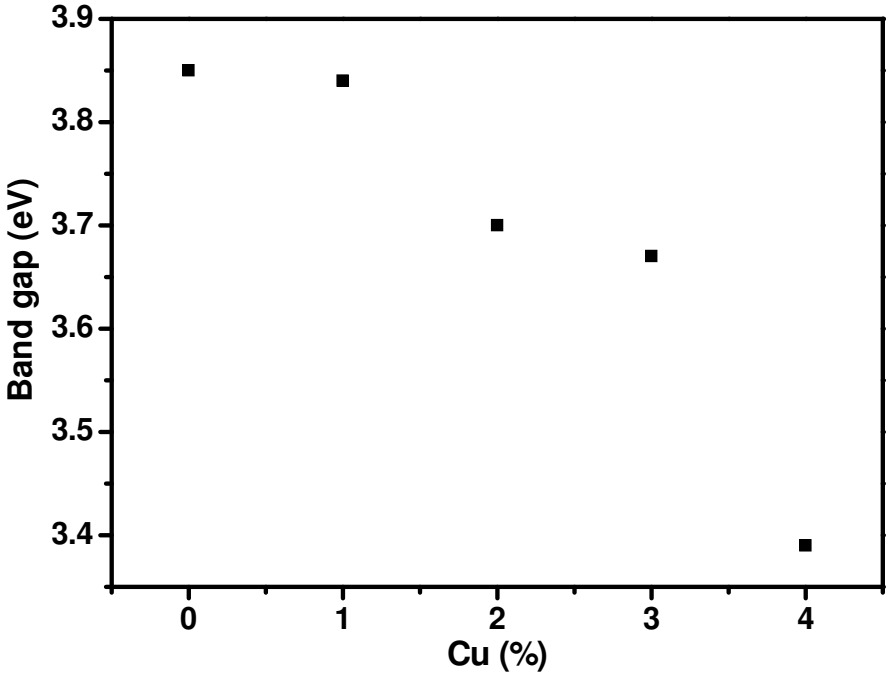

Figure 5.9: Variation in band gap of ZnS with Cu doping.

Table 5.2: Calculated band gap values and corresponding absorption wavelengths of $Zn_{1-x}Cu_xS$; x = 0, 0.01, 0.02, 0.03 and 0.04.

$Zn_{1-x}Cu_xS$	Band gap (eV)	Absorption wavelength (nm)
x=0	3.85	322.60
x=0.01	3.84	323.53
x=0.02	3.70	335.67
x=0.03	3.67	338.42
x=0.04	3.39	366.37

5.2.5 Photoluminescence studies

Figure 5.10 shows photoluminescence (PL) emission spectra of all synthesised NPs. PL emission spectra have been recorded at room temperature with an excitation wavelength of 320 nm. As can be clearly seen in the figure, undoped ZnS exhibits blue emission peak at ~ 436 nm which may be due to the presence of sulphur vacancies acting as donors, releasing electrons into the valence band during the transition [17]. With further addition of Cu (from x = 0 to 0.02) in host ZnS, emission peak has substantially red shifted from blue (436 nm) to green region (516 nm) which corresponds to lower energies. It is reported in literature that blue emission corresponds to the Cu ions lying in the interstices of ZnS lattice and green emission is observed when Cu ions substitute for Zn^{2+} ions in the lattice [18].

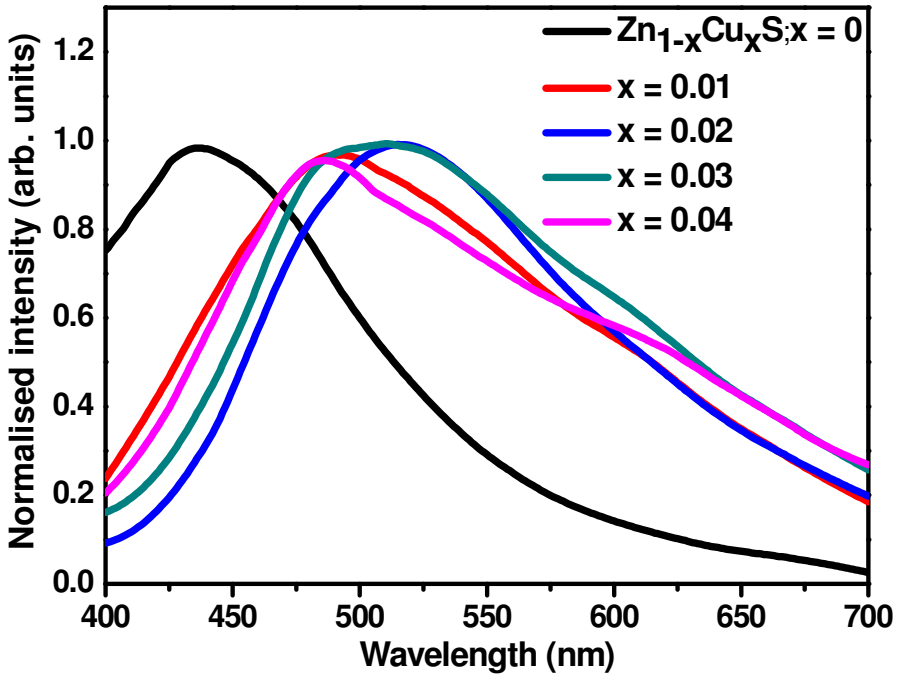

Figure 5.10: Photoluminescence emission spectra of $Zn_{1-x}Cu_xS$; x = 0, 0.01, 0.02, 0.03 and 0.04 at λ_{exc}=320 nm.

In the present case, blue emission has only appeared for undoped ZnS whereas in all the doped samples, green emission has appeared. Hence it is confirmed that Cu ion has entered the lattice by substitution for Zn^{2+} ions. It has been reported earlier that copper substitutes for Zn^{2+} as Cu^{2+} ($3d^9$) in ZnS give rise to green emission [19]. In the tetrahedral crystal field of the four S^{2-} ligands, the ground state of Cu^{2+} ($3d^9$) splits into higher lying t_2 levels and lower lying e levels [19]. When an electron is excited to the conduction band, and subsequently trapped by shallow (delocalised) donor levels (probably sulphur vacancies V_S), a green luminescence can occur, by recombination at the Cu impurity level [19-20]. As discussed by Wang et al. [21], the energy levels of Cu^{2+} ions vary depending upon dopant concentration which results in different emission wavelengths. The maximum red shift in our case is observed in $Zn_{1-x}Cu_xS$; x = 0.02. Further at higher doping content in $Zn_{1-x}Cu_xS$; x = 0.03, emission peak (~507nm) becomes broader. In particular, line width is determined by the product of ion density and the screening length in the luminescent region [22]. Therefore a large line width is expected from a region having a high charge density and large screening length. Hence, in the present case, $Zn_{1-x}Cu_xS$; x = 0.03 exhibits large number of free charge carriers which are expected to be useful in photocatalytic application. In $Zn_{1-x}Cu_xS$; x = 0.04, the emission peak shifts towards higher energy (~ 485 nm) indicating that Cu related green emission has been quenched at this Cu content. The shifting of emission peak towards higher energies in case of $Zn_{1-x}Cu_xS$; x = 0.04 may be caused by the formation of CuS as solubility product (k_{sp}) of CuS is very less (8×10^{-37}) as compared to that of ZnS (3×10^{-23}). So, there is a chance that CuS has formed although in less quantity because the XRD measurement did not detect any impurity phase (CuS) due to its measurement limit. Further, CuS itself do not show any luminescence under UV irradiation as these particles act as nonradiative recombination centres [20]. Therefore, in case of Cu (x=0.04) doped ZnS, emission peak has slightly blue shifted.

5.2.6 Photocatalytic studies

Photocatalytic degradation of crystal violet has been carried out to investigate the effect of Cu doping on photocatalytic activity of ZnS NPs. Figure 5.11(a-b) shows the spectral changes in absorbance of dye occurring during photocatalysis in time interval of 60 min. The characteristic absorption peak of this dye at 590 nm has been selected to monitor the photocatalytic degradation of the dye. By Beer Lambert law, the decrease in concentration of dye is recorded at different intervals of time to measure degradation rate. Figure 5.12 shows

the photo degradation of dye catalysed with $Zn_{1-x}Cu_xS$; x = 0, 0.01, 0.02, 0.03 and 0.04 in terms of change in concentration with respect to the initial concentration.

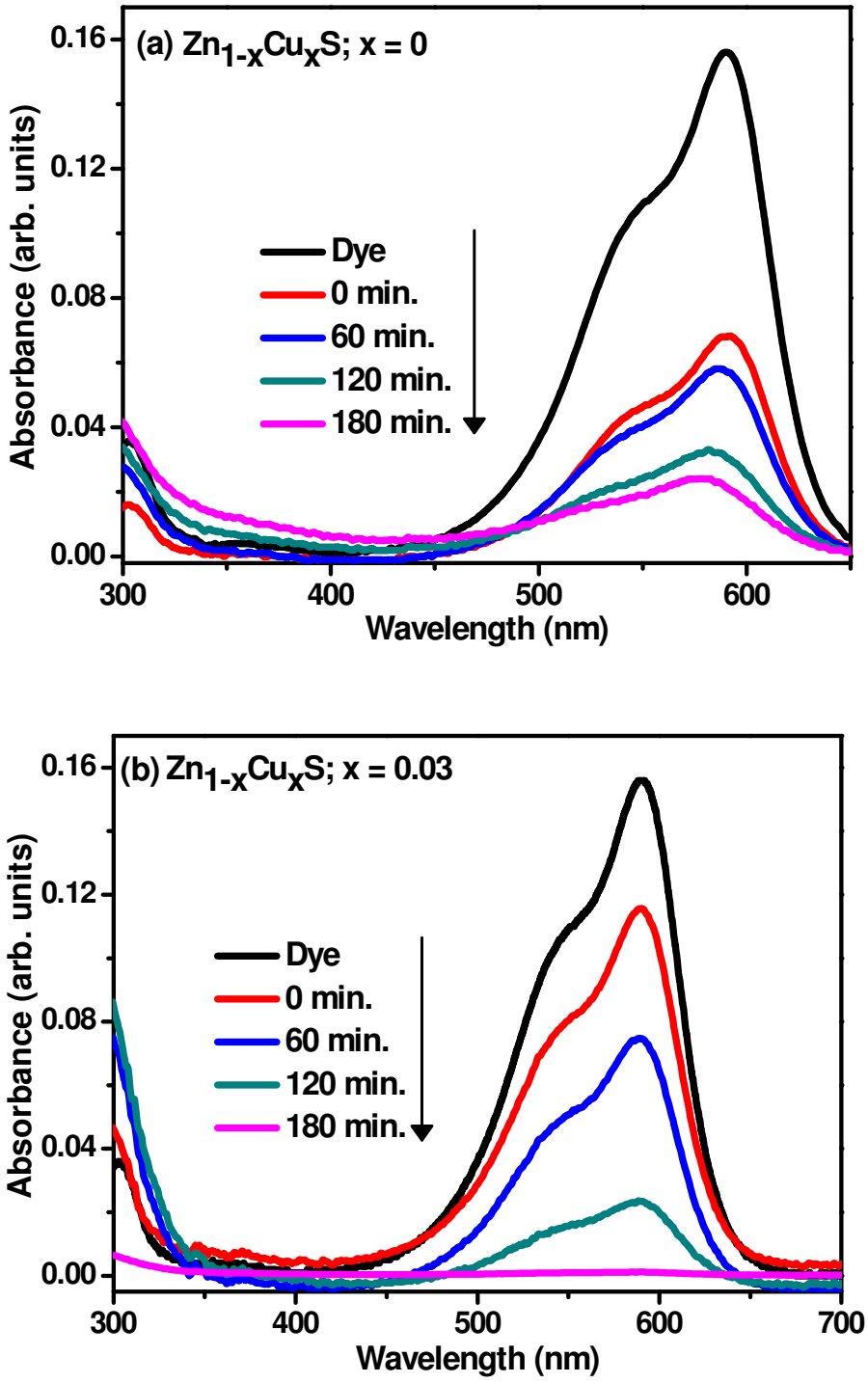

Figure 5.11: Absorbance spectra of crystal violet degraded in the presence of $Zn_{1-x}Cu_xS$ (a) x = 0, (b) x= 0.03.

As can be seen in figure, $Zn_{1-x}Cu_xS$; x = 0.01, 0.02 and 0.03 show better degradation as compared to that of undoped ZnS. Among the doped ZnS samples, $Zn_{1-x}Cu_xS$; x = 0.03

shows the best photocatalytic activity as compared to other doped samples. Photocatalytic activity of ZnS is observed to be minimum in case of higher Cu content $Zn_{1-x}Cu_xS$; x = 0.04.

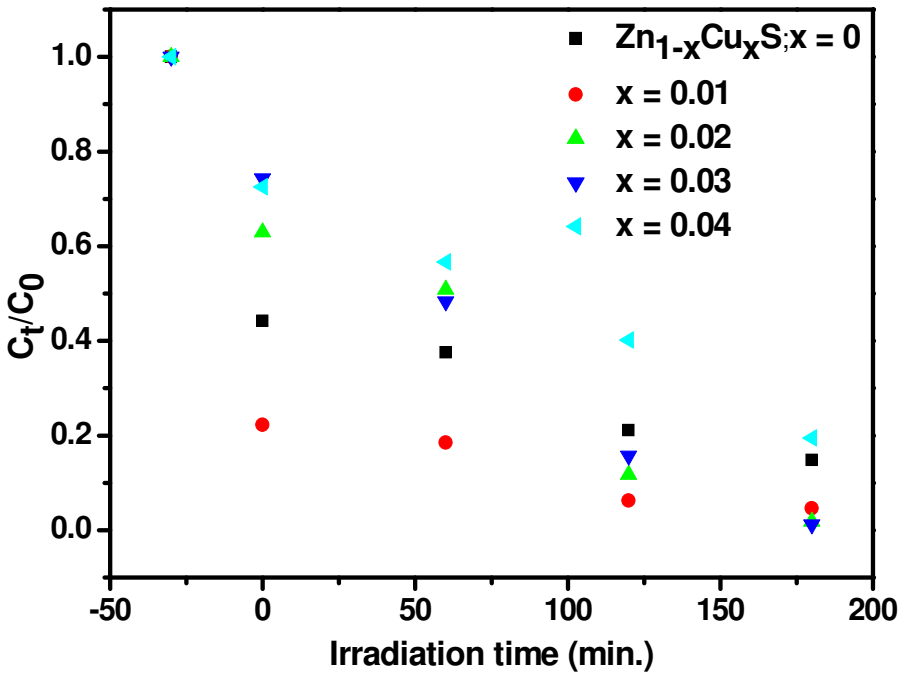

Figure 5.12: Variation of C_t/C_0 with irradiation time for $Zn_{1-x}Cu_xS$; x = 0, 0.01, 0.02, 0.03 and 0.04.

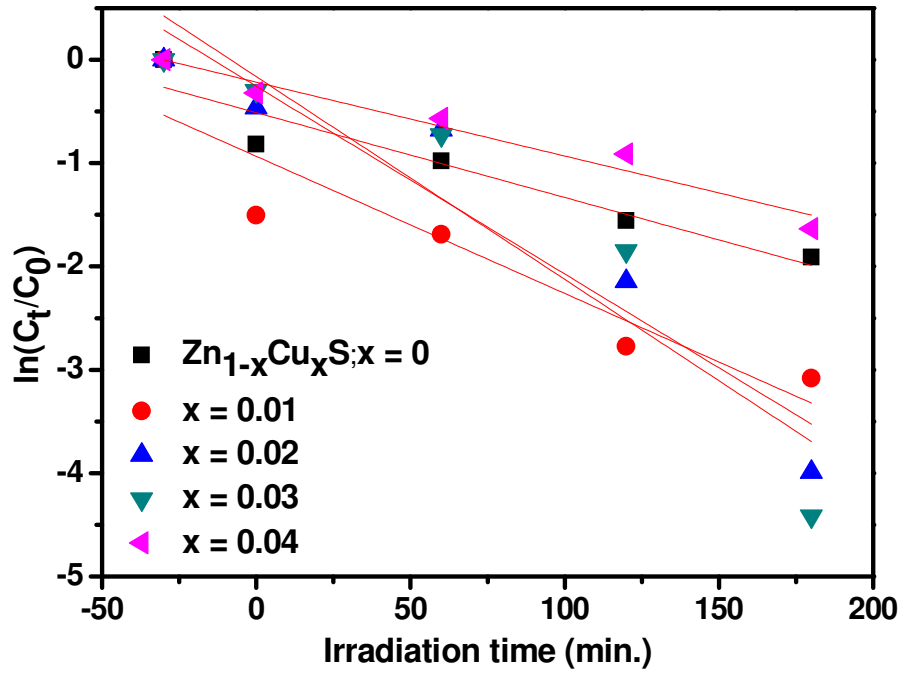

Figure 5.13: Plot between $\ln(C_t/C_0)$ and irradiation time to determine the value of rate constant k.

Since, in this study, concentration of solute is very low (1mg/L), so Langmuir-Hinshelwood kinetics model [23] can be simplified to pseudo first order kinetic model equation.

$$ln\left(\frac{C_t}{C_0}\right) = kT \qquad (5.4)$$

where C_t is the concentration of dye after irradiation in selected time interval t, C_0 is the initial concentration of dye, k is the first order rate constant, and T is irradiation time. Figure 5.13 shows the corresponding plot between $\ln(C_t/C_0)$ and irradiation time to determine the value of rate constant k. According to the first-order rate kinetics, $Zn_{1-x}Cu_xS$; x = 0.03 has recorded the highest degradation rate (k=0.0196 min^{-1}) among the other photocatalysts (Table 5.3).

The degradation efficiency has been calculated as

$$\%D = \left(1 - \frac{C_t}{C_0}\right) \times 100 \qquad (5.5)$$

where C_t is the concentration of dye after irradiation in selected time interval, C_0 is the initial concentration of dye. As shown in Figure 5.14, % degradation in presence of $Zn_{1-x}Cu_xS$; x = 0.03 is maximum (98.82%) among all the photocatalysts. Degradation percentage values for all samples have been summarized in Table 5.3. The order of photo degradation rate is obtained as

$Zn_{1-x}Cu_xS$; x = 0.03 > x = 0.02 > x = 0.01 > x = 0 > x = 0.04

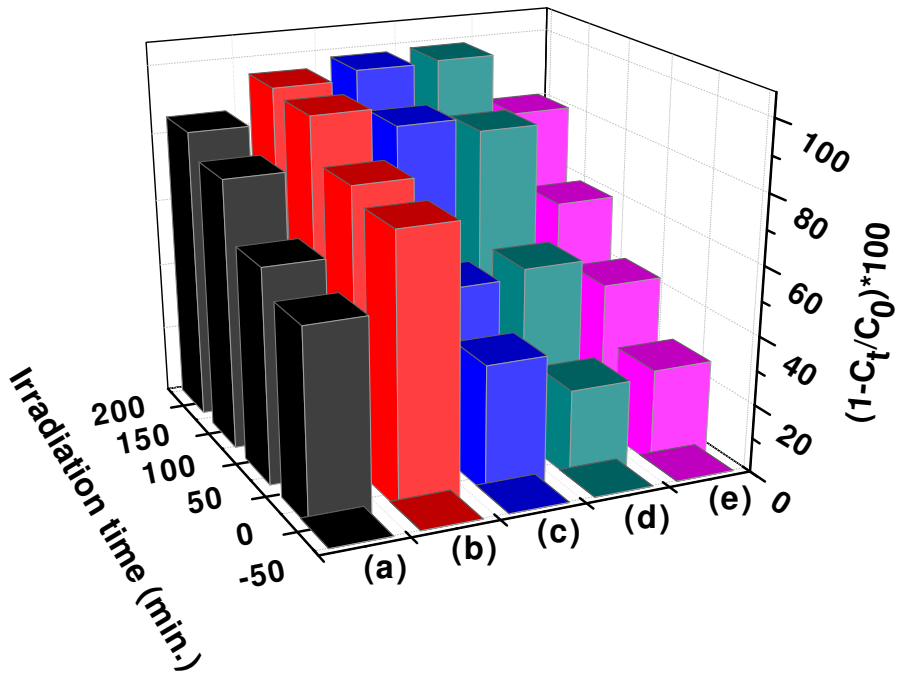

Figure 5.14: Degradation percentage of crystal violet in the presence of $Zn_{1-x}Cu_xS$ (a) x = 0, (b) 0.01, (c) 0.02, (d) 0.03 and (e) 0.04 at different irradiation times.

Various mechanisms of SC assisted photocatalytic degradation of dye have been proposed till now [24]. In first case, if the emission wavelength of the lamp is approximately equal to the λ_{max} of the dye, then dye itself acts as a sensitizer. When light is made to fall on aqueous solution of dye adsorbed on catalyst, then dye molecules get excited and inject electrons to the conduction band of the host semiconductor (photocatalyst) [24]. These electrons then react with molecular oxygen to produce various species having powerful oxidizing ability ($\cdot OH$, $\cdot O_2^-$) [25].

Table 5.3: First order rate constants for the photocatalytic degradation of crystal violet and corresponding percent degradation using $Zn_{1-x}Cu_xS$; x = 0, 0.01, 0.02, 0.03 and 0.04 as photocatalysts.

Photocatalyst	**Adj. R^2**	**k (min^{-1})**	**$(1-C_t/C_0)*100$**
$Zn_{1-x}Cu_xS$; x=0	0.89	0.0082	85.35
x=0.01	0.83	0.0133	95.50
x=0.02	0.89	0.0182	98.23
x=0.03	0.84	0.0196	98.82
x=0.04	0.95	0.0071	80.35

These in turn help in oxidation of dye which is adsorbed on the catalyst. In second case, if the emission wavelength of the lamp is approximately equal to the energy band gap of the SC photocatalyst, then electrons and holes generated in the wide band gap SC are considered to be responsible for the degradation of dye. The electrons combine with atmospheric oxygen to produce superoxide anions ($\cdot O_2^-$) and the holes combine with hydroxide ions to produce hydroxyl radicals ($\cdot OH$). This phenomenon defines the indirect oxidation of dyes. These free radicals ($\cdot OH$) are known to be very strong oxidizing agents [25]. As discussed earlier, ZnS is a semiconductor material and therefore, photodegradation of a dye is initiated by photoexcitation of semiconductor. Electron-hole pair is obtained from photoexcitation of ZnS. Therefore, in our case, dye is degraded by the phenomenon of indirect oxidation. In photocatalytic process, there are various factors which determine the photocatalytic efficiency of catalyst. Degradation efficiency depends largely on the total number of free charge carriers available on the catalyst surface. At nanoscale, the transportation length of electron-hole from crystal interface to the surface is short, which helps to accelerate the migration rate of charge carriers to the surface and hence to participate in photocatalytic process [15]. In the present case, dye is better degraded by $Zn_{1-x}Cu_xS$; x = 0.01, 0.02 and 0.03 as compared to that of undoped sample. This may be ascribed to the role of Cu^{2+} in

degradation. During photocatalysis in aqueous system, following set of reactions could take place

$$ZnS + h\upsilon \rightarrow e^- (C.B.) + h^+ (V.B.) \quad (5.6)$$

$$O_2 + e^- \rightarrow .O_2^- \quad (5.7)$$

$$H_2O + h^+ \rightarrow .OH + H^+ \quad (5.8)$$

$$Cu^{2+} + e^- \rightarrow Cu^{1+} \quad (5.9)$$

$$Cu^{1+} + h^+ \rightarrow Cu^{2+} \quad (5.10)$$

As discussed earlier, the resulting species are very strong oxidising agents. Moreover, in case of doped samples, trapping of electrons and holes by Cu ions extends the lifetime of charge carriers and hence prevents e^--h^+ recombination. Therefore, photocatalytic enhancement indicates that trapping of electrons and holes by Cu ion helped in efficient transfer of these electrons and holes to the reaction sites thus preventing non radiative recombination. Further, upon irradiation, Cu^{2+} ion combine with e^- to give Cu^{1+} which is well known oxidizing agent.

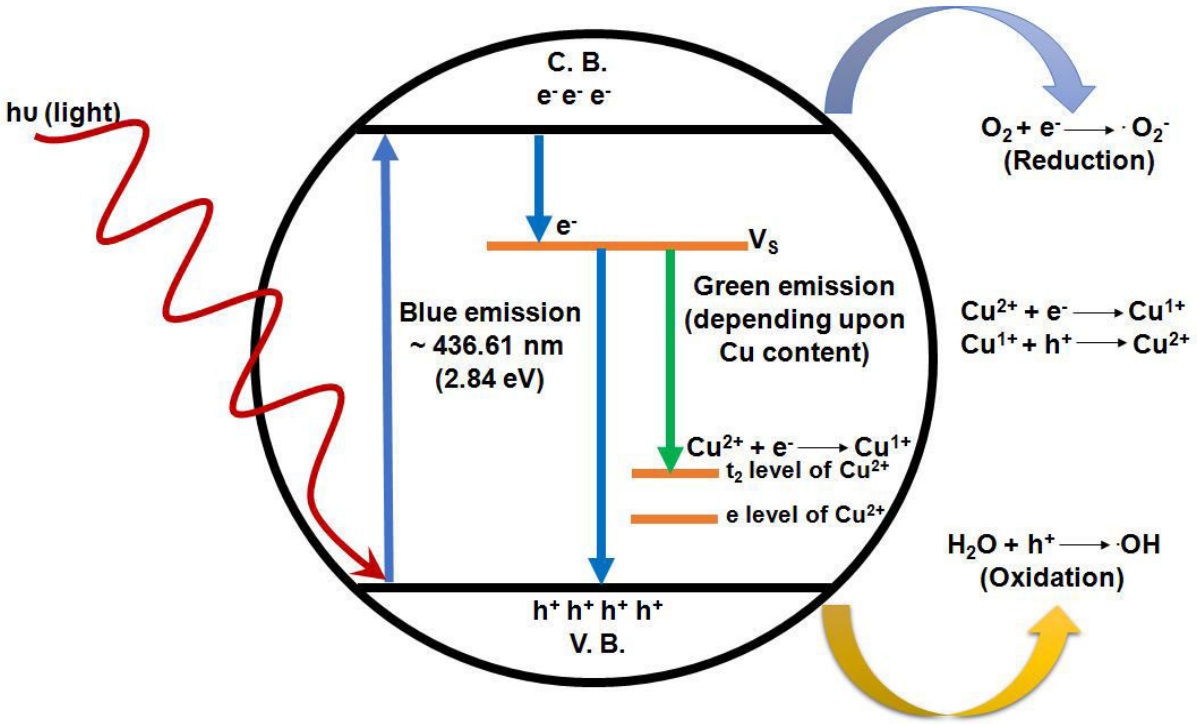

Figure 5.15: Schematic energy level diagram showing the emission and photocatalytic mechanism in undoped and Cu doped ZnS NPs.

Schematic energy level diagram showing the emission and photocatalytic mechanism in undoped and Cu doped ZnS NPs is shown in Figure 5.15. As expected, among these doped photocatalysts, $Zn_{1-x}Cu_xS$; x = 0.03 recorded highest degradation. It is attributed to the fact that in this particular sample, large number of free charge carriers is available which

participate in the process of photocatalysis (also discussed in section 5.2.5). $Zn_{1-x}Cu_xS$; x = 0.04 has shown minimum degradation of crystal violet. As discussed by Mohamed [2], excess Cu^{2+} can serve as a trap for both charge carriers and these trapped charge carriers may recombine through quantum tunnelling. Also, this observation is in accordance with the results obtained from UV-Vis analysis. The band gap of $Zn_{1-x}Cu_xS$; x = 0.04 is minimum and hence charge carriers may recombine easily resulting in lower degradation. Also, from photoluminescence results, at higher dopant concentration, CuS may form which act as non radiative recombination centre thereby decreasing photocatalytic activity.

5.3 Ni doped ZnS

5.3.1 XRD and EDX studies

Figure 5.16 shows the XRD patterns of $Zn_{1-x}Ni_xS$; x = 0, 0.01, 0.02, 0.03 and 0.04.

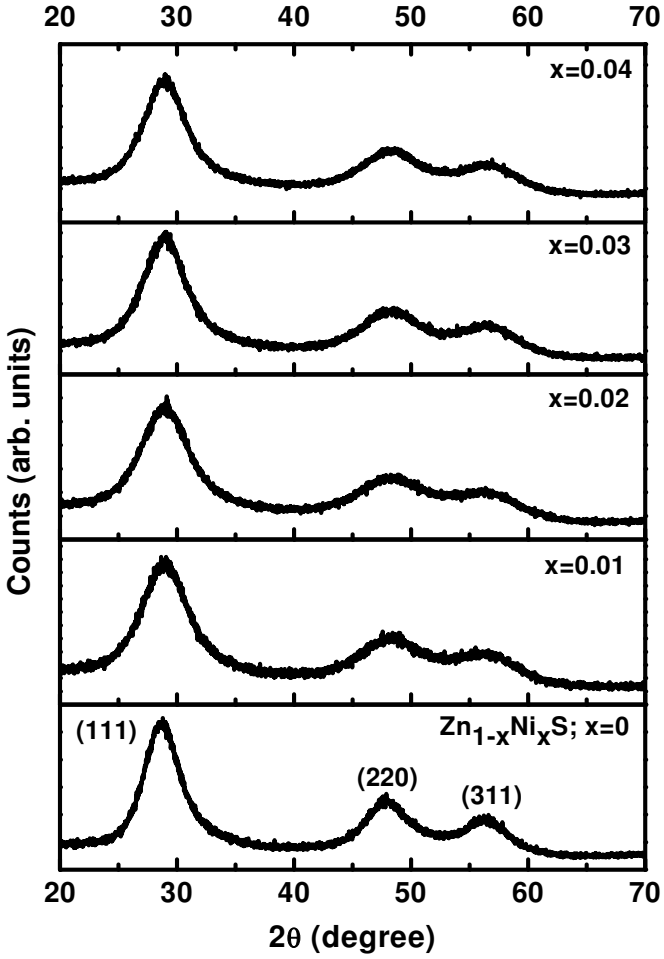

Figure 5.16: XRD patterns of $Zn_{1-x}Ni_xS$; x = 0, 0.01, 0.02, 0.03 and 0.04 in the range 20°-70°.

As can be seen in the figure, all samples exhibit cubic zinc blende phase with no impurity phase indicating that Ni is successfully doped in the host lattice.

However, the presence of Ni in prepared samples has been confirmed through Energy Dispersive X-ray (EDX) spectroscopy analysis. EDX patterns for $Zn_{1-x}Ni_xS$; x = 0, 0.01, 0.02, 0.03 and 0.04 are shown in Figure 5.17(a-e). Diffraction peaks from (111), (220) and (311) planes match well with those of the β-ZnS (cubic) reported in the ICDD Powder Diffraction File No.80-0020. In all the samples, broadening of diffraction peaks indicate nanosize formation of ZnS [7]. It is to be noted that in Figure 5.16, the XRD peaks of doped ZnS NPs have become weaker and broader as compared to that of undoped ZnS. This suggests that the crystallinity of $Zn_{1-x}Ni_xS$; x = 0.01, 0.02, 0.03 and 0.04 NPs has been deteriorated with the increase in Ni content in the source material. Decreased crystallinity of Ni doped samples as compared to that of undoped ZnS indicates the increase in disorder due to incorporation of impurity ions.

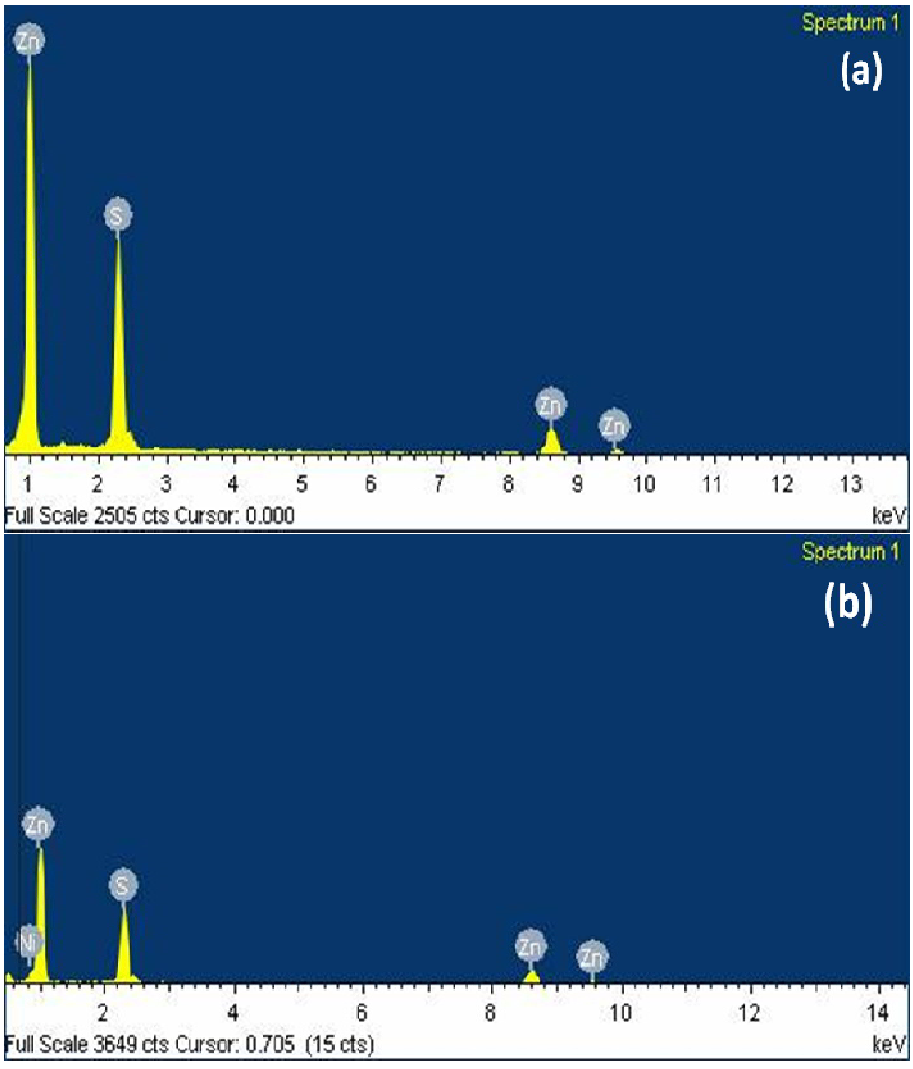

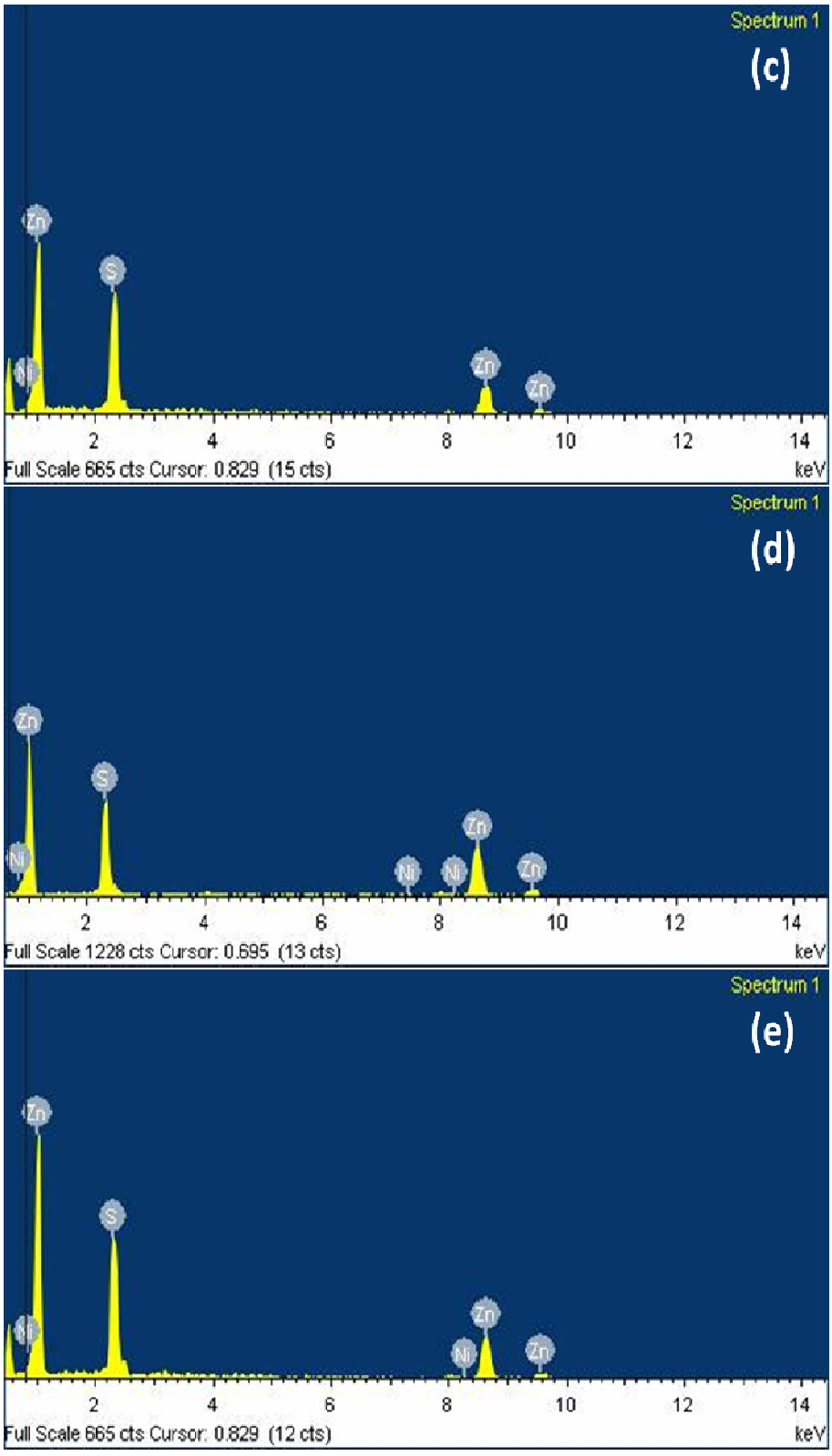

Figure 5.17: EDX patterns of $Zn_{1-x}Ni_xS$; (a) x = 0, (b) x=0.01, (c) x=0.02, (d) x=0.03 and (e) x=0.04.

To investigate the effect of Ni doping on ZnS host lattice, the most intense diffraction peak corresponding to (111) plane has been selected (Figure 5.18). A careful comparison of

diffraction peak in the range 2θ = 22°-38° for all samples indicates that this peak is slightly shifted towards higher angle which indicates that Ni is successfully substituted for Zn in the host lattice. Crystallite size of NPs has been calculated by following Scherrer's equation

$$t = \frac{k\lambda}{\beta\cos\theta} \qquad (5.1)$$

where k = 0.9, t is the crystallite size (Å), λ(Å), the wavelength of Cu Kα radiation and β is the corrected half width of the diffraction peak [8]. Crystallite size for all the samples has come in the range of 1.98-2.19 nm.

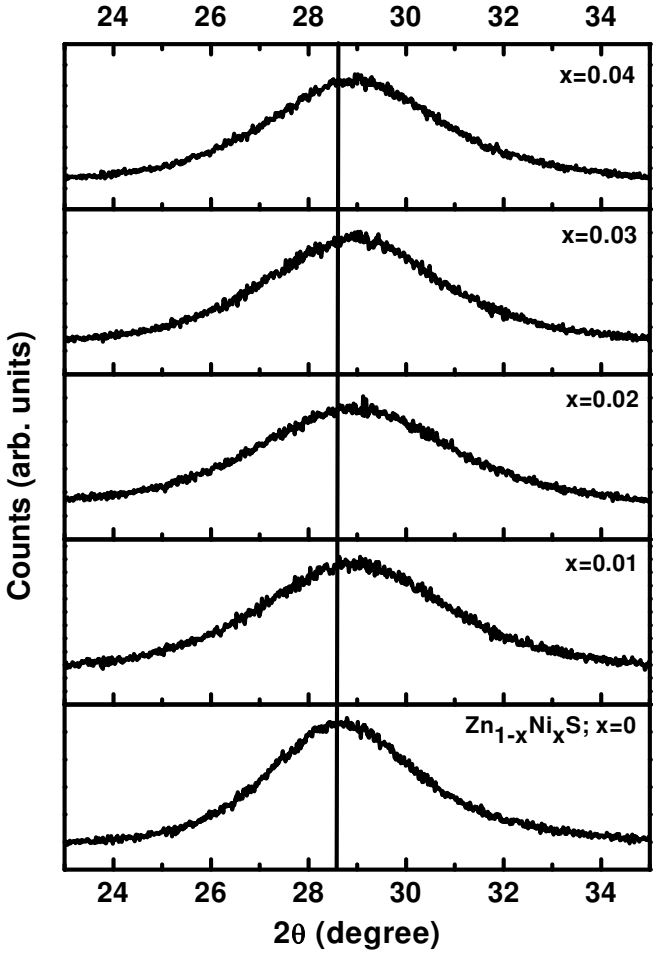

Figure 5.18: XRD patterns of $Zn_{1-x}Ni_xS$; x = 0, 0.01, 0.02, 0.03 and 0.04 in the range 22°-38°.

5.3.2 TEM analysis

Figure 5.19(a) shows the TEM image of one of the Ni doped ZnS sample. Nearly spherical particle of ZnS is clearly visible in the image. Amorphous layer of organic capping agent is also visible in the image. This confirms the effective capping of TG on the surface of ZnS.

Figure 5.19(b) shows high resolution TEM (HRTEM) micrograph of the same sample. In this micrograph, lattice fringing is clearly observed which indicates the well defined crystal structure of ZnS. The value of d spacing has come out to be 0.32 nm which corresponds to the (111) lattice plane spacing of ZnS in cubic phase.

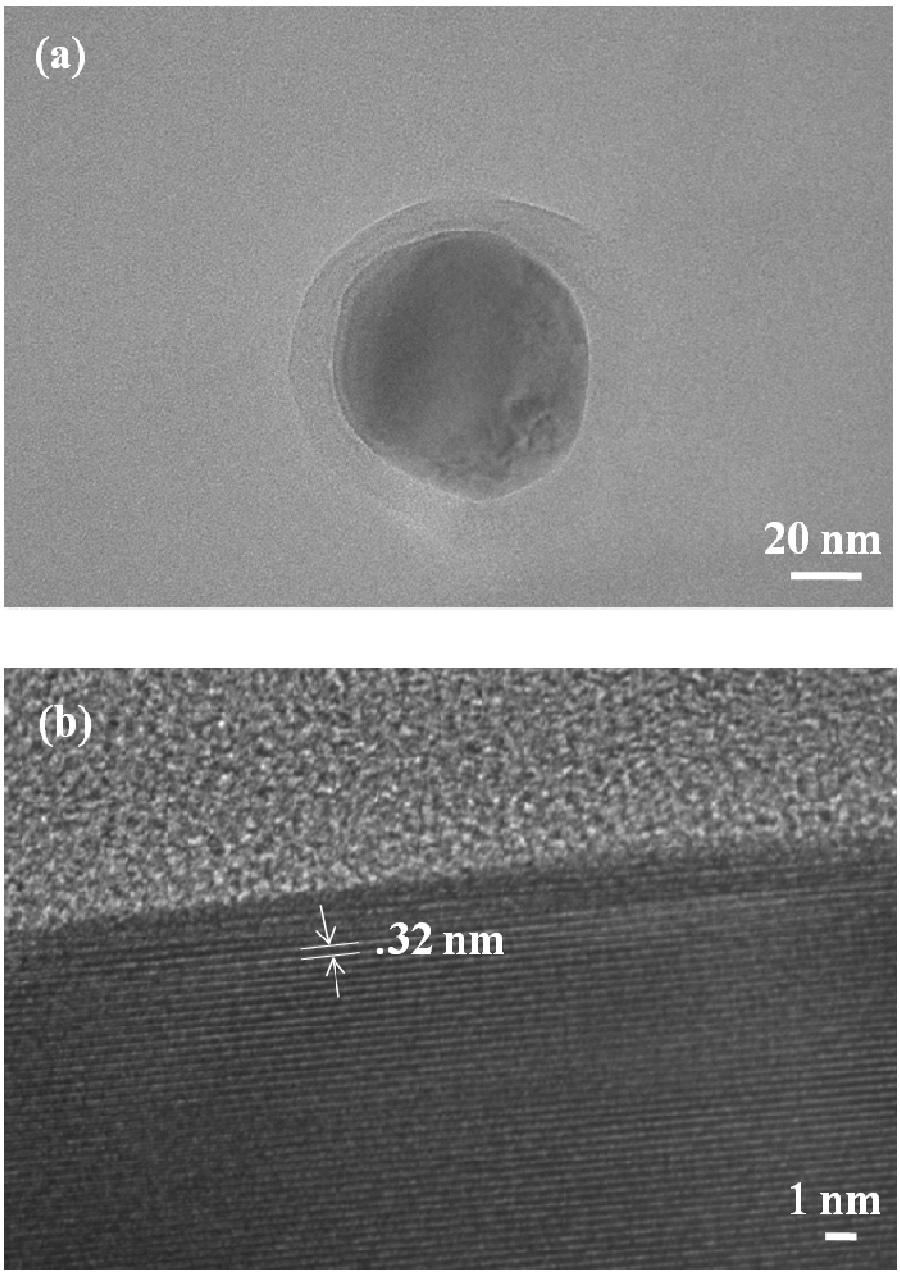

Figure 5.19: (a) TEM image of thioglycerol capped $Zn_{1-x}Ni_xS$; x = 0.02, (b) HRTEM image of the same sample.

5.3.3 FTIR Analysis

To investigate various functional groups present in TG capped and Ni doped ZnS, FTIR studies have been done. Figure 5.20 represents FTIR spectra of $Zn_{1-x}Ni_xS$; x = 0, 0.01.

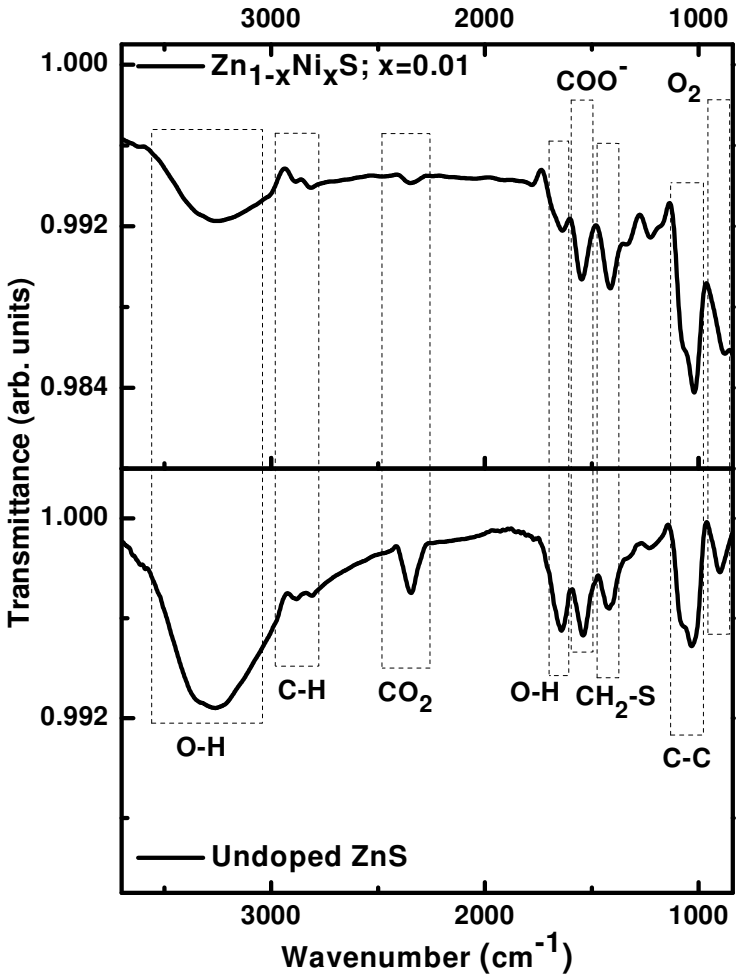

Figure 5.20: FTIR spectra of $Zn_{1-x}Ni_xS$; x = 0, 0.01.

Table 5.4: Peak assignment of various bonds in thioglycerol capped $Zn_{1-x}Ni_xS$; x = 0, 0.01.

Peak Position (cm^{-1}) $Zn_{1-x}Ni_xS$		**Peak assignment**
x=0	**x=0.01**	
3265	3262	O-H stretching [9]
2885	2886	C-H symmetrical stretching [9]
2810	2816	C-H asymmetrical stretching [9]
2346	2347	Interference from CO_2 [10]
1642	1638	O-H bending [9]
1540	1547	COO^- [11]
1416	1413	$–CH_2–S$ [12]
1033	1019	C–C stretch [12]
902	875	O_2 stretching and bending [13]

As can be seen in figure, both samples exhibit almost similar IR spectra. Therefore, we can say that doping has no profound effect on IR response of as prepared samples. The peak

positions for both samples alongwith peak assignments are given in Table 5.4. Pure TG exhibit S-H vibration band at 2557 cm^{-1}. This peak was not observed in both samples. It is attributed to the fact that the thiolate functions of the TG ligands are connected to the Zn^{2+} sites on the ZnS nanocrystals surfaces which confirm the capping of thioglycerol on ZnS surface [9].

5.3.4 UV-Vis studies

To investigate the effect of Ni doping on optical response of ZnS, UV-Vis studies have been performed for all samples in the range of 250-500 nm.

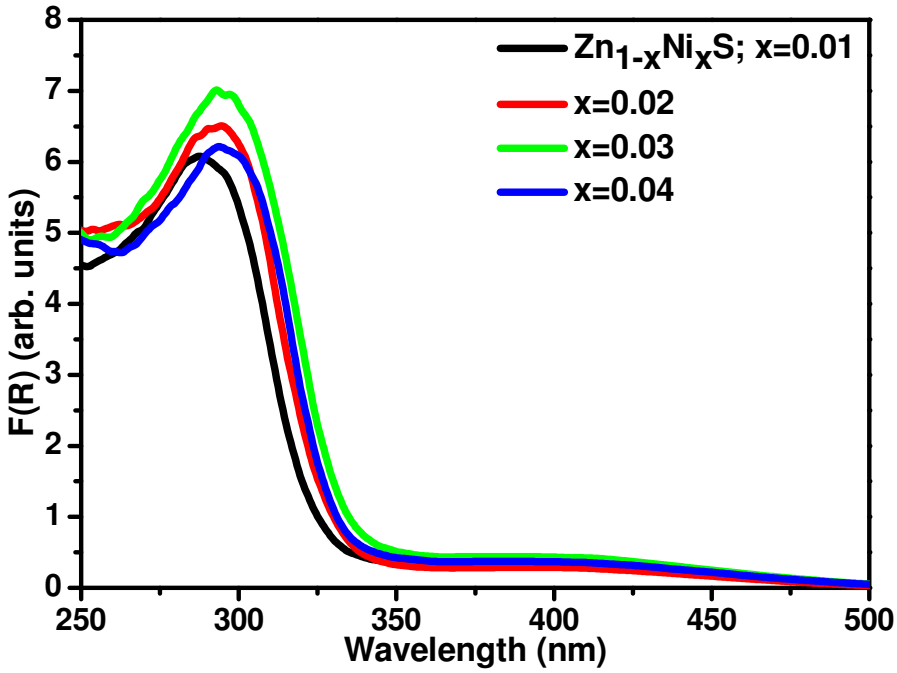

Figure 5.21: Absorption spectra of $Zn_{1-x}Ni_xS$; x = 0.01, 0.02, 0.03 and 0.04 plotted by Kubelka Munk method.

The relation between reflectance R and absorption coefficient α as given by Kubelka–Munk method [14] is

$$F(R) = \frac{(1-R)^2}{2R} = \frac{\alpha}{S} \qquad (5.2)$$

where F(R) is the Kubelka–Munk function, S is the scattering coefficient. From the above equation, F(R) can be assumed to be proportional to α [14]. Absorption spectra for all samples have been plotted by employing the above equation. As discussed earlier (section 5.2.4), band gap for undoped ZnS has come out to be 3.85 eV which is quite higher as compared to its bulk counterpart (3.54 eV). This variation in band gap indicates the formation of nano size compound showing strong quantum confinement effect. Figure 5.21 shows

optical response of all the samples synthesized with different dopant concentrations. It is clearly seen in the figure that absorbance of Ni doped ZnS is significantly increased in near visible region as compared to that of undoped ZnS.

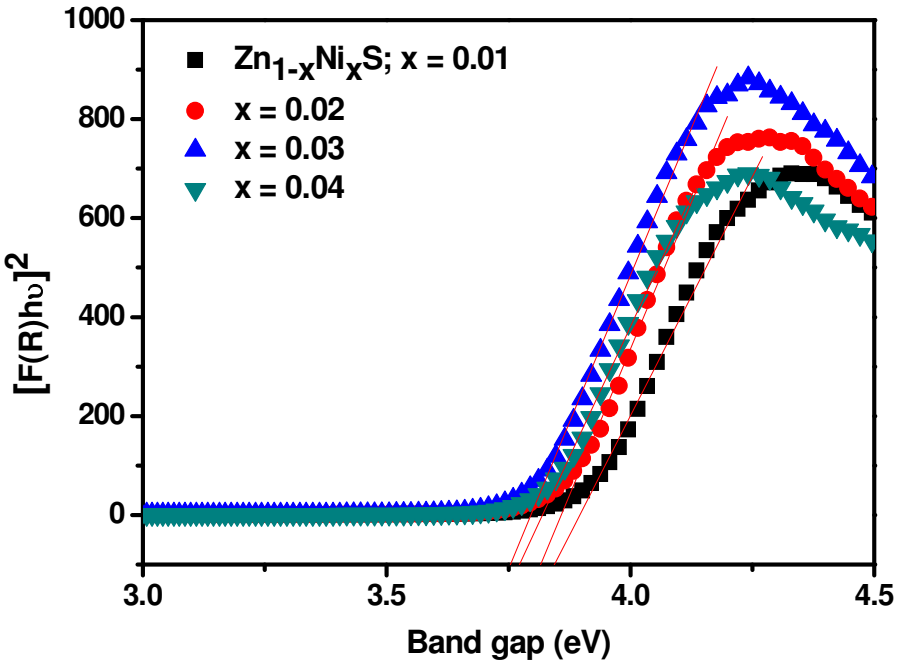

Figure 5.22: Tauc plots for $Zn_{1-x}Ni_xS$; x = 0.01, 0.02, 0.03 and 0.04 to determine band gap.

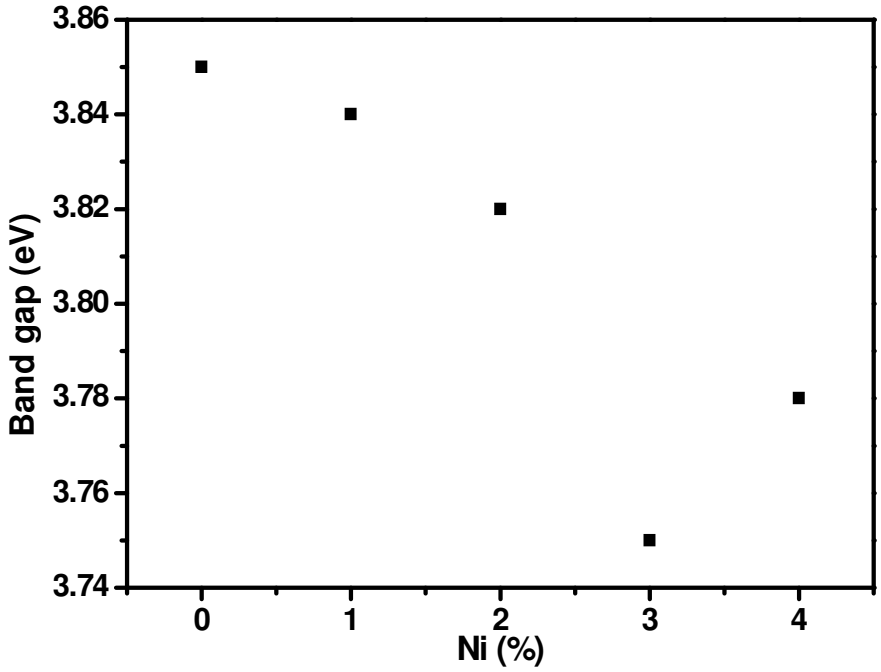

Figure 5.23: Variation in band gap of ZnS with Ni doping.

The relation between the incident photon energy (hυ) and the absorption coefficient (α) or F(R) is given by [14]

$$[F(R)h\upsilon]^{1/n} = A(h\upsilon - E_g) \qquad (5.3)$$

where A is a constant and E_g is the band gap of the material. The exponent n depends on the type of the transition i.e. 2, 3, 1/2, 1/3 values corresponding to indirect allowed, indirect forbidden, direct allowed and direct forbidden transitions. As shown in the Figure 5.22, square of the absorbed energy (F(R)hυ) have been plotted against photon energy (hυ) to determine the energy for direct gap transition. Band gap energies for all samples have been determined by extrapolating the straight portion of the graph on hυ axis at F(R)=0. From Figure 5.23, it is observed that band gap of $Zn_{1-x}Ni_xS$ has decreased from x=0 to x=0.03 whereas for x=0.04, it has increased slightly. The observed red shift in the absorption band edge with nickel doping in ZnS may be due to the sp-d exchange interactions between the band electrons and the localized d-electrons of the Ni^{2+} ions. In case of x=0.04, band gap is larger than the undoped ZnS, which can be explained by the Burstein–Moss shift [26-27]. According to the Burstein-Moss shift, at high doping content, the Fermi level shifts into the conduction band.

Table 5.5: Calculated band gap values and corresponding absorption wavelengths of $Zn_{1-x}Ni_xS$; x = 0, 0.01, 0.02, 0.03 and 0.04.

$Zn_{1-x}Ni_xS$	**Band gap (eV)**	**Absorption wavelength (nm)**
x=0	3.85	322.60
x=0.01	3.84	322.60
x=0.02	3.82	325.23
x=0.03	3.75	331.30
x=0.04	3.78	328.67

This results in the absorption transition from valence band to the Fermi level in the conduction band, instead from the top of the valence band to the bottom of the conduction band due to the donor electron filling of the conduction band [27]. Hence, the changes of transition levels lead to the energy gap broadening that resulted in increased band gap for $Zn_{1-x}Ni_xS$; x = 0.04. In their work, Sabri et al. [28] have observed the initial red shift of absorption wavelength at lower Mn content in Mn doped ZnO NPs whereas the blue shift has been observed at higher Mn content. They have also attributed this phenomenon to the Burstein-Moss shift. Band gap values along with corresponding absorption wavelengths are given in Table 5.5.

5.3.5 Photoluminescence studies

To investigate the effect of Ni doping on emission characteristics of ZnS, PL spectra of all the samples have been recorded. Figure 5.24 shows the emission spectra of $Zn_{1-x}Ni_xS$; x = 0, 0.01, 0.02, 0.03 and 0.04.

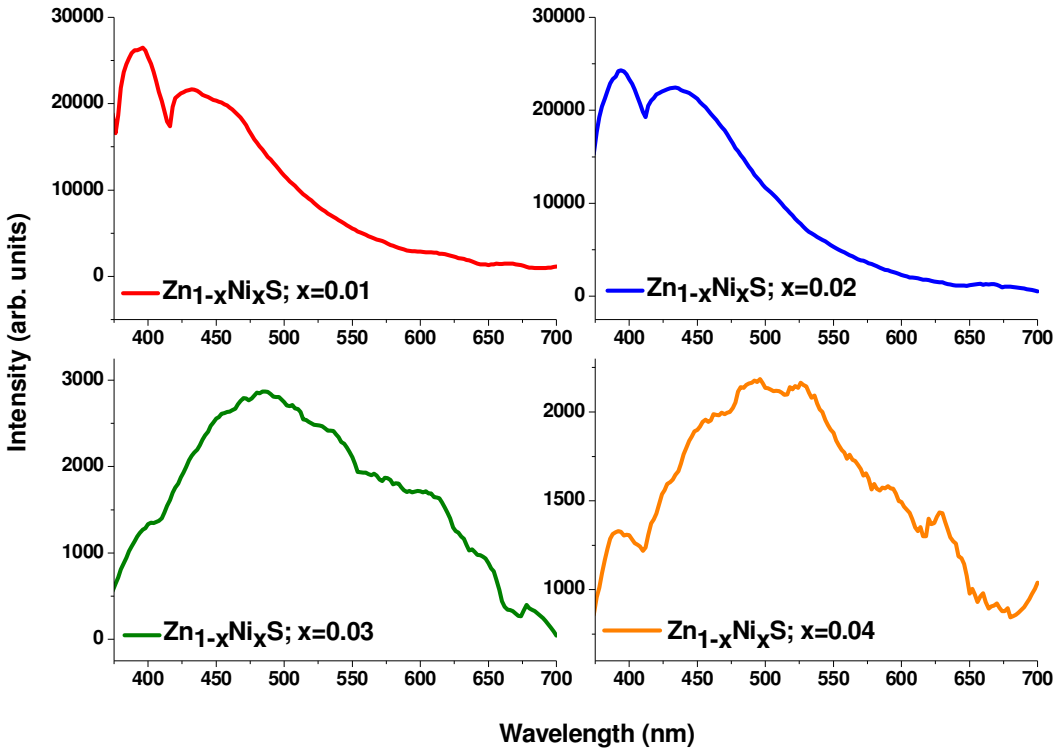

Figure 5.24: Photoluminescence emission spectra of $Zn_{1-x}Ni_xS$; x = 0.01, 0.02, 0.03 and 0.04 at λ_{exc}=320 nm.

It is clearly observed in the Figure 5.23 that as doping content in the host lattice is increased, emission intensity keeps on decreasing and is minimum in case of $Zn_{1-x}Ni_xS$; x = 0.04. In ZnS:Ni^{2+} semiconductor nanomaterials, the lowest multiplet term 3F of the free Ni^{2+} ion split into $^3T_1$, $^3T_2$ and $^3A_2$ through the anisotropic hybridization. Due to the d-d optical transitions of Ni^{2+}, the luminescent center of Ni^{2+} is formed in ZnS [29]. In their work, Podlowski et al. [30] have reported that d-d transitions within Ni^{2+} ion in Ni^{2+} doped CdS and ZnS are essentially non radiative due to which emission intensity is decreased. In case of $Zn_{1-x}Ni_xS$; x = 0.03 and 0.04, overall emission intensity has sharply decreased and ZnS related emission has also suppressed. Borse et al. [31] have also observed luminescence quenching due to incorporation of Ni ions in ZnS lattice. According to them, Ni ions have acted as electron trapping centres which results in non-radiative recombination. Photoexcited electrons are preferentially transferred to nickel ion induced trapping centres as compared to anion vacancy

defect centres. In our case, sulphur vacancies related peak (~436 nm) is reduced as compared to that of sulphur interstiatials which is at ~392 nm with Ni doping. Hence, in the present case, similar to the results observed by Borse et al. [31], photoexcited electrons are preferentially transferred to nickel ion induced trapping centres as compared to anion vacancy defect centres which acted as non radiative recombination centres thereby reducing the emission intensity. At higher dopant concentrations ($Zn_{1-x}Ni_xS$; x = 0.03 and 0.04), red shift in emission intensity peak has been observed. This suggests that trap states have been created by Ni ion between the valance band and conduction band. Therefore, a least quantum of energy has been provided to the nearest neighbour atom or lattice whenever the electron makes transition from the conduction band to trap state. As a result, the emission energy has been reduced thereby shifting the emission spectrum towards longer wavelength. Murugadoss et al. [32] have observed red shift of 445 nm emission peak in ZnS with Ni doping. Luminescence quenching at higher concentrations of Ni ion has been attributed to increase in the radiationless transitions by the higher concentration of Ni ions. It is worth mentioning that source of Ni ions selected also affects luminescence spectra of Ni doped ZnS. Yang et al. [33] have reported a single peak (~ 520 nm) using $NiSO_4$ as a source of Ni ions. But Murugadoss et al. [32] have observed two peaks using $Ni(CH_3COO)_2$ as a source of Ni ions. In the present case, $Ni(CH_3COO)_2$ has been used as a source of Ni ion but no new peak has been observed with respect to undoped ZnS in luminescence spectra.

5.3.6 Photocatalytic studies

Photocatalytic degradation of crystal violet has been done to investigate the effect of Ni doping on photocatalytic activity of ZnS NPs. For illustration, the spectral changes taking place in absorbance of dye during photochemical reaction catalysed by $Zn_{1-x}Ni_xS$; x = 0.01 and x=0.04 are shown in Figure 5.25(a-b) for time interval of 60 min. The characteristic absorption peak of this dye at 590 nm has been selected to monitor the photocatalytic degradation of the dye. By Beer Lambert law, the decrease in concentration of dye has been recorded at different intervals of time to measure degradation rate. Figure 5.26 shows the comparative degradation behaviour of dye catalysed with $Zn_{1-x}Ni_xS$; x = 0, 0.01, 0.02, 0.03 and 0.04 in terms of change in concentration with respect to the initial concentration. As can be seen in figure, all Ni doped samples have shown lower degradation as compared to that of undoped sample. $Zn_{1-x}Ni_xS$; x = 0.04 has recorded the lowest degradation among all the doped samples.

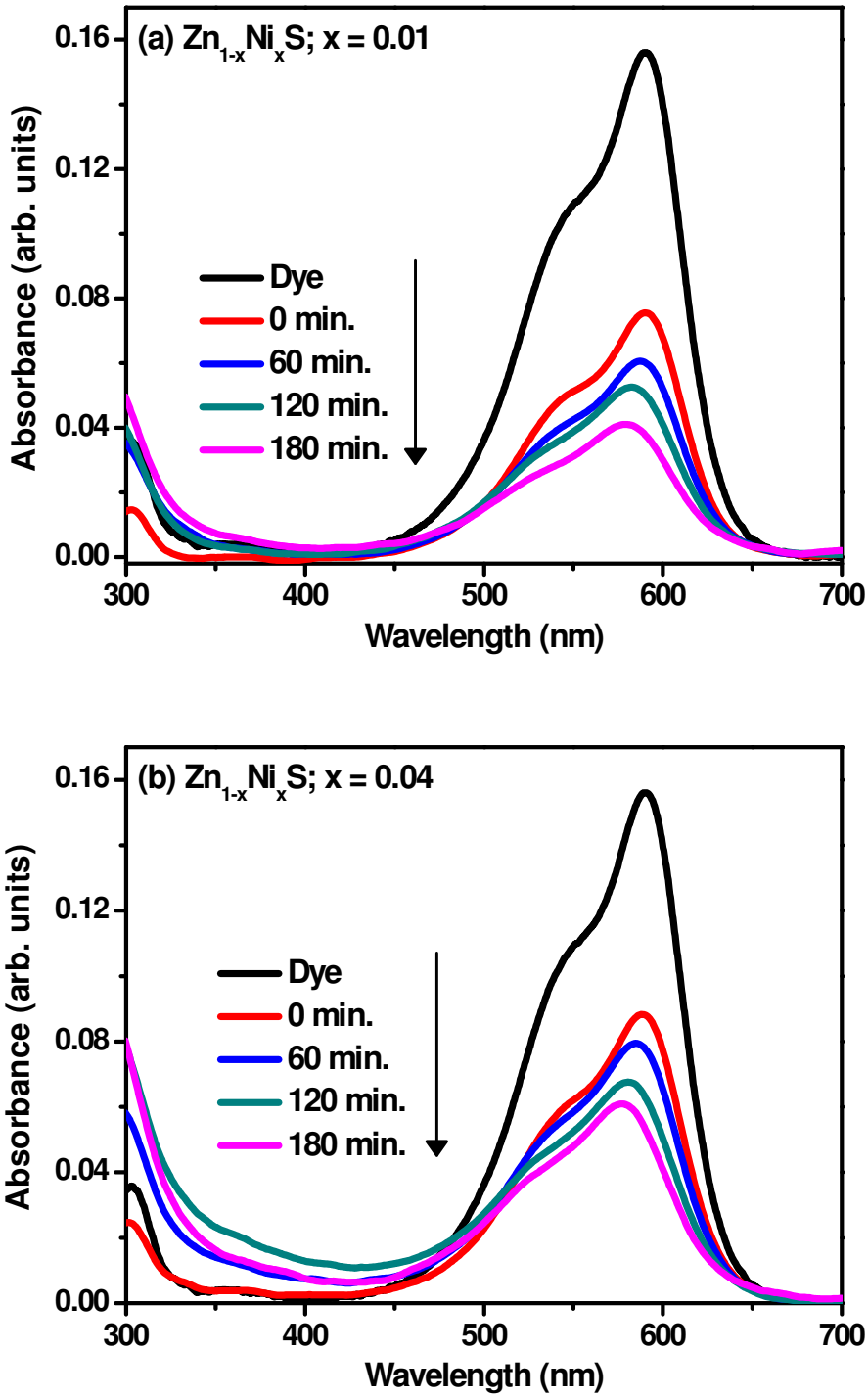

Figure 5.25: Absorbance spectra of crystal violet degraded in the presence of $Zn_{1-x}Ni_xS$ (a) x = 0.01, (b) x= 0.04.

Since, in this study, concentration of solute is very low (1mg/L), so Langmuir-Hinshelwood kinetics model [23] can be simplified to pseudo first order kinetic model equation.

$$ln\left(\frac{C_t}{C_0}\right) = kT \qquad (5.4)$$

where C_t is the concentration of dye after irradiation in selected time interval t, C_0 is the initial concentration of dye, k is the first order rate constant, and T is irradiation time.

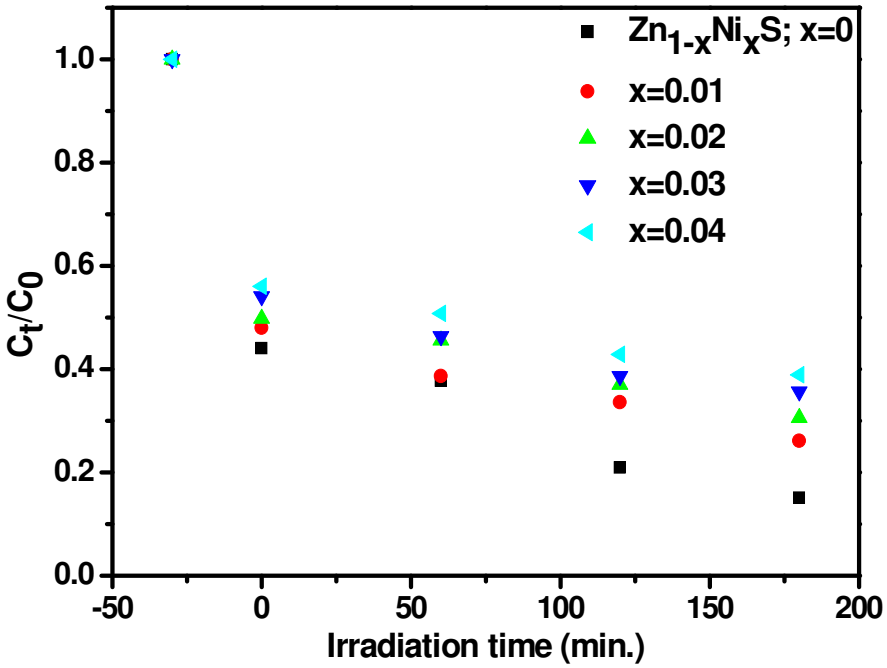

Figure 5.26: Variation of C_t/C_0 with irradiation time for $Zn_{1-x}Ni_xS$; x = 0, 0.01, 0.02, 0.03 and 0.04.

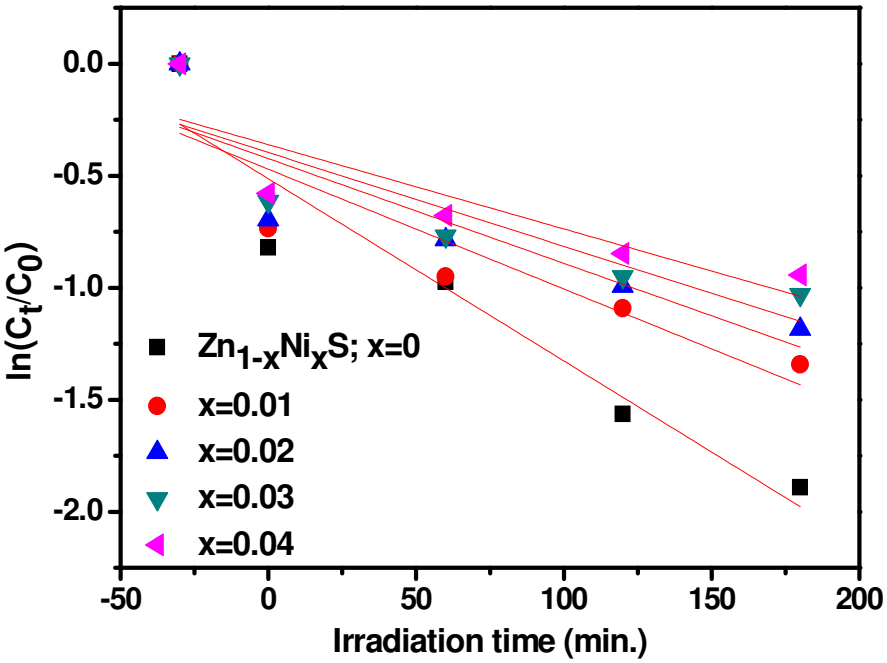

Figure 5.27: Plot between $\ln(C_t/C_0)$ and irradiation time to determine the value of rate constant k.

Figure 5.27 shows plot between $\ln(C_t/C_0)$ and irradiation time to determine the value of rate constant k. Degradation rate has come out to be minimum in case of $Zn_{1-x}Ni_xS$; x = 0.04 ($k=0.0038\ min^{-1}$). The degradation percentage has been calculated as

$$\%D = \left(1 - \frac{C_t}{C_0}\right) \times 100 \qquad (5.5)$$

where C_t is the concentration of dye after irradiation in selected time interval, C_0 is the initial concentration of dye. As shown in Figure 5.28, % degradation in presence of undoped ZnS is maximum (85.35%) among all the photocatalysts. Degradation percentage values for all samples have been summarized in Table 5.6. The order of photo degradation rate is obtained as

$$Zn_{1-x}Ni_xS;\ x = 0 > x = 0.01 > x = 0.02 > x = 0.03 > x = 0.04$$

Decreased photocatalytic activity of Ni doped ZnS NPs may be attributed to the changed absorption characteristics of ZnS on doping with Ni.

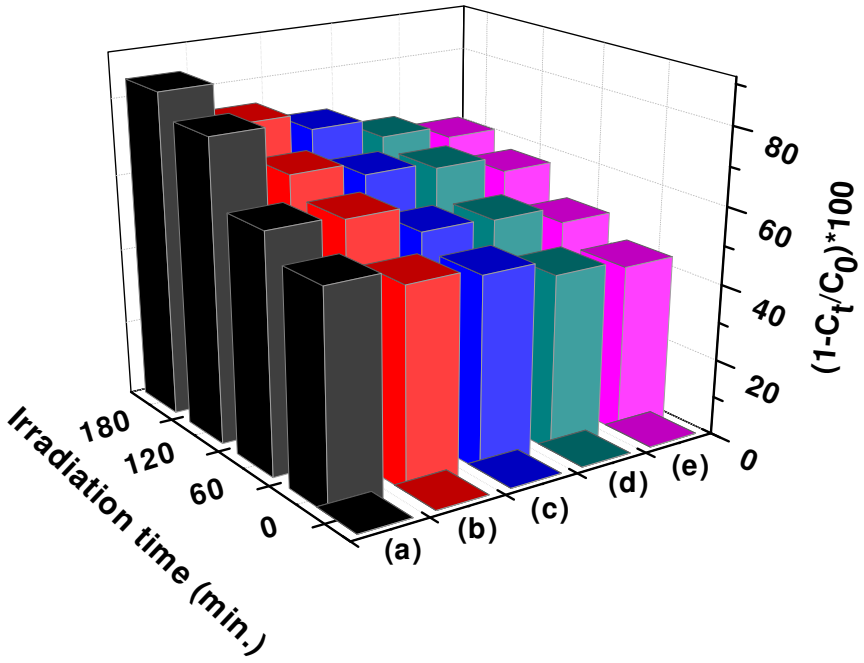

Figure 5.28: Degradation percentage of crystal violet in the presence of $Zn_{1-x}Ni_xS$ (a) x = 0, (b) 0.01, (c) 0.02, (d) 0.03 and (e) 0.04 at different irradiation times.

When semiconductor is photoexcited, electrons are promoted to conduction band leaving holes in valence band. These charge carriers may recombine (radiatively or non radiatively) or may be trapped in centres created by dopant ions or intrinsic defects. These trapped charge carriers may also recombine or may be transported to the surface to participate in the reactions which are occurring on the surface of photocatalyst. In the present study, Ni ions have formed trap states within the energy gap of ZnS. The obtained results are in accordance with the PL results which are discussed in section 5.3.5. Photoluminescence intensity has

been quenched by Ni doping in $Zn_{1-x}Ni_xS$ from x=0.01 to x=0.04. There is a strong correlation between the photoluminescence and photocatalytic properties of an optically active material. As discussed in PL section, emission intensity has decreased with the increase in dopant content which indicates that non-radiative recombination is taking place thereby preventing the charge carriers to participate in the photocatalytic process. Hence, we can say that in case of Ni doped ZnS, non radiative e^--h^+ recombination dominates over interfacial charge transfer. Kaneva et al. [34] have reported the deceleration of photocatalytic process in the presence of 1% to 15% Ni doped ZnO thin films both under UV and visible illumination. They have stated that Ni^{2+} may act like a p-type dopant into ZnO, working as a charge-carrier recombination center thus enhancing the recombination of electron-hole pairs thereby decreasing the effective charge carrier concentration. The decreasing of effective charge carrier concentration has lowered the band bending on the crystallite surface, which has decreased the driving force acting on photogenerated electrons and holes. This decrease in driving force has reduced charge carrier separation thereby quenching the photocatalytic activity.

Table 5.6: First order rate constants for the photocatalytic degradation of crystal violet and corresponding percent degradation using $Zn_{1-x}Ni_xS$; x = 0, 0.01, 0.02, 0.03 and 0.04 as photocatalysts.

Photocatalyst	Adj. R^2	k (min^{-1})	$(1-C_t/C_0)*100$
$Zn_{1-x}Ni_xS$; x=0	0.89	0.0082	85.35
x=0.01	0.74	0.0053	73.88
x=0.02	0.72	0.0047	69.43
x=0.03	0.70	0.0042	64.33
x=0.04	0.69	0.0038	61.08

5.4 Mn doped ZnS

5.4.1 XRD and EDX studies

Figure 5.29 shows the XRD patterns of $Zn_{1-x}Mn_xS$; x = 0, 0.01, 0.02, 0.03 and 0.04. As can be seen in the figure, all samples exhibit cubic zinc blende phase with no impurity phase indicating that Mn is successfully doped in the host lattice. However, the presence of Mn in prepared samples has been confirmed through Energy Dispersive X-ray (EDX) spectroscopy analysis. EDX patterns for $Zn_{1-x}Mn_xS$; x = 0, 0.01, 0.02, 0.03 and 0.04 are shown in Figure 5.30(a-e). Diffraction peaks from (111), (220) and (311) planes match well with those of the β-ZnS (cubic) reported in the ICDD powder diffraction file no.80-0020. In all the samples,

broadening of diffraction peaks indicates the presence of nanosize ZnS [7]. The XRD peaks of doped ZnS NPs have become weaker and broader as compared to that of undoped ZnS.

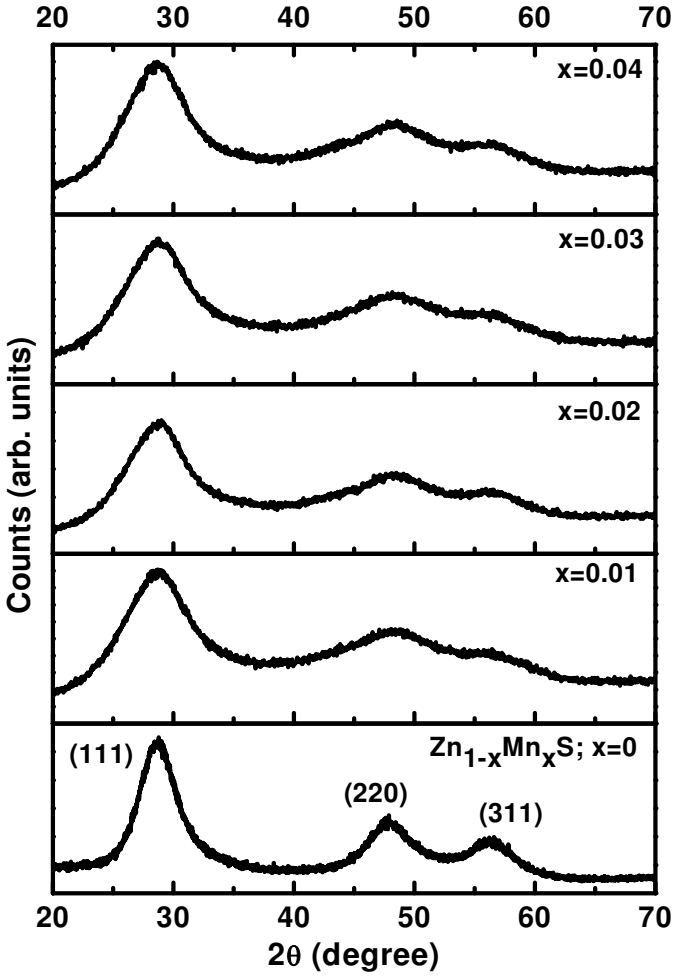

Figure 5.29: XRD patterns of $Zn_{1-x}Mn_xS$; x = 0, 0.01, 0.02, 0.03 and 0.04 in the range 20°-70°.

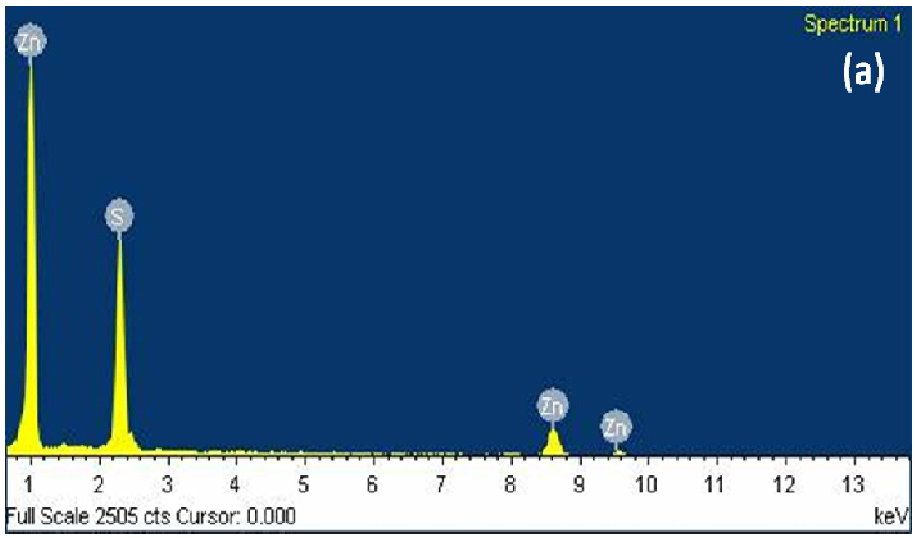

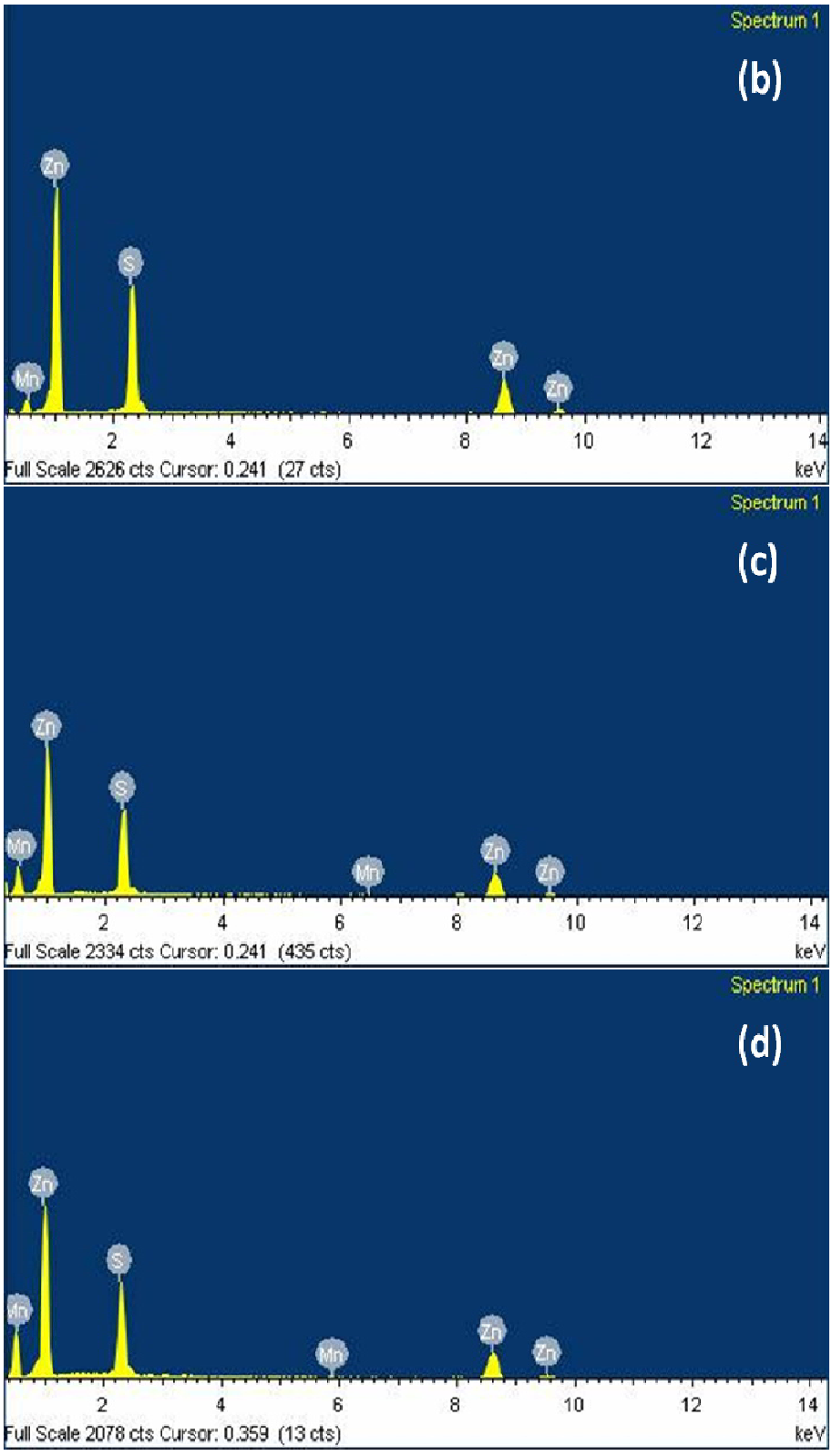
Spectrum 1
(b)
Zn
S
Mn
Zn
Zn
2
4
6
8
10
12
14
Full Scale 2626 cts Cursor: 0.241 (27 cts)
keV
Spectrum 1
(c)
Zn
S
Mn
Mn
Zn
Zn
2
4
6
8
10
12
14
Full Scale 2334 cts Cursor: 0.241 (435 cts)
keV
Spectrum 1
(d)
Zn
S
Mn
Mn
Zn
Zn
2
4
6
8
10
12
14
Full Scale 2078 cts Cursor: 0.359 (13 cts)
keV

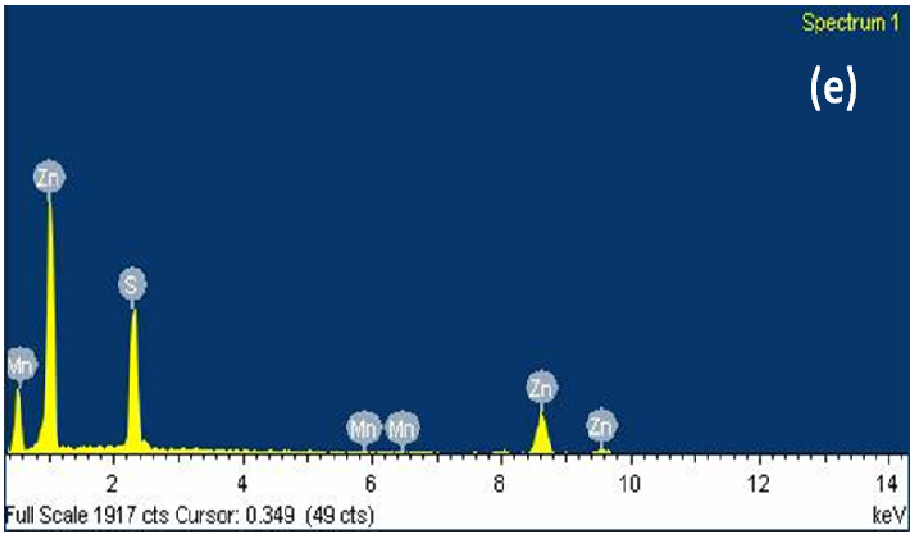

Figure 5.30: EDX patterns of $Zn_{1-x}Mn_xS$; (a) x = 0, (b) x=0.01, (c) x=0.02, (d) x=0.03 and (e) x=0.04.

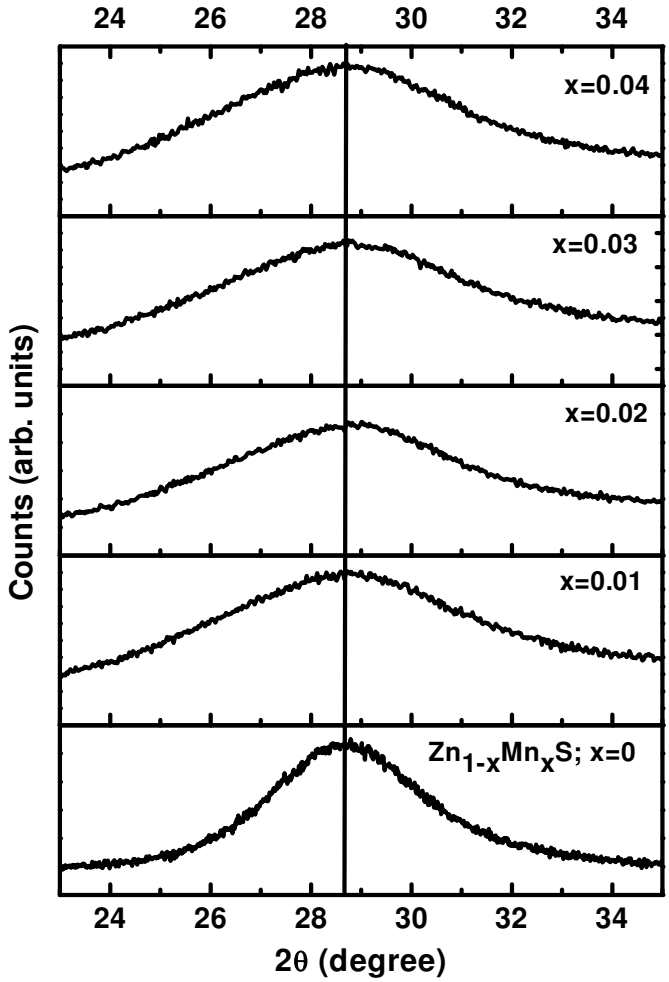

Figure 5.31: XRD patterns of $Zn_{1-x}Mn_xS$; x = 0, 0.01, 0.02, 0.03 and 0.04 in the range 22°-38°.

This further suggests that the crystallinity of $Zn_{1-x}Mn_xS$; x = 0.01, 0.02, 0.03 and 0.04 NPs has been decreased with the increase in Mn content in the source materials.

To investigate the effect of Mn doping on ZnS host lattice, the most intense diffraction peak corresponding to (111) plane has been selected (Figure 5.31). A careful comparison of diffraction peak in the range 2θ = 22°-38° for all samples has been done. Larger line broadening in case of Mn doped samples indicates their smaller crystallite size as compared to that of undoped ZnS sample. No appreciable peak shift has been observed in any sample which may be attributed to the very small difference in ionic radius of Mn^{2+} (0.66) and Zn^{2+} (0.6). Crystallite size of NPs ($Zn_{1-x}Mn_xS$; x = 0, 0.01, 0.02, 0.03 and 0.04) has been calculated by following Scherrer's equation

$$t = \frac{k\lambda}{\beta\cos\theta} \qquad (5.1)$$

where k = 0.9, t is the crystallite size (Å), λ(Å), the wavelength of Cu Kα radiation and β is the corrected half width of the diffraction peak [8]. Crystallite size has come out in the range 1.9-2.0 nm. Decreased crystallinity of Mn doped samples as compared to that of undoped ZnS indicates the increase in disorder due to incorporation of impurity ions.

5.4.2 TEM analysis

Figure 5.32(a) shows TEM micrograph of one of the doped sample $Zn_{1-x}Mn_xS$; x=0.01.

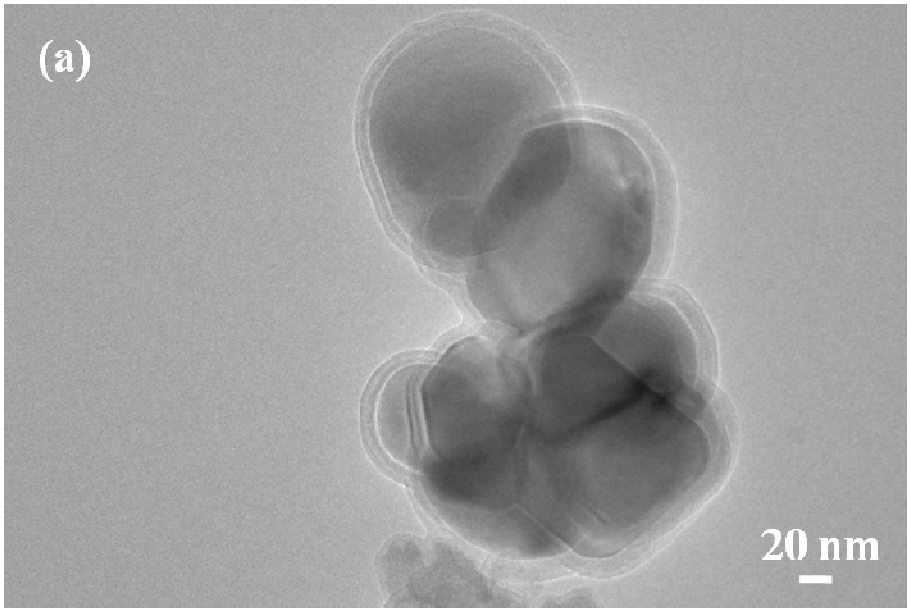

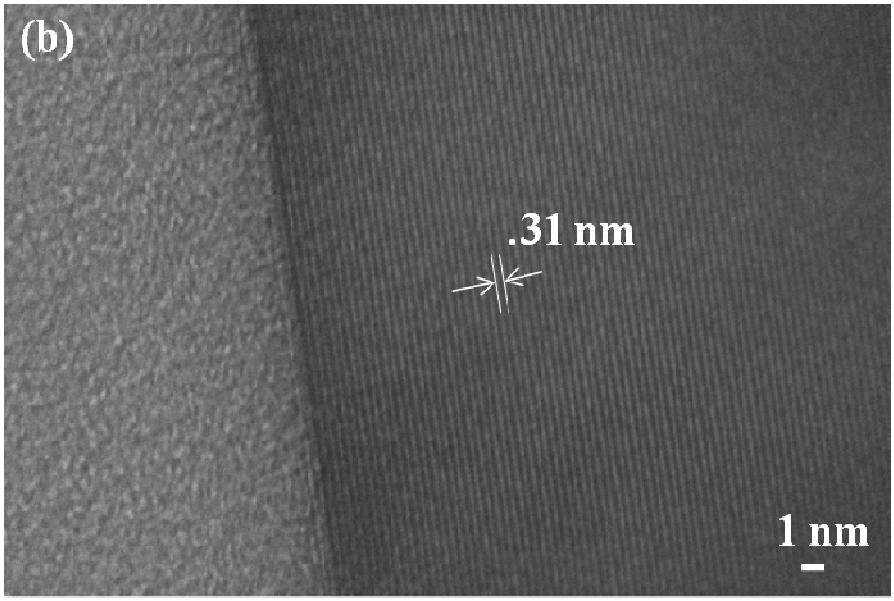

Figure 5.32: (a) TEM image of thioglycerol capped $Zn_{1-x}Mn_xS$; x = 0.01, (b) HRTEM image of the same sample.

As observed in Figure 5.32(a), the particles of doped ZnS are irregularly spherical. The NPs have grown due to overnight ageing and also the sample was prepared at 80 °C to make the doping efficient. Amorphous layer corresponding to thioglycerol is clearly seen around the NPs surface which confirms that effective capping is obtained on NPs surface. From the high-resolution TEM (HRTEM) image in Figure 5.32(b), the lattice fringes can be clearly observed, suggesting the well-defined crystal structure. The fringe with lattice spacing of ca. 0.31 nm corresponds to the (111) plane of the cubic ZnS which is in good agreement with the XRD pattern.

5.4.3 FTIR Analysis

To investigate various functional groups present in TG capped and Mn doped ZnS, FTIR studies have been done. Figure 5.33 represents FTIR spectra of $Zn_{1-x}Mn_xS$; x = 0, 0.03. As can be seen in figure, both samples exhibit almost similar IR spectra. Therefore, we can say that doping has no profound effect on IR response of as prepared samples. The peak positions for both samples alongwith peak assignments are given in Table 5.7. Pure TG exhibit S-H vibration band at 2557 cm^{-1}. This peak was not observed in both samples. It is attributed to the fact that the thiolate functions of the TG ligands are connected to the Zn^{2+} sites on the ZnS nanocrystals surfaces which confirm the capping of thioglycerol on ZnS surface [9].

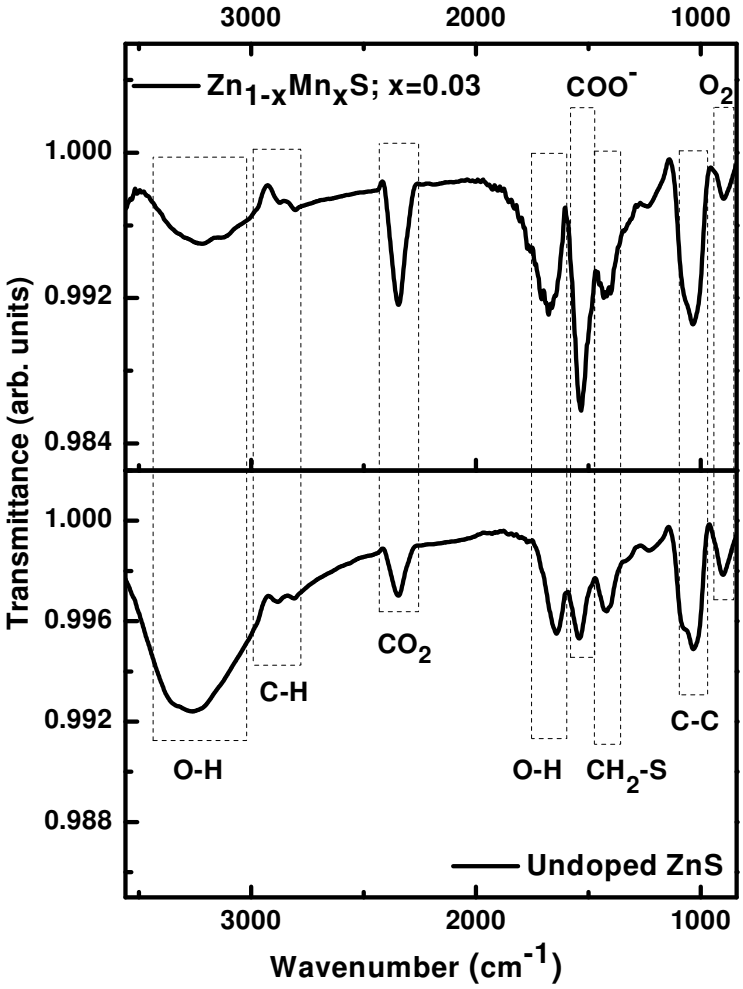

Figure 5.33: FTIR spectra of $Zn_{1-x}Mn_xS$; x = 0, 0.03.

Table 5.7: Peak assignment of various bonds in thioglycerol capped $Zn_{1-x}Mn_xS$; x = 0, 0.03.

Peak Position (cm^{-1}) $Zn_{1-x}Mn_xS$		**Peak assignment**
x=0	**x=0.03**	
3265	3217	O-H stretching [9]
2885	2873	C-H symmetrical stretching [9]
2810	2802	C-H asymmetrical stretching [9]
2346	2345	Interference from CO_2 [10]
1642	1675	O-H bending [9]
1540	1533	COO^- [11]
1416	1421	$–CH_2–S$ [12]
1033	1030	C–C stretch [12]
902	898	O_2 stretching and bending [13]

5.4.4 UV-Vis studies

To investigate the effect of Mn doping on optical response of ZnS, UV-Vis studies have been performed for all samples in the range of 250-500 nm. Figure 5.34 shows optical response of all the samples synthesized with different dopant concentrations.

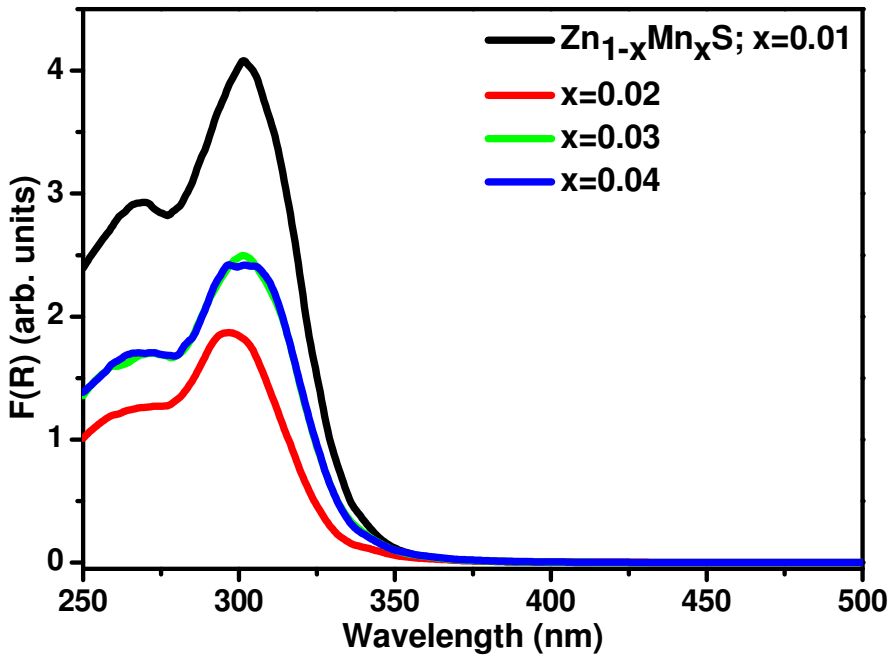

Figure 5.34: Absorption spectra of $Zn_{1-x}Mn_xS$; x = 0.01, 0.02, 0.03 and 0.04 plotted by Kubelka Munk method.

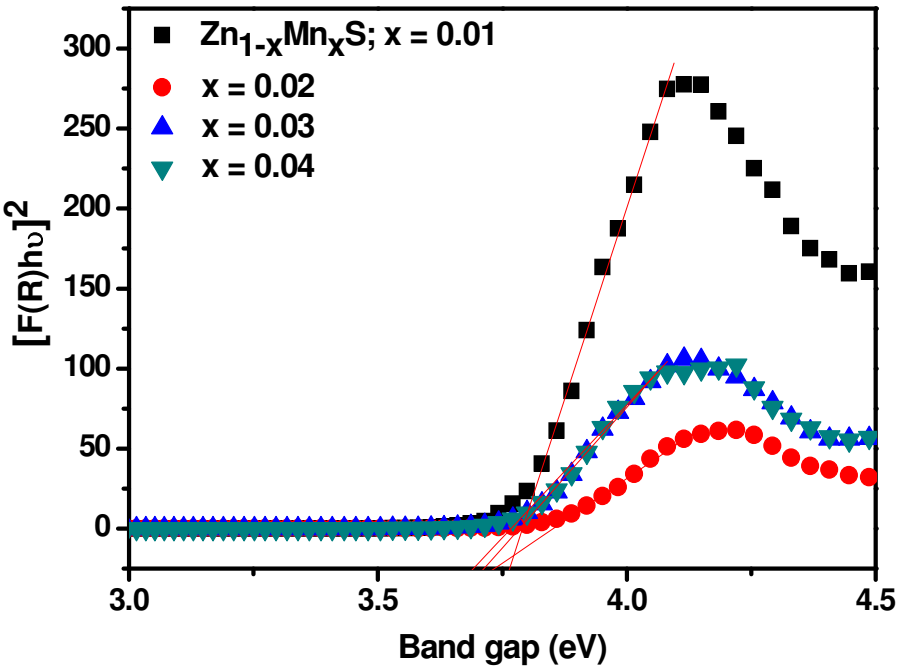

Figure 5.35: Tauc plots for $Zn_{1-x}Mn_xS$; x = 0.01, 0.02, 0.03 and 0.04 to determine band gap.

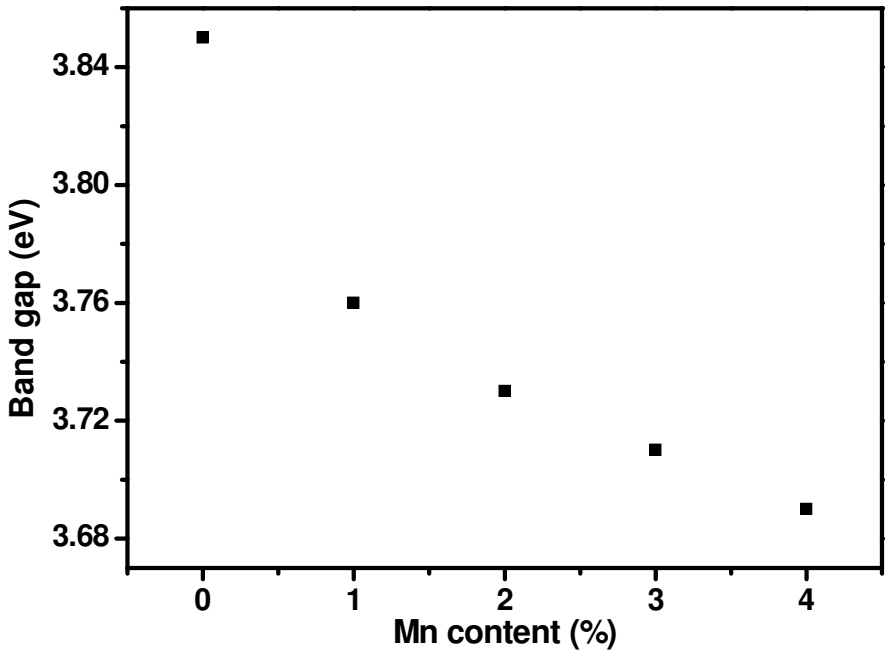

Figure 5.36: Variation in band gap of ZnS with Mn doping.

The observed change in absorption spectra is due to the dopant ions. Band gap for undoped ZnS came out to be 3.85 eV which is quite higher as compared to its bulk counterpart (3.54 eV). This variation in band gap indicates nano size formation showing strong quantum confinement effect. The relation between the incident photon energy (hυ) and the absorption coefficient (α) or F(R) is given by [14]

$$[F(R)h\upsilon]^{1/n} = A(h\upsilon - E_g) \qquad (5.3)$$

where A is a constant and E_g is the band gap of the material and the exponent n depends on the type of the transition i.e. 2, 3, 1/2, 1/3 values corresponding to indirect allowed, indirect forbidden, direct allowed and direct forbidden transitions. As shown in the Figure 5.35, square of the absorbed energy (F(R)hυ) have been plotted against photon energy (hυ) to determine the energy for direct gap transition. Band gap energies for all samples have been determined by extrapolating the straight portion of the graph on hυ axis at F(R)=0. Variation of band gap with Mn content has been shown in Figure 5.36. It is observed that band gap of $Zn_{1-x}Mn_xS$ decreased from x=0 to x=0.04. The band gap shrinkage in doped samples is quite obvious due to the introduction of impurity levels in the host lattice and sp-d exchange interactions between the band electrons and the localized d-electrons of the Mn^{2+} ions. Band gap values along with corresponding absorption wavelengths have been given in Table 5.8.

Table 5.8: Calculated band gap values and corresponding absorption wavelengths of $Zn_{1-x}Mn_xS$; x = 0, 0.01, 0.02, 0.03 and 0.04.

$Zn_{1-x}Mn_xS$	Band gap (eV)	Absorption wavelength (nm)
x=0	3.85	322.60
x=0.01	3.76	330.42
x=0.02	3.73	333.07
x=0.03	3.71	334.87
x=0.04	3.69	336.68

5.4.5 Photoluminescence studies

Figure 5.37(a) shows the photoluminescence emission spectra of Mn doped ZnS NPs in the range 350-800 nm. As can be seen in the figure, unlikely to undoped ZnS which exhibit emission spectra in blue region, $Zn_{1-x}Mn_xS$; x = 0.01, 0.02, 0.03 and 0.04 exhibit sharp well defined emission peak in orange-red region of visible spectra. Simultaneously, intensity of emission peaks in blue region has also increased. When Mn^{2+} ions are substituted for host cation sites, the mixing between the s-p electrons of the host ZnS and the d electrons of Mn^{2+} occurs and makes the forbidden transition of $^4T_1$ - $^6A_1$ partially allowed, resulting in the characteristic emission of Mn^{2+} [35]. Contrary to this, the addition of Mn^{2+} ions to the outside of preformed ZnS results in ultraviolet emission [36]. Hence, in the present case, it is confirmed that Mn^{2+} is being substituted in the host lattice. This emission peak keeps on increasing with the increase in doping content. No luminescence quenching has been observed even at higher Mn dopant concentration which is in line with the previously reported results. As reported by Bol et al. [37], concentration quenching is caused by energy migration from donor to traps, which are present in a low concentration. Quenching requires efficient high donor concentrations for migration of energy via an array of donors to traps as migration is limited to very short distances. In case of Mn^{2+}, the transition involved in the energy migration is spin forbidden $^6A_1$ - $^4T_1$ transition within the $3d^5$ configuration of the Mn^{2+} ion. Hence, non radiative energy transfer between neighboring Mn^{2+} ions via dipole-dipole interaction is not efficient. As this transition is forbidden and only transfer between nearest neighbor Mn^{2+} ions is expected hence, concentration of Mn^{2+} ions at which energy migration is expected to be observed is high. In case of $Zn_{1-x}Mn_xS$; x = 0.01 and 0.02, the peak position is at ~607 nm. At higher dopant content i. e. in case of $Zn_{1-x}Mn_xS$; x = 0.03, 0.04, this emission peak is slightly red shifted to 610 nm. Many research groups have reported this red shift in Mn^{2+} related emission in ZnS [38-41]. Cruz et al. [38] have attributed this red shift to decrease in the density of surface states with increasing particle size

or by strong electron-phonon coupling in quantum dots. Hu et al. [39] have ascribed this shift due to hybridization of s-p states of ZnS and d states of Mn^{2+} ion.

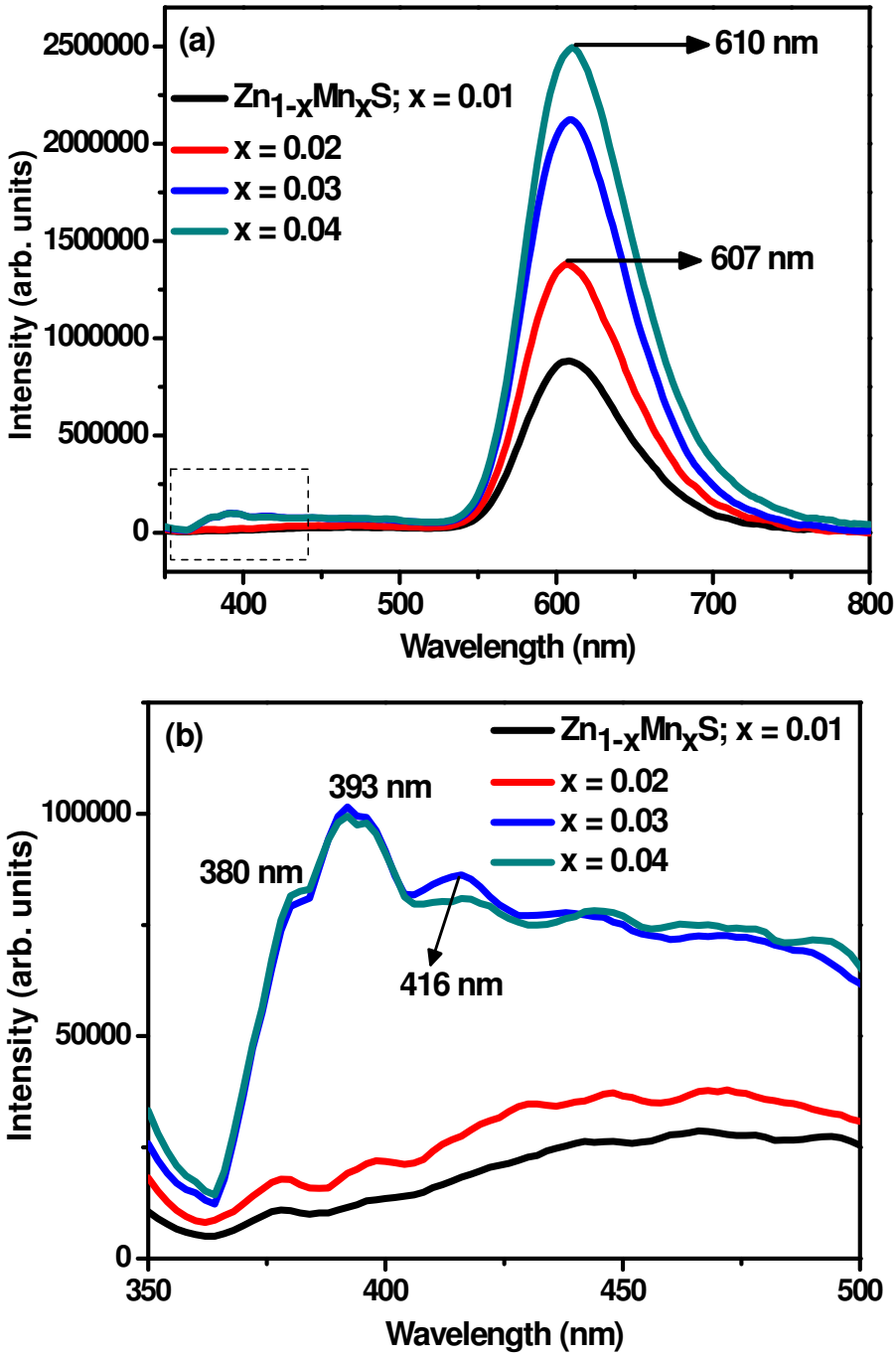

Figure 5.37: Photoluminescence emission spectra of $Zn_{1-x}Mn_xS$; x = 0.01, 0.02, 0.03 and 0.04 in the range (a) 350-800 nm and (b) 350-500 nm.

According to Koda et al., [40] when a metal ion occupies a certain position in a crystal, the crystal field strength affecting that particular ion increases. Therefore in case of Mn^{2+} doped ZnS, with increasing concentration of Mn^{2+} in ZnS, more Mn^{2+} ions enter into the ZnS host

and the space containing the ions becomes smaller resulting in increased crystal field. Hence, the transition energy between the $^4T_1$ and $^6A_1$ levels of Mn^{2+} decreases and it may cause a red shift in the PL spectra. Peng et al. [41] have suggested that the red shift of the peak is an effect of doping. When Mn^{2+} enters the ZnS host lattice, it introduces lattice distortion (due to difference in ionic radii of both ions) that would influence the energy level structure of ZnS. In the region from 350-500 as shown in Figure 5.37(b), there are emission peaks located at ~380, 393 and 416 nm in case of $Zn_{1-x}Mn_xS$; x = 0.03 and 0.04. Emission peaks located at ~380 and 393 nm are due to radiative recombination of interstitial sulfur. Emission peak observed at ~416 nm in case of $Zn_{1-x}Mn_xS$; x = 0.03 and 0.04 is attributed to interstitial zinc [42]. Peng et al. [41] have reported the enhancement in both the blue emission and the orange emission with increase in Mn^{2+} concentration. They have explained that the Mn^{2+} emission grows without the expense of host related emission. But the enhancement in host related emission is negligible as compared to that of impurity ions. As no well defined emission peak is observed in the blue region in case of $Zn_{1-x}Mn_xS$; x = 0.01 and 0.02, hence energy transfer between the ZnS host and the Mn^{2+} impurity in these particular samples is very efficient. Hence, these results show that the doped Mn^{2+} ions in ZnS are the major luminescent component and can drastically change emission properties of the host ZnS.

5.4.6 Photocatalytic studies

Photocatalytic degradation of crystal violet has been done to investigate the effect of Mn doping on photocatalytic activity of ZnS NPs. As a demonstration, spectral changes taking place in absorbance of dye during photochemical reaction catalysed by $Zn_{1-x}Mn_xS$; x = 0.01 and x=0.03 are shown in Figure 5.38(a-b) for the time interval of 60 min. The characteristic absorption peak of this dye at 590 nm has been selected to monitor the photocatalytic degradation of the dye. By Beer Lambert law, the decrease in concentration of dye is recorded at different intervals of time to measure degradation rate. Figure 5.39 shows the comparative degradation behaviour of dye catalysed with $Zn_{1-x}Mn_xS$; x = 0, 0.01, 0.02, 0.03 and 0.04 in terms of change in concentration with respect to the initial concentration. As can be seen in figure, $Zn_{1-x}Mn_xS$; x = 0.01 and 0.02 show lower degradation as compared to that of undoped ZnS. At higher doping concentrations i. e. in $Zn_{1-x}Mn_xS$; x = 0.03 and 0.04, photocatalytic degradation slightly increased but still less than that of undoped ZnS. $Zn_{1-x}Mn_xS$; x = 0.02 recorded the lowest degradation among all the doped samples.

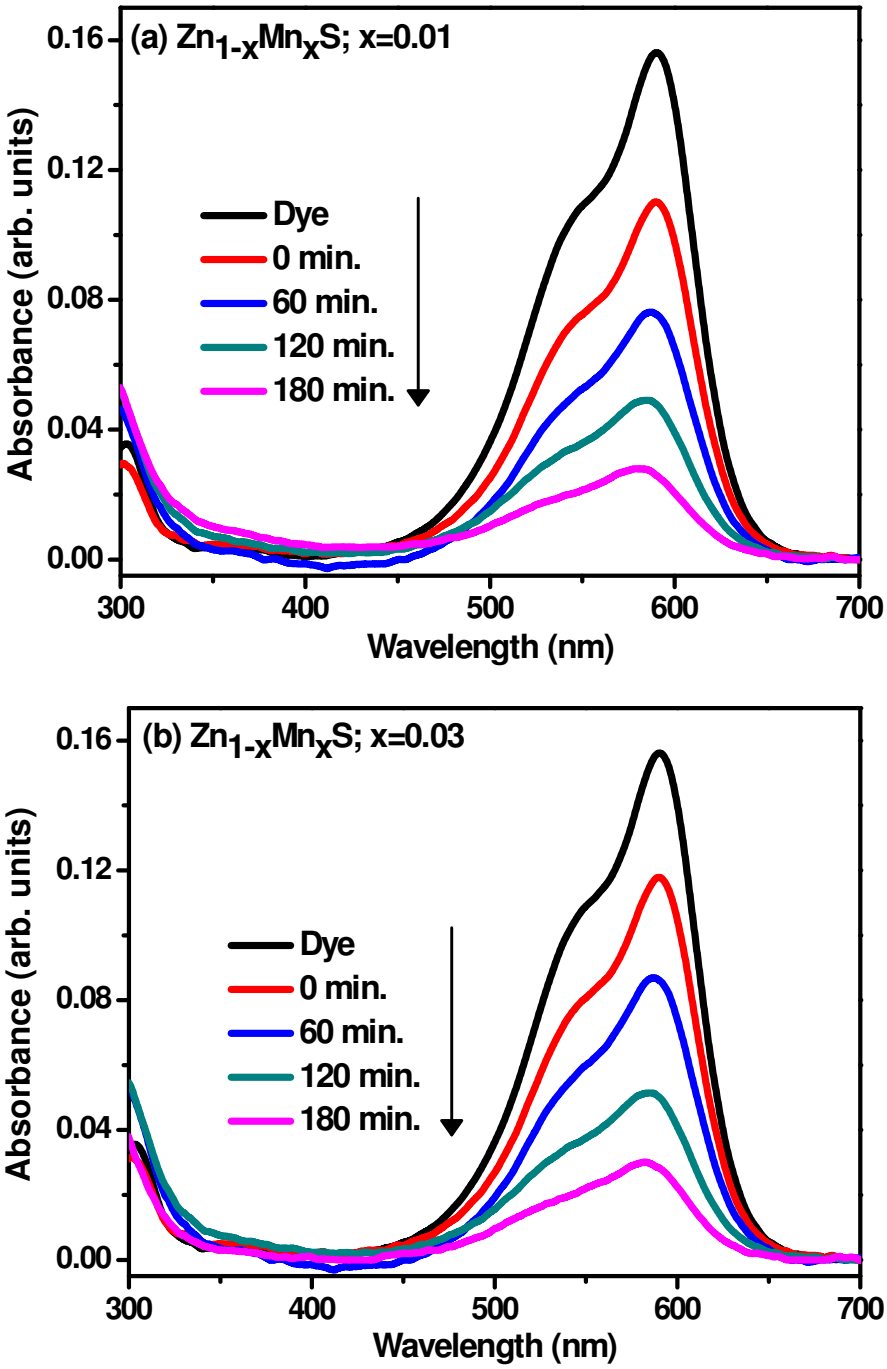

Figure 5.38: Absorbance spectra of crystal violet degraded in the presence of $Zn_{1-x}Mn_xS$ (a) x = 0.01, (b) x= 0.03.

Since, in this study, concentration of solute is very low (1mg/L), so Langmuir-Hinshelwood kinetics model [23] can be simplified to pseudo first order kinetic model equation.

$$ln\left(\frac{C_t}{C_0}\right) = kT \qquad (5.4)$$

where C_t is the concentration of dye after irradiation in selected time interval t, C_0 is the initial concentration of dye, k is the first order rate constant, and T is irradiation time.

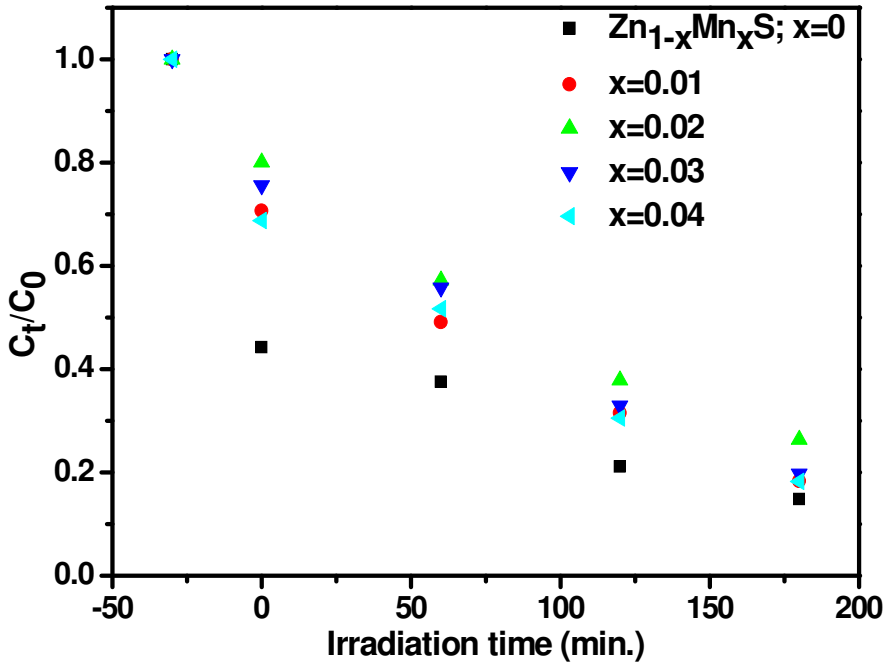

Figure 5.39: Variation of C_t/C_0 with irradiation time for $Zn_{1-x}Mn_xS$; x = 0, 0.01, 0.02, 0.03 and 0.04.

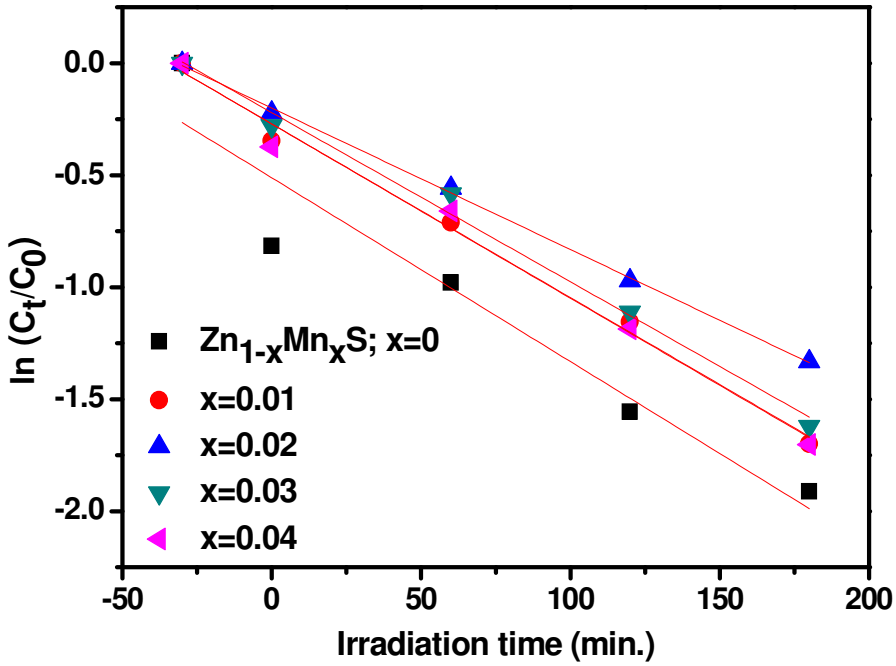

Figure 5.40: Plot between $\ln(C_t/C_0)$ and irradiation time to determine the value of rate constant k.

Figure 5.40 shows plot between $\ln(C_t/C_0)$ and irradiation time to determine the value of rate constant k. Degradation rate has come out to be minimum in case of $Zn_{1-x}Mn_xS$; x = 0.02 (k=0.0063 min^{-1}). The degradation percentage has been calculated as

$$\%D = \left(1 - \frac{C_t}{C_0}\right) \times 100 \qquad (5.5)$$

where C_t is the concentration of dye after irradiation in selected time interval, C_0 is the initial concentration of dye. As shown in Figure 5.41, % degradation in presence of undoped ZnS has been recorded maximum (85.35%) among all the photocatalysts.

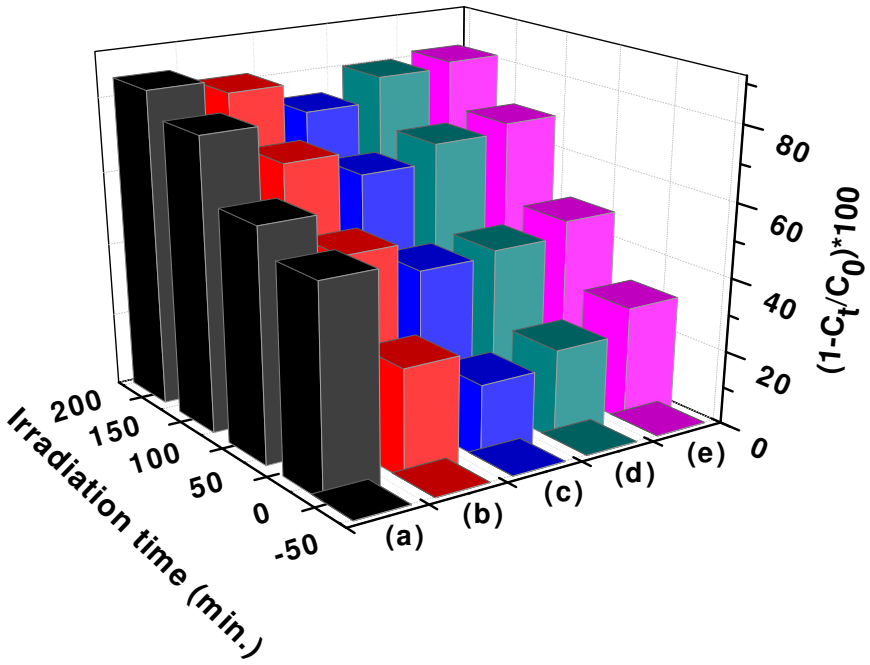

Figure 5.41: Degradation percentage of crystal violet in the presence of $Zn_{1-x}Mn_xS$ (a) x = 0, (b) 0.01, (c) 0.02, (d) 0.03 and (e) 0.04 at different irradiation times.

Table 5.9: First order rate constants for the photocatalytic degradation of crystal violet and corresponding percent degradation using $Zn_{1-x}Mn_xS$; x = 0, 0.01, 0.02, 0.03 and 0.04 as photocatalysts.

Photocatalyst	**Adj. R^2**	**k (min^{-1})**	**$(1-C_t/C_0)*100$**
$Zn_{1-x}Mn_xS$; x=0	0.89	0.0082	85.22
x=0.01	0.99	0.0078	81.72
x=0.02	0.99	0.0063	73.63
x=0.03	0.99	0.0075	80.25
x=0.04	0.98	0.0078	81.78

Degradation percentage values along with corresponding rate constants for all samples have been summarized in Table 5.9. The order of photo degradation rate is obtained as

$$Zn_{1-x}Mn_xS;\ x = 0 > x = 0.04 > x = 0.01 > x = 0.03 > x = 0.02$$

Decreased photocatalytic activity of Mn doped ZnS NPs is explained by the photoluminescence results. It is generally observed in Mn^{2+} doped ZnS that spin forbidden transition related to Mn^{2+} states give rise to sharp intense peak in orange red region. This transition happens due to efficient transfer of energy from host ZnS to Mn^{2+} ion which

implies that efficient radiative recombination has been resulted from this transition. However, in a photocatalytic process, maximum charge separation is needed to make the charge carriers available to participate in the processes which are taking place on the surface of semiconductor photocatalyst. In photoluminescence, efforts are being made to make the radiative recombination dominant to achieve high quantum yield. In this way, photoluminescence and photocatalytic processes are different. When semiconductor is photoexcited, electrons are promoted to conduction band leaving holes in valence band. These charge carriers may recombine (radiatively or non radiatively) or may be trapped in centres created by dopant ions or intrinsic defects. These trapped charge carriers may also recombine or may be transported to the surface to participate in the reactions which are occurring on the surface of photocatalyst. As in case of $Zn_{1-x}Mn_xS$; x =0.01 and 0.02, there is efficient energy transfer from the host ZnS to Mn^{2+} ion, hence no host related peak is observed. Due to the efficient transfer of energy resulting in radiative recombination, there are no charge carriers available which can participate in photocatalytic process. When ZnS is photoexcited, the electrons jump to conduction band and are quickly transported to the impurity states created by Mn^{2+} where due to hybridization of sp orbitals of ZnS and d orbital of Mn^{2+}, spin forbidden transition takes place (discussed in section 5.4.5) resulting in orange-red emission. The more efficient this transfer will be, the less charge carriers will be available for photocatalytic process. Hence photocatalytic activity is decreased in $Zn_{1-x}Mn_xS$; x =0.01 and 0.02. However, at higher dopant concentrations ($Zn_{1-x}Mn_xS$; x =0.03 and 0.04), ZnS related emission peaks have appeared indicating less efficient transfer from host to impurity ion. Hence some charge carriers will be available for the degradation of dye. That is why a slight increase in photocatalytic activity in presence of $Zn_{1-x}Mn_xS$; x =0.03 and 0.04 has been observed. Very fewer reports are available which demonstrate the effect of Mn^{2+} doping on photocatalytic activity of ZnS NPs. The presented results are somewhat similar to that observed by Ashkarran [43]. In his results, photocatalytic activity is observed to be absent where photoluminescence is observed. These results indicate that although Mn^{2+} ion can improve the overall quantum efficiency of ZnS in visible region but can deteriorate its photocatalytic activity.

5.5 Ag_2S modified ZnS

5.5.1 Synthesis

$Zn_{1-x}Ag_xS$; x = 0, 0.01, 0.02, 0.03 and 0.04 NPs were synthesized using simple chemical precipitation route. The details of the synthesis procedure have been given in chapter 3.

During synthesis, some observations were made which needs to be discussed in this section. When capping agent (thioglycerol) was added to the homogeneously stirred solution of $Zn(ac)_2$ and $AgNO_3$, some complex was formed. In the other experiments i. e. in the synthesis of Cu, Ni and Mn doped ZnS NPs, no such complex formation has been observed (the solution was transparent as expected). Hence in this case, it is anticipated that this complex has formed by the reaction of Ag^{1+} ions with RSH (molecular formula of thioglycerol is $C_3H_8O_2S$) alongwith other reactions which are taking place simultaneously. The complex has formed by the reaction

$$Ag^{1+} + RSH \rightarrow RSAg + H^{+} \quad (5.11)$$

$$2Ag^{1+} + S^{2-} \rightarrow Ag_2S \quad (5.12)$$

$$Zn^{2+} + S^{2-} \rightarrow ZnS \quad (5.13)$$

The formation of this complex has also been observed by Chen et al. [44] in the preparation of thiol-derivatized AgI NPs. In their work, RSAg complex was formed as a side product and XRD analysis revealed amorphous nature of this complex. It could not be removed in their procedure because of its small K_{sp} value in water. In another work, in the method to synthesize CdS NPs, cadmium thiolate complex has been successfully separated from CdS NPs since it is soluble in high pH (=11) solution [45]. In the work of Chen et al. [44], RSAg was also found to be soluble in high pH solution, but Ag_2O was irreversibly formed. However, this complex was reduced by increasing the $[I^-]/[RSH]$ ratio. They have obtained almost pure thiol covered AgI NPs with a particle size of 15 nm with $[I^-]/[RSH]$ ratio of 9. However, in the present case, ratio of S^{2-} and RSH is very large (~48 times) and constant in all the samples. Hence the reaction was further allowed to proceed similar to that of other doped ZnS NPs. The results of as synthesized samples are discussed below. However, the investigation of exact value of RSAg complex formed is beyond the scope of the present study.

5.5.2 XRD and EDX studies

Figure 5.42 shows the XRD patterns of $Zn_{1-x}Ag_xS$; x = 0, 0.01, 0.02, 0.03 and 0.04. At lower $AgNO_3$ content i. e. upto x=0.02, the samples exhibit cubic zinc blende phase with no impurity phase. Diffraction peaks from (111), (220) and (311) planes match well with those of the β-ZnS (cubic) reported in the ICDD card no.80-0020. Broadening of diffraction peaks indicates formation of nanosize ZnS [7]. However, in $Zn_{1-x}Ag_xS$; x = 0.02, sharpness in

diffraction peaks is observed which indicates the increase in crystallite size due to the addition of $AgNO_3$.

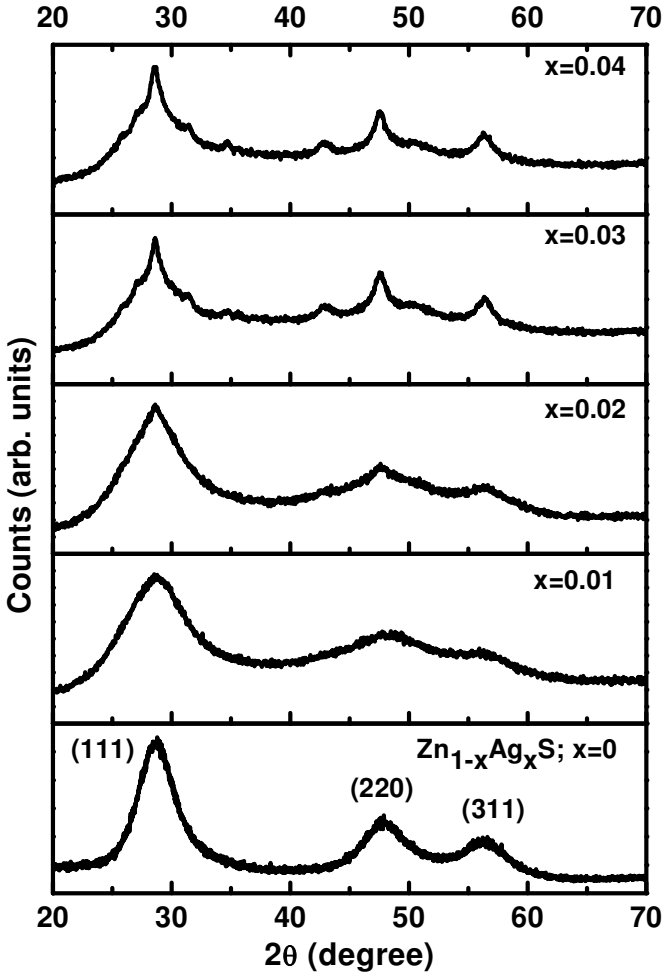

Figure 5.42: XRD patterns of $Zn_{1-x}Ag_xS$; x = 0, 0.01, 0.02, 0.03 and 0.04 in the range 20°-70°.

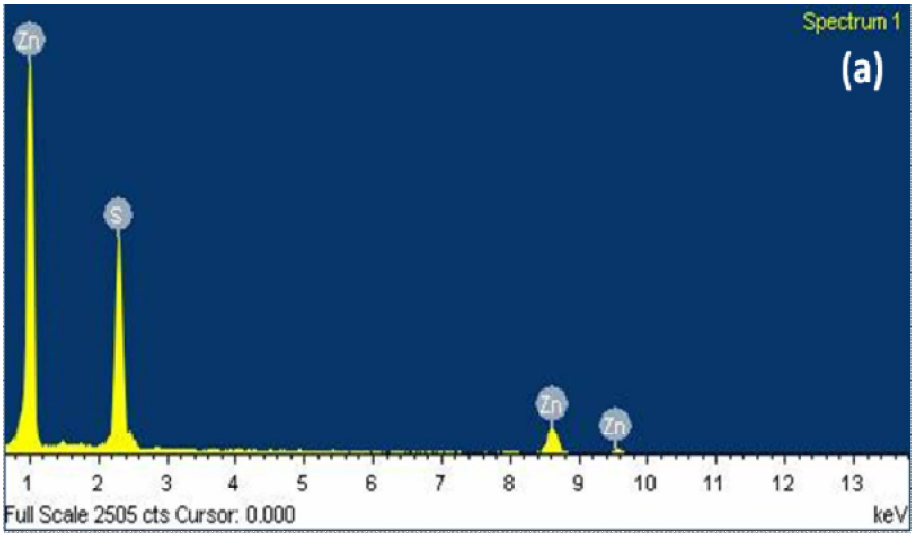

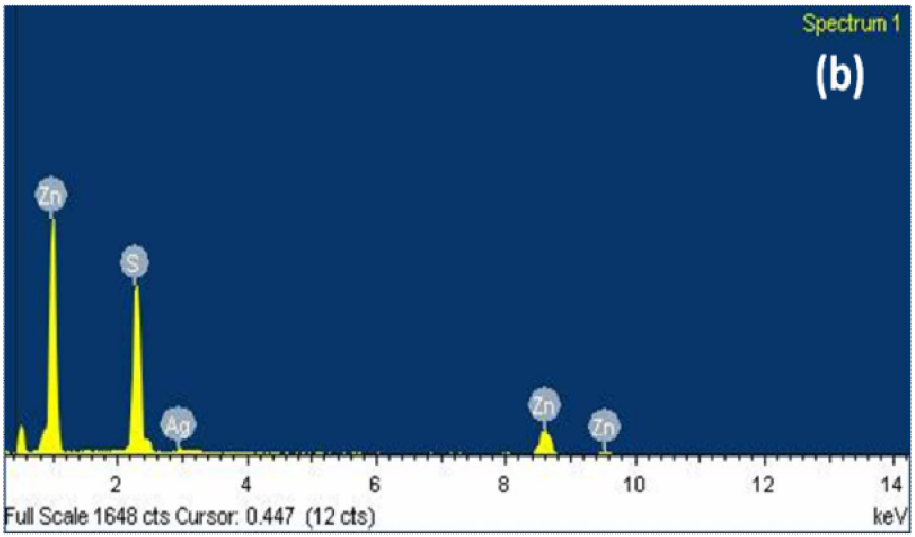
Spectrum 1
(b)
Zn
S
Ag
Zn
Zn
2
4
6
8
10
12
14
Full Scale 1648 cts Cursor: 0.447 (12 cts)
keV

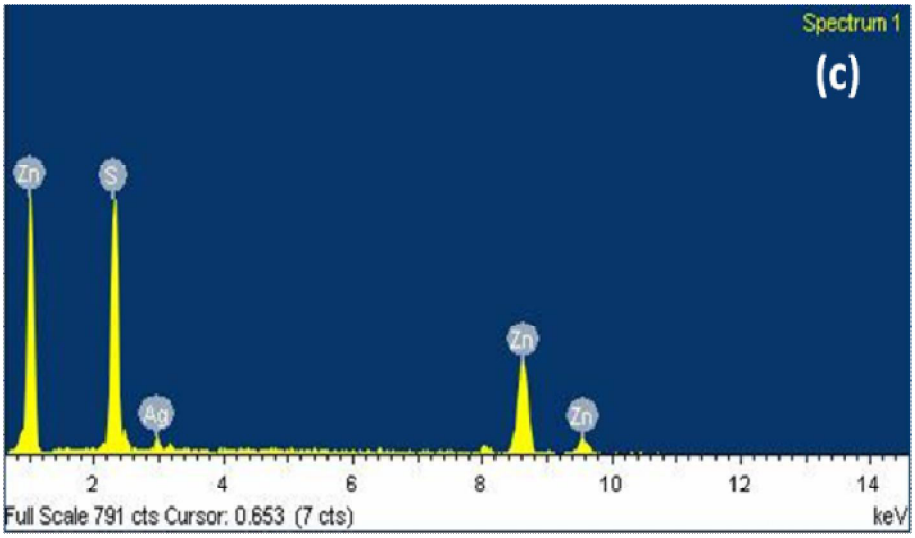
Spectrum 1
(c)
Zn
S
Ag
Zn
Zn
2
4
6
8
10
12
14
Full Scale 791 cts Cursor: 0.653 (7 cts)
keV

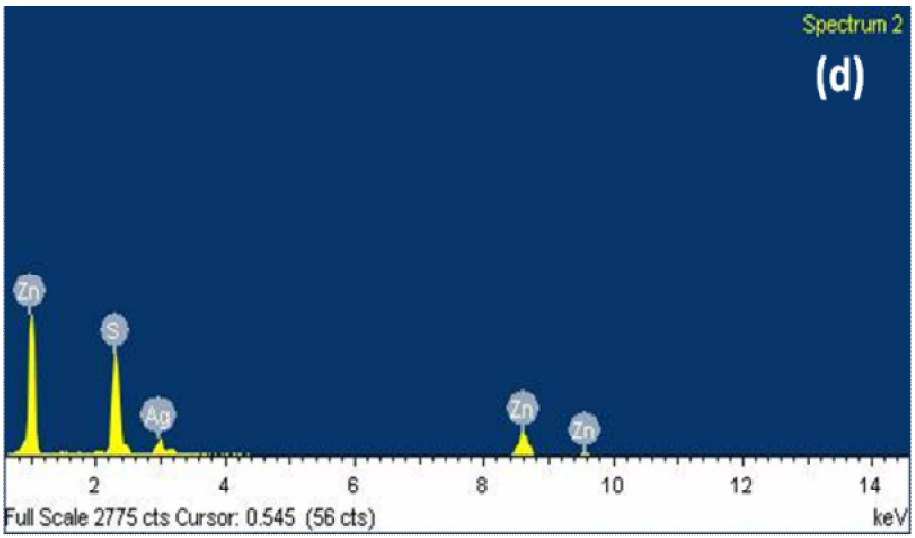
Spectrum 2
(d)
Zn
S
Ag
Zn
Zn
2
4
6
8
10
12
14
Full Scale 2775 cts Cursor: 0.545 (56 cts)
keV

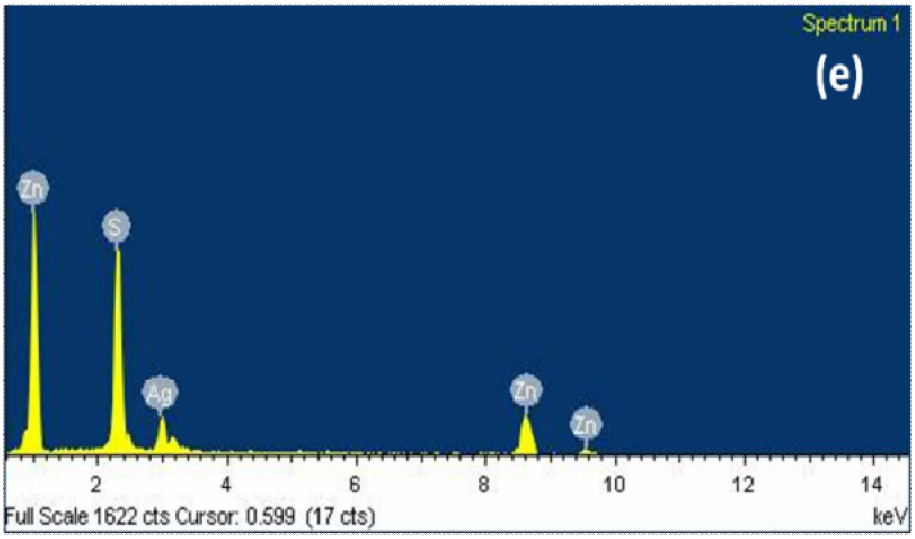

Figure 5.43: EDX patterns of $Zn_{1-x}Ag_xS$; (a) x = 0, (b) x=0.01, (c) x=0.02, (d) x=0.03 and (e) x=0.04.

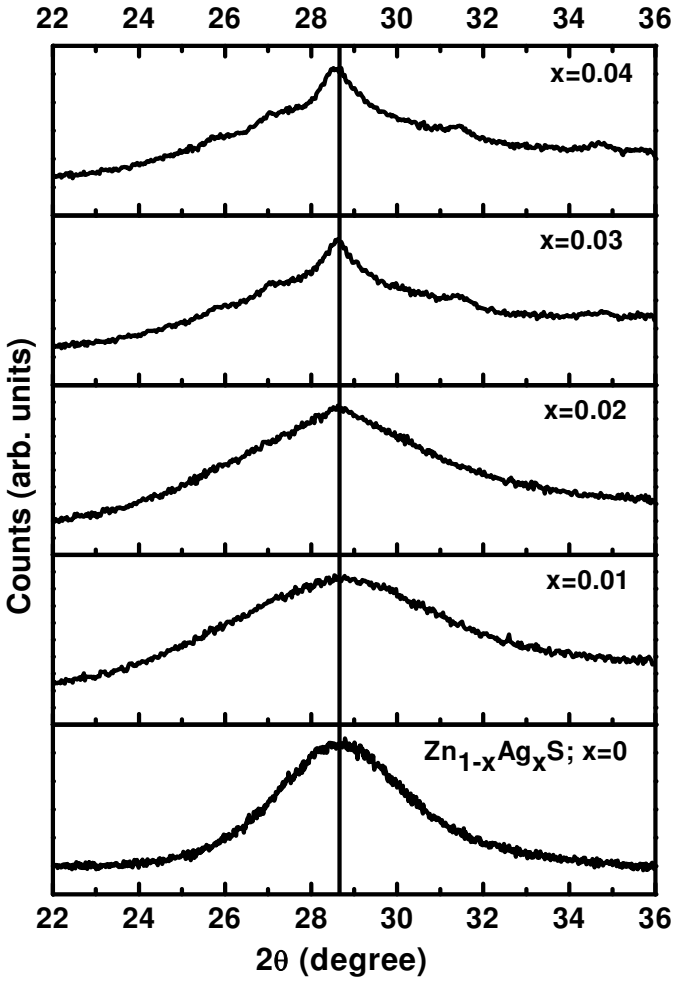

Figure 5.44: XRD patterns of $Zn_{1-x}Ag_xS$; x = 0, 0.01, 0.02, 0.03 and 0.04 in the range 22°-38°.

At higher $AgNO_3$ content i. e. in $Zn_{1-x}Ag_xS$; x = 0.03 and 0.04, additional peaks are observed which match well with those of monoclinic Ag_2S (ICDD card no. 14-0072). The presence of Ag in prepared samples has also been confirmed through Energy Dispersive X-ray (EDX) spectroscopy analysis. EDX patterns for $Zn_{1-x}Ag_xS$; x = 0, 0.01, 0.02, 0.03 and 0.04 are shown in Figure 5.43(a-e). Crystallite size of NPs has been calculated by following Scherrer's equation

$$t = \frac{k\lambda}{\beta\cos\theta} \qquad (5.1)$$

where k = 0.9, t is the crystallite size (Å), λ(Å), the wavelength of Cu Kα radiation and β is the corrected half width of the diffraction peak [8]. Crystallite size for all the samples is in the range of 1.9-4.0 nm. A careful comparison of diffraction peak in the range 2θ = 22°-38° for all samples (Figure 5.44) indicates that no appreciable peak shift was observed in any sample and hence possibility of doping of Ag^+ ion in ZnS has been ruled out.

5.5.3 TEM analysis

Figure 5.45 shows HRTEM micrograph of $Zn_{1-x}Ag_xS$; x=0.01. Lattice fringing is clearly observed in the figure. The value of d spacing came out to be 0.32 nm which corresponds to (111) plane of cubic ZnS. Images were taken at different sites of interests and no lattice spacing other than 0.32 nm was observed. This suggests that Ag_2S has not formed and the entire amount of thioglycerol has been utilized in forming RSAg complex.

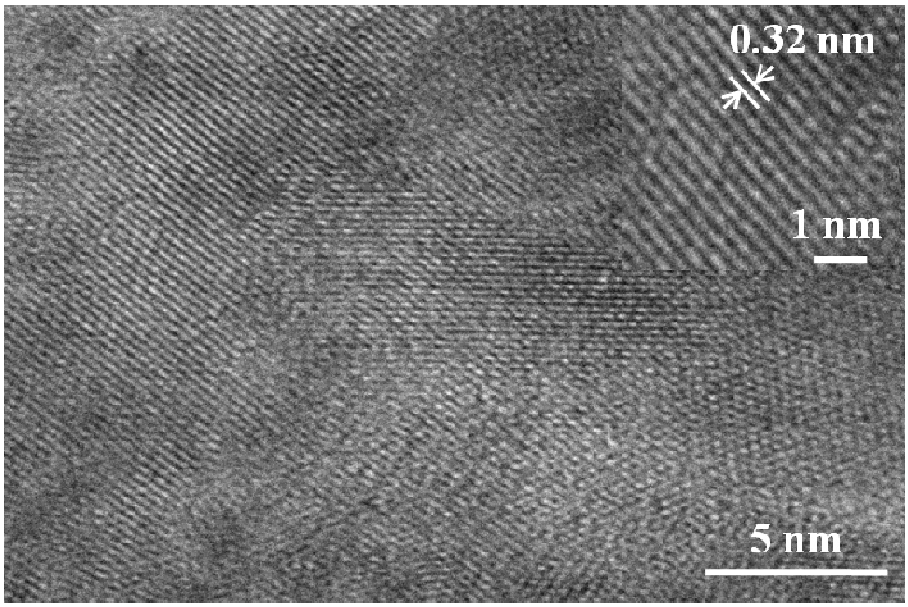

Figure 5.45: HRTEM image of thioglycerol capped $Zn_{1-x}Ag_xS$; x = 0.01. Inset shows the portion of same image at 1 nm scale.

However in $Zn_{1-x}Ag_xS$; x=0.02, lattice spacing of 0.26 nm has been observed which suggests that some amount of Ag_2S is present in the sample. Figure 5.46(a) shows that the particles of $Zn_{1-x}Ag_xS$; x=0.02 are nearly spherical. The NPs have grown due to overnight ageing and also the sample was prepared at 80 °C. The two particles which have been observed in Figure 5.46(a) are not of same size i. e. one particle is a bit larger than that of other. This suggests that the NPs exhibit polydispersity. Amorphous layer corresponding to thioglycerol (or we can say RSAg complex) is clearly visible around the NPs surface. Figure 5.46 (c) shows the HRTEM image of the same sample. Lattice fringing is clearly observed in the image indicating crystalline nature of the sample.

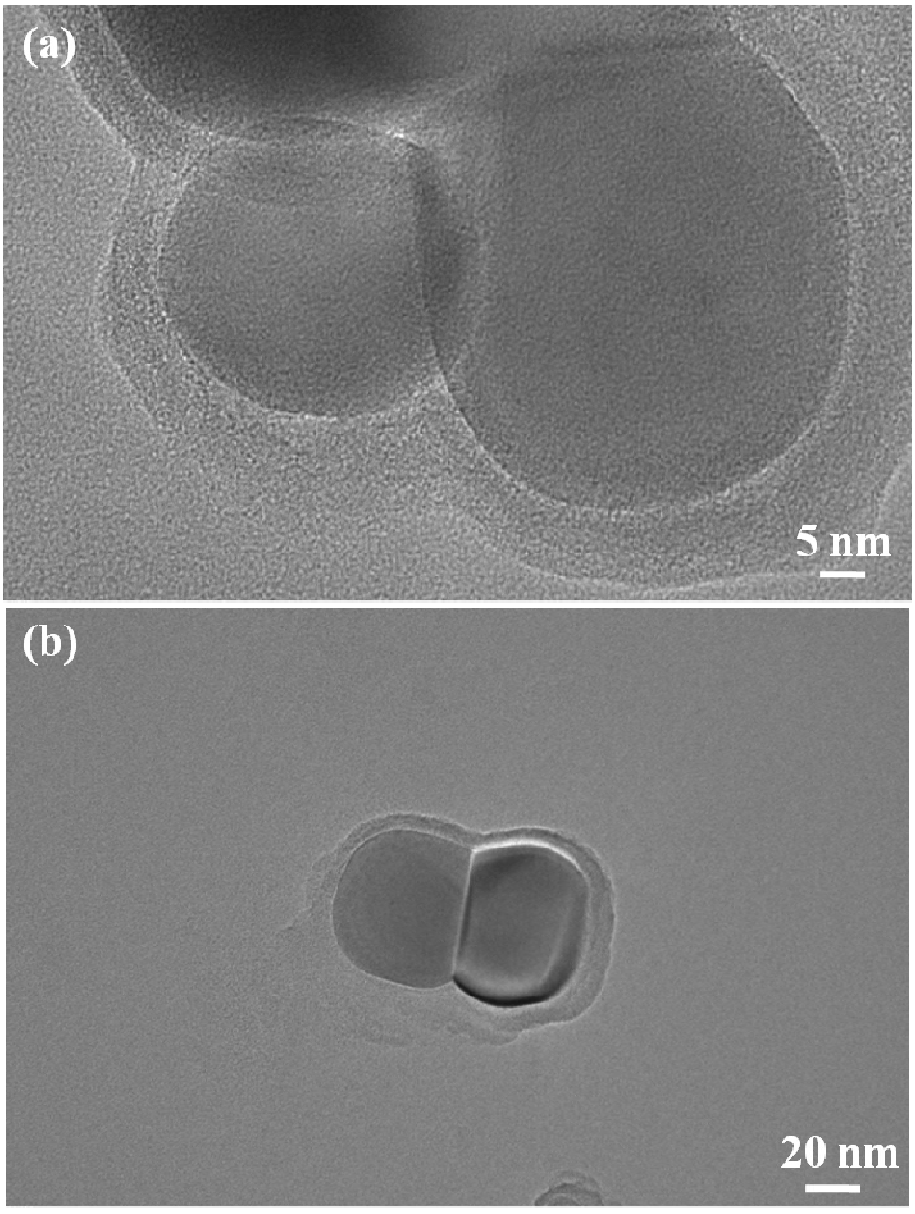

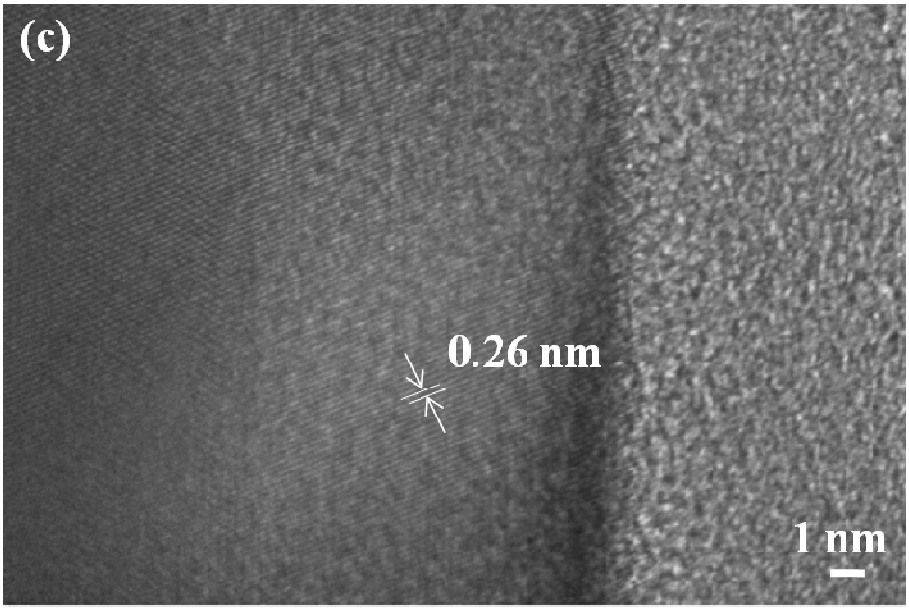

Figure 5.46: (a-b) TEM images of thioglycerol capped $Zn_{1-x}Ag_xS$; x = 0.02 (c) HRTEM image of the same sample.

Fringing has been measured by Axio Vision Rel. 4.8 software and the value has come out to be 0.26 nm which corresponds to $(\bar{1}21)$ plane of monoclinic Ag_2S. From this observation, it is confirmed that alongwith complex formation, Ag_2S has also been formed in $Zn_{1-x}Ag_xS$; x=0.02. Figure 5.47(a-b) shows HRTEM images of $Zn_{1-x}Ag_xS$; x=0.03. Two types of fringing (0.32 nm and 0.26 nm) is also observed in this sample which is similar to that of $Zn_{1-x}Ag_xS$; x=0.02. This suggests that along with ZnS formation, Ag_2S phase has formed which has also been confirmed from XRD analysis.

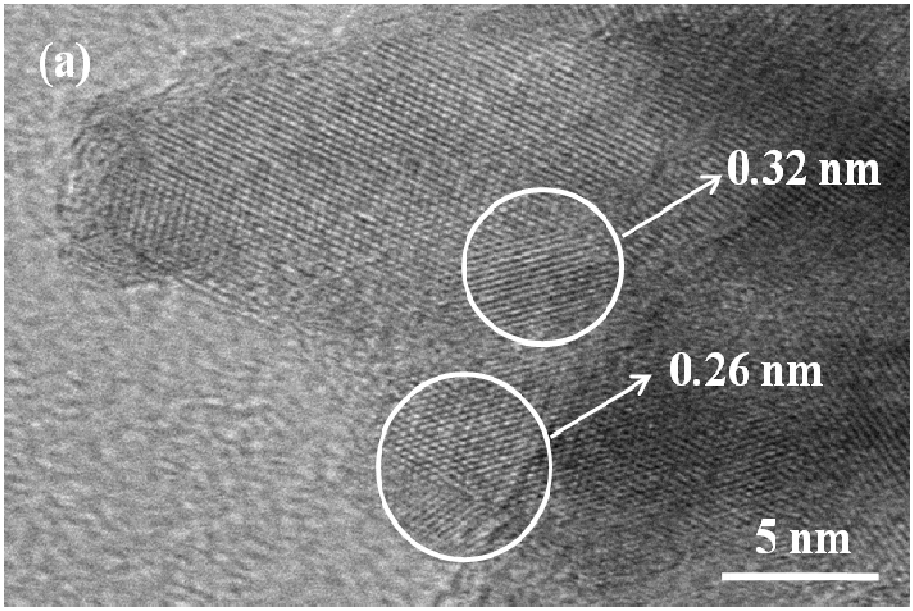

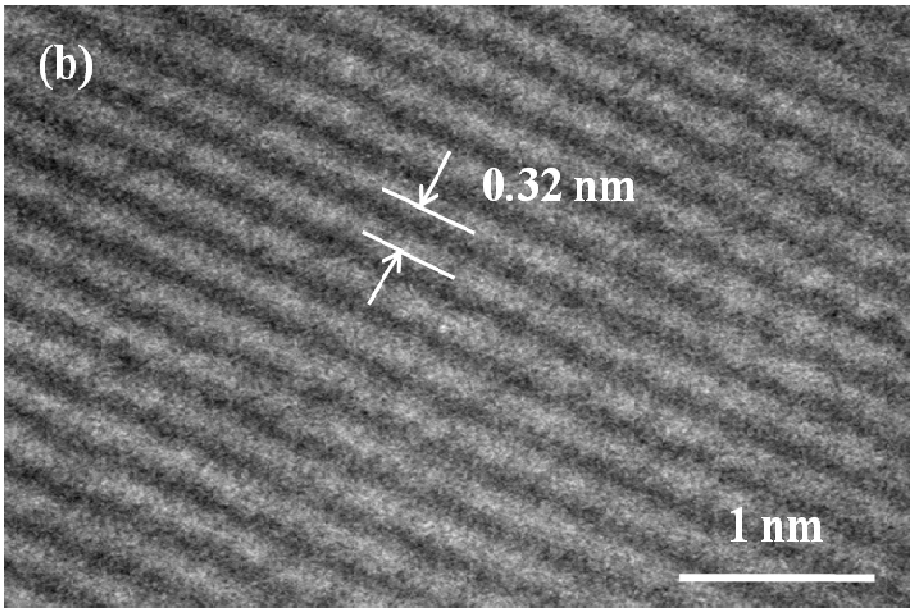

Figure 5.47: (a-b) HRTEM images of thioglycerol capped $Zn_{1-x}Ag_xS$; x = 0.03.

5.5.4 FTIR Analysis

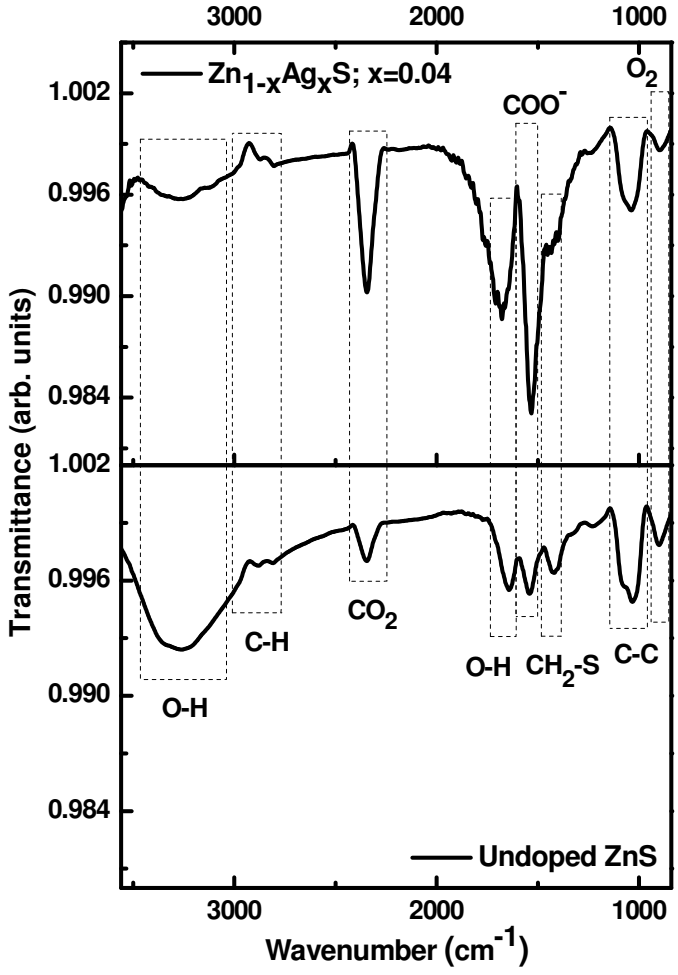

Figure 5.48: FTIR spectra of $Zn_{1-x}Ag_xS$; x = 0, 0.04.

To investigate various functional groups present in TG capped ZnS and $Zn_{1-x}Ag_xS$, FTIR studies have been done. Figure 5.48 represents FTIR spectra of $Zn_{1-x}Ag_xS$; x = 0, 0.04. As can be seen in figure, both samples exhibit almost similar IR spectra. Therefore, we can say that $AgNO_3$ has no profound effect on IR response of as prepared samples. The peak positions for both samples alongwith peak assignments are given in Table 5.10. Pure TG exhibit S-H vibration band at 2557 cm^{-1}. This peak was not observed in both samples. It is attributed to the fact that the thiolate functions of the TG ligands are connected to the Zn^{2+} sites on the ZnS nanocrystals surfaces which confirm the successful capping of thioglycerol on ZnS surface [9].

Table 5.10: Peak assignment of various bonds in thioglycerol capped $Zn_{1-x}Ag_xS$; x = 0, 0.04.

Peak Position (cm^{-1}) $Zn_{1-x}Ag_xS$		**Peak assignment**
x=0	**x=0.04**	
3265	3257	O-H stretching [9]
2885	2872	C-H symmetrical stretching [9]
2810	2804	C-H asymmetrical stretching [9]
2346	2342	Interference from CO_2 [10]
1642	1679	O-H bending [9]
1540	1531	COO^- [11]
1416	1430	$–CH_2–S$ [12]
1033	1038	C–C stretch [12]
902	898	O_2 stretching and bending [13]

5.5.5 UV-Vis studies

To investigate the effect of the addition of $AgNO_3$ on optical response of ZnS, UV-Vis studies have been performed for all samples in powder form. The relation between reflectance R and absorption coefficient α as given by Kubelka-Munk method [14] is

$$F(R) = \frac{(1-R)^2}{2R} = \frac{\alpha}{S} \qquad (5.2)$$

where F(R) is the Kubelka-Munk function, S is the scattering coefficient. From the above equation, the Kubelka-Munk function F(R) can be assumed to be proportional to α [14]. Absorption spectra for all samples plotted by employing the above equation are given in Figure 5.49. It is clearly seen in the figure that absorbance of $Zn_{1-x}Ag_xS$; x = 0.01, 0.02, 0.03 and 0.04 is significantly increased in near visible region as compared to that of undoped ZnS. In case of $Zn_{1-x}Ag_xS$; x = 0.01 and 0.02, absorbance peak in UV region is sharply defined

indicating that no additional phase has formed. Complex formed during the synthesis has affected the absorption spectra which causes a decrease in absorbance in UV region indicating that this complex has hindered the penetration of light into ZnS. However, absorption is significantly reduced in case of $Zn_{1-x}Ag_xS$; x = 0.03 and 0.04. At higher $AgNO_3$ content, in addition to RSAg complex, sufficient amount of Ag_2S has also formed. Due to its smaller band gap (0.9 to 1.05 eV), Ag_2S absorbs visible light. In case of $Zn_{1-x}Ag_xS$; x = 0.03 and 0.04, due to large difference in solubility of Ag_2S ($K_{sp} = 6.3\times10^{-50}$) and ZnS ($2.5\times10^{-22}$), Ag_2S has formed as confirmed from XRD analysis of these samples. Hence layer of Ag_2S particles formed on the surface of ZnS inhibit direct penetration of UV light into ZnS thereby reducing the absorption in UV region. From this result, it is further confirmed that Ag_2S has been loaded on the surface of ZnS (otherwise separate peak may have been appeared corresponding to Ag_2S in visible region). As ZnS is not directly exposed to UV light, hence decrease in absorption in UV region is observed for $Zn_{1-x}Ag_xS$; x = 0.03 and 0.04. However, absorbance has increased in the near visible region due to Ag_2S. Also, with increase in $AgNO_3$ content, absorption edge is red shifted indicating narrowing of band gap. Broadening of absorbance peak incase of $Zn_{1-x}Ag_xS$; x = 0.03 and 0.04 also indicate increased polydispersity in these samples.

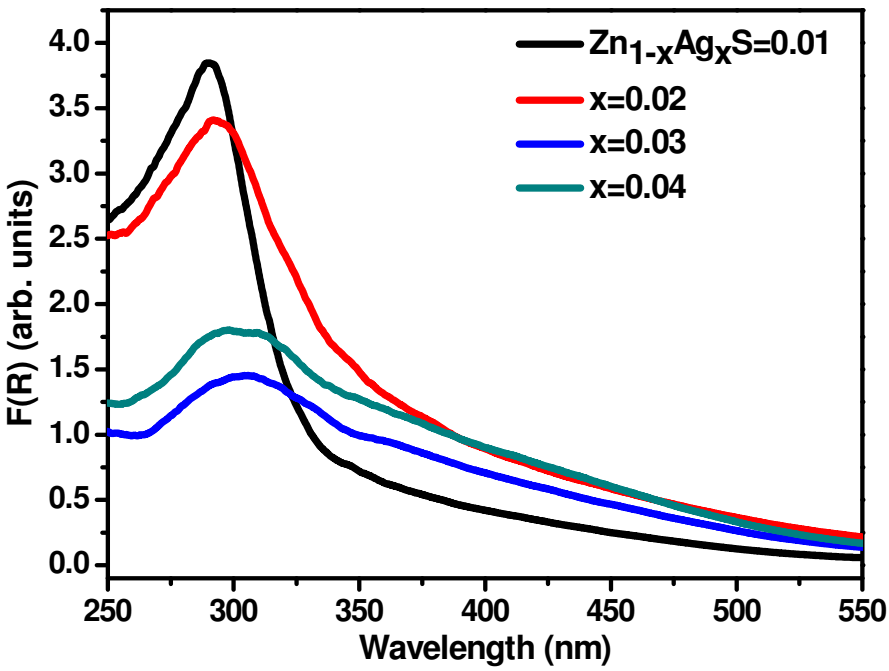

Figure 5.49: Absorption spectra of $Zn_{1-x}Ag_xS$; x = 0.01, 0.02, 0.03 and 0.04 plotted by Kubelka Munk method.

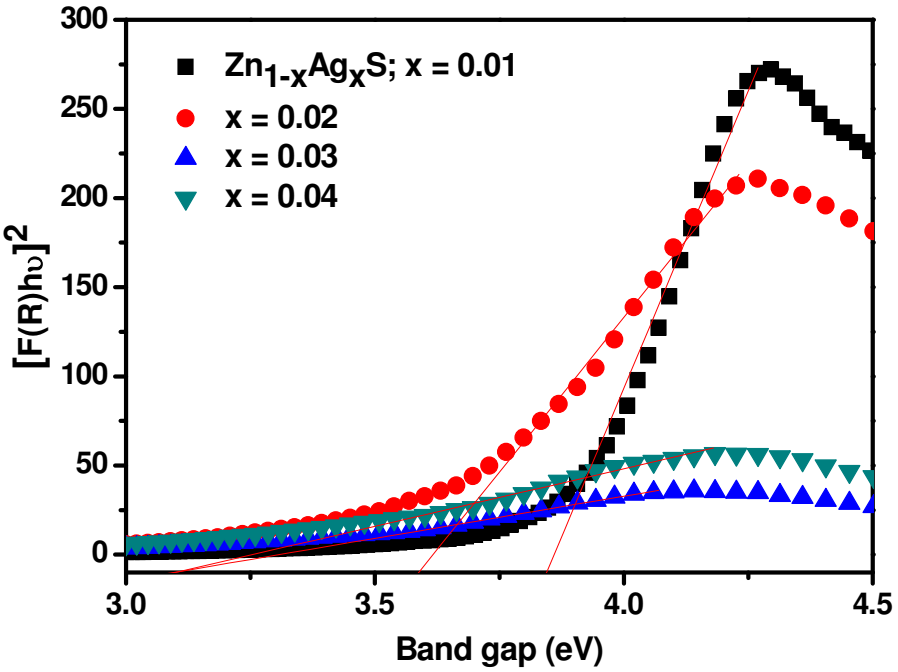

Figure 5.50: Tauc plots for $Zn_{1-x}Ag_xS$; x = 0.01, 0.02, 0.03 and 0.04 to determine band gap.

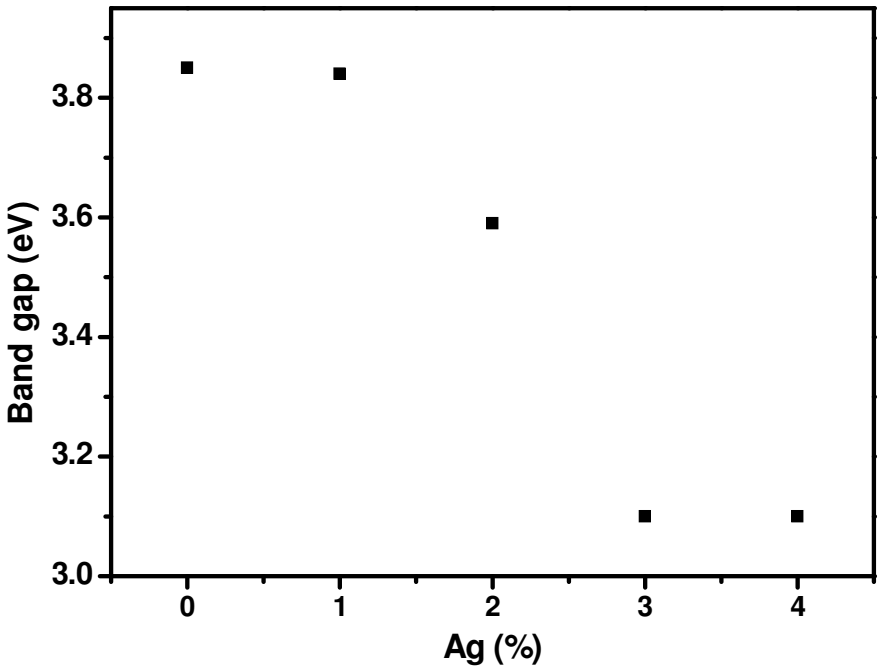

Figure 5.51: Variation in band gap of ZnS with the addition of $AgNO_3$.

The relation between the incident photon energy (hυ) and the absorption coefficient (α) or F(R) is given by [14]

$$[F(R)h\upsilon]^{1/n} = A(h\upsilon - E_g) \quad (5.3)$$

where A is a constant and E_g is the band gap of the material and the exponent n depends on the type of the transition i.e. 2, 3, 1/2, 1/3 values corresponding to indirect allowed, indirect forbidden, direct allowed and direct forbidden transitions.

As shown in the Figure 5.50, square of the absorbed energy (F(R)hυ) have been plotted against photon energy (hυ) to determine the energy for direct gap transition. Band gap energies for all samples have been determined by extrapolating the straight portion of the graph on hυ axis at F(R)=0. Variation in band gap of ZnS with $AgNO_3$ content has been described in Figure 5.51. Band gap values along with corresponding absorption wavelengths are given in Table 5.11.

Table 5.11: Calculated band gap values and corresponding absorption wavelengths of $Zn_{1-x}Ag_xS$; x = 0, 0.01, 0.02, 0.03 and 0.04.

$Zn_{1-x}Ag_xS$	Band gap (eV)	Absorption wavelength (nm)
x=0	3.85	322.60
x=0.01	3.84	323.53
x=0.02	3.59	346.06
x=0.03	3.10	400.76
x=0.04	3.10	400.76

5.5.6 Photoluminescence studies

As photoluminescence (PL) studies of an optically active material provides valuable information about the defects presents on its surface, hence PL emission spectra of all the prepared samples have been recorded at fixed excitation wavelength; λ_{exc}=300 nm. Figure 5.52 shows the emission spectra of $Zn_{1-x}Ag_xS$; x = 0.01, 0.02, 0.03 and 0.04. As can be seen in the figure, all samples have reduced emission intensity as compared to that of unmodified ZnS sample which show emission in UV-blue region (discussed in chapter 4). Contrary to unmodified ZnS, all Ag_2S modified ZnS NPs show yellow emission accompanied by red shift at higher Ag_2S content in the system. The emission intensity has reached to its minimum in $Zn_{1-x}Ag_xS$; x = 0.02. Further, with increase in Ag_2S content i. e. in $Zn_{1-x}Ag_xS$; x = 0.03 and 0.04, emission intensity has slightly increased. The emission peak observed at ~ 577.23 nm in case of $Zn_{1-x}Ag_xS$; x = 0.01 has shifted to ~ 588.97 nm for $Zn_{1-x}Ag_xS$; x = 0.04 which directly indicates the effect of RSAg and Ag_2S on emission properties of ZnS. Similar red shift has been observed in Ni^{2+} doped ZnS samples which is attributed to the formation of Ni^{2+} centres in the host ZnS lattice. The observed trend in emission intensity can be explained by the role

of Ag ions in ZnS. It is possible that in case of $Zn_{1-x}Ag_xS$; x = 0.01, 0.02, RSAg complex is responsible for the luminescence quenching of ZnS.

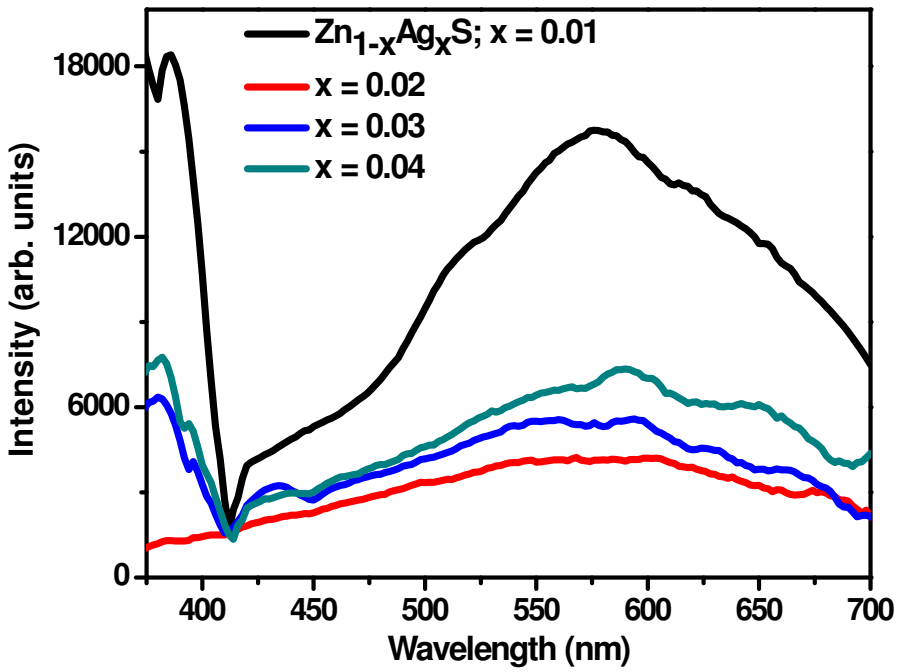

Figure 5.52: Photoluminescence emission spectra of $Zn_{1-x}Ag_xS$; x = 0.01, 0.02, 0.03 and 0.04.

This complex may have inhibited the direct penetration of light into ZnS thereby reducing emission intensity as compared to that of undoped ZnS. As the solubility product constant of Ag_2S (K_{sp} = 6.3×10^{-50}) is very small as compared to that of ZnS (2.5×10^{-22}), hence it is expected that at higher concentration of $AgNO_3$, in addition to complex formation, Ag_2S has also formed on the surface of ZnS. As Ag_2S content is increased in the system, the corresponding layer becomes thick which partially or wholly shields the surface of ZnS and the emission intensity increases depending upon the content of Ag_2S. Increase in emission intensity may also be due to the passivation of the core surface and the elimination of the surface trap states. Chaudhuri et al. [46] have reported that in case of Ag_2S-ZnS core shell particles, at higher content of shell material, the external shell thickness is sufficiently large. Therefore, inspite of mixing between two layers at the interface, the external shell layer is sufficiently thick to passivate the emission of the core. As a result, QY and stability has increased. It may be noted that the emission peak in $Zn_{1-x}Ag_xS$; x = 0.03, 0.04 has also got broadened. In particular, line width is determined by the product of ion density and the screening length in the luminescent region [22]. Therefore a large line width is expected from a region having a high charge density and large screening length. Hence it is expected that in

case of $Zn_{1-x}Ag_xS$; x = 0.03, 0.04, more charge carriers are available for a sufficient time which is beneficial in photocatalytic process. Chaudhuri et al. [46] have prepared the double-shell hollow ZnS-Ag_2S NPs. The light emission properties of hollow Ag_2S/ZnS (Ag_2S-core and ZnS-shell) have come out to be maximum (39%) as compared to those of hollow ZnS/Ag_2S (21%) or pure ZnS NPs (14%). They have reported that these properties highly depend on the external ZnS layer thickness. Xu et al. [47] have synthesized flower-like ZnO-Ag_2O composites via simple chemical precipitation route. It has been reported that the band edge emission intensity of pure ZnO is drastically quenched by the increased loading of Ag_2O particles. This indicates the existence of a direct interaction between Ag_2O and ZnO enhancing the non-radiative relaxation of excitons formed in ZnO. The results have demonstrated that the Ag_2O particles block both direct and trap-related charge carrier recombination pathways. This is due to the fact that Ag_2O particles on the ZnO surface can extract electrons from the conduction band of ZnO and act as a sink which can store and shuttle photogenerated electrons.

5.5.7 Photocatalytic studies

Photocatalytic degradation of crystal violet has been done to demonstrate the photocatalytic activity of $Zn_{1-x}Ag_xS$; x = 0.01, 0.02, 0.03 and 0.04 NPs. Spectral changes taking place in absorbance of dye during photochemical reaction catalysed by $Zn_{1-x}Ag_xS$; x = 0.03 and x=0.04 are shown in Figure 5.53(a-b) in time interval of 60 min.

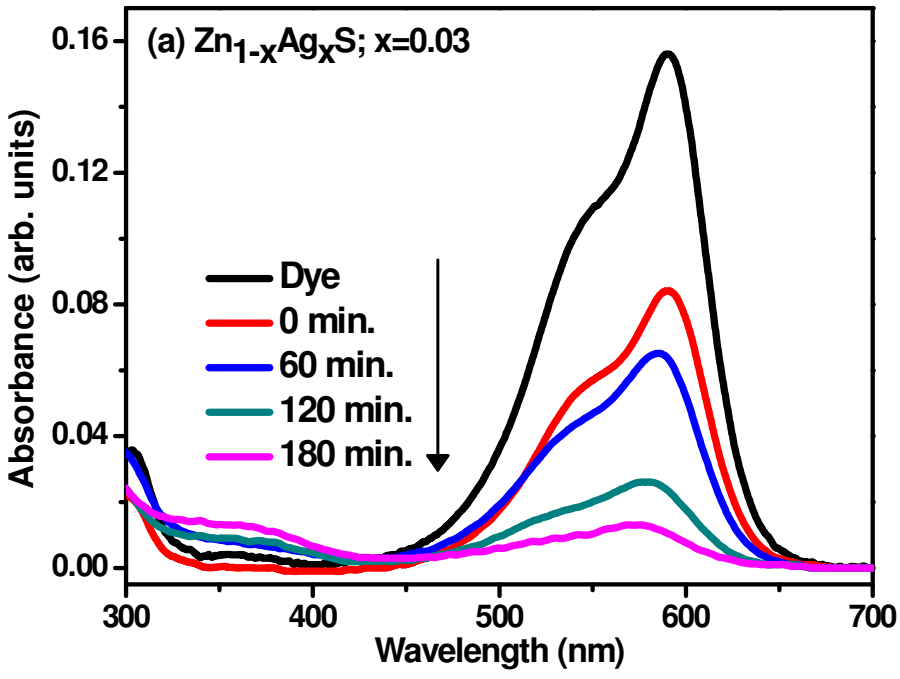

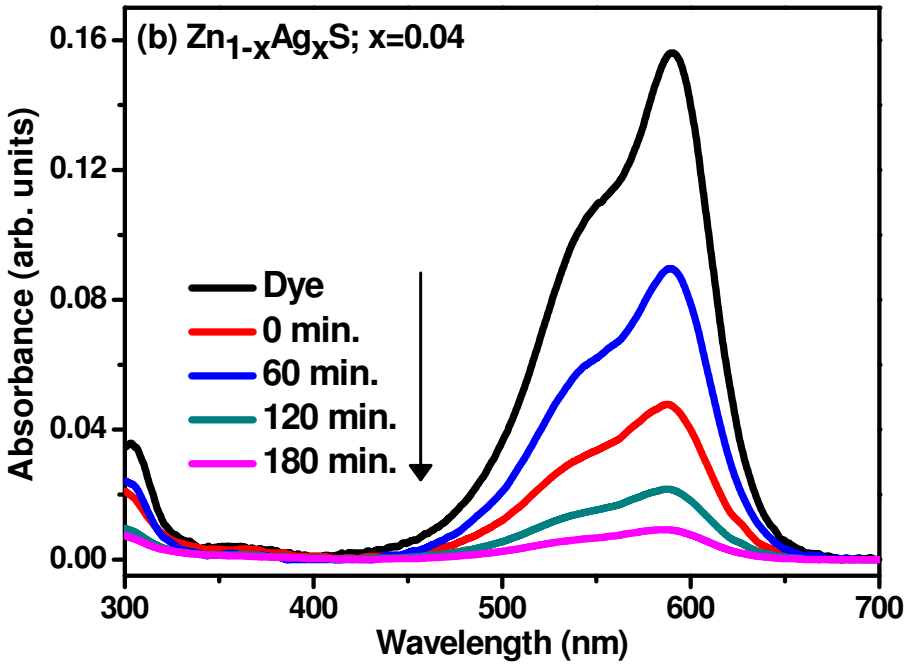

Figure 5.53: Absorbance spectra of crystal violet degraded in the presence of $Zn_{1-x}Ag_xS$ (a) x = 0.03, (b) x= 0.04.

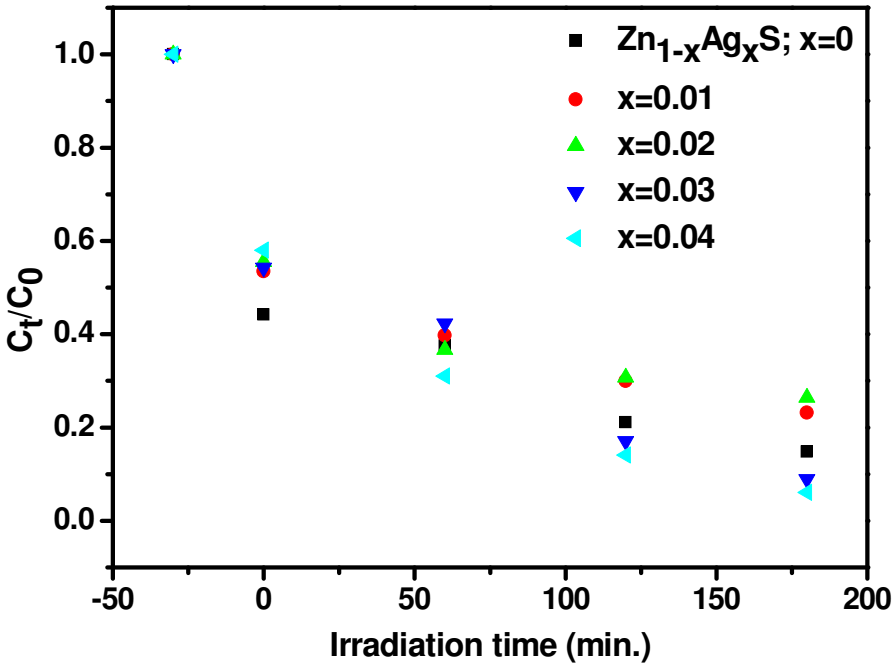

Figure 5.54: Variation of C_t/C_0 with irradiation time for $Zn_{1-x}Ag_xS$; x = 0, 0.01, 0.02, 0.03 and 0.04.

The characteristic absorption peak of this dye at 590 nm has been selected to monitor the photocatalytic degradation of the dye. By Beer Lambert law, the decrease in concentration of dye is recorded at different intervals of time to measure degradation rate. Figure 5.54 shows the comparative degradation behaviour of dye catalysed with $Zn_{1-x}Ag_xS$; x = 0, 0.01, 0.02,

0.03 and 0.04 in terms of change in concentration with respect to the initial concentration. As can be seen in figure, $Zn_{1-x}Ag_xS$; x = 0.01 and 0.02 show lower degradation as compared to that of undoped ZnS. At higher Ag_2S content i. e. in $Zn_{1-x}Ag_xS$; x = 0.03 and 0.04, photocatalytic degradation has increased fairly as compared to that of undoped ZnS. $Zn_{1-x}Ag_xS$; x = 0.02 recorded the lowest degradation among all the doped samples.

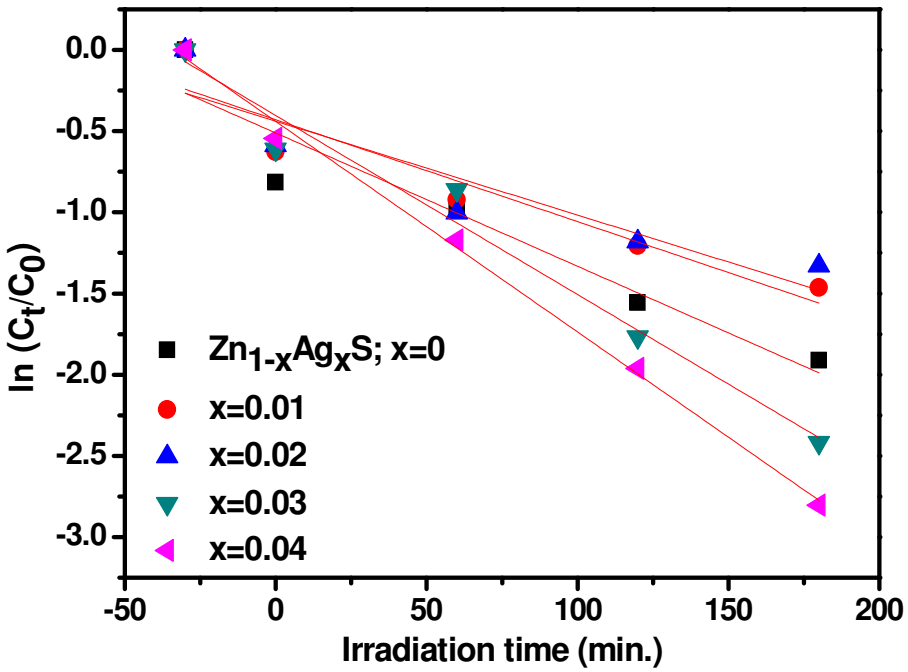

Figure 5.55: Plot between $\ln(C_t/C_0)$ and irradiation time to determine the value of rate constant k.

Since, in this study, concentration of solute is very low (1mg/L), so Langmuir-Hinshelwood kinetics model [23] can be simplified to pseudo first order kinetic model equation.

$$ln\left(\frac{C_t}{C_0}\right) = kT \qquad (5.4)$$

where C_t is the concentration of dye after irradiation in selected time interval t, C_0 is the initial concentration of dye, k is the first order rate constant, and T is irradiation time. Figure 5.55 shows plot between $\ln(C_t/C_0)$ and irradiation time to determine the value of rate constant k. Degradation rate has come out to be maximum in case of $Zn_{1-x}Ag_xS$; x = 0.04 (k=0.0130 min^{-1}). The degradation percentage has been calculated as

$$\%D = \left(1 - \frac{C_t}{C_0}\right) \times 100 \qquad (5.5)$$

where C_t is the concentration of dye after irradiation in selected time interval, C_0 is the initial concentration of dye. As shown in Figure 5.56, % degradation in presence of $Zn_{1-x}Ag_xS$; x = 0.04 has been recorded maximum (93.95%) among all the photocatalysts. Degradation

percentage values along with corresponding rate constants for all samples have been summarized in Table 5.12. The order of photo degradation rate is obtained as

$$Zn_{1-x}Ag_xS;\ x = 0.04 > x = 0.03 > x = 0 > x = 0.01 > x = 0.02$$

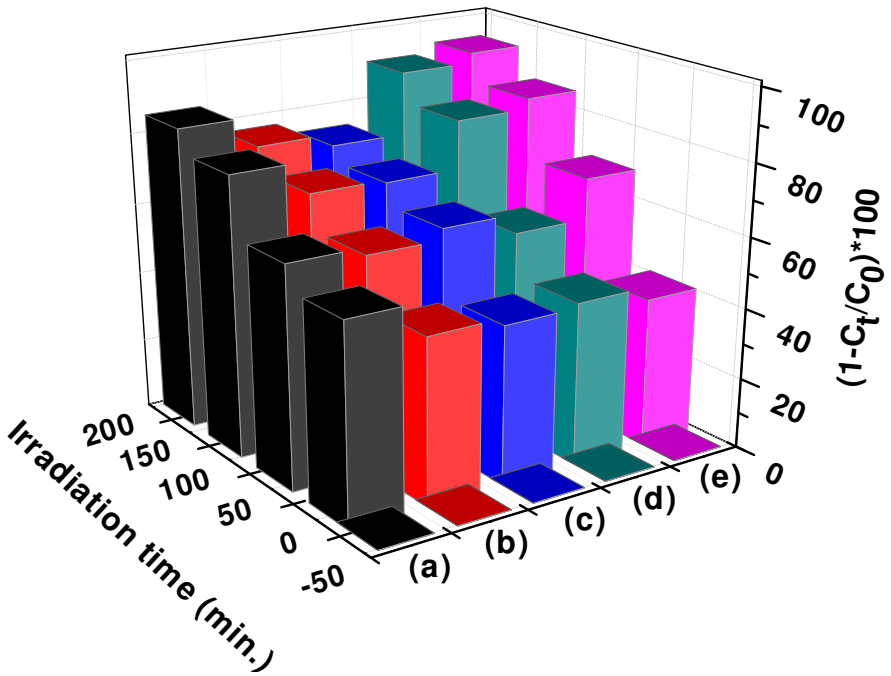

Figure 5.56: Degradation percentage of crystal violet in the presence of $Zn_{1-x}Ag_xS$ (a) x = 0, (b) 0.01, (c) 0.02, (d) 0.03 and (e) 0.04 at different irradiation times.

Table 5.12: First order rate constants for the photocatalytic degradation of crystal violet and corresponding percent degradation using $Zn_{1-x}Ag_xS$; x = 0, 0.01, 0.02, 0.03 and 0.04 as photocatalysts.

Photocatalyst	**Adj. R^2**	**k (min^{-1})**	**$(1-C_t/C_0)*100$**
$Zn_{1-x}Ag_xS$; x=0	0.89	0.0082	85.35
x=0.01	0.87	0.0063	76.88
x=0.02	0.81	0.0058	73.57
x=0.03	0.97	0.0110	91.08
x=0.04	0.99	0.0130	93.95

The observed trend in photocatalytic activity of Ag_2S modified ZnS is in accordance with the PL results as discussed in the previous section. In PL studies, we have observed decrease in PL emission intensity as the content of $AgNO_3$ is increased in the system i. e. from $Zn_{1-x}Ag_xS$; x = 0 to $Zn_{1-x}Ag_xS$; x = 0.02. Similarly, in photocatalytic degradation of crystal violet, same trend has been observed i. e. photocatalytic activity has been decreased in $Zn_{1-x}Ag_xS$; x = 0.01 and 0.02 as compared to that of undoped ZnS ($Zn_{1-x}Ag_xS$; x = 0). This suggests that there is a strong correlation between PL and photocatalytic properties of the as prepared samples. In case of $Zn_{1-x}Ag_xS$; x = 0.01 and 0.02, as discussed in section 5.5.6, PL intensity

has reduced as compared to that of undoped ZnS. Also, from XRD results, no additional peak has been observed in these samples. Hence, complex formation RSAg has hindered the light to penetrate in ZnS thereby reducing its emission intensity thereby reducing the photocatalytic activity of ZnS.

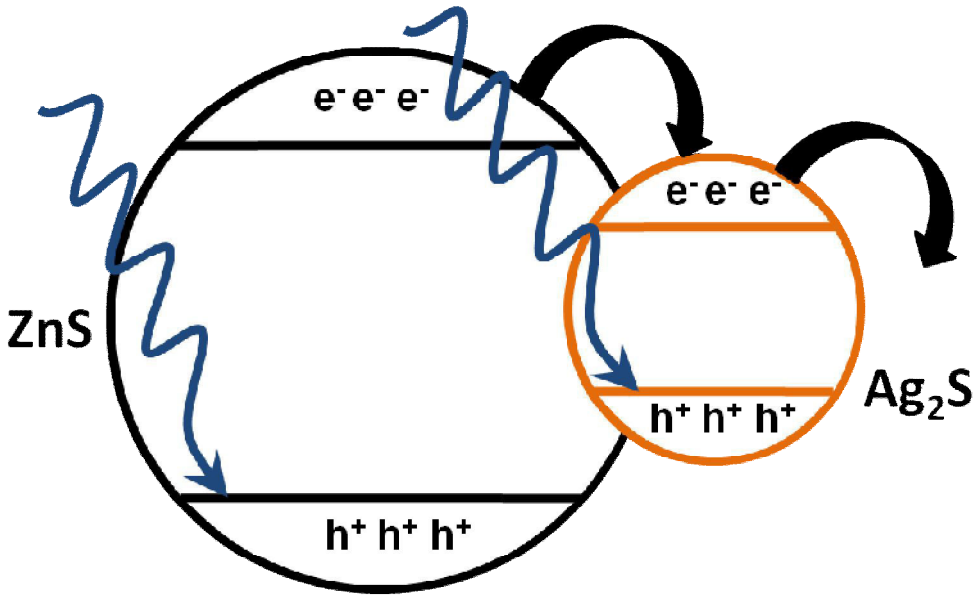

Figure 5.57: Possible mechanism of photocatalysis in presence of $Zn_{1-x}Ag_xS$; x = 0.03 and 0.04 photocatalysts.

In case of $Zn_{1-x}Ag_xS$; x = 0.03 and 0.04, in addition to passivating the defect states, Ag_2S has been loaded on the surface of ZnS and there is a strong coupling between both of them. Also, from UV-Vis studies, absorbance peak in UV region has decreased in case of $Zn_{1-x}Ag_xS$; x = 0.03 and 0.04 which suggests that ZnS is shielded by Ag_2S particles. So, when ZnS is photoexcited, due to coupling of ZnS and Ag_2S, the photogenerated electrons in conduction band of ZnS may be transported to the conduction band of Ag_2S and hence will participate in photocatalytic process. Hence from the photocatalytic results, it is concluded that transfer of electrons from conduction band of ZnS to the conduction band of Ag_2S is responsible for the observed enhancement in photocatalytic activity of these samples. The possible mechanism is shown in Figure 5.57.

References

[1] J. Cao, J. Yang, Y. Zhang, L. Yang, Y. Wang, M. Wei, Y. Liu, M. Gao, X. Liu and Z. Xie, Optimized doping concentration of manganese in zinc sulfide nanoparticles for yellow-orange light emission. Journal of Alloys and Compounds, **486** (2009) 890-894.

[2] S.H. Mohamed, Photocatalytic, optical and electrical properties of copper-doped zinc sulphide thin films. Journal of Physics D: Applied Physics, **43** (2010) 035406-035413.

[3] J.W. Jang, S.H. Choi, J.S. Jang, J.S. Lee, S. Cho and K.H. Lee, N-Doped ZnS Nanoparticles Prepared through an Inorganic-Organic Hybrid Complex ZnS $(piperazine)_{0.5}$. Journal of Physical Chemistry C, **113** (2009) 20445-20451.

[4] M.W. Porambo, H.R. Howard and A.L. Marsh, Dopant Effects on the Photocatalytic Activity of Colloidal Zinc Sulfide Semiconductor Nanocrystals for the Oxidation of 2-Chlorophenol. Journal of Physical Chemistry C, **114** (2010) 1580-1585.

[5] M. Muruganandham and Y. Kusumoto, Synthesis of N, C codoped hierarchical porous microsphere ZnS as a visible light-responsive photocatalyst. Journal of Physical Chemistry C, **113** (2009) 16144-16150.

[6] H.R. Pouretedal, A. Norozi, M.H. Keshavarz and A.F. Semnani, Nanoparticles of zinc sulfide doped with manganese, nickel and copper as nanophotocatalyst in the degradation of organic dyes. Journal of Hazardous Materials, **162** (2009) 674-681.

[7] S. Yang, Y. Liu, Y. Guo, J. Zhao, H. Xu and Z. Wang, Preparation of rutile titania nanocrystals by liquid method at room temperature. Materials Chemistry and Physics, **77** (2002) 501-506.

[8] S.T. Tan, B.J. Chen, X.W. Sun, W.J. Fan, H.S. Kwok, X.H. Zhang and S.J. Chua, Blueshift of optical band gap in ZnO thin films grown by metal-organic chemical-vapor deposition. Journal of Applied Physics **98** (2005) 013505(1)-013505(5).

[9] A. Aboulaich, L. Balan, J. Ghanbaja, G. Medjahdi, C. Merlin and R. Schneider, Aqueous Route to Biocompatible ZnSe:Mn/ZnO Core/Shell Quantum Dots Using 1-Thioglycerol As Stabilizer, Chemistry of Materials, **23** (2011) 3706-3713.

[10] C.B. Mendive, D. Hansmann, T. Bredow and D. Bahnemann, New Insights into the Mechanism of TiO_2 Photocatalysis: Thermal Processes beyond the Electron Hole Creation, Journal of Physical Chemistry C, **115** (2011) 19676-19685.

[11] R. Gui, X. An, H. Su, W. Shen, L. Zhu, X. Ma, Z. Chen and X. Wang, Rhodamine 6G conjugated-quantum dots used for highly sensitive and selective ratiometric fluorescence sensor of glutathione. Talanta, **94** (2012) 295-300.

[12] S.R. Husain, F. Ahmad and M. Ahmad, Synthesis of sulfur-Containing derivatives from olefinic fatty esters. Journal of the American Oil Chemists' Society, **60** (1983) 1340-1344.

[13] B.S.R. Devi, R. Raveendran and A.V. Vaidyan, Synthesis and characterization of Mn^{2+}-doped ZnS nanoparticles. Pramana, **68** (2007) 4679-687.

[14] C.C. Hu, J.N. Nian and H. Teng, Electrodeposited p-type Cu_2O as photocatalyst for H_2 evolution from water reduction in the presence of WO_3. Solar Energy Materials and Solar Cells, **92** (2008) 1071-1076.

[15] D. Beydoun, R. Amal, G. Low and S. McEvoy, Role of nanoparticles in Photocatalysis. Journal of Nanoparticle Research, **1** (1999) 439-458.

[16] J. Cui and U. Gibson, Thermal modification of magnetism in cobalt-doped ZnO nanowires grown at low temperatures, Physical Review B, **74** (2006) 045416(1)-045416(8).

[17] S. Liu, H. Zhang and M.T. Swihart, Spray pyrolysis synthesis of ZnS nanoparticles from a single-source precursor. Nanotechnology, **20** (2009) 235603-235610.

[18] L. Sun, C. Liu, C. Liao and C. Yan, ZnS nanoparticles doped with Cu(I) by controlling coordination and precipitation in aqueous solution. Journal of Materials Chemistry, **9** (1999) 1655-1657.

[19] P. Peka and H.J. Schulz, Empirical one-electron model of optical transitions in Cu-doped ZnS and CdS. Physica B, **193** (1994) 57-65.

[20] W.Q. Peng, G.W. Cong, S.C. Qu and Z.G. Wang, Synthesis and photoluminescence of ZnS:Cu nanoparticles. Optical Materials, **29** (2006) 313-317.

[21] M. Wang, L. Sun, X. Fu, C. Liao and C. Yan, Synthesis and optical properties of ZnS:Cu(II) nanoparticles. Solid State Communications, **115** (2000) 493-496.

[22] T.N. Morgan, Broadening of Impurity Bands in Heavily Doped Semiconductors. Physical Reviw, **13**9 (1965) A343-A348.

[23] C. Lizama, J. Freer, J. Baeza and H. Mansila, Optimized photodegradation of Reactive Blue 19 on TiO_2 and ZnO suspensions. Catalysis Today, **76** (2002) 235-246.

[24] I.K. Konstantinou and T.A. Albanis, TiO_2-assisted photocatalytic degradation of azo dyes in aqueous solution: kinetic and mechanistic investigations: A review. Applied Catalysis B, **49** (2004) 1-14.

[25] C.A.K. Gouvea, F. Wypych, S.G. Moraes, N. Duran, N. Nagata and P.P. Zamor, Semiconductor-assisted photocatalytic degradation of reactive dyes in aqueous solution. Chemosphere, **40** (2000) 433-440.

[26] H.S. Yoon, K.S. Lee, T.S. Lee, B. Cheong, D.K. Choi, D.H. Kim and W.M. Kim, Properties of fluorine doped ZnO thin films deposited by magnetron sputtering. Solar Energy Materials & Solar Cells, **92** (2008) 1366-1372.

[27] S. Karamat, S. Mahmood, J.J. Lin, Z.Y. Pan, P. Lee, T.L. Tan, S.V. Springham, R.V. Ramanujan and R.S. Rawat, Structural, optical and magnetic properties of $(ZnO)_{1-x}(MnO_2)_x$ thin films deposited at room temperature. Applied Surface Science, **254** (2008) 7285-7289.

[28] N.S. Sabri, A.K. Yahya and M.K. Talari, Emission properties of Mn doped ZnO nanoparticles prepared by mechanochemical processing. Journal of Luminescence, **132** (2012) 1735-1739.

[29] P. Yang, M.K. Lu, D. Xu, D. Yuan, J. Chang, G.J. Zhou and M. Pan, Strong green luminescence of Ni^{2+}-doped ZnS nanocrystals. Applied Physics A: Materials Science & Processing, **74** (2002) 257-259.

[30] L. Podlowski, R. Heitz, A. Hoffmann and I. Broser, Nonradiative recombination processes of Ni impurities in CdS and ZnS. Journal of Luminescence, **53** (1992) 401-405.

[31] P.H. Borse, N. Deshmukh, R.F. Shinde, S.K. Date and S.K. Kulkarni, Luminescence quenching in ZnS nanoparticles due to Fe and Ni doping, Journal of Materials Science, **34** (1999) 6087-6093.

[32] G. Murugadoss and M. Rajesh Kumar, Synthesis and optical properties of monodispersed Ni^{2+}-doped ZnS Nanoparticles. Applied Nanoscience, **4** (2014) 67-75.

[33] P. Yang, M. Lu, D. Xu, D. Yuan, C. Song, S. Liu, X. Cheng, Luminescence characteristics of ZnS nanoparticles co-doped with Ni^{2+} and Mn^{2+}. Optical Materials, **24** (2003) 497-502.

[34] N.V. Kaneva, D.T. Dimitrov and C.D. Dushkin, Effect of nickel doping on the photocatalytic activity of ZnO thin films under UV and visible light. Applied Surface Science, **257** (2011) 8113-8120.

[35] R.N. Bhargava and D. Gallagher, Optical Properties of Manganese-Doped Nanocrystals of ZnS. Physical Review Letters, **72** (1994) 416-419.

[36] K. Sooklal, B.S. Cullum, S.M. Angel and C.J. Murphy, Photophysical Properties of ZnS Nanoclusters with Spatially Localized Mn^{2+}. Journal of Physical Chemistry, **100** (1996) 4551-4555.

[37] A.A. Bol and A. Meijerink, Luminescence Quantum Efficiency of Nanocrystalline ZnS:Mn^{2+}. 1. Surface Passivation and Mn^{2+} Concentration. Journal of Physical Chemistry B, **105** (2001) 10197-10202.

[38] A.B. Cruz, Q. Shen and T. Toyoda, Studies on the effect of UV irradiation on Mn-doped ZnS nanoparticles. Materials Science and Engineering: C, **25** (2005) 761-765.

[39] H. Hu and W. Zhang, Synthesis and properties of transition metals and rare-earth metals doped ZnS nanoparticles. Optical Materials, **28** (2006) 536-550.

[40] T. Koda, S. Shionoya, M. Ichikawa and S. Minomura, Effect of pressure on the luminescence of zinc sulphide phosphors. Journal of Physics and Chemistry of Solids, **27** (1966) 1577-1586.

[41] W.Q. Peng, S.C. Qu, G.W. Cong, X.Q. Zhang and Z.G. Wang, Optical and magnetic properties of ZnS nanoparticles doped with Mn^{2+}. Journal of Crystal Growth, **282** (2005) 179-185.

[42] D. Denzler, M. Olschewski and K. Sattler, Luminescence studies of localized gap states in colloidal ZnS nanocrystals. Journal of Applied Physics, 84 (1998) 2841- 2846.

[43] A.A. Ashkarran, Absence of photocatalytic activity in the presence of the photoluminescence property of Mn-ZnS nanoparticles prepared by a facile wet chemical method at room temperature. Materials Science in Semiconductor Processing, **17** (2014) 1-6.

[44] S. Chen, T. Ida and K. Kimura, Thiol-Derivatized AgI Nanoparticles: Synthesis, Characterization, and Optical Properties. Journal of Physical Chemistry B, **102** (1998) 6169-6176.

[45] T. Vossmeyer, L. Katsikas, M. Giersig, I.G. Popovic, K. Diesner, A. Chemseddine and H. Weller, CdS Nanoclusters: Synthesis, Characterization, Size Dependent Oscillator Strength, Temperature Shift of the Excitonic Transition Energy, and Reversible Absorbance Shift. Journal of Physical Chemistry, **98** (1994) 7665-7673.

[46] R.G. Chaudhuri and S. Paria, Optical Properties of Double-Shell Hollow ZnS-Ag_2S Nanoparticles. Journal of Physical Chemistry C, **117** (2013) 23385-23390.

[47] L. Xu, B. Wei, W. Liu, H. Zhang, C. Su and J. Che, Flower-like ZnO-Ag_2O composites: precipitation synthesis and photocatalytic activity. Nanoscale Research Letters, **8** (2013) 536(1-7).

CHAPTER 6

RESULTS AND DISCUSSION

ZnS/ZnO and ZnS/Ag_2S Nanocomposites

Overview

The present chapter describes the studies of ZnS/ZnO and ZnS/Ag_2S nanocomposites (NCs) prepared via chemical precipitation route. Structural studies have been done using X-Ray diffraction (XRD) technique, transmission electron microscopy (TEM) and high resolution transmission electron microscopy (HRTEM). UV-Vis spectroscopy and photoluminescence (PL) spectroscopy has been utilized to investigate the absorption and emission characteristics of NCs. Photocatalytic degradation of crystal violet has also been carried out with the aim to study photocatalytic properties of as prepared ZnS/ZnO NCs. At the end of the chapter, a brief introduction has been given about core shell particles. Structural and optical studies of as synthesized ZnS-ZnO core shell nanoparticles (CSNPs) have also been done to demonstrate their superior photocatalytic activity in degrading the organic pollutants.

6.1 Nanocomposites

6.1.1 Introduction

As discussed in the previous chapter, dopant ions may enhance or reduce the photocatalytic activity of a semiconductor depending upon the type of transition involved in the emission pathway as has been the case of Ni and Mn doping where a decrease in photocatalytic activity has been observed due to formation of dopant centres in the host which acted as recombination centres. The recombination of charge carriers is highly undesirable in a photocatalytic process. A suitable alternative of doping metal ions in the semiconductors is the utilization of composites of two or more semiconducting materials having suitable band gap positions in the related area. Recently, various research groups have reported the preparation and photocatalytic properties of the composites of these materials. In ZnS/ZnO system, chemical bonding between zinc and oxide or sulphur is expected to be modified resulting in enhanced optical properties [1]. Gu et al. [2] have synthesized ZnS/ZnO composites confined in mesoporous silica. They have observed enhancement in blue emission at the expense of UV emission. However, photocatalytic studies were not conducted by them. Xiaodan et al. [3] have prepared ZnS/ TiO_2 composites and studied the degradation of the aqueous parathion methyl. The photocatalytic activity of these composites has been reported to be higher than that of commercially available anatase TiO_2, pure anatase TiO_2, or cubic ZnS NPs. CuS/ZnS composites have been synthesized by Yu group [4] via ion exchange method. The as synthesized CuS/ZnS composite hollow spheres have shown enhanced visible-light photocatalytic activity due to heterojunction structures, intense UV-visible absorption and hierarchically nanoporous structure. Considering the above points, we have synthesized composites of ZnS and ZnO via simple chemical precipitation route. The details of synthesis procedure have already been discussed in chapter 3. Ratio of sulphur source and oxygen source has also been varied to optimize the composition for their application in related area. Photocatalytic degradation of crystal violet has also been carried out to demonstrate the effect of sulphur and oxygen source composition on photocatalytic properties of the composites. For simplification, ZnS, $ZnO_{0.25}S_{0.75}$, $ZnO_{0.5}S_{0.5}$ and $ZnO_{0.75}S_{0.25}$ have been coded as z1, z2, z3 and z4. As discussed in the previous chapter, photocatalytic activity of $Zn_{1-x}Ag_xS$; x = 0.01 and 0.02 was decreased and it was predicted that formation of RSAg complex is responsible for the observed decrease. To further confirm this result, composites of ZnS and Ag_2S have been prepared with same composition but without thioglycerol. The obtained results of the prepared composites are described below.

6.1.2 ZnS/ZnO nanocomposites

6.1.2.1 XRD analysis

Figure 6.1 shows the XRD patterns of the synthesized ZnO_xS_{1-x}; x=0.25, 0.5 and 0.75 NCs. As can be seen in the Figure 6.1, pure ZnS (z1) exhibits cubic zinc blende phase having diffraction peaks located at 29.03°, 48.26°, 57.42° corresponding to (111), (220) and (311) planes respectively. It is to be noted that the peaks observed in the XRD pattern match well with those of the ZnS (cubic) reported in the JCPDS File No.77-2100.

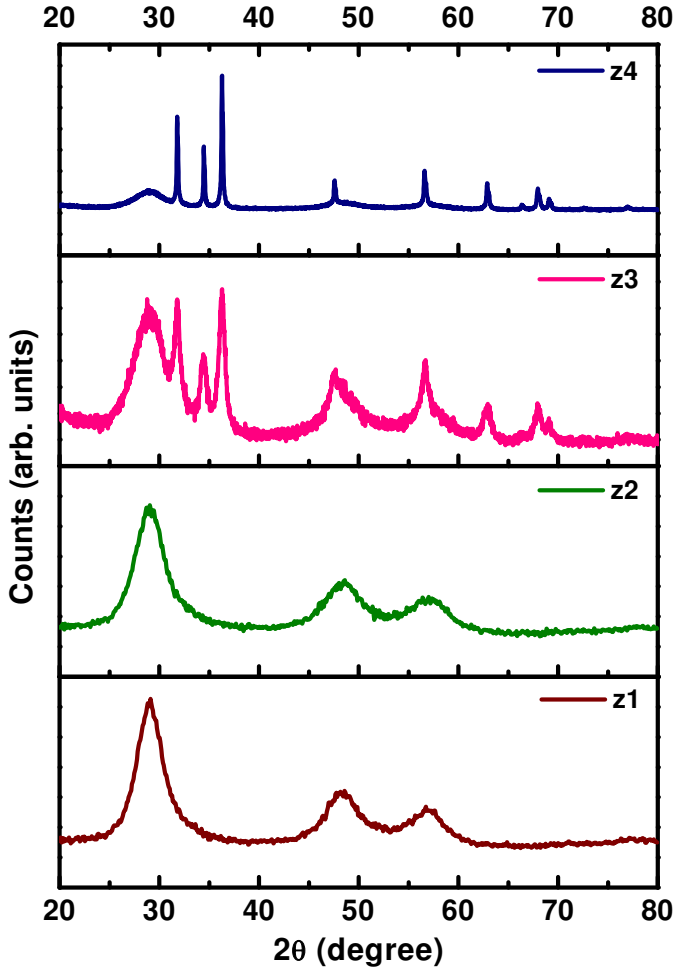

Figure 6.1: XRD patterns of ZnS/ZnO NCs.

Pure ZnO hexagonal phase having diffraction peaks are located at 31.71°, 34.41°, 36.26°, 47.53°, 56.51°, 62.78°, 66.34°, 67.91°, 69.05° and 76.89°. These peaks correspond to (100), (002), (101), (102), (110), (103), (200), (112), (201) and (202) respectively. The peaks observed in the XRD pattern of composites match with those of the ZnO (hexagonal) reported in the JCPDS File No.36-1451. As can be seen in the Figure 6.1, z2 does not exhibit diffraction peaks corresponding to ZnO phase. This observation may be attributed to the fact

that there is a lot of difference between the solubility product of ZnO and ZnS (solubility product for ZnO and ZnS is $6.8*10^{-17}$ mol^2dm^{-6} and $2.5*10^{-22}$ mol^2dm^{-6} respectively). The smaller the value of solubility product, the lower will be its solubility. Hence, as the concentration of O source is very less as compared to S source in z2, ZnO may not be formed. In sample z3, diffraction peaks corresponding to hexagonal ZnO and cubic ZnS have been observed. Sample z3 exhibits main diffraction peaks (28.98°, 31.78°, 34.43°, 36.27°) corresponding to ZnS and ZnO phase of almost same intensity which implies that this sample is composed of equal amount of ZnS and ZnO content. Also, as we carefully observe the spectra, sharpness of peaks keeps on increasing with the increase in ZnO content in the system indicating enhanced crystallinity of the NCs. This means that particle size has increased with the increase in ZnO content. In their work, Li et al. [5] have also reported that particle size of ZnO is greater than that of ZnS due to difference in the crystal lattice energy of both. Crystal lattice energy of ZnS is -3319 KJ/mol and that of ZnO is -4097 KJ/mol.

6.1.2.2 TEM analysis

TEM micrographs have been recorded to investigate the size and morphology of ZnS/ZnO NCs. Figure 6.2(a-b) shows the TEM micrographs of z2. As observed in the image, there is abundance of spherical particles in the system. From Figure 6.2(a), it can be seen that most of the particles lie in the range of 10-17 nm. However, due to the large specific surface area and high surface energy, some of the particles form aggregates. It might also be due to the lack of any capping agent used during synthesis process.

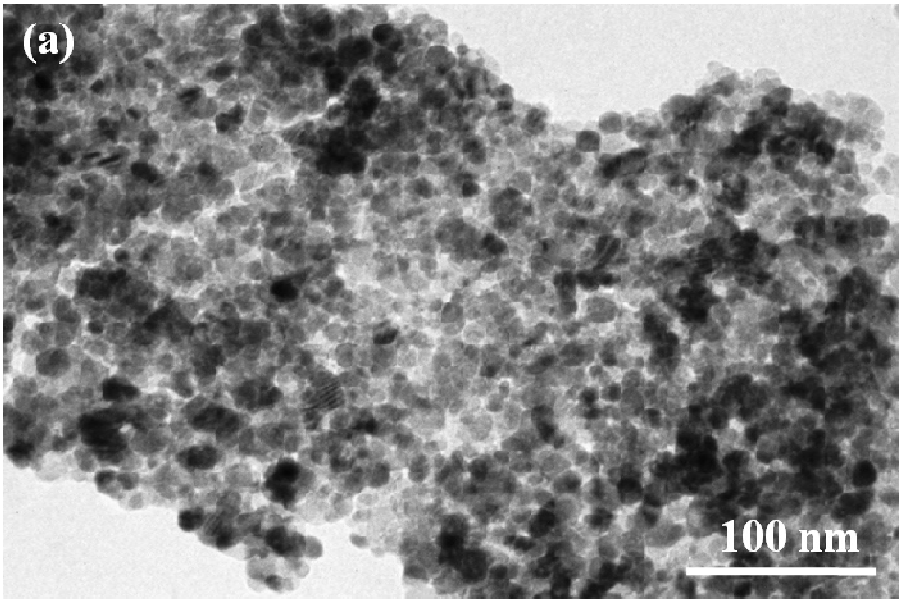

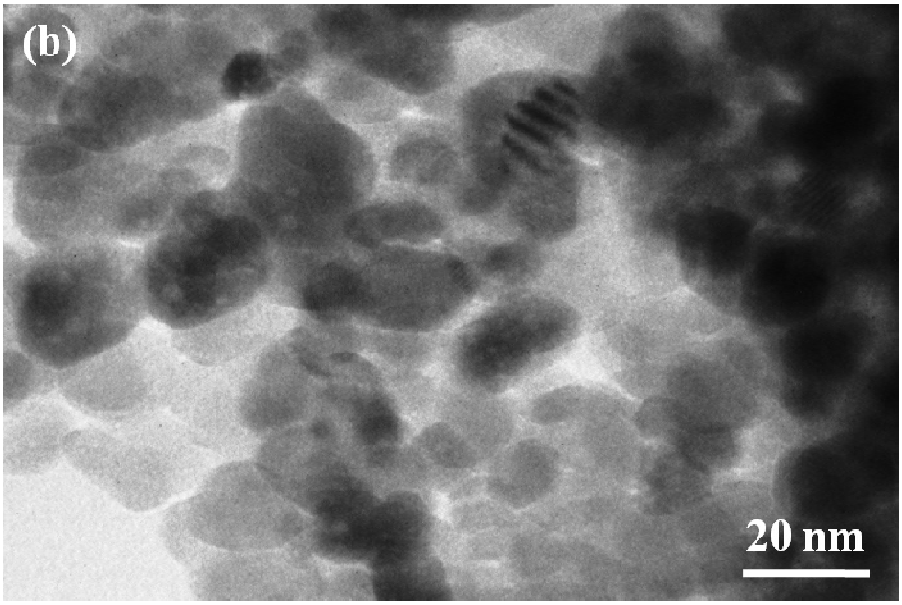

Figure 6.2: (a-b) TEM images of z2.

6.1.2.3 UV-Vis studies

UV-Vis studies have been performed for all samples to investigate the optical response of the composites. Figure 6.3 shows the diffuse reflectance spectra of all the samples in the range 300-550 nm.

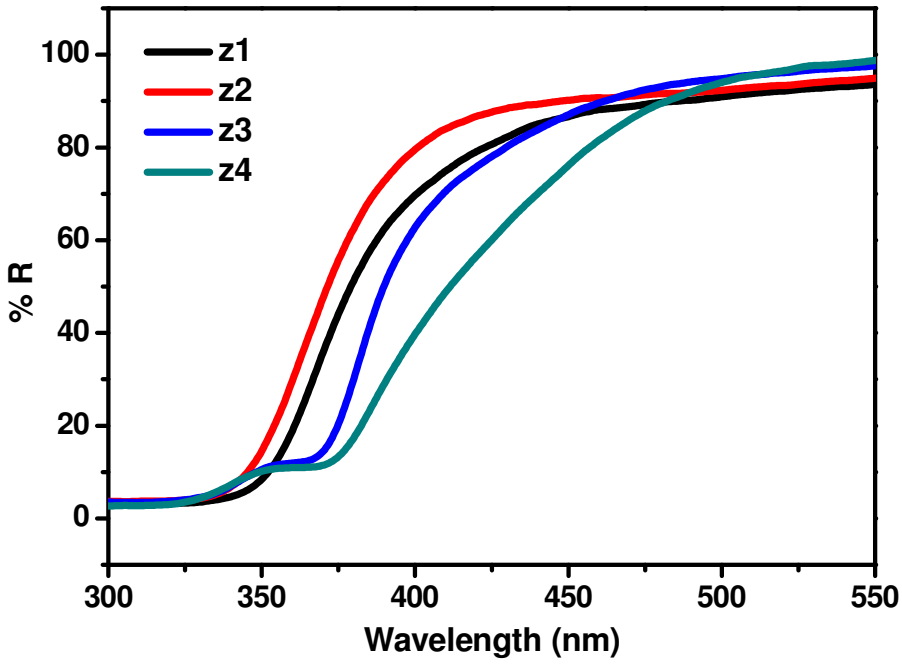

Figure 6.3: Diffuse reflectance spectra of ZnS/ZnO NCs.

It is important to mention here that ZnS phase is formed easily at room temperature but, generally, the reaction of $Zn(ac)_2$ and NaOH yields $Zn(OH)_2$ at lower temperature. So, calcination is required to get pure ZnO phase. Therefore, for comparative study, pure ZnS is heat treated at 250 °C. The relation between reflectance R and absorption coefficient α as given by Kubelka–Munk method [6] is

$$F(R) = \frac{(1-R)^2}{2R} = \frac{\alpha}{S} \qquad (6.1)$$

where F(R) is the Kubelka–Munk function, S is the scattering coefficient. From the above equation, the Kubelka–Munk function F(R) can be assumed to be proportional to α [6]. Absorption spectra for all samples have been plotted by employing the above equation.

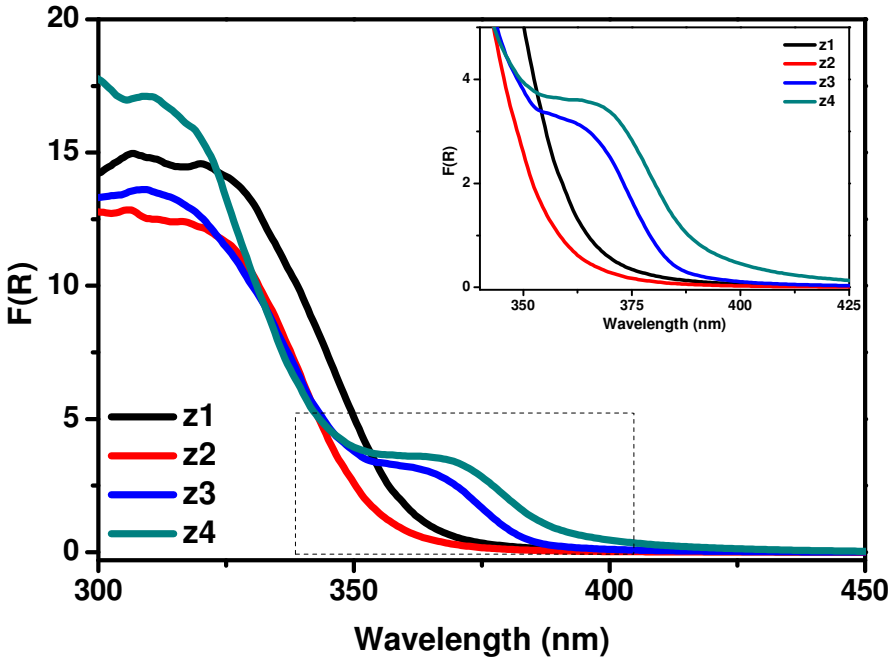

Figure 6.4: Absorption spectra of ZnS/ZnO NCs plotted by Kubelka Munk method.

As can be seen in Figure 6.4, absorption spectra is blue shifted in case of ZnO_xS_{1-x}; x=0.25. This observation can be explained on the basis of XRD studies. Diffraction peaks are broadened in case of z2 as compared to that of z1 which indicates that crystallite size of z2 is smaller as compared to that of z1. The addition of NaOH solution has not resulted in the phase formation of ZnO since it is clear from XRD results that no diffraction peak has appeared related to ZnO phase in this particular sample. In case of ZnO_xS_{1-x}; x=0.5 and 0.75, absorption spectra has been substantially red shifted indicating narrowing of band gap. Also, z3 and z4 exhibit enhanced absorptivity in near visible region as compared to z1 and z2. The

relation between the incident photon energy (hυ) and the absorption coefficient (α) or F(R) is given by [6]

$$[F(R)h\upsilon]^{1/n} = A(h\upsilon - E_g) \qquad (6.2)$$

where A is a constant and E_g is the band gap of the material and the exponent n depends on the type of the transition i.e. 2, 3, 1/2, 1/3 values corresponding to indirect allowed, indirect forbidden, direct allowed and direct forbidden transitions. As shown in the Figure 6.5, square of the absorbed energy [F(R)hυ] were plotted against photon energy (hυ) to determine the energy for direct gap transition. Band gap energies for all samples have been determined by extrapolating the straight portion of the graph on hυ axis at F(R)=0.

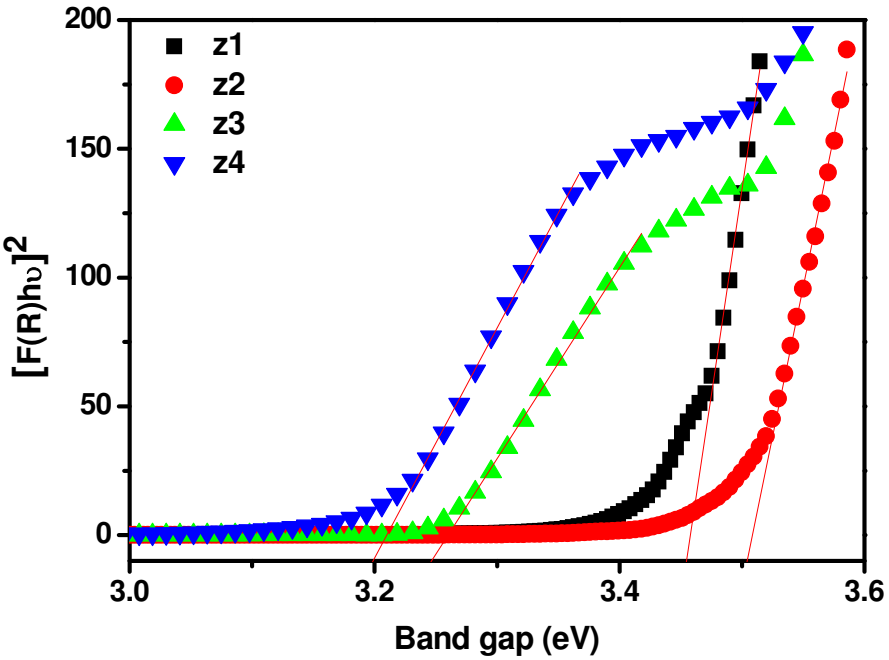

Figure 6.5: Tauc plots for ZnS/ZnO NCs to determine band gap.

Variation of band gap with different compositions of Na_2S and NaOH is shown in Figure 6.6. It has been reported in earlier works that hybrid orbitals made of an oxynitride and an oxysulphide form a stable valence band in a more negative position causing reduction in band gap [7]. Also, as discussed by Kim et al. [1], in ZnS/ZnO composite system, the potential energy of the top of the valence band may be formed by O2p atomic orbitals (i.e. O2p-S3p repulsion) which helps in diminution of the band gap of ZnS/ZnO nanocomposite. Another reason for the observed red shift might be due to the increase in grain size resulting in reduction of effective band gap due to the formation of ZnS/ZnO composite as is evident from XRD diffraction peaks of the samples. Formation of ZnS/ZnO nanocomposite has also

been confirmed by XRD analysis of the samples as discussed in section 6.1.2.1. Band gap values along with corresponding absorption wavelengths are given in Table 6.1.

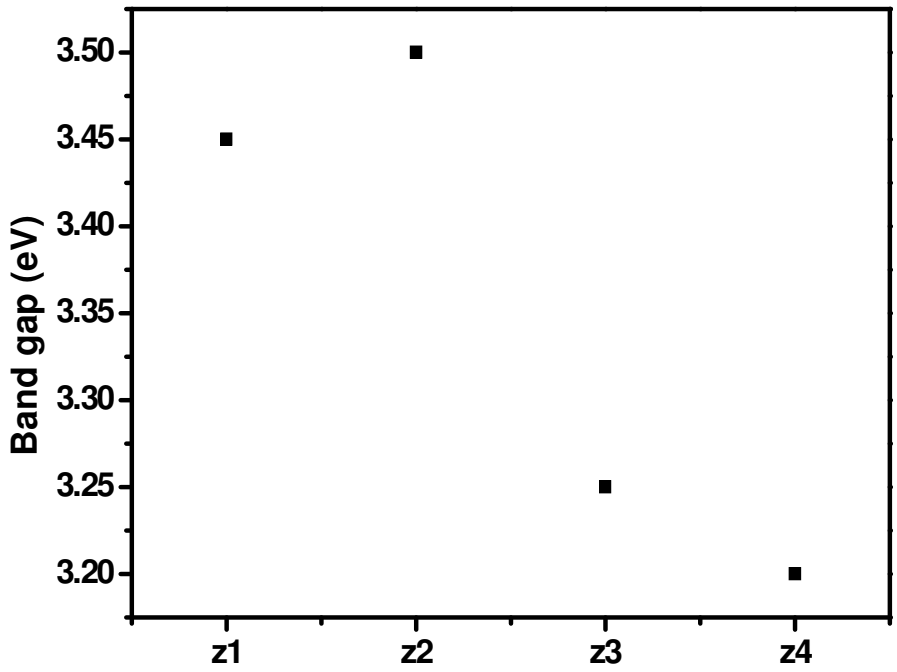

Figure 6.6: Band gap variation in as prepared ZnS/ZnO NCs.

Table 6.1: Calculated band gap values and corresponding absorption wavelengths of ZnS/ZnO NCs.

Sample	Band gap (eV)	Absorption wavelength (nm)
z1	3.45	360.11
z2	3.50	354.96
z3	3.25	382.27
z4	3.20	388.24

6.1.2.4 Photoluminescence studies

The study of photoluminescence (PL) properties of a material provides information about the defects present in it. Figure 6.7 shows the PL excitation spectra at emission wavelength λ_{em}=508 nm. As can be seen in the figure, all samples exhibit sharp excitation peak at ~350 nm. Therefore, emission spectra have been recorded at 350 nm for all samples. As shown in Figure 6.8, all the five samples exhibit almost similar PL emission spectra with a variation in emission intensity. No new emission peak related to ZnO has been observed in ZnS/ZnO NCs. The most dominant emission peaks in all the samples are centred around 468 nm, 507 nm and 623 nm. Among them, emission peak at ~507 nm is the most intense peak in each sample. The emission spectra covers blue, green and red region of visible spectrum. It is well

reported that emission peak in ZnS at 460 nm is due to transfer of electron from sulphur vacancies to zinc vacancies [8-9]. The emission intensity of the most dominant peak (~507 nm) follows the order

$$z2 < z1 < z3 < z4$$

The obtained results can be correlated to UV-Vis results discussed in the previous section as absorption and emission characteristics of a material are strongly dependant on each other. In UV-Vis absorption spectra (Figure 6.4), z2 shows blue shift in absorption wavelength as compared to other prepared NCs and the same sample exhibits maximum emission intensity. As the absorption spectra of the NCs is red shifted, their corresponding emission intensity also decreases. Also, from XRD results, as the content of ZnO in NCs is increased, corresponding crystallinity has also increased. It has been reported earlier that calcination has profound effect on structural and optical properties of a material. Grain size has been increased with increase in calcinations temperature and accordingly, crystallinity has also been increased. As the grain size increases, it will affect emission characteristics of a material. The excitation and emission spectrum of an optical material will shift towards higher wavelengths. In the present case, all samples exhibit sharp excitation peak at 350 nm indicating increase in particle size (compared to that of undoped ZnS discussed in previous chapters). Shi et al. [10] have reported that with increasing calcination temperature, emission spectra of TiO_2 have shifted to longer wavelengths. In their work, the sample calcined at 500 °C has displayed a visible luminescence band centered at 505 nm. While, a near-infrared luminescence band centered at 835 nm has appeared when calcination temperature is increased. Further increase in calcination temperature has resulted in stronger near infra-red emission and visible emission has been quenched. ZnS is known to emit in blue region at excitation wavelength of ~ 325 nm when not subjected to calcination. We anticipate that with calcination, grain size has increased and accordingly absorption has shifted towards longer wavelengths and hence ZnS and ZnS/ZnO NCs show strong excitation peak at 350 nm wheras nano ZnS show strong excitation at ~325 nm. Therefore, in case of calcined ZnS, accordingly the emission spectra have shifted towards longer wavelength region. Green emission peak centered at ~507 nm is related to elemental S species on the ZnS nanostructure surfaces [11]. Ye et al. [11] have observed green emission peak centered at 535 nm at excitation wavelength of 375 nm. As the sulphur content in the system is reduced, corresponding green emission has also decreased. Hence, as the content of ZnO is increased in the system, emission intensity related to sulphur species has decreased without any appreciable peak shift. It further confirms that this green emission is due to sulphur species.

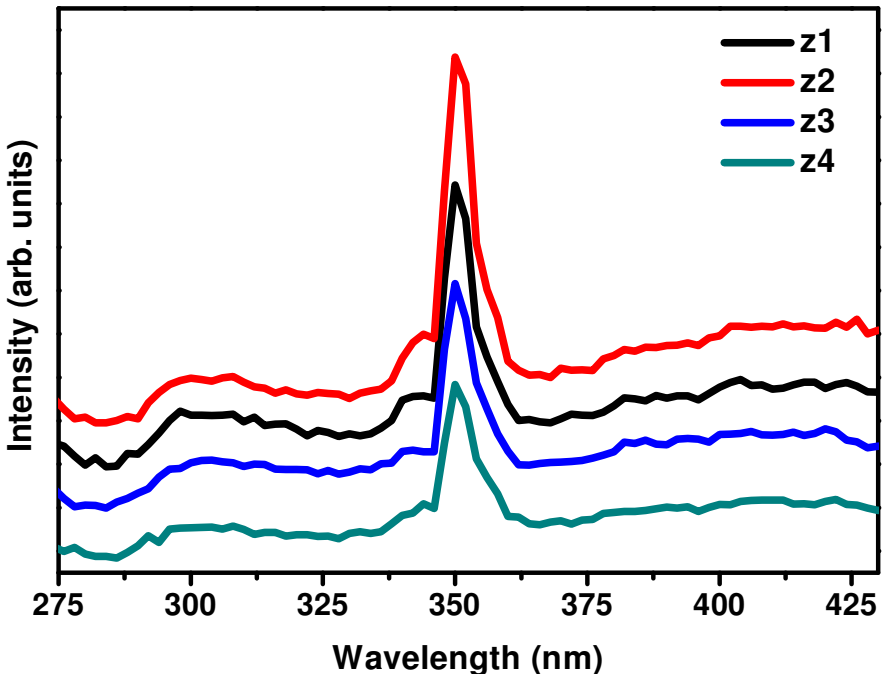

Figure 6.7: Photoluminescence excitation spectra of ZnS/ZnO NCs at λ_{em}=508 nm.

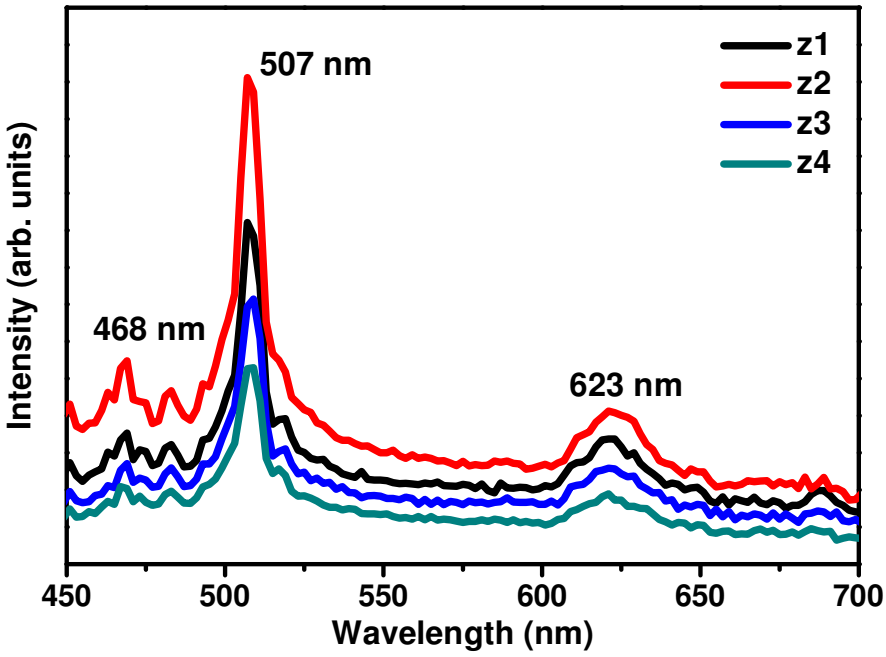

Figure 6.8: Photoluminescence emission spectra of ZnS/ZnO NCs at λ_{exc}=350 nm.

Further, it is reported that the excitonic PL intensity of ZnO nanoparticles decreases as the particle size increases. This has been ascribed to the decrease in the content of surface oxygen vacancy and defect with increasing particle size [12]. Similar to this result, in the present

case, with increase in ZnO content, emission intensity related to 507 nm has decreased which further confirms the increase in particle size with increase in ZnO content.

6.1.2.5 Photocatalytic studies

Photocatalytic degradation of crystal violet has been carried out to demonstrate the photocatalytic activity of as prepared ZnS/ZnO NCs. The characteristic absorption peak at 590 nm has been selected to monitor the photocatalytic degradation of the dye. Figure 6.9 shows the spectral changes occurring in the aqueous solution of crystal violet at different irradiation times in the presence of z3 and z4. As can be seen in Figure 6.9, the absorption peak corresponding to crystal violet has diminished gradually in presence of catalyst z3 and z4 with increasing irradiation time. Figure 6.10 shows the adsorption and degradation behaviour of the dye catalysed with all the samples (z1, z2, z3 and z4) in terms of change in concentration with respect to the initial concentration of dye. By Beer Lambert law, the decrease in concentration of dye is recorded at different intervals of time to measure degradation rate. As can be seen in Figure 6.10, all ZnS/ZnO NCs have degraded the dye more efficiently as compared to that of ZnS. The order of photo degradation rate is obtained as

$$z3 > z2 > z4 > z1$$

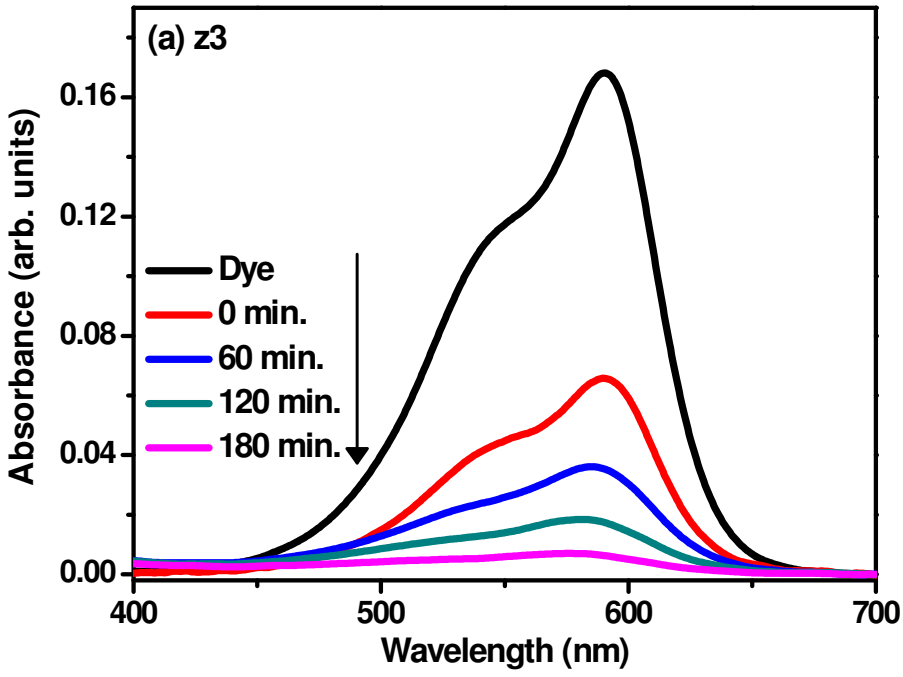

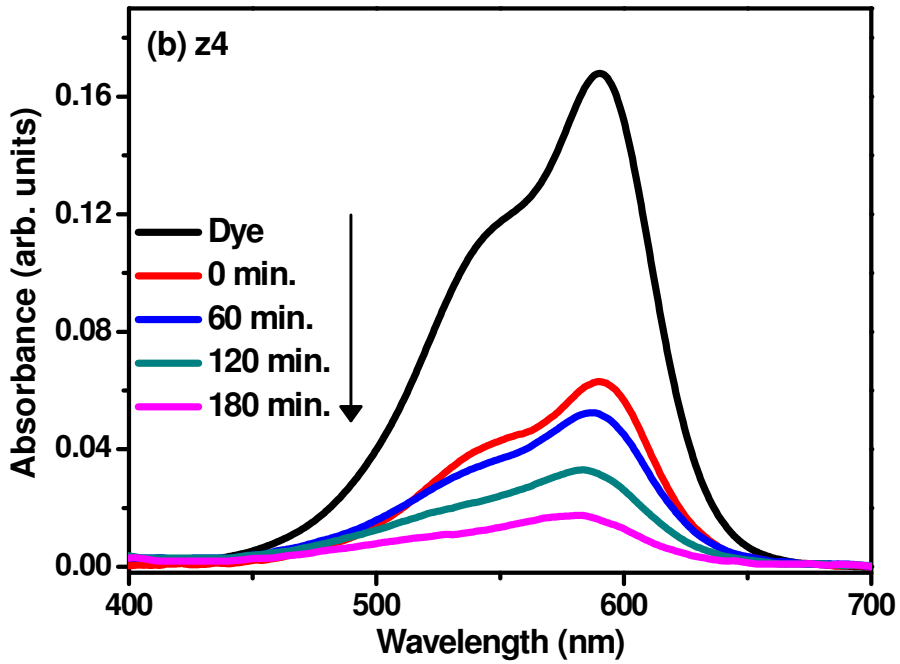

Figure 6.9: Absorbance spectra of crystal violet degraded in the presence of (a) z3, (b) z4.

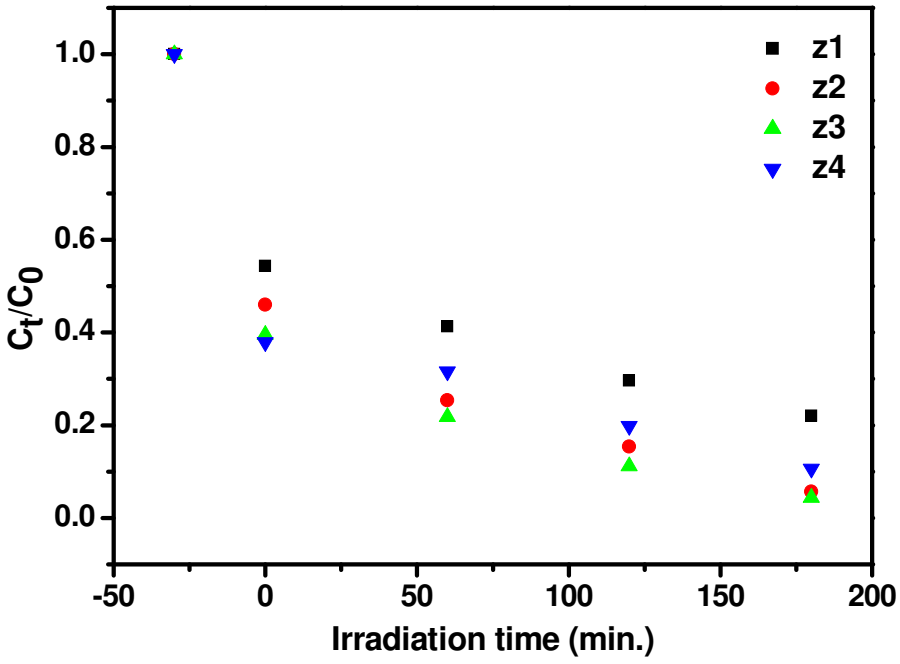

Figure 6.10: Variation of C_t/C_0 with irradiation time for z1, z2, z3 and z4.

Since, in this study, concentration of solute is very low (1mg/L), so Langmuir-Hinshelwood kinetics model [13] can be simplified to pseudo first order kinetic model equation.

$$ln\left(\frac{C_t}{C_0}\right) = kT \qquad (6.3)$$

where C_t is the concentration of dye after irradiation in selected time interval, C_0 is the initial concentration of dye, k is the first order rate constant, and T is irradiation time.

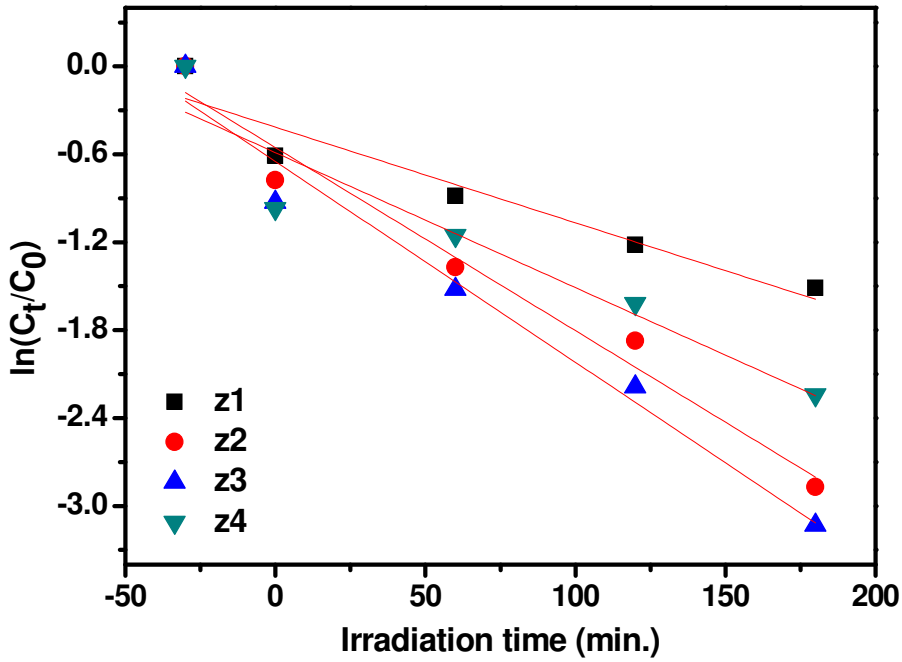

Figure 6.11: Plot between $\ln(C_t/C_0)$ and irradiation time to determine the value of rate constant k.

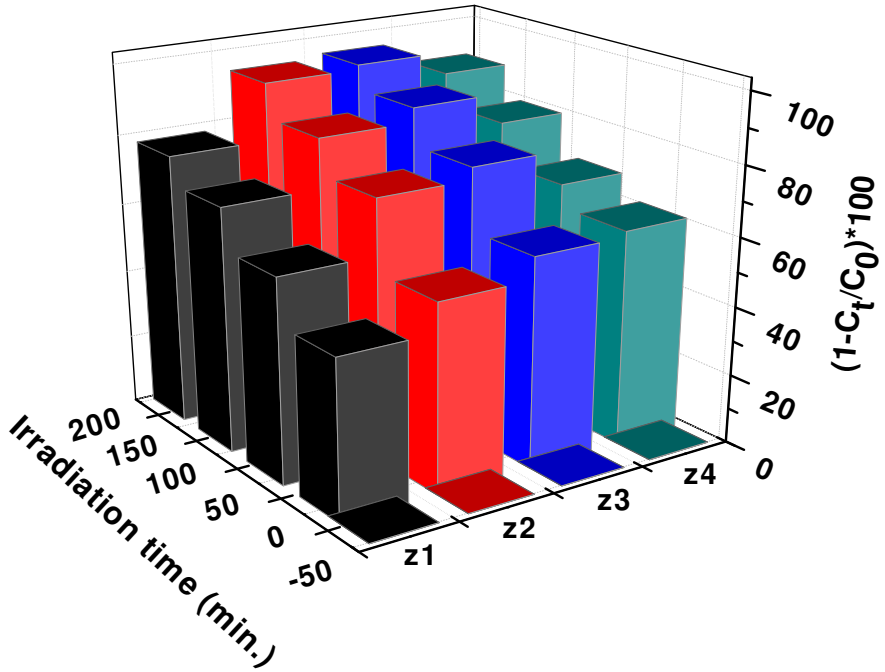

Figure 6.12: Degradation percentage of crystal violet in the presence of z1, z2, z3 and z4 at different irradiation times.

The value of rate constant (k) for different photochemical reactions has been obtained from the slope of plots of Figure 6.11. Figure 6.12 shows % degradation of dye in different intervals of irradiation time. The percent degradation has been calculated as

$$\%D = \left(1 - \frac{C_t}{C_0}\right) \times 100 \qquad (6.4)$$

where C_t is the concentration of dye after irradiation in selected time interval, C_0 is the initial concentration of dye. Table 6.2 summarizes the value of rate constants and percent degradation obtained for photochemical reactions catalysed with as prepared samples. The value of k has been recorded to be largest (0.0137 min^{-1}) for the photochemical reaction catalysed with z3 as compared to that of other catalyst assisted photochemical reactions. Also, percent degradation in presence of z3 is highest (95.63%) among all the photocatalysts employed.

Table 6.2: First order rate constants for the photocatalytic degradation of crystal violet and corresponding percent degradation using z1, z2, z3 and z4 as photocatalysts.

Photocatalyst	Adj R^2	Rate Constant k (min^{-1})	$(1-C_t/C_0)*100$
z1	0.90	0.0065	77.98
z2	0.96	0.0125	94.33
z3	0.96	0.0137	95.63
z4	0.88	0.0092	89.37

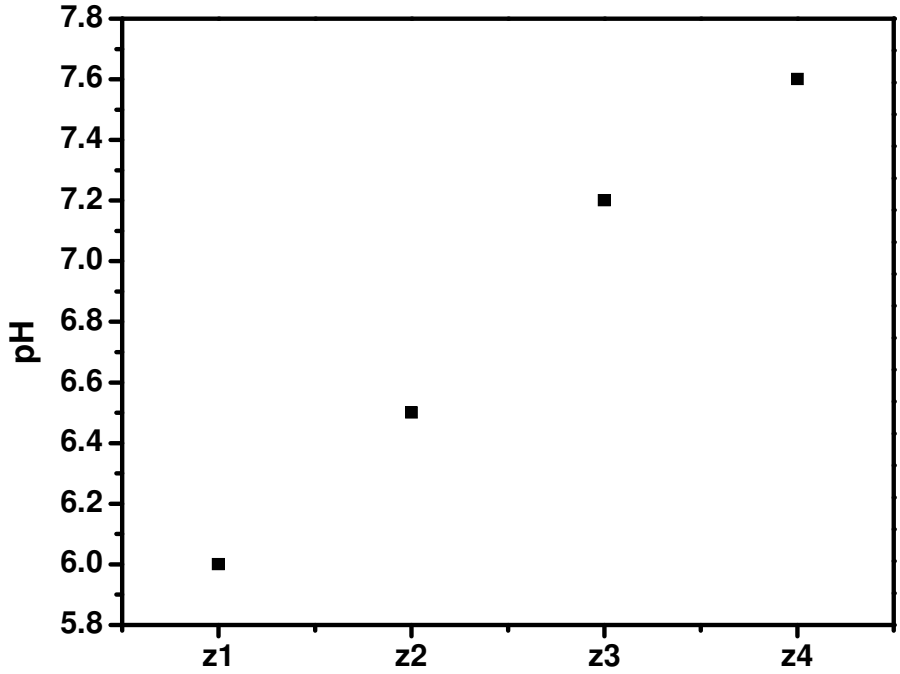

Figure 6.13: Variation in pH of solution in which the composites have been synthesized.

The superior photocatalytic activity of ZnS/ZnO NCs is attributed to the enhanced absorption characteristics of these composites. Absorption spectra of z2 is blue shifted indicating smaller particle size. Photocatalysts z3 and z4 have shown increase in absorption in near visible

region. These results are in line with the results obtained by Kim et al. [1]. However, composition of composites has not been varied in their work. They have attributed the superior photocatalytic activity of zincoxysulphide composite to the band gap diminution of this composite as compared to that of ZnS and ZnO. They have reported that oxysulfide in ZnO_xS_{1-x} has lifted HOMO level up, thus band gap has been decreased (2.4 eV). This band gap was narrow enough to absorb visible light and form electron-hole pairs for photocatalysis, effectively. In the present case, band gap diminution has also been observed in UV-Vis studies. So, enhanced absorption in near visible region has facilitated more charge carriers to participate in the photocatalytic process. Apart from this, the most important parameter which needs to be investigated during the photocatalytic studies of a material is the pH of the solution in which the material is being synthesized. During synthesis of these photocatalysts, pH of the solution has been monitored and it has been observed that that as O source i. e. NaOH is increased in the system, pH of the solution has also increased. With increase in pH of the solution, the surface of the photocatalyst has been made anionic. As the dye (crystal violet) used in the entire study is cationic in nature, hence more molecules will get adsorbed on the surface of the photocatalyst which is more anionic and accordingly, degradation will be more in that case. Decrease in photocatalytic activity has been observed in case of z4 although there is sufficient adsorption of dye molecules. This may be attributed to the increase in grain size as is clearly visible from XRD and UV-Vis results. Increase in grain size has resulted in increase in volume recombination thereby reducing photocatalytic activity. This study demonstrates the combined role of pH (in which the photocatalyst is being synthesized), absorption and emission characteristics of the photocatalyst in investigating the photocatalytic properties of the same.

Table 6.3: pH of the solution in which the different photocatalysts have been synthesized.

Photocatalyst	pH
z1	6
z2	6.5
z3	7.2
z4	7.6

6.1.3 ZnS/Ag_2S nanocomposites

6.1.3.1 XRD analysis

Figure 6.14 shows the XRD patterns of $Zn_{1-x}Ag_xS$; x = 0, 0.01, 0.02, 0.03 and 0.04 NCs. Diffraction peaks from (111), (220) and (311) planes match well with those of the β-ZnS (cubic) reported in the ICDD card no.80-0020. As can be clearly seen in the figure, diffraction peaks have become sharp as the content of $AgNO_3$ is increased in the system which suggests the increase in crystallinity and crystallite size with the increase in $AgNO_3$ content. At higher $AgNO_3$ content, i. e. in $Zn_{1-x}Ag_xS$; x = 0.02, 0.03 and 0.04, additional diffraction peaks with very less intensity have also appeared which match well with those of monoclinic Ag_2S (ICDD card no. 14-0072). At lower $AgNO_3$ content i. e. upto x=0.01, the samples exhibit cubic zinc blende phase with no additional phase. However, sharpness in diffraction peaks is observed which indicates the increase in crystallite size due to the addition of $AgNO_3$.

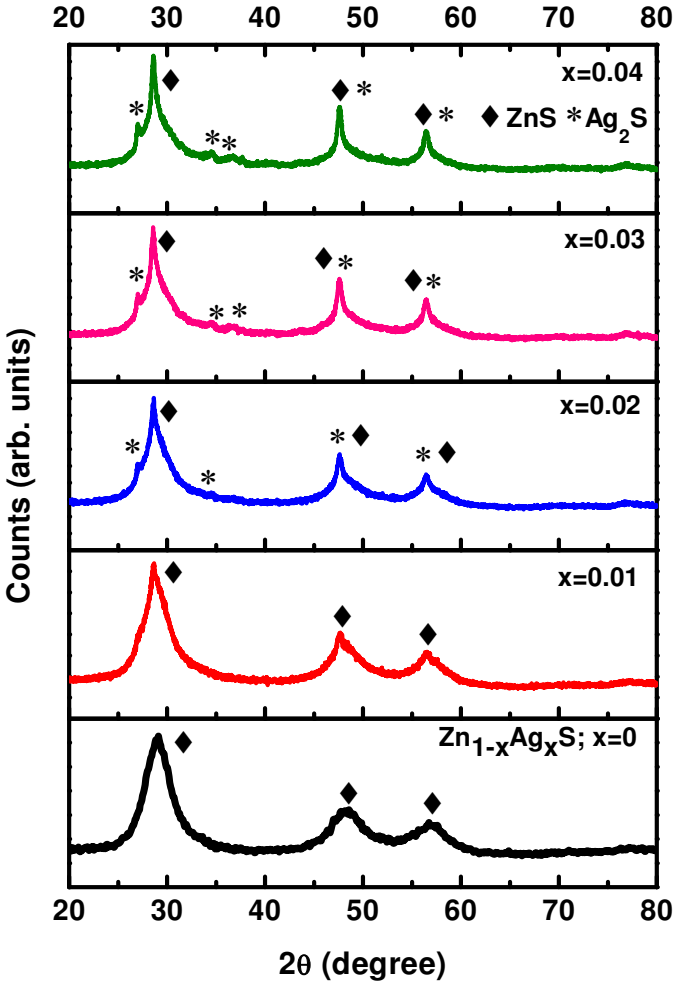

Figure 6.14: XRD patterns of ZnS/Ag_2S NCs.

Crystallite size of NPs has been calculated by following Scherrer's equation

$$t = \frac{k\lambda}{\beta\cos\theta} \qquad (6.5)$$

where k = 0.9, t is the crystallite size (Å), λ(Å), the wavelength of Cu Kα radiation and β is the corrected half width of the diffraction peak [14]. Crystallite size for all the samples has come out in the range of 2.99-3.87 nm and it increased as $AgNO_3$ content in the system is increased.

6.1.3.2 TEM analysis

Figure 6.15 shows the HRTEM images of one of $Zn_{1-x}Ag_xS$; x = 0.04 NC. Well defined lattice fringes have been observed in the image. The value of d spacing as shown in the image 6.15(a) came out to be ~0.2 nm and 0.24 nm which correspond to (220) plane of cubic ZnS and (121) plane of monoclinic Ag_2S respectively. In Figure 6.15(b), the measured value of d spacing is 0.26 nm which corresponds to $(\bar{1}21)$ plane of monoclinic Ag_2S. Hence it is confirmed that alongwith ZnS, Ag_2S phase has also formed.

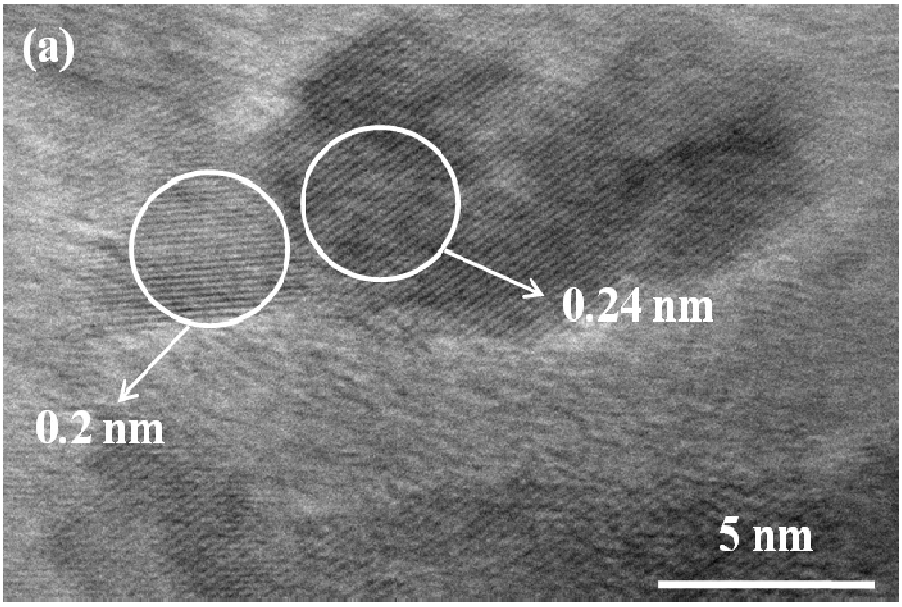

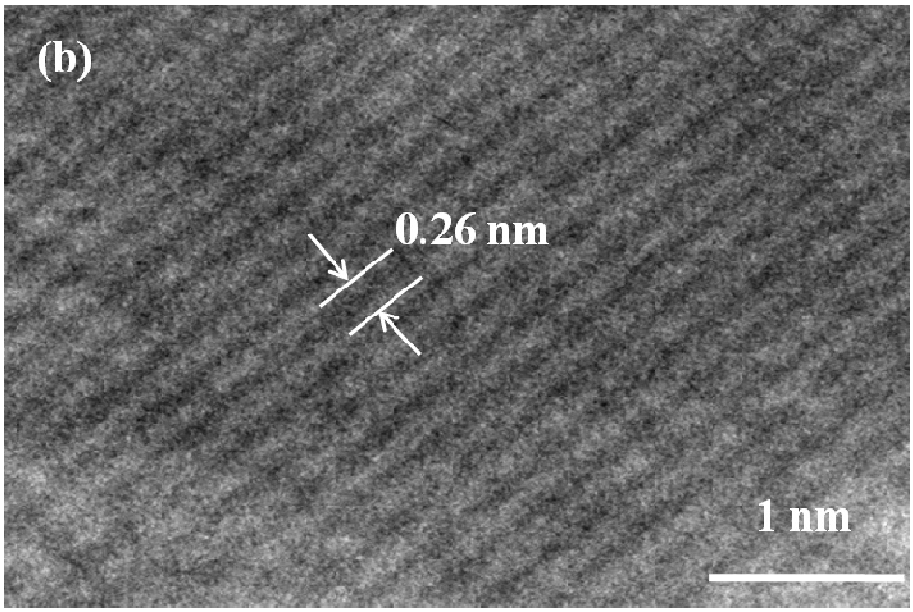

Figure 6.15: HRTEM images of $Zn_{1-x}Ag_xS$; x = 0.04.

6.1.3.3 UV-Vis analysis

UV-Vis studies have been performed to investigate the effect of the addition of $AgNO_3$ on optical response of ZnS in powder form. Absorption spectra for all samples are given in Figure 6.16.

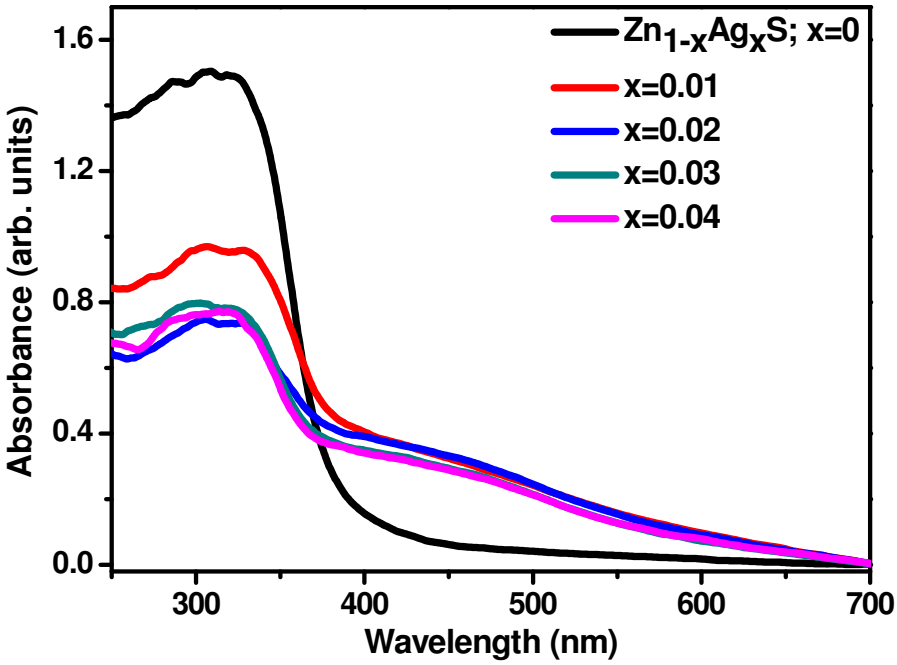

Figure 6.16: Absorption spectra of $Zn_{1-x}Ag_xS$; x = 0, 0.01, 0.02, 0.03 and 0.04 NCs.

It is clearly seen in the figure that absorbance of $Zn_{1-x}Ag_xS$; x = 0.01, 0.02, 0.03 and 0.04 is significantly increased in near visible region as compared to that of undoped ZnS. However,

absorption in UV region is significantly reduced in case of $Zn_{1-x}Ag_xS$; x = 0.01, 0.02, 0.03 and 0.04. Due to its smaller band gap (0.9 to 1.05 eV), Ag_2S absorbs visible light. In case of $Zn_{1-x}Ag_xS$; x = 0.01, 0.02, 0.03 and 0.04, due to large difference in solubility of Ag_2S (K_{sp} = 6.3×10^{-50}) and ZnS (2.5×10^{-22}), Ag_2S has formed as confirmed from XRD analysis of these samples. Hence layer of Ag_2S particles formed on the surface of ZnS inhibit direct penetration of UV light into ZnS thereby reducing the absorption in UV region. From this result, it is further confirmed that Ag_2S has been loaded on the surface of ZnS (otherwise separate peak corresponding to Ag_2S in visible region might have appeared). As ZnS is not directly exposed to UV light, hence decrease in absorption in UV region is observed for $Zn_{1-x}Ag_xS$; x = 0.01, 0.02, 0.03 and 0.04. However, absorbance has been increased in the near visible region due to Ag_2S. The observed results are in line with the results observed by Xu et al. [15]. In their work, the absorption in the UV range due to ZnO has gradually quenched, while there is an obvious increase in the visible light range with the elevated loading of Ag_2O. As we know that in a UV light-excited photocatalytic process, UV light absorption by semiconductor photocatalyst is essential for the effective generation of electron and holes, hence photocatalytic activity would be determined by both the quantity of generated charge carriers and the effective separation processes (relaxation of charge carriers).

6.1.3.4 Photoluminescence studies

To investigate emission characteristics of ZnS/Ag_2S NCs, PL emission spectra of all the samples have been recorded at excitation wavelength λ_{em}=390 nm. Figure 6.17(a-b) shows the PL emission spectra of ZnS and Ag_2S/ZnS NCs respectively. All the samples exhibit two emission peaks centred at 486 nm and 530 nm. It is well reported in literature that 486 nm emission peak in ZnS is due to the sulphur vacancy related emissions [8]. It is also well reported that emission peak observed at 530 nm is due to the presence of ZnS self-activated luminescence centres, probably arising from the vacancy states and interstitial states [16]. The ratio of intensity of emission peak observed at 530 nm and 486 nm I_{530}/I_{486} follows the following order

$$Zn_{1-x}Ag_xS;\ x = 0.04 > x = 0.03 > x = 0.02 > x = 0.01 > x = 0$$

This suggests that intensity of emission peak at 530 nm is increasing with the increase in Ag_2S content in the system. As discussed earlier, emission peak at 530 nm is due to the presence of ZnS self-activated luminescence centres arising from the vacancy states and interstitial states. Hence we can say that Ag_2S has passivated the ZnS surface and have eliminated the surface trap states. Further, from UV-Vis studies, it is expected that the

lowering in absorbance of ZnS absorption peak is due to the presence of Ag_2S shell on the surface of ZnS.

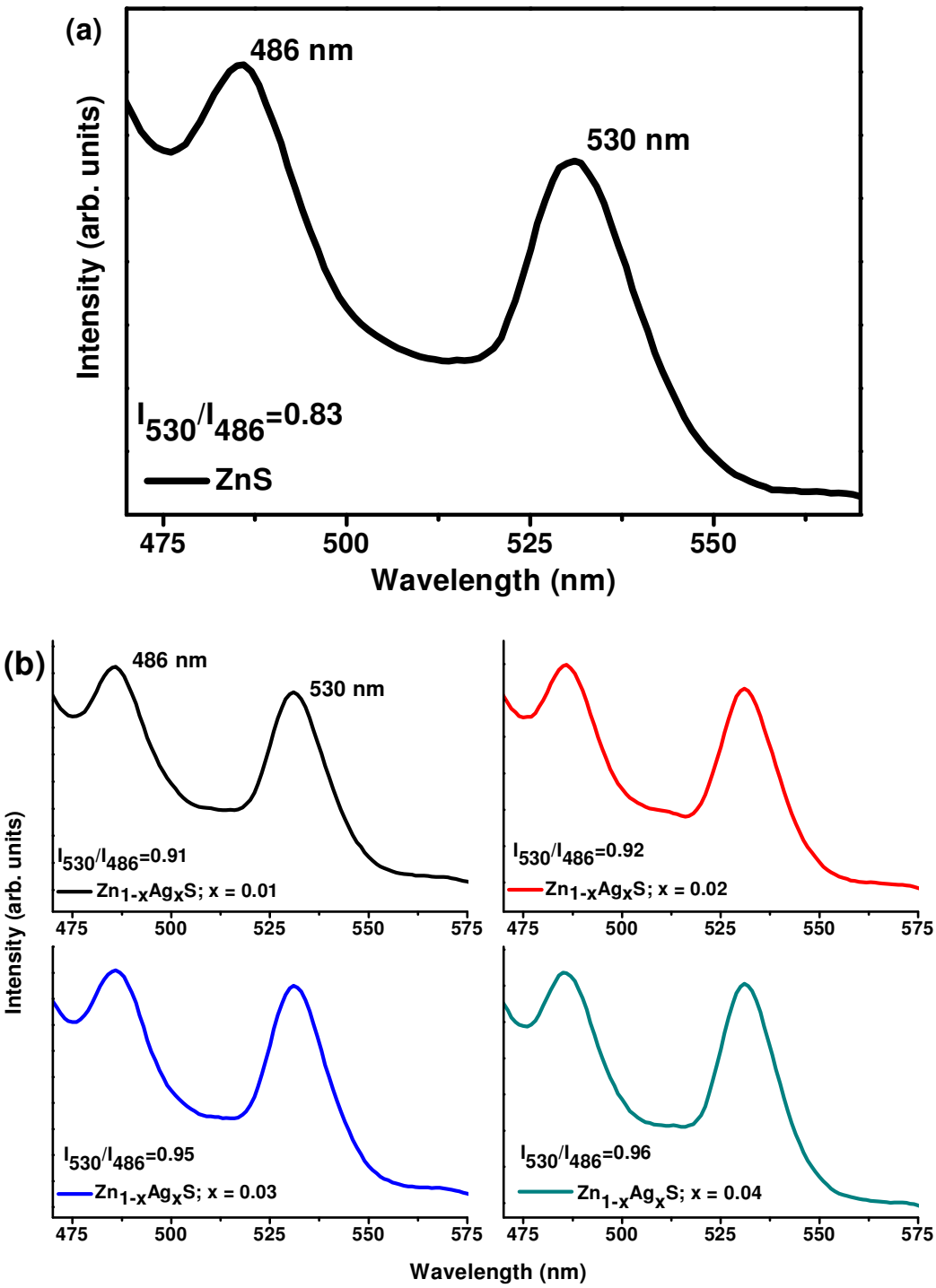

Figure 6.17: Photoluminescence emission spectra of (a) ZnS and (b) ZnS/Ag_2S NCs at λ_{exc}=390 nm.

Hence, it can be said that Ag_2S deposited on ZnS surface has passivated the defect states thereby resulting in increase in emission intensity of 530 nm peak. Chaudhuri et al. [17] have

prepared double-shell hollow ZnS-Ag_2S nanoparticles and it has been observed that the presence of Ag_2S in the form of a double-shell hollow particle has enhanced the light emission properties. Also, the presence of Ag_2S as an inner shell has enhanced quantum yield to more extent as compared to Ag_2S as an outer shell. It has also been reported by them that the quantum yield of hollow Ag_2S/ZnS nanoparticles also depends on the thickness of the ZnS layer. Quantum yield was observed to be maximum at a certain shell thickness, but below and above that thickness, it has decreased due to passivation of emission of the Ag_2S layer because of the thicker ZnS shell layer.

6.1.3.5 Photocatalytic studies

Photocatalytic degradation of crystal violet has been carried out to investigate the photocatalytic activity of as prepared composites of $Zn_{1-x}Ag_xS$; x = 0.01, 0.02, 0.03 and 0.04. Spectral changes taking place in absorbance of dye during photochemical reaction catalysed by $Zn_{1-x}Ag_xS$; x = 0.03 and x=0.04 are shown in Figure 6.18(a-b) in time interval of 60 min. By Beer Lambert law, the decrease in concentration of dye is recorded at different intervals of time to measure degradation rate. Figure 6.19 shows the comparative degradation behaviour of dye catalysed with $Zn_{1-x}Ag_xS$; x = 0, 0.01, 0.02, 0.03 and 0.04 in terms of change in concentration with respect to the initial concentration. As can be seen in figure, all the composites show superior photocatalytic activity as compared to that of ZnS alone.

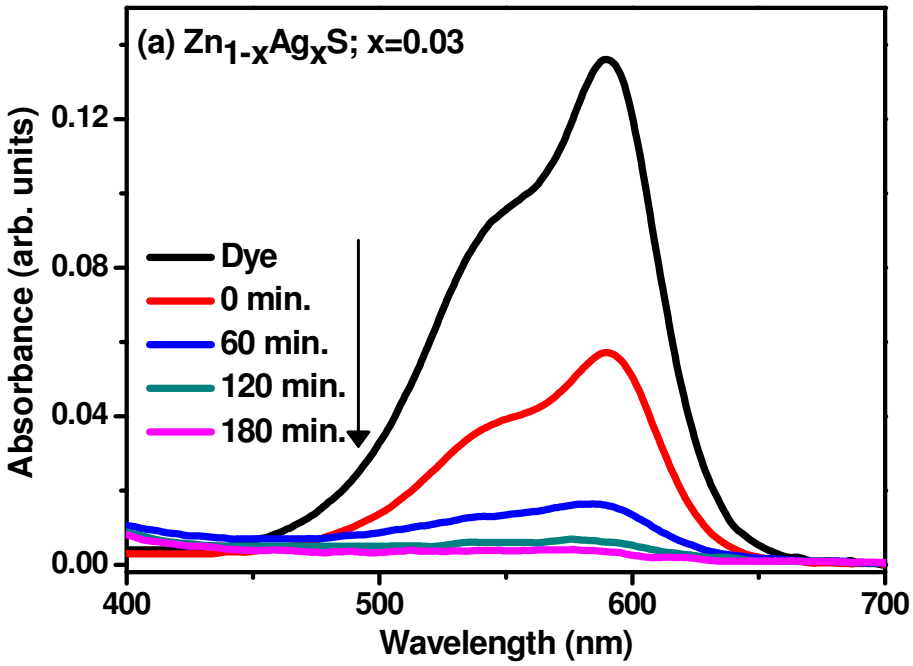

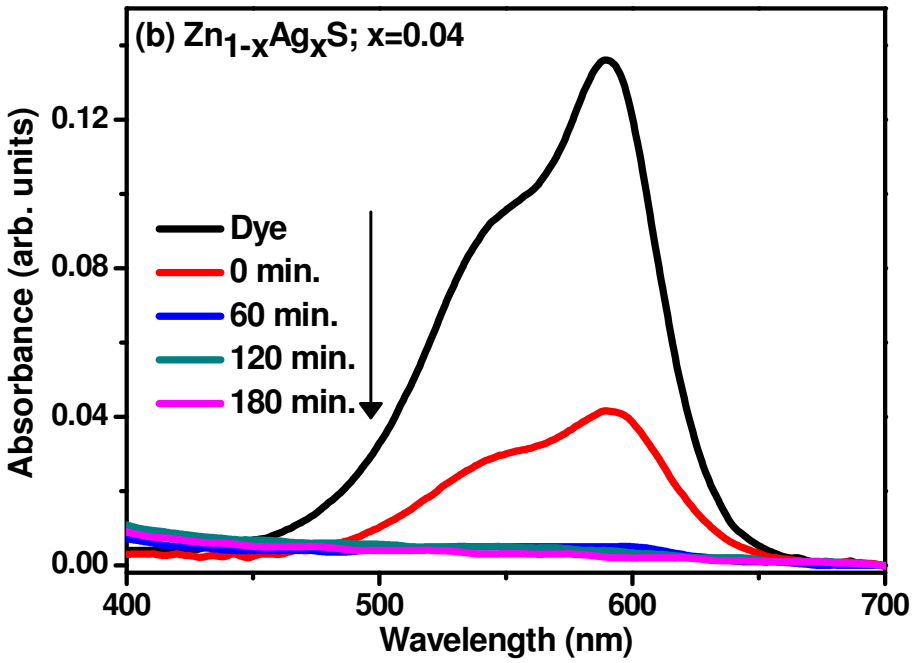

Figure 6.18: Absorbance spectra of crystal violet degraded in the presence of $Zn_{1-x}Ag_xS$ (a) x = 0.03, (b) x= 0.04 NCs.

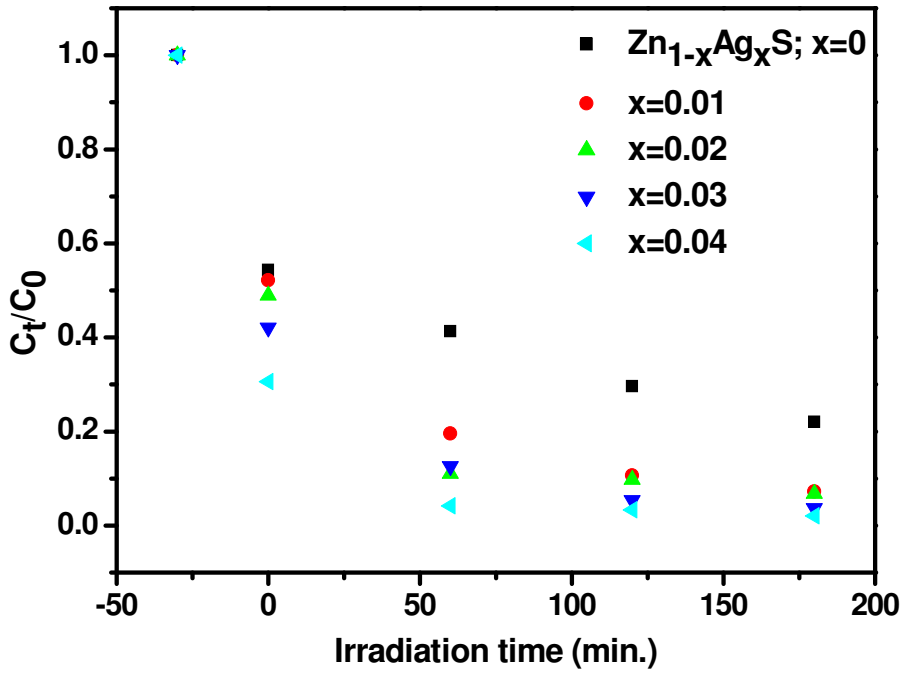

Figure 6.19: Variation of C_t/C_0 with irradiation time for $Zn_{1-x}Ag_xS$; x = 0, 0.01, 0.02, 0.03 and 0.04 NCs.

Among all the employed photocatalysts, $Zn_{1-x}Ag_xS$; x = 0.04 recorded the maximum degradation. Since, in this study, concentration of solute is very low (1mg/L), so Langmuir-Hinshelwood kinetics model [13] can be simplified to pseudo first order kinetic model equation.

$$ln\left(\frac{C_t}{C_0}\right) = kT \qquad (6.3)$$

where C_t is the concentration of dye after irradiation in selected time interval t, C_0 is the initial concentration of dye, k is the first order rate constant, and T is irradiation time. Figure 6.20 shows plot between $\ln(C_t/C_0)$ and irradiation time to determine the value of rate constant k.

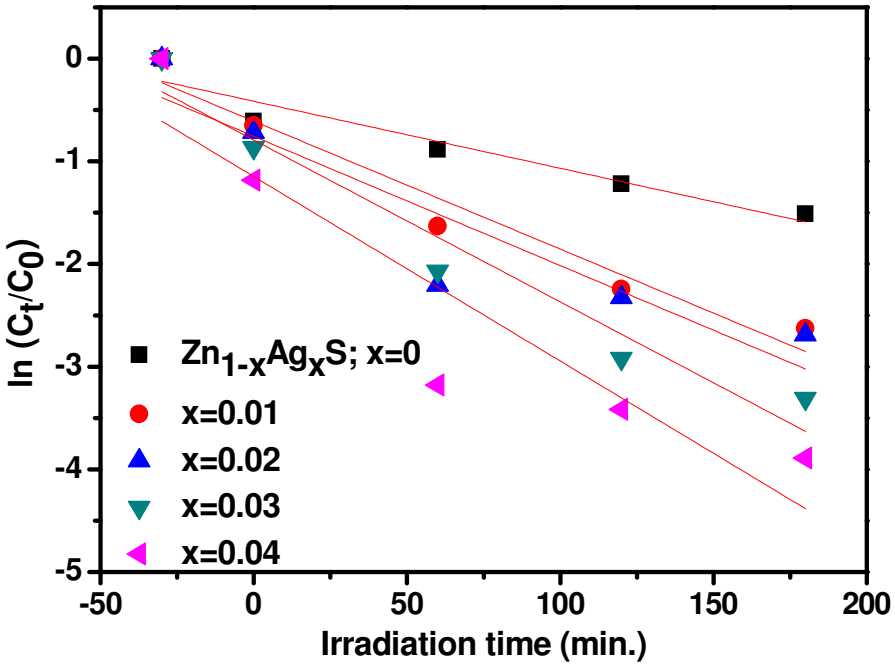

Figure 6.20: Plot between $\ln(C_t/C_0)$ and irradiation time to determine the value of rate constant k.

Degradation rate has come out to be maximum in case of $Zn_{1-x}Ag_xS$; x = 0.04 (k=0.0180 min^{-1}). The degradation percentage has been calculated as

$$\%D = \left(1 - \frac{C_t}{C_0}\right) \times 100 \qquad (6.4)$$

where C_t is the concentration of dye after irradiation in selected time interval, C_0 is the initial concentration of dye. As shown in Figure 6.21, % degradation in presence of $Zn_{1-x}Ag_xS$; x = 0.04 has been recorded maximum (97.96%) among all the photocatalysts. Degradation percentage values along with corresponding rate constants for all samples are summarized in Table 6.4. The order of photo degradation rate is obtained as

$Zn_{1-x}Ag_xS$; x = 0.04 > x = 0.03 > x = 0.02 > x = 0.01 > x = 0

The results obtained from this study are somewhat different from that obtained in case of $Zn_{1-x}Ag_xS$ system as discussed in chapter 5. The only difference between the present system and

the system discussed in chapter 5 is that in latter, capping agent thioglycerol has been used whereas in the present system, no capping agent has been used.

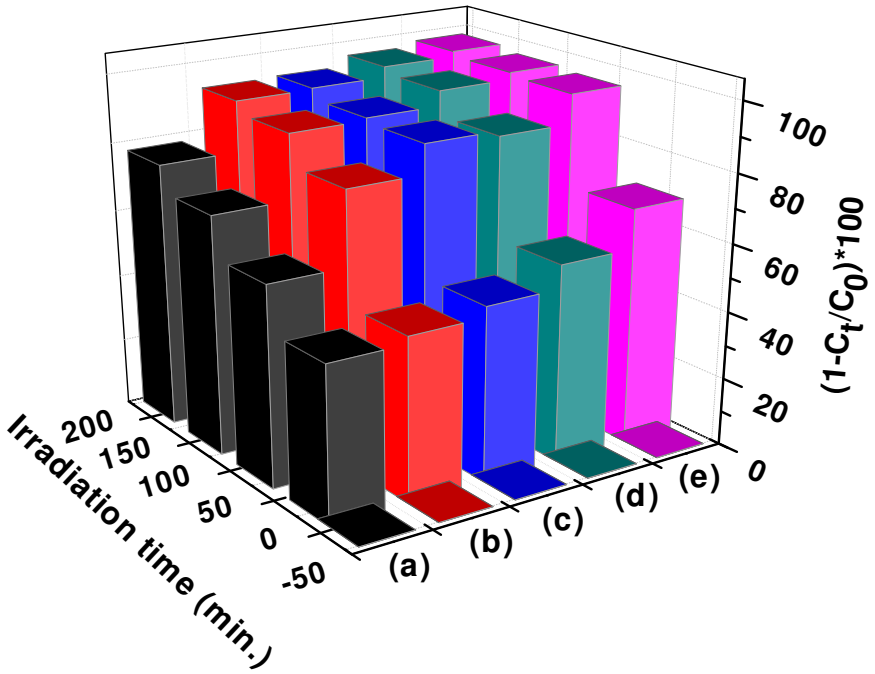

Figure 6.21: Degradation percentage of crystal violet in the presence of $Zn_{1-x}Ag_xS$ (a) x = 0, (b) 0.01, (c) 0.02, (d) 0.03 and (e) 0.04 NCs at different irradiation times.

Table 6.4: First order rate constants for the photocatalytic degradation of crystal violet and corresponding percent degradation using $Zn_{1-x}Ag_xS$; x = 0, 0.01, 0.02, 0.03 NCs as photocatalysts.

Photocatalyst	Adj R^2	Rate Constant k (min^{-1})	$(1-C_t/C_0)*100$
$Zn_{1-x}Ag_xS$; x = 0	0.90	0.0065	77.98
x=0.01	0.94	0.0125	92.77
x=0.02	0.82	0.0126	93.21
x=0.03	0.93	0.0158	96.35
x=0.04	0.81	0.0180	97.96

As discussed in chapter 5, at lower $AgNO_3$ content, i. e. in case of $Zn_{1-x}Ag_xS$; x = 0.01 and 0.02, RSAg complex was formed due to which photocatalytic activity upto this content was observed to be decreased. It was anticipated that the complex hindered the absorption of light due to which no charge carriers were generated which could otherwise have participated in the photocatalytic process. The results obtained in the present study also support this anticipation. In the present study, during synthesis, no complex was formed and hence there is a linear dependence of photocatalytic activity of as prepared samples with the $AgNO_3$

content. As $AgNO_3$ content is increased in the system, more Ag_2S particles have formed which coupled with ZnS and hindered the radiative recombination of charge carriers which further participated in photocatalytic process. Apart from ZnS, Ag_2S particles are also photoexcited simultaneously due to their smaller band gap and hence helped in photocatalytic process. When the two semiconductors ZnS and Ag_2S are coupled, the photoexcited electrons on the conduction band of ZnS can be transferred to the more positive conduction band of Ag_2S. Thus, the Ag_2S coupling with ZnS provides an effective way for the separation of photoexcited electron-hole pairs and the photocatalytic reaction is significantly enhanced [15]. Xu et al. [15] have prepared flower like ZnO-Ag_2O composites. They have ascribed the improved photocatalytic activity of composites as compared to ZnO alone to the formation of p-n junction (due to the deposited Ag_2O) at the interface of ZnO and Ag_2O, which resulted in the transfer of photocarriers and suppressed the electron-hole recombination rate. Zhang et al. [18] have synthesized ZnS-Ag_2S microspheric composites. Enhancement in photocatalytic activity of the composites has been attributed to the Ag_2S loading which has provided an effective way for the separation of photoexcited electron-hole pairs. It should be noted that the synthesis procedure adopted by both the groups is generally a two step process. In their work, Xu et al. [15] have first prepared ZnO and in the next step, Ag_2O/ZnO has been formed by redispersing already synthesized ZnO. In the present work, no two step synthesis procedure is followed (as discussed in chapter 3 under section 3.2.3). Zhang et al. [18] have also adopted two step synthesis process. They have synthesized these composites in Teflon autoclave at temperature of 140 °C. In the present study, synthesis temperature has been kept at 80 °C and in a single step, composites of ZnS-Ag_2S have formed. Thus, with very simple synthesis procedure at relatively lower temperature, composites of ZnS-Ag_2S have formed which are able to degrade crystal violet very efficiently. Further, it can also be concluded that a very small amount of Ag_2S as compared to that of ZnS can enhance photocatalytic activity of the latter to an appreciable extent.

6.2 ZnS-ZnO core shell nanoparticles

6.2.1 Introduction

Organically passivated core nanostructures exhibit surface related defects and trap states which act as fast non-radiative de-excitation channels for photogenerated charge carriers thereby reducing their overall quantum yield. Non radiative recombination is also not desired in photocatalytic application of semiconductor photocatalysts as it reduces participation of

charge carriers in the photocatalytic degradation of organic pollutants. An important strategy developed to passivate these trap states is the growth of an inorganic shell of any semiconductor which results in core shell system. Depending upon their relative valence and conduction band positions, core shell systems have been divided into three types; (a) type I, (b) reverse type I and (c) type II. In type I core shell systems, band gap of shell materials is larger than that of the core semiconductor. In this type of core shell system, the charge carriers are confined in core. As the name suggests, reverse type I systems are those in which band gap of shell material is less than that of the core. Charge carriers are partially or completely confined in a shell depending upon shell thickness. In type II of core shell systems, either valence band edge or conduction band edge of shell material is located in the band gap of the core semiconductor. When excited, the resulting staggered band alignment leads to a spatial separation of charge carriers in different regions of core shell structure [19]. In both type I and reverse type I core shell systems, the shell is generally grown to passivate the surface of core with the aim to improve its optical properties. The shell physically separates the surface of optically active core from its surrounding medium. Hence, the chances of optical properties of core to change e. g. by the presence of oxygen or water molecules are significantly reduced which make the core photo stable. Shell growth is accompanied by red shift in UV-Vis absorption spectra and photoluminescence wavelength. This red shift is attributed to a partial leakage of exciton into the shell material. In their work, Jiang et al. [20] have reported that as compared with the uncoated ZnS:Mn nanoparticles, the Mn emission intensity of ZnO coated ZnS:Mn has shown a strong increase followed by a gradual decline, which was led by the opposite effects of ZnO shells. They have discussed that surface passivation has resulted in luminescence enhancement whereas a decrease in the luminescent centers (Mn^{2+} ions) have lead to luminescence weakening. Dabbousi et al. [21] have found that the quantum yield of ZnS overcoated samples reaches a maximum value after 1.3 monolayers of ZnS is added. In their study, Perera et al. [22] have demonstrated that both core- and shell-localized electrical charges can be efficiently extracted to the surface of the NP where they can exchange energy with the external environment. Through lifetime studies, they have shown that the transfer of photoinduced charges from the core domain to the surface of the core/shell nanocrystals is approximately an order of magnitude faster than electron−hole recombination time. Lin et al. [23] have fabricated ZnO-ZnS core shell nanocables using electrospun ZnO nanofibers as a template. Enhancement in UV-photocatalytic activity has been observed using this core-shell structure due to the increased photon efficiency and charge carrier separation. In the present study, ZnS is employed as core

and shell of ZnO is grown on the surface of ZnS. Hence, it is reverse type I core shell system. It has been reported by Yamabi et al. [24] that to grow ZnO on a substrate, it is essential that pH of the solution should be greater than 9. Hence, in the synthesis of ZnS-ZnO core shell system, pH in which ZnS core has been synthesized is fixed at 10. It is necessary that the temperature for shell growth should be lower than the temperature used for core synthesis. Further, as discussed in chapter 4, UV-Vis irradiation of ZnS NPs has resulted in better photocatalytic activities, hence, ZnS core is UV-Vis irradiated before the growth of shell. The details of experimental procedure have been discussed in chapter 3. Comparative results of ZnS (z1) as discussed in the previous section and as prepared ZnS-ZnO core shell nanoparticles (CS NPs) are discussed below.

6.2.2 XRD studies

Figure 6.22 shows the diffraction pattern of ZnS-ZnO CS NPs. For comparative studies, XRD patterns of ZnS (z1) and ZnS synthesized at pH 10 are also shown.

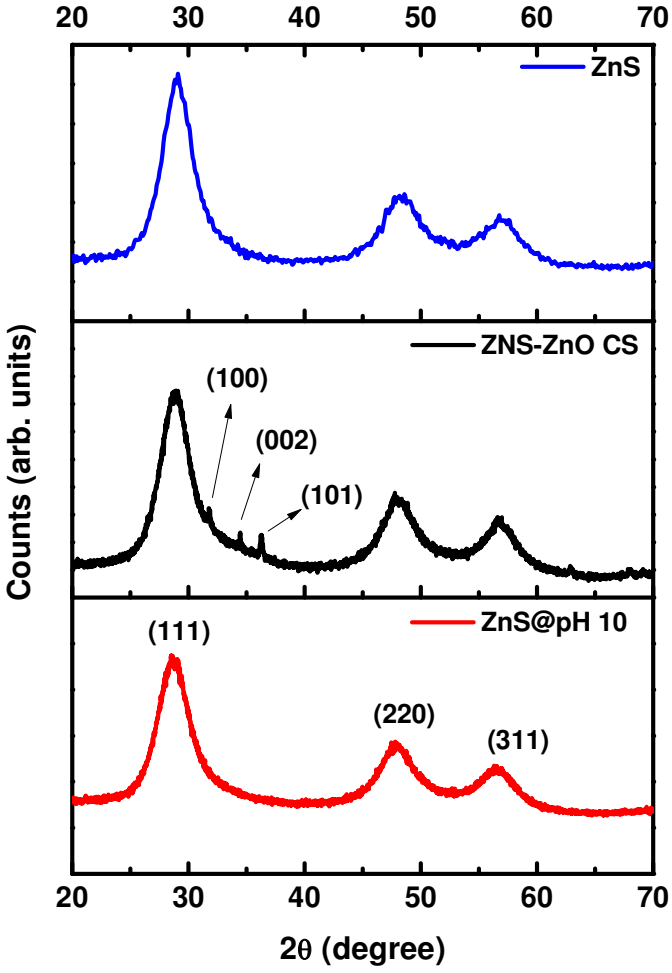

Figure 6.22: XRD patterns of ZnS, ZnS-ZnO CS and ZnS prepared at pH 10.

As can be seen in the figure, ZnS-ZnO CS NPs exhibit the most intense peaks at 28.84, 48.05 and 56.75 which correspond to (111) (220) and (311) planes related to cubic ZnS (JCPDS file no.77-2100). Apart from these peaks, peaks with very less intensity are located at 31.78, 34.43 and 36.27 corresponding to (100), (002) and (101) planes of hexagonal ZnO which match well with the JCPDS file no.36-1451. The appearance of these peaks is quite obvious which is due to ZnO shell grown on the surface of ZnS core. As the amount of ZnO grown is very less therefore, peaks are of very less intensity. This confirms the successful growth of ZnO on ZnS surface.

6.2.3 TEM studies

Figure 6.23 (a) shows the TEM micrograph of ZnS-ZnO CS NPs. Nearly spherical particles are clearly visible in the image. Figure 6.23 (b) shows the HRTEM micrograph of ZnS-ZnO CS NPs. The image shows lattice fringes which indicate the crystalline nature of the as prepared CS NPs. Lattice spacing has been calculated with AxioVision-LE software. An appropriate area has been selected of the same image (highlighted in the box) which clearly shows the interface between ZnS and ZnO NPs. As can be seen in Figure 6.23 (c), the zoomed area of Figure 6.23(b) shows the lattice spacing of 0.32 nm and 0.26 nm which corresponds to (111) lattice plane of a cubic ZnS crystal and the (002) lattice plane of a hexagonal ZnO crystal. This further confirms the growth of ZnO on ZnS.

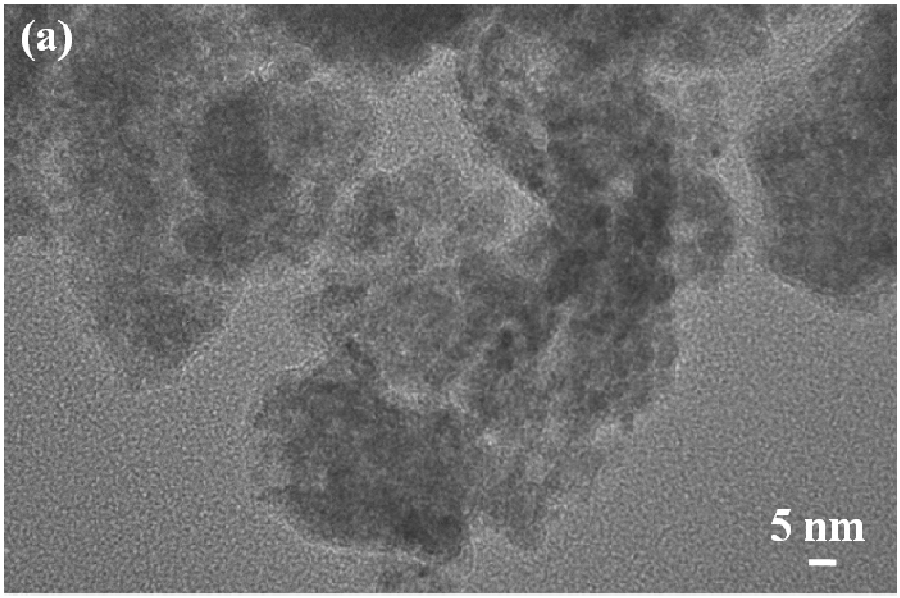

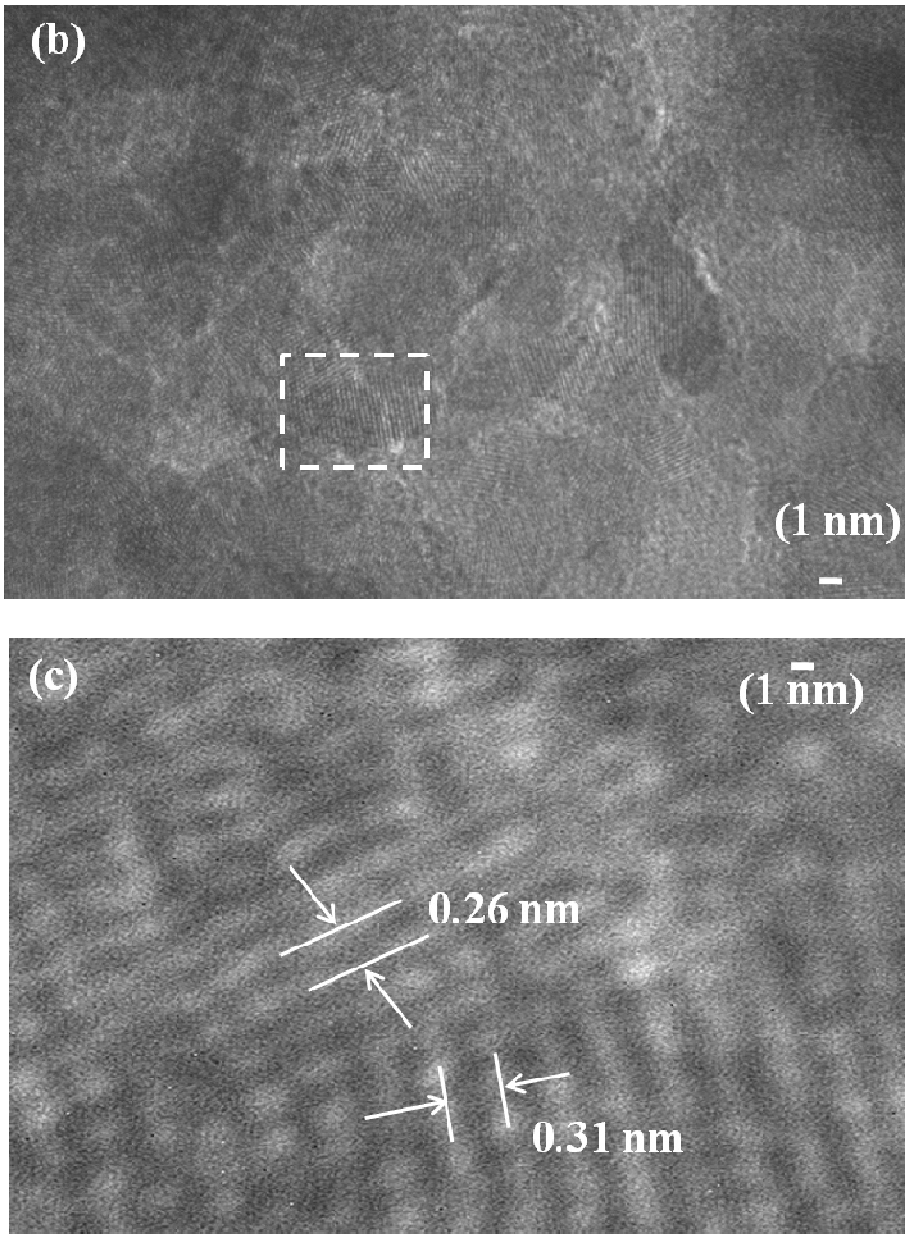

Figure 6.23: (a) TEM image of ZnS-ZnO CSNPs, (b-c) HRTEM image of the same sample.

6.2.4 UV-Vis studies

UV-Vis studies have been performed for ZnS-ZnO CS NPs and comparison of optical properties of this material has been done with that of the ZnS (z1 as discussed in section 6.1.2) and ZnS NPs synthesized at pH 10 (discussed in chapter 4). The relation between reflectance R and absorption coefficient α as given by Kubelka–Munk method [6] is

$$F(R) = \frac{(1-R)^2}{2R} = \frac{\alpha}{S} \qquad (6.1)$$

where F(R) is the Kubelka–Munk function, S is the scattering coefficient. From the above equation, the Kubelka–Munk function F(R) can be assumed to be proportional to α [6]. Absorption spectra for all samples have been plotted by employing the above equation.

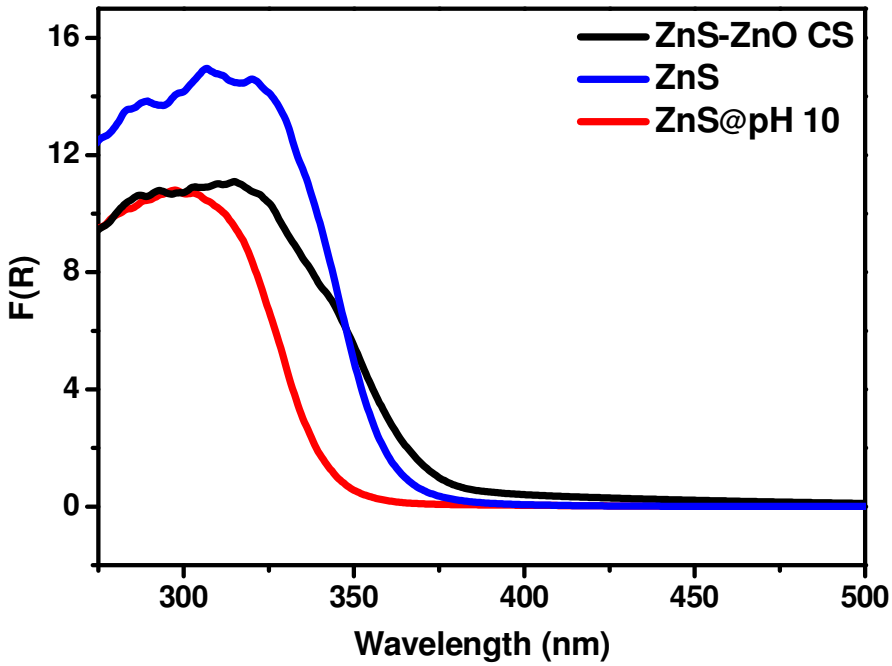

Figure 6.24: Absorption spectra of ZnS-ZnO CS, ZnS and ZnS synthesized at pH 10.

As can be seen in Figure 6.24, absorption spectra of ZnS-ZnO CSNPs is fairly red shifted as compared to that of ZnS and ZnS synthesized at pH 10 indicating an increased leakage of the exciton into the ZnO shell. The similar phenomenon has been reported by Dabbousi et al. [21]. They have observed red shift in absorption spectra of (CdSe) ZnS CS quantum dots. This shifting has increased as the thickness of the ZnS shell increases. It may be kept in mind that unlikely ZnS-ZnO CS NPs and ZnS, ZnS synthesized at pH 10 has not been heat treated. With heat treatment, the size of grains becomes larger and this is accompanied by red shift in absorption spectra. The observed red shift in absorption spectra of CS NPs as compared to ZnS is due to the growth of ZnO shell on ZnS core as both are treated under similar conditions (calcined at 250 °C for 3 h). The relation between the incident photon energy (hυ) and the absorption coefficient (α) or F(R) is given by [6]

$$[F(R)\,h\upsilon]^{1/n} = A(h\upsilon - E_g) \qquad (6.2)$$

where A is a constant and E_g is the band gap of the material and the exponent n depends on the type of the transition i.e. 2, 3, 1/2, 1/3 values corresponding to indirect allowed, indirect forbidden, direct allowed and direct forbidden transitions. As shown in the Figure 6.25,

square of the absorbed energy [F(R)hυ] has been plotted against photon energy (hυ) to determine the energy for direct gap transition. Band gap energies for all samples have been determined by extrapolating the straight portion of the graph on hυ axis at F(R)=0. Band gap values along with corresponding absorption wavelengths are given in Table 6.5.

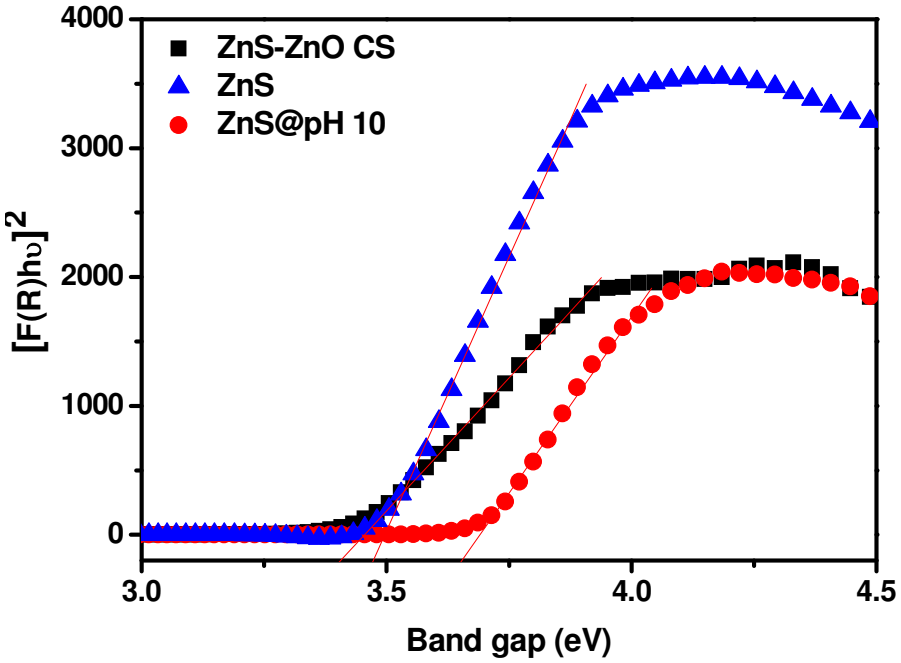

Figure 6.25: Tauc plots for ZnS-ZnO CS, ZnS and ZnS synthesized at pH 10 to determine band gap.

Table 6.5: Calculated band gap values and corresponding absorption wavelengths of ZnS@pH 10, ZnS and ZnS-ZnO CS.

Sample	Band gap (eV)	Absorption wavelength (nm)
ZnS@pH 10	3.66	339.44
ZnS	3.45	360.11
ZnS-ZnO CS	3.41	364.33

6.2.5 Photoluminescence studies

Figure 6.26(a) shows the photoluminescence emission spectra of as prepared ZnS-ZnO CSNPs at excitation wavelength, λ_{exc}=350 nm. Inset of the figure shows excitation spectra of the same sample at emission wavelength, λ_{em}=508 nm. As can be seen in the figure that these CS NPs show sharp excitation peak at 450 nm. Hence, emission spectra of this sample has also been recorded at 450 nm which is shown in Figure 6.26(b). At excitation of 350 nm, these particles exhibit weak emission spectra with a peak located at 508 nm. However, at

λ_{exc}=450 nm, the main emission peaks have been observed at 506 nm, 562 nm and 586 nm. For comparative study, excitation and emission spectra of ZnS as discussed in the section 6.1.2.4 has been plotted as shown in Figure 6.27. Unlikely CSNPs, ZnS exhibits sharp excitation peak at 350 nm at same emission wavelength. Hence, emission spectra at excitation wavelength of 350 nm has been recorded.

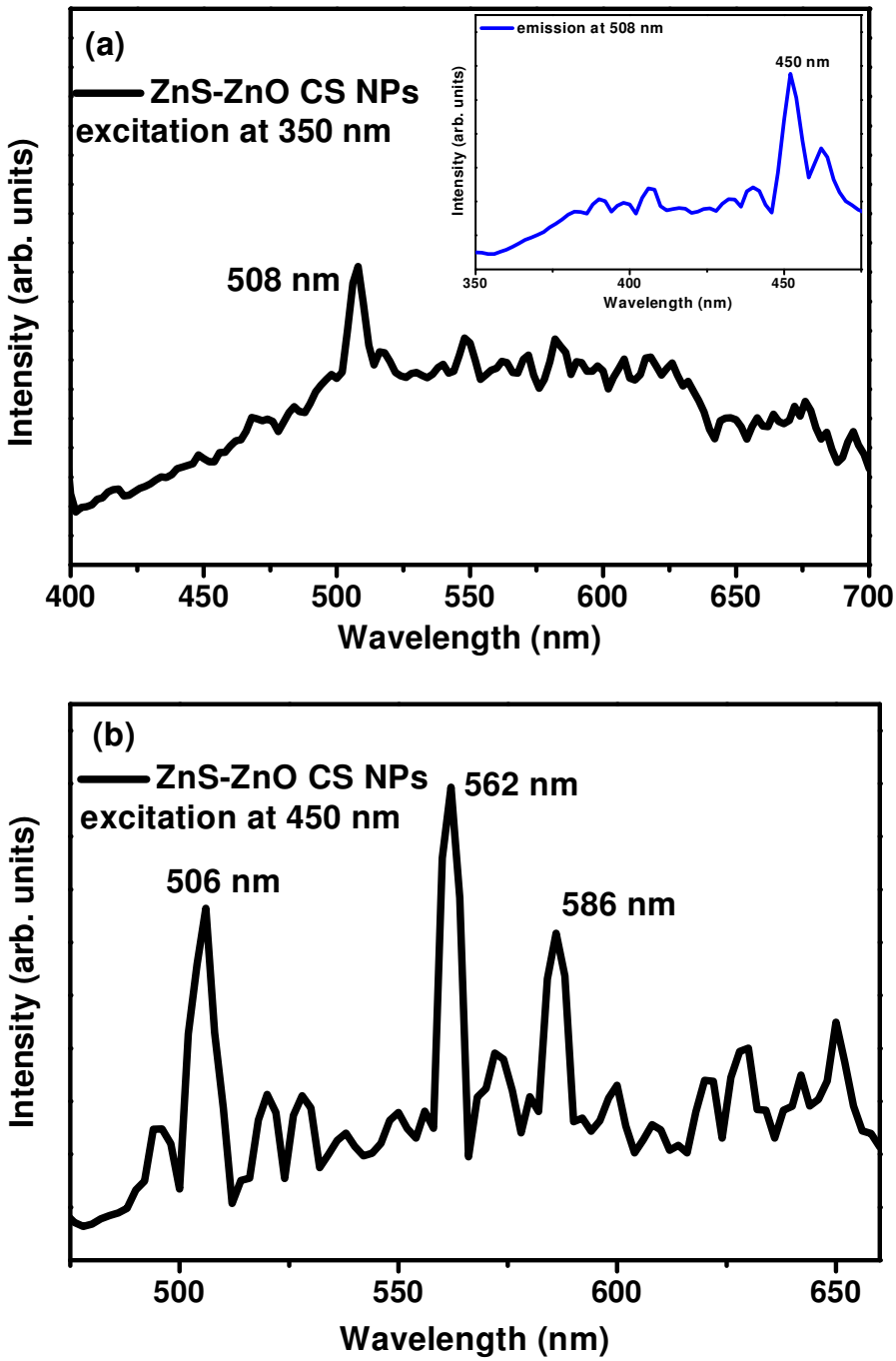

Figure 6.26: Photoluminescence emission spectra of ZnS-ZnO CSNPs (a) at λ_{exc}=350 nm. Inset of the figure shows excitation spectra at λ_{em}=508 nm and (b) at λ_{exc}=450 nm.

As can be seen in the figure, ZnS exhibit main emission peaks at 468 and 507 nm. It is well reported that emission peak in ZnS 460 nm is due to transfer of electron from sulphur vacancies to zinc vacancies [8-9]. As discussed in the section 6.1.2.4, 507 nm emission peak is due to sulphur species. In CS NPs, the emission peak at 506 nm is of less intensity while the most intense peak is located at 562 nm. It is generally reported that emission peaks located at ~ 560 nm and ~588 nm are due to oxygen deficiency [25-26]. Djurisic et al. [26] have attributed the orange band at around 596 nm to be due to oxygen interstitials. A careful comparison of the emission spectra of ZnS (Figure 6.27) and ZnS-ZnO CSNPs (Figure 6.26(a)) at fixed excitation wavelength of 350 nm shows that peak intensity related to sulphur species (~507 nm) has been reduced significantly in ZnS-ZnO CSNPs as compared to that of ZnS. However, at excitation wavelength of 450 nm, emission intensity corresponding to oxygen species is higher as compared to that of sulphur species in ZnS-ZnO CSNPs. This suggests that a layer of ZnO has formed on the surface of ZnS which has reduced the emission phenomenon related to sulphur. However, as ZnO is on surface, hence oxygen vacancies are more as compared to that of sulphur. As number of vacancies or defects is directly related to the emission intensity of that defect or vacancy related peak, hence emission intensity related to oxygen vacancies is higher.

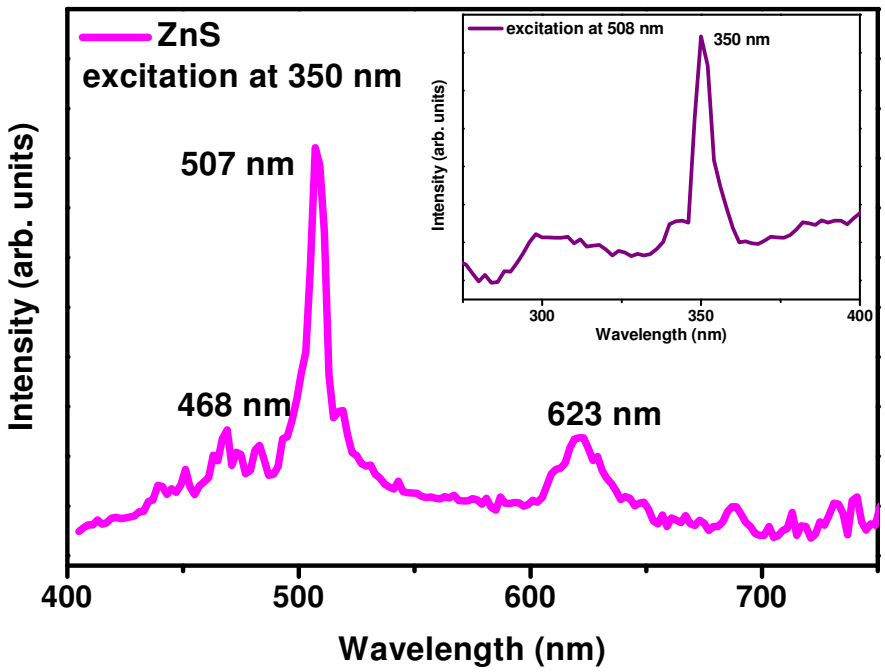

Figure 6.27: Photoluminescence emission spectra of ZnS/ZnO NCs at λ_{exc}=350 nm. Inset of the figure shows excitation spectra at λ_{em}=508 nm.

6.2.6 Photocatalytic studies

Photocatalytic degradation of crystal violet has been carried out to demonstrate the photocatalytic activity of as prepared ZnS-ZnO CSNPs. The characteristic absorption peak at 590 nm has been selected to monitor the photocatalytic degradation of the dye. Figure 6.28 shows the spectral changes occurring in the aqueous solution of crystal violet at different irradiation times in the presence of ZnS-ZnO CSNPs. The absorption peak corresponding to crystal violet has diminished gradually in presence of photocatalyst with increasing irradiation time. Figure 6.29 shows the adsorption and degradation behaviour of the dye catalysed with ZnS-ZnO CSNPs in terms of change in concentration with respect to the initial concentration of dye. By Beer Lambert law, the decrease in concentration of dye is recorded at different intervals of time to measure degradation rate. For comparative studies, results of ZnS (discussed in section 6.1.2.5) and ZnS synthesized at pH 10 (discussed in chapter 4) have been incorporated from the previous studies. The order of photo degradation rate is obtained as

ZnS-ZnO CS NPs > ZnS@pH 10 > ZnS

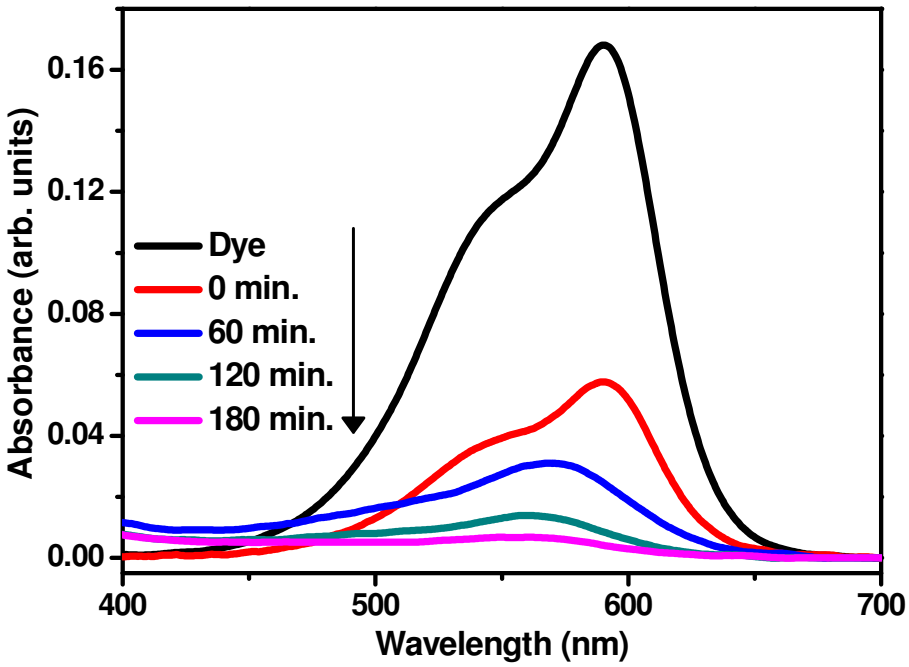

Figure 6.28: Absorbance spectra of crystal violet degraded in the presence of ZnS-ZnO CS.

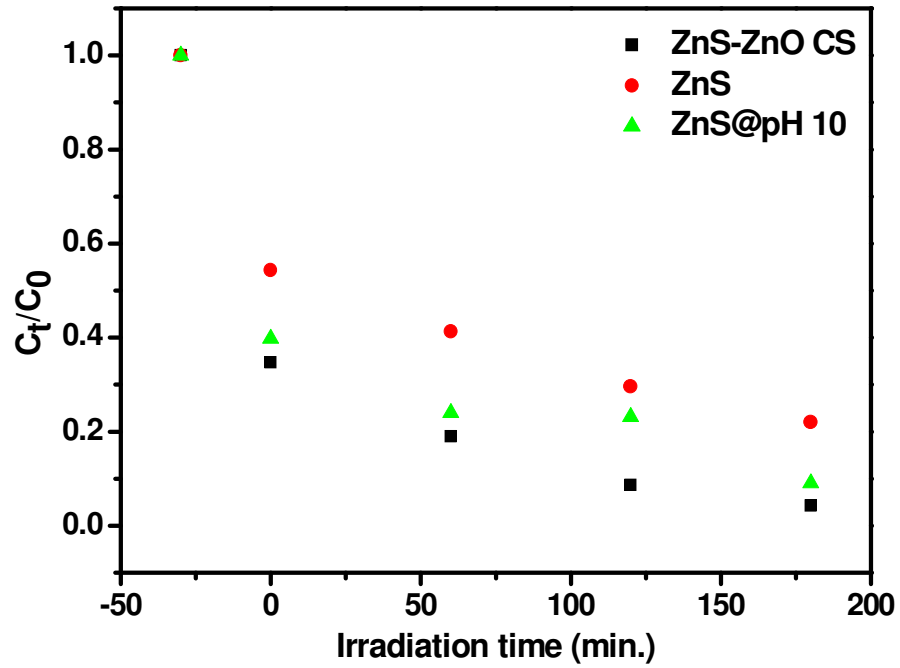

Figure 6.29: Variation of C_t/C_0 with irradiation time for ZnS-ZnO CS, ZnS and ZnS synthesized at pH 10.

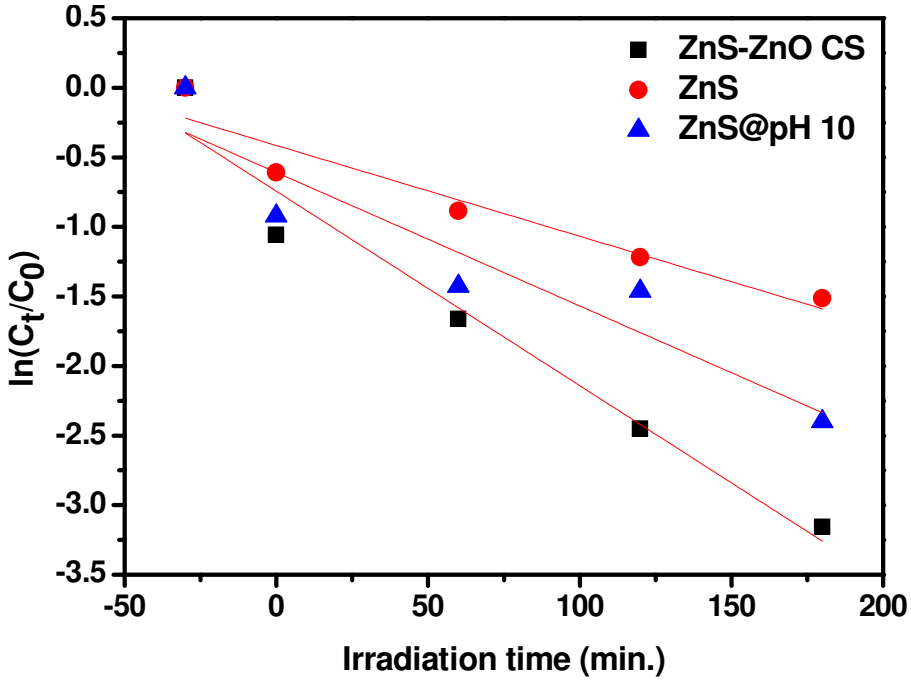

Figure 6.30: Plot between $\ln(C_t/C_0)$ and irradiation time to determine the value of rate constant k.

Since, in this study, concentration of solute is very low (1mg/L), so Langmuir-Hinshelwood kinetics model [13] can be simplified to pseudo first order kinetic model equation.

$$ln\left(\frac{C_t}{C_0}\right) = kT \qquad (6.3)$$

where C_t is the concentration of dye after irradiation in selected time interval, C_0 is the initial concentration of dye, k is the first order rate constant, and T is irradiation time.

The value of rate constant (k) for different photochemical reactions has been obtained from the slope of plots of Figure 6.30. Figure 6.31 shows % degradation of dye in different intervals of irradiation time. The percent degradation has been calculated as

$$\%D = \left(1 - \frac{C_t}{C_0}\right) \times 100 \qquad (6.4)$$

where C_t is the concentration of dye after irradiation in selected time interval, C_0 is the initial concentration of dye.

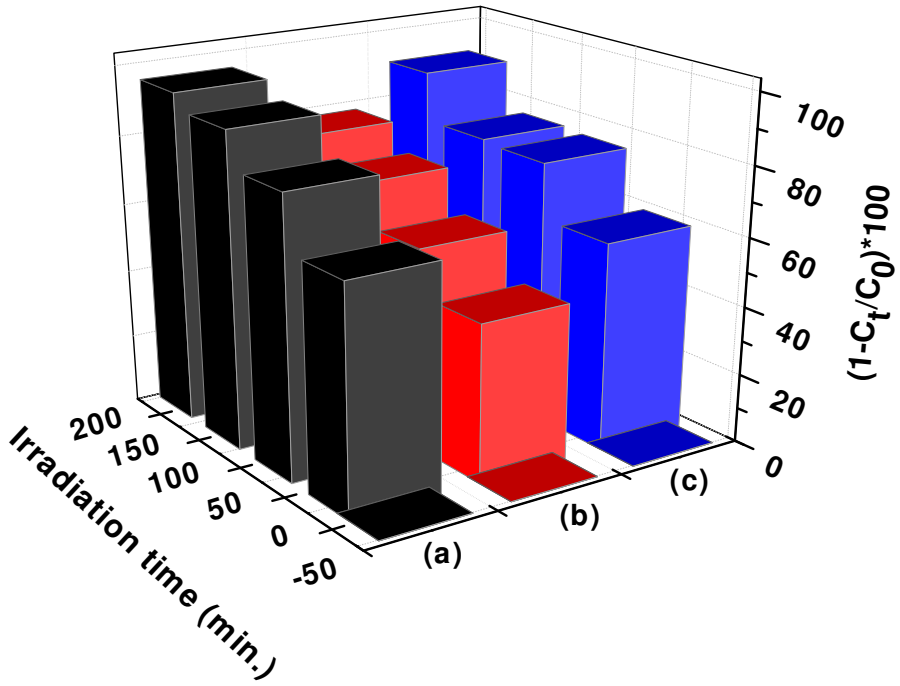

Figure 6.31: Degradation percentage of crystal violet in the presence of (a) ZnS-ZnO CS, (b) ZnS and (c) ZnS synthesized at pH 10 at different irradiation times.

Table 6.6: First order rate constants for the photocatalytic degradation of crystal violet and corresponding percent degradation using ZnS-ZnO CS, ZnS and ZnS synthesized at pH 10 as photocatalysts.

Photocatalyst	Adj. R^2	k (min^{-1})	$(1-C_t/C_0)*100$
ZnS	0.90	0.0065	77.98
ZnS@pH 10	0.85	0.0096	90.93
ZnS-ZnO CS	0.95	0.0140	95.75

Table 6.6 summarizes the value of rate constants and percent degradation obtained for photochemical reactions catalysed with as prepared samples. The value of k has been recorded to be largest (0.0140 min^{-1}) for the photochemical reaction catalysed with CSNPs as compared to that of other catalyst assisted photochemical reactions. Also, percent degradation in presence of CS NPs has been recorded to be highest (95.75%) among all the photocatalysts employed. In the present core shell system, one or both charge carriers are partially or completely confined in shell depending upon shell thickness [19]. When semiconductor is photoexcited, electrons in the valence band jump into conduction band leaving behind a hole in valence band. As small band gap semiconductor i. e. ZnO is also photoexcited simultaneously, hence more charge carriers will be available for the photocatalytic process. It has been reported by Lu et al. [27] that smaller band gap semiconductors need lower energy to produce charge carriers and also transfer of electrons between the core and the shell is more efficient. Furthermore, lifetime of the photogenerated charge carriers is also longer. In addition, relative band positions of both semiconductors also play a major role in charge carrier dynamics. The proposed mechanism is given in the Figure 6.32.

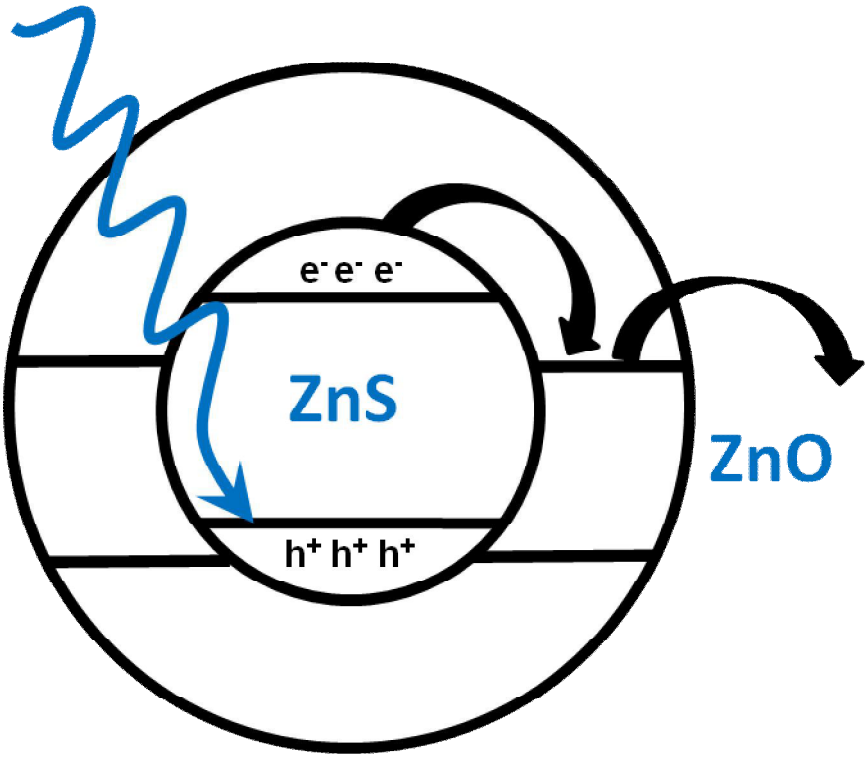

Figure 6.32: Proposed mechanism for photocatalytic application of ZnS-ZnO CSNPs.

The conduction band of ZnS lies at a more negative potential than that of ZnO, while the valence band of ZnO is more positive than that of ZnS. When ZnS is photoexcited, the generated electrons will be transferred to the conduction band of ZnO due to the very small

difference in the energy bands giving enough time to participate in the photocatalytic process. Further, capping of ZnO on ZnS has also led to the passivation of defect states which may act as non-radiative recombination centres. Further, it is well reported that oxygen vacancies can favour the adsorbed O_2 to capture photo-induced electrons, simultaneously producing $\cdot O_2$ radical groups and these radical groups are active to promote the oxidation of organic substances [28-29]. Thus, it is possible that oxygen vacancies and defects favour the photocatalytic reactions. In PL studies (section 6.2.5), emission peaks related to oxygen vacancies are stronger. Hence, the stronger the emission intensity in PL spectra, the larger the content of oxygen vacancies or defects and the higher will be the photocatalytic activity. In ZnS, various factors are responsible for the observed less photocatalytic activity. Less absorbance in near visible region, absence of surface modification and volume recombination has deteriorated the photocatalytic activity of ZnS. Further, ZnS synthesized at pH 10 (although organic capping with thioglycerol has been done) has shown less photocatalytic activity as compared to that of ZnS-ZnO CSNPs. Hence, we can say that ZnS-ZnO CSNPs can serve as a better photocatalyst as compared to bare or organically passivated semiconductor NPs.

References

[1] C. Kim, S.J. Doh, S.G. Lee, S.J. Lee and H.Y. Kim, Visible-light absorptivity of a zincoxysulfide (ZnO_xS_{1-x}) composite semiconductor and its photocatalytic activities for degradation of organic pollutants under visible-light irradiation. Applied Catalysis A-General, **330** (2007) 127-133.

[2] F.N. Gu, M.B. Yue, Z.Y. Wu, L.B. Sun, Y. Wang and J.H. Zhu, Enhanced blue emission from ZnS-ZnO composites confined in SBA-15. Journal of Luminescence, **128** (2008) 1148-1154.

[3] Y. Xiaodan, W. Qingyin, J. Shicheng, G. Yihang, 2006. Nanoscale ZnS/TiO_2 composites: Preparation, characterization, and visible-light photocatalytic activity. Materials Characterization, **57** (2006) 333-341.

[4] J. Yu, J. Zhang and S. Liu, Ion-Exchange Synthesis and Enhanced Visible-Light Photoactivity of CuS/ZnS Nanocomposite Hollow Spheres. Journal of Physical Chemistry C, **114** (2010) 13642-13649.

[5] W.J. Li, E.W. Shi and T. Fukuda, Particle size of powders under hydrothermal conditions. Crystal Research and Technology, **38** (2003) 847-858.

[6] C.C. Hu, J.N. Nian and H. Teng, Electrodeposited p-type Cu_2O as photocatalyst for H_2 evolution from water reduction in the presence of WO_3. Solar Energy Materials and Solar Cells, **92** (2008) 1071-1076.

[7] D. Beydoun, R. Amal, G. Low and S. McEvoy, Role of nanoparticles in Photocatalysis. Journal of Nanoparticle Research, **1** (1999) 439-458.

[8] A.K. Kole, C.S. Tiwary and P. Kumbhakar, Ethylenediamine assisted synthesis of wurtzite zinc sulphide nanosheets and porous zinc oxide nanostructures: near white light photoluminescence emission and photocatalytic activity under visible light irradiation. Crystal Engineering Communications, **15** (2013) 5515-5525.

[9] R. Sarkar, C.S. Tiwary, P. Kumbhakar, S. Basu and A.K. Mitra, Yellow-orange light emission from Mn^{2+}-doped ZnS nanoparticles. Physica E, **40** (2008) 3115-3120.

[10] J. Shi, J. Chen, Z. Feng, T. Chen, Y. Lian, X. Wang and C. Li, Photoluminescence Characteristics of TiO_2 and Their Relationship to the Photoassisted Reaction of Water/Methanol Mixture. Journal of Physical Chemistry C, **111** (2007) 693-699.

[11] C.H. Ye, X.S. Fang, G.H. Li and L.D. Zhang, Origin of the green photoluminescence from zinc sulfide nanobelts. Applied Physics Letters, **85** (2004) 3035-3037.

[12] J. Liqiang, Q. Yichun, W. Baiqi, L. Shudan, J. Baojiang, Y. Libin, F. Wei, F. Honggang and S. Jiazhong, Review of photoluminescence performance of nano-sized semiconductor materials and its relationships with photocatalytic activity. Solar Energy Materials & Solar Cells, **90** (2006) 1773-1787.

[13] C. Lizama, J. Freer, J. Baeza and H. Mansila, Optimized photodegradation of Reactive Blue 19 on TiO_2 and ZnO suspensions. Catalysis Today, **76** (2002) 235-246.

[14] S.T. Tan, B.J. Chen, X.W. Sun, W.J. Fan, H.S. Kwok, X.H. Zhang and S.J. Chua, Blueshift of optical band gap in ZnO thin films grown by metal-organic chemical-vapor deposition. Journal of Applied Physics **98** (2005) 013505(1)-013505(5).

[15] L. Xu, B. Wei, W. Liu, H. Zhang, C. Su and J. Che, Flower-like ZnO-Ag_2O composites: precipitation synthesis and photocatalytic activity. Nanoscale Research Letters **8** (2013) 536(1-7).

[16] X. Fan, X.-M. Meng, X.-H. Zhang, S.-K. Wu and S.-T. Lee, Formation of ZnS/SiO_2 nanocables. Applied Physics Letters **86** (2005) 173111-173111-3.

[17] R.G. Chaudhuri and S. Paria, Optical Properties of Double-Shell Hollow ZnS-Ag_2S Nanoparticles. Journal of Physical Chemistry C **117** (2013) 23385-23390.

[18] H. Zhang, B. Wei, L. Zhu, J. Yu, W. Sun and L. Xu, Cation exchange synthesis of ZnS-Ag_2S microspheric composites with enhanced photocatalytic activity. Applied Surface Science **270** (2013) 133-138.

[19] P. Reiss, M. Protière and L. Li, Core/Shell Semiconductor Nanocrystals. Small, **5** (2009) 154-168.

[20] D. Jiang, L. Cao, W. Liu, G. Su, H. Qu, Y. Sun and B. Dong, Synthesis and Luminescence Properties of Core/Shell ZnS:Mn/ZnO Nanoparticles. Nanoscale Research Letters, **4** (2009) 78-83.

[21] B.O. Dabbousi, J.R. Viejo, F.V. Mikulec, J.R. Heine, H. Mattoussi, R. Ober, K.F. Jensen and M.G. Bawendi, (CdSe) ZnS Core-Shell Quantum Dots: Synthesis and Characterization of a Size Series of Highly Luminescent Nanocrystallites. Journal of Physical Chemistry B, **101** (1997) 9463-9475.

[22] D. Perera, R. Lorek, R.S. Khnayzer, P. Moroz, T. O'Connor, D. Khon, G. Diederich, E. Kinder, S. Lambright, F.N. Castellano and M. Zamkov, Photocatalytic Activity of Core/Shell Semiconductor Nanocrystals Featuring Spatial Separation of Charges. Journal of Physical Chemistry C, **116** (2012) 22786−22793.

[23] D. Lin, H. Wu, R. Zhang, W. Zhang and W. Pan, Facile Synthesis of Heterostructured ZnO-ZnS Nanocables and Enhanced Photocatalytic Activity. Journal of the American Ceramic Society, **93** (2010) 3384-3389.

[24] S. Yamabi and H. Imai, Growth conditions for wurtzite zinc oxide films in aqueous solutions. Journal of Materials Chemistry, **12** (2002) 3773-3778.

[25] M.L. Cui, X.M. Wu, L.J. Zhuge and Y.D. Meng, Effects of annealing temperature on the structure and photoluminescence properties of ZnO films. Vacuum, **81** (2007) 899-903.

[26] A.B. Djurišić, Y.H. Leung, K.H. Tam, L. Ding, W.K. Ge, H.Y. Chen and S. Gwo, Green, yellow and orange defect emission from ZnO nanostructures: Influence of excitation wavelength. Applied Physics Letters, **88** (2006) 103107-103109.

[27] M.Y. Lu, J. Song, M.P. Lu, C.Y. Lee, L.J. Chen and Z.L. Wang, ZnO-ZnS Heterojunction and ZnS Nanowire Arrays for Electricity Generation. ACS Nano, **3** (2009) 357-362.

[28] A.L. Linsebigler, G. Lu and Jr. J.T. Yates, Photocatalysis on TiO_2 Surfaces: Principles, Mechanisms, and Selected Results. Chemical Reviews, **95** (1995) 735-758.

[29] M.R. Hoffmann, S.T. Martin, W. Choi and D. Bahnemann, Environmental applications of semiconductor photocatalysis. Chemical Reviews, **95** (1995) 69-96.

CHAPTER 7
CONCLUSIONS AND FUTURE SCOPE

Overview

The present chapter summarizes the results obtained from various experiments discussed in the previous chapters. Effect of UV irradiation and pH of the solution (in which NPs are being synthesized) on photocatalytic properties of undoped ZnS have been summarized. Results obtained from the studies of doped ZnS NPs have also been concluded. Further, conclusions made from the study of composites and core shell particles have also been summarized. Based on the observation of the present work, some suggestions to carry out more work in this field have been given at the end of this chapter.

7.1 Conclusions

In the present work, ZnS nanoparticles (NPs) with varying experimental conditions are synthesized. The main objective behind this work was to study the effect of various experimental conditions on structural and optical properties of ZnS nanoparticles (NPs) with the aim to utilize them in photocatalytic degradation of organic pollutants. ZnS NPs have been successfully doped with different concentrations of Cu, Ni and Mn ions by chemical precipitation method. ZnS has also been modified by Ag_2S NPs with the aim to utilize them in the field of photocatalysis. Structural, optical and photocatalytic properties of ZnS/ZnO nanocomposites (NCs) and ZnS-ZnO core shell nanoparticles (CS NPs) have also been investigated.

For comparison purposes, structural and optical studies of undoped ZnS NPs have been done. XRD pattern has shown the diffraction peaks corresponding to pure zinc blende phase. Peak broadening has been attributed to the formation of ZnS NPs. From, UV-Vis studies, it has been concluded that the absorption spectra of as prepared ZnS NPs has been fairly blue shifted as compared to its bulk counterpart indicating quantum confinement effect. Successful capping of thioglycerol (TG) on the surface of NPs has been confirmed from TEM and FTIR studies. Photoluminescence spectra of undoped ZnS have shown three emission peaks located at 364, 397 and 436 nm. Emission peak observed at 436 nm has been attributed to the presence of sulphur vacancies acting as donors, releasing electrons into the valence band during the transition. In our case, emission peak due to sulphur interstitials (392 nm) is lower than that of emission related to sulphur vacancies. Therefore, sulphur interstitial sites were more likely to become passivated by TG as compared to sulphur vacancies. Photocatalytic studies of undoped ZnS NPs have been investigated by employing crystal violet as a model pollutant. The value of rate constant has come out to be 0.0082 min^{-1} according to the first-order rate kinetics. The degradation percentage in this photochemical reaction has come out to be 85.35%. Apart from this, UV irradiation studies of undoped ZnS NPs have shown better photocatalytic activity. The proposed mechanism for this observation has also been discussed. Also, structural, optical and photocatalytic studies of ZnS NPs synthesized at different pH values i. e. 5.6, 8, 10 and 12 have revealed that instead of particle size, it is the pH of the solution (in which NPs are being prepared) which plays dominant role in the process of photocatalysis. Photoluminescence studies show the decrease in overall intensity of ZnS NPs with the increase in pH of solution from 5.6 to 8, 10 and 12. The decrease in intensity has been attributed to the decrease in surface defects as pH is increased. Photocatalytic studies show the superior photocatalytic activity of the photocatalyst prepared

at pH 12 as compared to other photocatalysts. Lower PL intensity of ZnS synthesized at pH 12 has led to the lower recombination rate of photo-induced electron-hole pairs which has led to the higher photocatalytic activity of this sample. It has also been emphasized that interaction of dye molecules with catalyst surface largely depends on the surface charge of both. If the dye is cationic in nature, then the catalyst surface should be negatively charged in order to have sufficient adsorption. The dye (crystal violet) used in this work is cationic in nature. So, ZnS synthesized at pH 12 has facilitated more adsorption of dye molecules and hence more degradation has been observed.

Doping of metal ions have profound effect on structural, optical and photocatalytic properties of ZnS. XRD patterns of doped NPs have shown decreased crystallinity as compared to that of undoped ZnS. This has been attributed to the substitution of metal ions (Cu, Mn and Ni) in the host ZnS lattice. EDS spectra of all the doped samples have confirmed the presence of main elements i. e. Zn, S and M in M doped samples (M=Cu, Ni, Mn). In Cu dopd samples, sufficient absorption in near visible region as compared to that of undoped ZnS has been observed. Similarly, absorption has also enhanced in near visible region incase of Ni and Mn doped ZnS NPs. Alongwith enhancement in absorption in near visible region, a red shift in absorption spectra has also been observed indicating reduction in the optical band gap. However, in case of Ni doped ZnS, a blue shift has been observed in $Zn_{1-x}Ni_xS$; x = 0.04 which has been attributed to the Burstein-Moss shift. Photoluminescence studies have shown the effect of doping on the emission properties of ZnS. Incase of Cu doped ZnS, emission has been shifted to green region as compared to that of undoped ZnS which emit in blue region. It has been reported in literature that blue emission corresponds to the Cu ions lying in the interstices of ZnS lattice and green emission is observed when Cu ions substitute for Zn^{2+} ions in the lattice. Hence, it confirms the successful doping of Cu ions in ZnS. However, in case of Ni ion doped ZnS, luminescence quenching has been observed with the increase in doping content. Based on literature reports, it has been discussed that photoexcited electrons have preferentially been transferred to nickel ion induced trapping centres as compared to anion vacancy defect centres which have acted as non radiative recombination centres thereby reducing the emission intensity. Incase of Mn doped ZnS, Mn^{2+} ions have been substituted for host cation sites which is attributed to the mixing between the s-p electrons of the host ZnS and the d electrons of Mn^{2+} which makes the forbidden transition of $^4T_1$ - $^6A_1$ partially allowed, resulting in the characteristic emission of Mn^{2+}. Contrary to this, the addition of Mn^{2+} ions to the outside of preformed ZnS results in ultraviolet emission [35]. Hence, it has been confirmed that Mn^{2+} is being substituted in the host lattice. This emission

peak keeps on increasing with the increase in doping content. No luminescence quenching has been observed even at higher Mn dopant concentration which is in line with the previously reported results. Phtotcatalytic studies of these doped ZnS NPs have revealed that Cu doping is most efficient in enhancing photocatalytic properties of ZnS due to trapping of electrons and holes by Cu ions which extends the lifetime of charge carriers and hence prevents e^--h^+ recombination. The optimal Cu ion content for the efficient degradation of crystal violet is determined to be $Zn_{1-x}Cu_xS$; x = 0.03. Degradation of upto 99% has been achieved when $Zn_{1-x}Cu_xS$; x = 0.03 is used as photocatalyst as compared to that of undoped ZnS with the aid of which 85% degradation is observed. Contrary to this, Ni and Mn doped samples have shown decreased photocatalytic activity of ZnS NPs. The decrease in photocatalytic activity of Ni doped samples as compared to that of undoped ZnS has been attributed to the effect of Ni^{2+} ions. As discussed in PL studies, these ions have acted as non radiative recombination centres thereby preventing the charge carriers to participate in the photocatalytic process. Decreased photocatalytic activity of Mn doped ZnS NPs ($Zn_{1-x}Mn_xS$; x =0.01 and 0.02) has also been explained by the photoluminescence results. As discussed in PL results, there is efficient transfer of energy from host ZnS to Mn^{2+} ion which implies that efficient radiative recombination has resulted from this transition. However, in a photocatalytic process, maximum charge separation is needed to make the charge carriers available to participate in the processes which are taking place on the surface of semiconductor photocatalyst. In photoluminescence, efforts are being made to make the radiative recombination dominant to achieve high quantum yield. In this way, photoluminescence and photocatalytic processes are different. However, at higher dopant concentrations ($Zn_{1-x}Mn_xS$; x =0.03 and 0.04), ZnS related emission peaks have appeared indicating less efficient transfer from host to impurity ion. Here some charge carriers are available for the degradation of dye causing a slight increase in photocatalytic activity in presence of $Zn_{1-x}Mn_xS$; x =0.03 and 0.04. During the synthesis of $Zn_{1-x}Ag_xS$; x =0.01 and 0.02, RSAg complex alongwith Ag_2S and ZnS has formed which is responsible for observed decrease in PL intensity and photocatalytic activity. UV-Vis studies have shown the enhanced absorption characteristics in near visible region. However, decrease in absorbance in UV region has been observed incase of $Zn_{1-x}Ag_xS$; x =0.03 and 0.04 which is attributed to the loading of Ag_2S on the surface of ZnS. Band gap has also been significantly reduced with the increase in $AgNO_3$ content. The decrease in PL emission intensity from $Zn_{1-x}Ag_xS$; x =0 to 0.02 is attributed to the inhibition of penetration of light into ZnS due to the formation of RSAg complex. Slight increase in emission intensity has been attributed to the passivation of

the core surface and the elimination of the surface trap states. This intensity is still less than that of undoped ZnS indicating that there is sufficient relaxation of charge carriers due to strong coupling of ZnS and Ag_2S. Similar to the PL emission results, photocatalytic activity of $Zn_{1-x}Ag_xS$; x =0.01, 0.02 has also been reduced due to the inhibition of penetration of light into ZnS by RSAg complex. However, an appreciable enhancement in photocatalytic activity of $Zn_{1-x}Ag_xS$; x =0.03 and 0.04 has been observed. This is due to coupling of ZnS and Ag_2S due to which the photogenerated electrons in conduction band of ZnS are transported to the conduction band of Ag_2S and hence participate in photocatalytic process. Degradation percentage in case of $Zn_{1-x}Ag_xS$; x = 0.04 has come out to be 93.95% which is quite higher than that of undoped ZnS.

The concluding remarks of this discussion are that dopant ions may reduce or enhance the photocatalytic activity of a semiconductor depending upon the type of transition involved in the emission pathway. It is well known fact that composites can change/enhance the overall optical properties of a material than its constituents. ZnS/ZnO NCs have shown enhanced absorption characteristics in near visible region. The effect of particle size on emission intensity is clearly visible in PL emission spectra. As the ZnO content in the system has increased, the corresponding PL emission intensity has decreased. All the composites have shown enhanced photocatalytic activity due to enhanced absorption characteristics. Dependence of pH of solution in which composites have been synthesized has also been discussed. Photocatalytic activity has increased with the increase in pH of the solution. Degradation percent in presence of ZnO_xS_{1-x}; x=0.5 has been recorded to be highest (95.63%) among all the NCs. The observed decrease in photocatalytic activity of ZnO_xS_{1-x}; x=0.75 has been attributed to the increase in particle size due to which volume recombination has taken place thereby decreasing photocatalytic activity. This study has demonstrated the combined effect of pH (in which the photocatalyst is being synthesized), absorption and emission characteristics of the photocatalyst in investigating the photocatalytic properties of the same. The UV irradiation studies have resulted in better degradation of crystal violet, hence, the as synthesized core of ZnS has been UV irradiated and after that ZnO shell has been grown. These CS NPs have shown enhanced optical and photocatalytic studies as compared to ZnS alone. The emission intensity related to oxygen vacancies is higher as compared to that of sulphur vacancies which suggests that surface of ZnS has been passivated by ZnO shell. It is well reported that oxygen vacancies can favour the adsorbed O_2 to capture photo-induced electrons, simultaneously producing $\cdot O_2$ radical groups and these radical groups are active to promote the oxidation of organic substances. Thus, it is possible that oxygen vacancies and

defects favour the photocatalytic reactions. Percent degradation in presence of CS NPs has been recorded to be highest (95.75%). These CS NPs have shown superior photocatalytic activity as compared to that of ZnS alone and thioglycerol capped ZnS NPs synthesized at pH 10. Hence, ZnS-ZnO CS NPs can serve as a better photocatalyst as compared to bare or organically passivated semiconductor NPs.

7.2 FUTURE SCOPE

Although extensive study has been done to improve photocatalytic properties of ZnS, still there are many more possibilities of further investigations. Based on the present work, the suggested possibility to further improve the efficiency of this photocatalyst can be undertaken. These are listed below.

- Based on the above studies, effect of UV irradiation can be investigated on optical and photocatalytic properties of organically passivated semiconductor photocatalysts.
- In our work, Cu doping in ZnS has shown remarkable enhancement in photocatalytic activity. Hence to further improve the activity, Cu doped ZnS can be synthesized at different pH to get the optimum synthesis conditions for superior photocatalytic activity.
- Composites with suitable band gap positions can be synthesized by simple chemical precipitation method. Further, effect of suitable doping can also be investigated on photocatalytic properties of doped composites.
- Ratio of ZnS-ZnO core-shell can be optimized to get the desired optical and photocatalytic properties.
- Based on our preliminary results (not discussed here), effect of temperature (at which photochemical reaction has been carried out) can be investigated as very small variation in temperature has enhanced the photocatalytic activity of doped ZnS NPs.